Numerical and Experimental Analysis of Injection and Mixture Formation in High-Performance CNG Engines

Doctoral Dissertation
Doctoral Program in Energy Engineering (30th Cycle)

Numerical and Experimental Analysis of Fuel Injection and Mixture Formation in High-Performance Natural Gas Engines

Methodologies and Applications

Jiajie Xu

Supervisors

Prof. Mirko Baratta, Supervisor
Prof. Ezio Spessa, Co-Supervisor

Doctoral Examination Committee

Prof. Stefano Fontanesi, Università degli Studi di Modena e Reggio Emilia
Prof. José Pastor, Universidad Politècnica de València
Prof. Tommaso Lucchini, Politecnico di Milano
Prof. Stefano D'Ambrosio, Politecnico di Torino
Prof. Roberto Finesso, Politecnico di Torino

Politecnico di Torino
December 28, 2018

Contents

1 INTRODUCTION 1

1.1 A TECHNO-ENVIRONMENTAL DILEMMA 2
1.2 THE ACCELERATING CHALLENGES 3
1.2.1 CO_2 emission and climate change 3
1.2.2 Noxious emissions and air pollution 6
1.2.3 Fuel consumption and energy security 9
1.3 NATURAL GAS AS AN ALTERNATIVE FUEL 11
1.3.1 Characteristics of natural gas 12
1.3.2 SI stoichiometric natural gas engines 15
1.3.3 SI lean burn natural gas engines 22
1.3.4 CI natural gas engines 26
1.4 FINAL REMARKS ON NATURAL GAS FUELING 29
1.4.1 A proposal for engine solution 29
1.4.2 Sources and supplies 31
1.4.3 Costs 33
1.4.4 A viable gas future 35

2 PISI NATURAL GAS ENGINE 38

2.1 BACKGROUND 39
2.1.1 Port injection of natural gas 39
2.1.2 Underexpanded gas jet 44
2.1.3 RANS and turbulence modeling 49
2.2 ENGINE CONFIGURATION 53
2.3 NUMERICAL MODEL DESCRIPTION 54
2.3.1 Computational domain 54
2.3.2 Numerical modeling strategies 55
2.3.3 Injector model 57
2.4 RESULTS OF INJECTOR MODELING 58
2.4.1 Source cell locations 58
2.4.2 Grid dependence 62

2.4.3 Injector model validation 67
2.5 RESULTS OF MIXTURE FORMATION 71
2.5.1 Injection timing and inter-cylinder fuel distribution 71
2.5.2 Two-stage mixing process 72
2.5.3 Injection timing and mixture formation 76
2.5.4 Injected fuel traveling 80
2.6 COMPARISON WITH PREMIXED SIMULATION 82
2.6.1 Intake mass flow rate 82
2.6.2 Volumetric efficiency 84
2.6.3 Turbulence level and flow motion 85

3 DIRECT GAS INJECTOR 90

3.1 BACKGROUND 91
3.2 SCHLIEREN FLOW VISUALIZATION 91
3.2.1 Fundamentals of schlieren optics 92
3.2.2 Experimental setup 95
3.2.3 Image processing 97
3.2.4 Schlieren imaging results 98
3.3 NUMERICAL MODELING OF TRANSIENT INJECTION 101
3.3.1 Outward-opening injector model 101
3.3.2 Computational domain 104
3.3.3 Numerical modeling strategies 105
3.3.4 Transport of species 110
3.4 NUMERICAL RESULTS AND DISCUSSION 115
3.4.1 Jet penetration 115
3.4.2 Jet structure comparison 116
3.4.3 Nearfield underexpansion structure 124
3.4.4 Transient jet development 127
3.4.5 Mixing characteristics 129
3.4.6 Jet unsteadiness and asymmetry 131

4 DISI NATURAL GAS ENGINE 133

4.1 BACKGROUND 134
4.2 ENGINE CONFIGURATION 137
4.3 PLIF EXPERIMENT 139
4.3.1 Fundamentals of LIF photophysics 140
4.3.2 Experimental setup 145

4.3.3 Image processing 146
4.4 NUMERICAL MODELING 148
4.5 RESULTS AND DISCUSSION 150
4.5.1 Injector implementation 150
4.5.2 Mixture formation: low-end full-load 153
4.5.3 Mixture formation: low-speed part-load 157
4.5.4 Mixture formation: high-speed full-load 163
4.5.5 Engine power curve 166

5 CONCLUSIONS 168

REFERENCES 177

ACKNOWLEDGMENT 217

> No one is an artist unless he carries his picture in his head before painting it, and is sure of his method and composition.
>
> — Claude Monet

Chapter 1

INTRODUCTION

…We envisage a world free of poverty, hunger, disease and want, where all life can thrive. We envisage a world free of fear and violence. A world with universal literacy…

…A world where human habitats are safe, resilient and sustainable and where there is universal access to affordable, reliable and sustainable energy…

…We envisage a world of universal respect for human rights and human dignity, the rule of law, justice, equality and non-discrimination; of respect for race, ethnicity and cultural diversity; and of equal opportunity permitting the full realization of human potential and contributing to shared prosperity…

…A world in which consumption and production patterns and use of natural resources – from air to land, from rivers, lakes and aquifers to oceans and seas – are sustainable…

…One in which humanity lives in harmony with nature and in which wildlife and other living species are protected…

— The United Nations

"Transforming our world: the 2030 Agenda for Sustainable Development"

1.1 A Techno-environmental dilemma

There is a dilemma, as there is always a dilemma, a dilemma which the entire transport industry and all the end consumers have been striving to reconcile – the dilemma between the rising demand for the freedom of human mobility and the imperative to curb the negative environmental impacts caused by such services in which energy is converted through human devices.

The logic behind such statement is that, before pinpointing the technicalities, or in other words, answering the question "how", another preceding question is to be first answered – "why" we have to do a certain thing and hence why we have to know "how" to. Specific to the automotive industry, the answer to questions like "why internal combustion engines", "why burning fuels", "why more horsepower" or even "why cars" in the first place is that humans always crave for mobility, the freedom to move people and goods around effortlessly and comfortably. Then the reason for the decade-long endeavors to improve fuel economy and reduce exhaust emissions is to try to decelerate the natural environment deterioration and resource depletion accompanying the ever-accelerating number of automobiles on the road. Therefore, it is appropriate to articulate first and foremost the mobility-environment dilemma, the origin of all technical details then to cope with it.

To simply recognize the dilemma in such way, nonetheless, is a misconception, given the fact that the very existence of humanity, along with the freedom thereof, is naturally and undeniably underpinned by the sustained health of the planet Earth and its environment. It would be rather transgressing to conceive that the human mobility and the natural environment are the two equivalently important ends of a dilemma. However, human beings nowadays are too profoundly accustomed to the contemporary living standard to be willing to compromise, if not entirely abnegate, the comfort and convenience granted by those modern technologies that in many cases have detrimental effects on the environment.

As a consequence, underlain by the fact that all transport technologies in sight have environmental impacts to a greater or lesser degree, the real dilemma consists in preserving the environment while minimizing the concession of comfort people have to make, or alternatively, in maintaining or even improving the quality of life

through technological development and policy making, provided meanwhile that its environmental impacts can be well contained within appropriate limits, appropriate enough for the future sustenance of humanity at the very least. The latter statement of the dilemma, albeit optimistic about the sensitivity and adaptability of the Earth's environment, is more acceptable and practical, and is the ideology that has been encouraging the collective effort of continuing researches in the transport sector including academic researchers, vehicle manufacturers, transport service providers and infrastructure constructors.

Indeed, engineering, as much as life in that regard, is in essence a rigorous art, the art of dealing with dilemmas, of hence seeking the best or the most acceptable compromises, the optimum trade-offs in various fields, novel or traditional, through the application of knowledge and experience that the human race has accumulated with respect to the nature.

1.2 The accelerating challenges

The aforementioned techno-environmental ideology, rather than that of chasing pure technological indulgence only to achieve the freedom of mobility, has emerged as the motivation for the research and development activities in the global transport sector for the past decades, and will most likely continue to do even more so for the decades to come, as a result of growing environmental awareness worldwide. This is particularly true for the automotive industry, being a fundamental pillar and the most diffused and diversified element of the modern mobility system, and playing a key role in the economic activity and social connectivity. Indeed, the enormous and still ballooning number of in-use passenger and freight transport vehicles are manifesting consequences that have already had or will have adverse effects on the ecological and human well-being. Such great number and ubiquitousness, on the bright side, nonetheless, implies great relevance, responsibility and potential of the automotive industry to exert its influences in reshaping the human-environmental interactions, in order to address the deteriorating environment situation on a broad and significant scale.

In particular, internal combustion (IC) engines, which will continue to serve as the absolutely dominant technical solution to modern transportation as expected in the foreseeable future (IC engine-powered vehicles projected to account for about 90% share of the global fleet up to 2040 [1]), must meet challenges coming from three main environment-oriented aspects.

1.2.1 CO_2 emission and climate change

According to the United Nations Framework Convention of Climate Change

(UNFCCC) [2], climate change is defined as a change of climate which is attributed directly or indirectly to human activity that alters the composition of the global atmosphere and which is in addition to the natural climate variability observed over comparable time periods. Climate change attributable to human activities is thus distinguished from climate variability attributable to natural causes. Admittedly, anthropogenic interference with the climate system is clearly occurring, and in fact it is found that human influence has extremely likely been the predominant cause of the observed global warming since the mid-20th century [3].

Various adverse impacts of global warming on both natural and human systems have been manifesting on all the continents and across the oceans as the global average temperature continues to rise above preindustrial levels in century-scale term (see Figure 1.1). Water resources are affected by changing precipitation pattern, melting snow and ice, warming and thawing permafrost, and worldwide glacier retreat, as a result of alteration of the hydrological systems. Terrestrial, freshwater and marine plant and animal species are undergoing geographical and biological shifts, such as increased tree mortality, northward and deep distributional shifts of zooplankton and fishes, and coral bleaching and coral reef decline. In terms of food production, negative impacts of global warming on crop yield are more common than positive ones. Moreover, ecosystems and humanity are being exposed to the increase in climate extremes like heat waves, droughts, floods, cyclones and

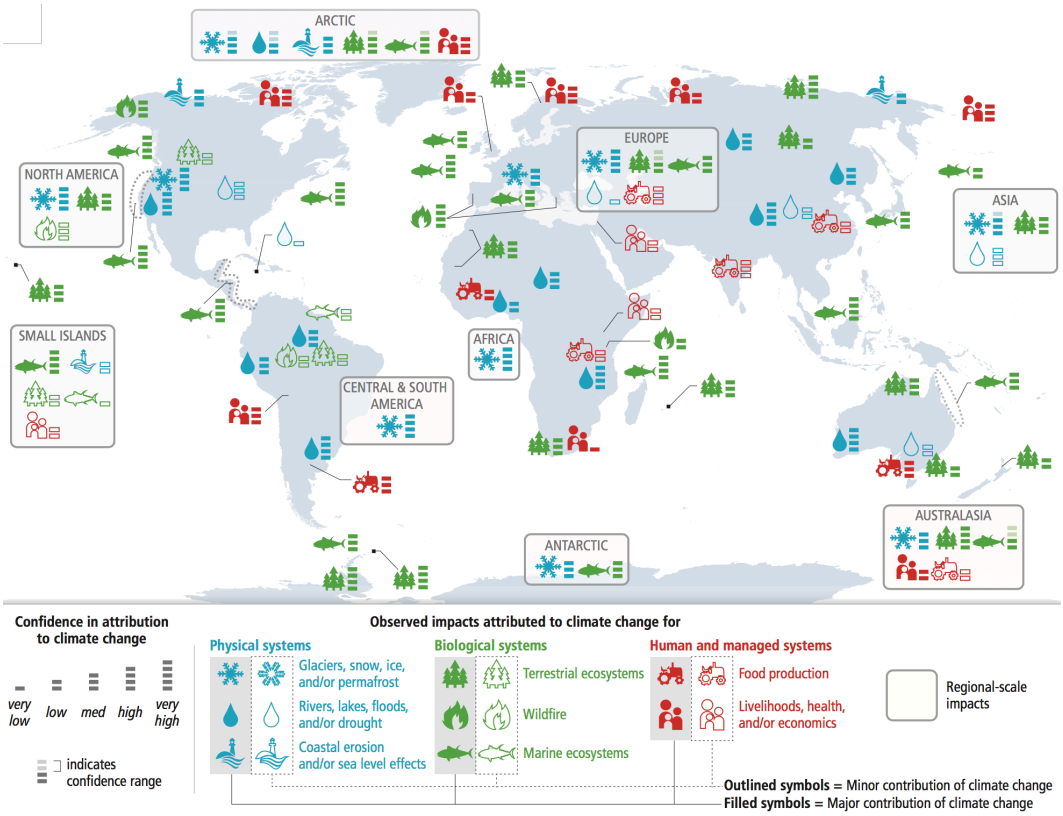

Figure 1.1 Global patterns of impacts in recent decades attributed to climate change [4]

wildfires which often lead to disruption of food and water supply, infrastructure and settlement damage or even morbidity and mortality. Rising sea level due to water thermal expansion and ice sheet shrinkage, especially in the Arctic and Greenland, has also provoked growing concerns.

The predominant human influence on the climate system has been the emission of greenhouse gas (GHG) species including carbon dioxide (CO_2), methane (CH_4), nitrous oxide (N_2O) and fluorinated gases, which are collectively measured in terms of CO_2-equivalents, or CO_2eq, based on their Global Warming Potentials (GWP) regarding a hundred-year time horizon. Over the period between 1970 and 2010, the annual anthropogenic GHG emissions have continued to grow at an accelerating pace, with larger absolute increase in more recent period and the largest emission in human history in the last decade. In particular, CO_2 emissions from fossil fuel combustion and industrial processes have always contributed the most and the percentage is still increasing (see Figure 1.2). This trend is mainly driven by the global economic and population growth that is expected to continue, as a result of the unambiguous connection between energy consumption and wealth.

It is estimated that, in the baseline scenario without additional countermeasures, the global mean surface temperature will rise by a threatening amount of 3.7 °C or even up to 4.8 °C during the 21st century compared to preindustrial levels [3], which would lead to significantly increased risks of irreversible impacts, such as widespread loss of biodiversity and reduced food security [4]. Consequently, grave concerns over the global warming have led up to the establishment of international

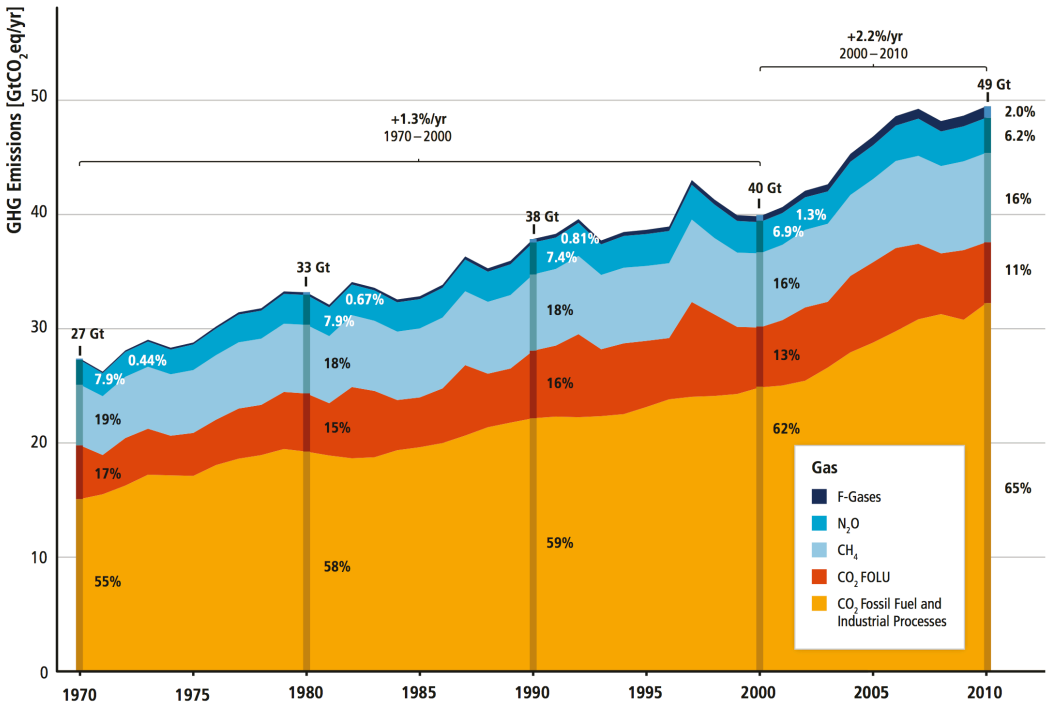

Figure 1.2 Total annual anthropogenic GHG emissions by group of gases [5]
CO_2 FOLU – CO_2 from forestry and other land use; F-Gases – fluorinated gases

instruments and agreements in order to mitigate GHG emissions, such as the Kyoto Protocol and the Paris Agreement, calling for human intervention to reduce the sources and reinforce the sinks of GHGs with the ultimate goal to stabilize GHG concentrations in the atmosphere at such a level that would prevent dangerous anthropogenic interference with the climate system [2][6][7][8]. Accordingly, numerical GHG emission targets have been set nationally, and consensus has been reached that the global warming should be limited well below 2.0 °C, or ideally further down to 1.5 °C, above preindustrial levels.

These countermeasures against anthropogenic GHG emissions have brought about important improvements as the energy-related CO_2 emissions plateaued for three successive years from 2014 to 2016 [9], despite an average annual growth of global gross domestic product (GDP) of 2.7%. Besides the stalled rise of emission numbers, the importance also comes from the implication of the weakened link between economic growth and CO_2 emissions, which is underlain by technological development and policy initiatives. Nevertheless, the risks of resumed emission increases pushed up by the ever-growing energy demand have never extinguished. In fact, CO_2 emissions in 2017 rose again by 1.4% and reached a historic high level which is equivalent to the emissions of 170 million additional cars [9], whereby a steeper emission reduction would be certainly compelled in the next few years in order to meet the targets stipulated in the Paris Agreement.

A large portion of anthropogenic GHG emissions is accounted for by CO_2 from fossil fuel combustion (see Figure 1.2), to which the transport sector is a significant contributor, since CO_2 is one of the normal combustion products from engines that are powering nearly all road, aviation, waterborne and a part of rail transport modes.

In 2010, for instance, the transport sector produced 7.0 $GtCO_2eq$ of direct GHG emissions, responsible for 14% of the total anthropogenic GHG emissions (see Figure 1.3). As a matter of fact, total vehicle emissions consist primarily of CO_2, with less than 5% non-CO_2 gases. Out of the 7.0 $GtCO_2eq$ of GHG emissions, 6.7 $GtCO_2eq$ were directly CO_2, which accounted for approximately 23% of the total energy-related CO_2 emissions [10]. From the historical perspective, emissions from the transport sector have more than doubled since 1970 and have increased faster than any other energy end-use sector. In particular, the increases in road vehicle GHG emissions have contributed more than 80% to the total emission increases in the transport sector, and in general the percentage of emissions accounted for by road vehicles has been growing rapidly (see Figure 1.4).

Therefore, it is evident that automotive IC engines play an important role in decreasing GHG (especially CO_2) emissions and mitigating the climate change.

1.2.2 Noxious emissions and air pollution

In addition to the normal combustion products under ideal conditions, namely

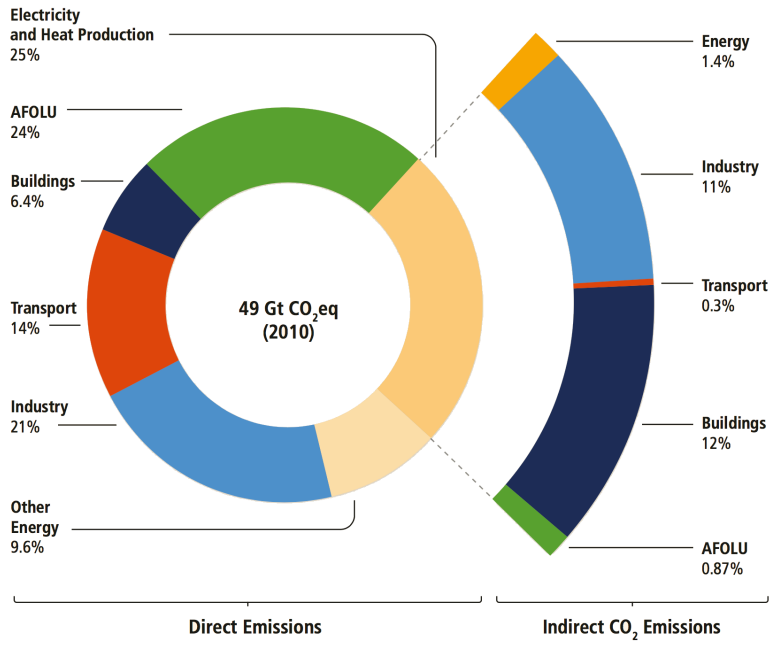

Figure 1.3 Total anthropogenic GHG emissions by economic sectors in 2010 [5]
AFOLU – agriculture, forestry and other land use
Other energy – energy sector other than electricity and heat production

CO_2, water, nitrogen and excess oxygen if any, other pollutants originate in motor vehicles as the combustion is always less than ideal in IC engines. Those noxious emissions include (1) nitrogen oxides, or NO_X, forming in the high-temperature burned gas zone due to chemical reactions involving nitrogen and oxygen atoms

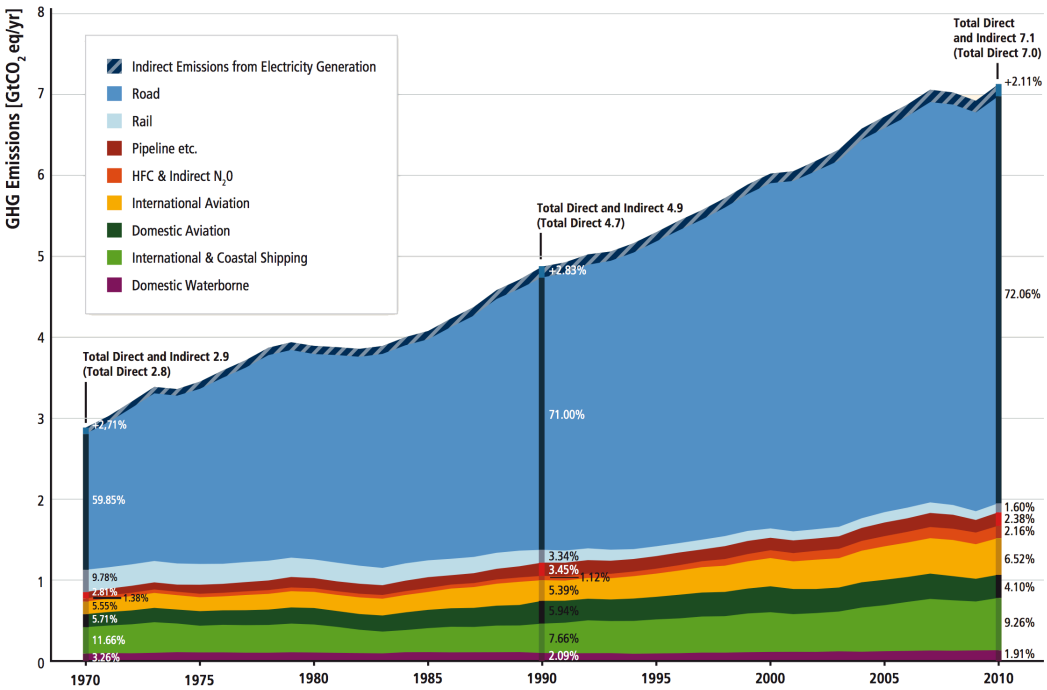

Figure 1.4 Direct GHG emissions of the transport sector by transport modes [10]

and molecules; (2) unburned or partially burned hydrocarbons, or HC, such as fuel molecules, aldehydes, ketones, etc.; (3) carbon monoxide, or CO, originating from incomplete oxidation through the fuel combustion mechanism and also from CO_2 dissociation at elevated temperature; and (4) particulate matter, or PM, consisting mainly of incomplete combustion-generated carbonaceous, or soot, from fuels, on which some organic compounds like paraffin and aromatics are absorbed together with some inorganic substances [11][12].

Those exhaust pollutant species, individually or in combination, often cause hazardous impacts on public health and natural environment [13][14]. Firstly, NO_X is rapidly oxidized by atmospheric ozone to NO_2 which exacerbates symptoms of respiratory diseases such as bronchitis with long-term exposure, and reduces lung function growth at NO_2 concentrations currently measured in European and North American cities. Secondly, NO_X and volatile organic compounds (VOCs) in the vehicle-emitted HC are precursors of ground-level ozone, the primary constituent of smog, as a result of photochemical reaction in the presence of sunlight. Excessive ozone in the air can also cause breathing problems, trigger asthma, reduce lung function and cause lung diseases. And many organic compounds in vehicular HC emissions, e.g. the polycyclic aromatic hydrocarbons (PAHs), are mutagenic and carcinogenic. Thirdly, when inhaled, CO competes with oxygen and persistently binds to hemoglobin to produce carboxyhemoglobin, rendering red blood cells ineffective in carrying oxygen, and hence is highly toxic. Besides fatal air poisoning at high indoor CO concentration, there is also concern that exposure to low levels of CO may have adverse effects on the cardiovascular and central nervous systems. CO is also a reactant contributing to the formation of tropospheric ozone. Finally, airborne PM, in particular the respirable particles with aerodynamic diameters of 10μm or less ($\leq PM_{10}$) that are able to penetrate the deepest part of the lungs, are the most notorious emissions, affecting more people than any other pollutant. And finer portion of the particulates, e.g. $PM_{2.5}$, can even reach the alveoli. Clinically, there is a close, quantitative correlation between exposure to high concentrations of small particulates (PM_{10} and $PM_{2.5}$) and increased morbidity and mortality, due to respiratory and cardiovascular diseases as well as lung cancer. Moreover, NO_X can react with certain ambient compounds in the presence of ultraviolet light and ozone to form nitrate aerosols, accounting for an important portion of atmospheric $PM_{2.5}$. Worse still, unlike other pollutant emissions, no threshold concentration has been identified for small PM below which no health hazard is observed. In addition to PM, the remaining part of the outdoor air pollutants has also been classified as group-1 carcinogenic to humans [15], making the ubiquitous life-sustaining air and its quality a major health concern.

It was reported that 92% of the world population was living in places where WHO air quality guideline standards were not met in 2014, and globally 3 million deaths were attributable to ambient air pollution in 2012 [16][17]. Urban outdoor air pollution is identified as one of the 19 leading risk factors globally, and one of

the 10 leading risk factors in mid-income and high-income countries, among other risk factors like high blood pressure, high cholesterol, tobacco use, etc. [18].

Although many air pollutants, for example ozone, PM and CO, also result from natural processes, anthropogenic activities have led to increases in many naturally present pollutants and introduced additional species to levels that have detrimental impacts. And those solely anthropogenic air pollutants are, in most cases, products of fossil fuel combustion. In fact, road transport emissions are the predominant contributor to overall NO_X and VOCs concentrations as well as CO in urban areas. Fuel combustion products from IC engines are also largely responsible for urban PM concentrations, which is due to the exhaust emissions of organic carbonaceous aerosols, the formation of $PM_{2.5}$ from elemental carbon produced by pyrolysis during fuel combustion, and their interaction with other pollutants [19].

In light of those hazardous effects of air-polluting species and the substantial contribution of vehicular emissions, IC engines are considered as a major source of ambient air pollution, especially in traffic-dense metropolitan areas, and are thereby subjected to increasingly stringent emission regulations such as the EURO 6 and Euro VI inside the European Union, the Tier III standards in the United States, and the CARB emission categories in the state of California US.

1.2.3 Fuel consumption and energy security

Energy is the fundamental currency of the universe and our society. The issue pertaining to energy sustainability and security that IC engines have been facing is twofold as a result of the tight interlocking relationship between motor vehicles and crude oil.

On the one hand, the largest portion of oil production is consumed by road transport and this trend is expected to continue according to the long-term forecast up to 2040 (see Table 1.1). In fact, the road transport sector alone represented 45% of global oil demand in the year of 2016, and is estimated to account for one out of every three additional barrels consumed between 2016 and 2040, despite downside shifting factors such as vehicle efficiency improvement driven by technological development, tightening energy policies and the increasing penetration of non-oil-fueled drives. Crude oil is a limited energy resource, hence non-renewable, and has been depleted rapidly by end users among which the road transport sector is undoubtedly the leading one. This pattern is further reinforced by other factors. Firstly, the world population is projected to grow, albeit with declining growth rate, from 7.6 billion in mid-2017 to 8.6 billion in 2030 and further up to 9.8 billion in 2050 [21]. Secondly, all major economies globally started to show positive, robust economic growth for 2017 and are expected to continue to do so in the future. The third factor is the ongoing, transformational trend of global urbanization, resulting in more people living in urban areas and therefore in higher demand for transport. All these three factors together – the momentum of larger and richer population, or

Table 1.1
Current and long-term oil demand by sector (unit: millions of barrels per day, or mb/d) [20]

	2016	2020	2025	2030	2035	2040	Growth 2016-2040
Road	43.0	45.4	46.8	47.7	48.2	48.4	5.4
Aviation	6.0	6.6	7.2	7.8	8.4	8.9	2.9
Rail & Dom. waterways	1.8	1.9	2.0	2.1	2.1	2.2	0.4
Marine bunkers	3.8	4.2	4.7	5.0	5.2	5.4	1.5
Transportation	**54.6**	**58.1**	**60.6**	**62.5**	**63.9**	**64.9**	**10.3**
Petrochemicals	12.6	13.4	14.3	15.0	15.9	16.5	3.9
Other industry	12.5	13.0	13.3	13.6	13.7	13.7	1.2
Industry	**25.5**	**26.4**	**27.6**	**28.6**	**29.6**	**30.2**	**5.1**
Resid./Comm./Agr.	10.5	10.9	11.4	11.7	12.0	12.1	1.7
Electricity generation	5.1	5.3	4.8	4.6	4.2	3.9	-1.2
Other uses	**15.6**	**16.2**	**16.1**	**16.3**	**16.2**	**16.0**	**0.4**
World total	**95.4**	**100.7**	**104.3**	**107.4**	**109.7**	**111.1**	**15.8**

in other words the rapidly expanding global middle class to be joined by billions of people in the next decades, coupled with the increasing urbanization level – are responsible for a projected worldwide addition of 954 million passenger cars to the current level of 1076 million and of 239 million commercial vehicles to the current 224 between 2016 and 2040 [20], only to be then multiplied by the increase in vehicle distance traveled. In fact, it is projected that the transport volume, in terms of vehicle-kilometers, will grow by 117-233% for surface passenger transport and by 132-323% for surface freight transport from 2010 to 2050 [22]. In summary, one of the two interlocking aspects between motor vehicles and oil is that the depletion, or preservation, of crude oil, a finite natural resource, depends largely on the fast-rising demand coming from the road transport sector.

On the other hand, oil remains the predominant energy source that fuels the transport sector, providing the vast majority of the total transport energy, whereas natural gas and electricity each contributed less than 1% in 2009 (see Figure 1.5). And this is particularly true for road transport, with light-duty vehicles (LDVs) consuming about a half and heavy-duty vehicles (HDVs) a quarter of the total transport energy, respectively [23]. Regardless of a decrease in share from 95% in 2015 to around 88% in 2040 as the use of alternative fuels becomes more popular, the absolute quantity of transport-related consumption of refined petroleum and other liquid fuels is expected to continuously grow [24]. In other words, motor vehicles, and hence IC engines, are and will still be heavily dependent on one single source of energy, oil, and are therefore sensitive and vulnerable to the variability in or the lack of abundance of crude oil supplies.

The twofold, mutually dependent relationship between oil and motor vehicles has two implications. It acknowledges the significant influence of IC engines on the

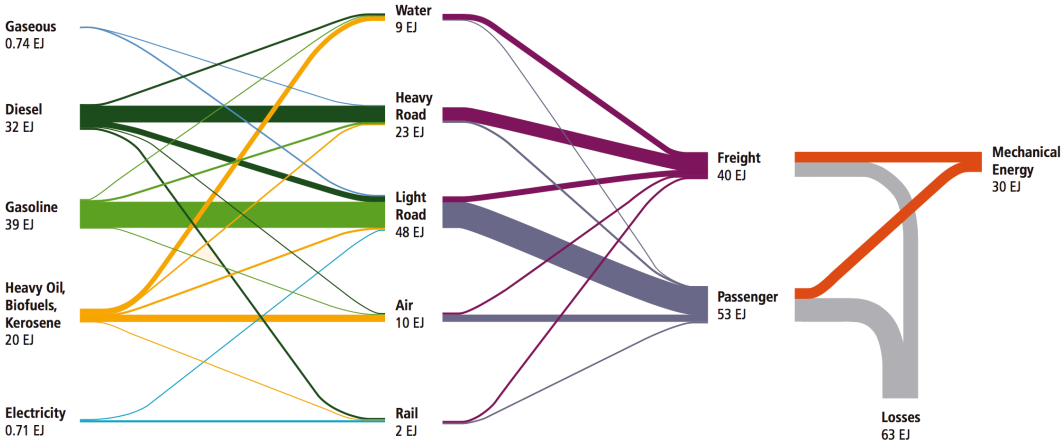

Figure 1.5 Energy consumption of fuels by transport sub-sectors in 2009 [5]

sustainable management of energy resources, but in the meanwhile poses a potential problem of energy security owing to the omnipresent involvement of automobiles in so many aspects of human activities.

1.3 Natural gas as an alternative fuel

The nature of the road transport sector, being the enormous number and usage involved across the world, defies the possibility of finding any monolithic solution in order to properly deal with the accelerating challenges about climate change, air quality deterioration and natural resource availability. And constraints like social acceptance, economic support, technological development and even time determine that those challenges the automotive industry faces must be multifaceted and hence have to be addressed by multifaceted means.

In general, the amount of CO_2 emitted from vehicle engines is characterized by two factors – first, the energy intensity, i.e. the amount of energy spent per unit of transport service provided; and second, the fuel carbon intensity, i.e. the number of carbon atoms in the fuel molecules and the net CO_2eq emitted for the fuel to be extracted, processed and made ready for refilling per unit of fuel chemical energy. Accordingly, CO_2 emissions can be decreased by reducing the energy intensity through engine efficiency improvement, and by reducing the fuel carbon intensity through switching to alternative power sources with lower carbon footprint such as hydrogen-rich hydrocarbons, sustainably derived biofuels, as well as electricity or hydrogen that are produced from renewable sources. In addition, well controlled combustion processes through optimized combustion systems in conjunction with dedicated aftertreatment systems can effectively reduce pollutant emissions, as far as IC engines are concerned. A fine example is modern gasoline engines equipped with three-way catalytic converters. Electric and hybrid electric powertrains also considerably reduce tank-to-wheels CO_2 and pollutant emissions, whereas the total

well-to-wheels emissions are dependent on, for instance, the methods of electricity generation, the management of electric grids and charging infrastructures, and the manufacturing and disposal of batteries. Finally, energy security and sustainability can be reinforced by diversifying the transport energy supplies and sources, thus diminishing the dependency on and slowing down the exhaustion of any single energy resource, most notably oil.

The adoption of alternative fuels is one of the viable approaches to all the three challenges. In fact, various alternative fuels have been considered for spark-ignition (SI) and compression-ignition (CI) engines since as early as 1980s [25], including but not limited to compressed natural gas (CNG), liquefied petroleum gas (LPG), hydrogen, methanol, ethanol, biodiesel, di-methyl ether (DME), jet-propellent-8 (JP-8) and naphtha, to be used alone or blended with conventional fuels [26][27] [28][29][30]. In particular, CNG has been gaining increasing popularity for both SI and CI engine applications. For instance, a strong increase is projected for the share of natural gas in total transport energy from 3% in 2012 to 11% in 2040 [31]. And in detail, 50% of bus energy consumption is projected to be natural gas in 2040, as well as 17% of freight rail, 7% of LDVs, and 6% of domestic marine vessels, while the share of liquid fuels is estimated to be 88% and electricity in total LDV energy consumption grows to 1%.

1.3.1 Characteristics of natural gas

Natural gas is a naturally occurring fossil fuel. It does not designate a unique type of fuel but a mixture that consists of a variety of gaseous species. Nevertheless, the primary constituent of natural gas is methane (CH_4) that almost exclusively characterizes the chemical properties of natural gas, whereas heavier hydrocarbons and inert diluents such as carbon dioxide and molecular nitrogen are also present in varying amount. Table 1.2 shows some typical compositions of natural gas that is used as transport fuel. The variation in gas composition depends on geographical source, season, climate, and treatment during production and transportation.

Table 1.2
Typical natural gas compositions by volume [32][33][34]

Component	Content (Vol %)		
Methane	94.42	92	88.1
Ethane	2.29	3	4.2
Propane	0.03	0.7	1.36
Butane	0.25	0.02	0.3
Pentane	0.01	0.1	0.06
Hexane	0.01	–	–
Carbon dioxide	0.57	0.6	5.2
Nitrogen	0.44	3	0.78

Natural gas is considered as one of the most promising alternative fuels for IC engine applications, in place of conventional liquid fuels (i.e. gasoline and diesel), owing to its distinctive and suitable physicochemical properties, and therefore has been extensively investigated [35][36][37][38][39][40]. The chemical properties determine the fuel applicability to combustion inside IC engines and the resultant emission formation, and the physical properties determine the possible preparation methods in order to form combustible mixtures. The physicochemical properties, pertaining to vehicular fuel applications and having the most profound implications on engine combustion, are presented in Table 1.3 for comparison between CNG and conventional diesel and gasoline fuels, whereby general characteristics of natural gas fueling are intuitively uncloaked on the basis of fundamental engine operating principles, regardless of particular engine configurations.

Being at gaseous state under normal atmospheric and typical engine operating conditions gives natural gas the inherent advantages of miscibility and diffusivity with air, also a gas, to produce adequately homogeneous air-fuel mixtures without undergoing atomization and vaporization, reducing the formation of local fuel-rich pockets and thus the likelihood of PM formation during combustion [42][43][44]. Also, in case of fuel leakage, natural gas is likely to disperse due to its much lower density than air, rather than forming a local inflammable or explosive mixture [45], or causing air poisoning and groundwater contamination.

Chemically, CH_4 has the highest hydrogen-to-carbon ratio among all stable hydrocarbons, since every carbon atom is saturated and covalently bond with four hydrogen atoms, resulting in a rather compact tetrahedral molecule. Such molecular structure gives CH_4 three major advantages over crude oil-based hydrocarbon fuels.

First, the hydrogen-rich composition lowers fuel carbon intensity. For example, by chemical stoichiometry, 1g of CH_4 produces 2.75g of CO_2, while 1g of gasoline produces 3.17g of CO_2. Then given the difference in the combustion enthalpy, i.e. the fuel lower heating value (LHV_f), complete combustion of CH_4 would produce

Table 1.3
Physicochemical properties of CNG vs diesel and gasoline at standard conditions [27][35][36][41]

	Diesel	**Gasoline**	**CNG**
Chemical formula, n = 4-12	$C_nH_{1.8n}$	$C_nH_{1.87n}$	CH_4
Density (kg/m^3)	832	750	0.725
Molar mass (g/mole)	170	114	17
Lower heating value, LHV_f (MJ/kg)	42.5	44.0	47.5
Stoichiometric air-to-fuel ratio, $(A/F)_{st}$	–	14.7	17.2
Octane number	–	85 - 98	≥ 120
Cetane number	40 - 50	5 - 20	–
Autoignition temperature (°C)	210 - 250	260 - 280	580 - 650
Flame propagation speed (m/s)	–	0.5	0.3 – 0.4
Adiabatic flame temperature (°C)	2054	2150	1890

even less CO_2 than gasoline would on an energy basis.

Second, there is no aromatic and polyaromatic compound or dissolved impurity in natural gas, and the small and simple molecular structure of CH_4 does not have carbon-carbon molecular bond. As a result, the combustion process is unlikely to form benzene ring and hence PAH, implying substantial potential for reducing PM emissions [38][46][47][48][49][50]. Furthermore, the simple chemical composition results in a relatively simple combustion chemistry system, and consequently the major HC emission is CH_4 itself rather than many other complicated intermediate compounds. With quite low PM and VOCs emissions, the contribution of natural gas fueled engines to smog formation is therefore marginal.

Third, the simple, stable molecular structure as well as the absence of long and branched carbon-carbon chains also grant CH_4 a strong resistance to knocking [27]. Knocking in SI engines is caused by unwanted autoignition of fuel outside the reach of the propagating flame front initiated by the spark plug. At typical engine-relevant thermodynamic states, a distinction is made between two fuel combustion regimes, namely conduction-diffusion-controlled deflagrative flames that are stabilized by premixed flame propagation with little chemical reactions ahead of the front, and ignition-delay-gradient-driven flames that are stabilized by autoignition [51]. These combustion regimes and related chemical kinetics of hydrocarbons are the subject of a wide body of studies [52][53]. Ignition delays depend on temperature, pressure, mixture equivalence ratio and fuel reactivity, and these variables, even at elevated temperatures and pressures under typical engine conditions, result in sufficiently longer ignition delay time for CH_4 than other hydrocarbon fuels to be consumed by the propagating flames prior to the onset of autoignition [54][55][56]. This quality of natural gas is reflected by its high research octane number, and such outstanding autoignition resistance has been well exploited in SI as well as in CI engines. As a side note, although the methane number which is referenced to hydrogen-methane mixtures, is a more appropriate designation since natural gas exceeds the maximum scale of octane number, the corresponding translated octane numbers are typically used for comparison purposes.

Adiabatic flame temperature and laminar flame speed are another two chemical properties of natural gas with important influences on engine applications. Laminar flame speed, in particular, depends on the combination of diffusivity, exothermicity and reactivity, and is a fundamental property of fuels. It serves as the key parameter in characterizing fuel combustion phenomena like flame stabilization, extinction and turbulent flame structure. As the primary constituent of natural gas, CH_4 in fact has the lowest laminar flame speed among all hydrocarbon fuels [57][58][59]. The mechanism of NO_X formation in both SI and CI engines is highly controlled by the temperature of the working fluid wherein nitrogen and oxygen are present. Since CH_4 burns at lower temperature and at lower flame speed than diesel and gasoline do, the engine-out NO_X emissions are expected to be reduced, under comparable operating conditions [45][60][61]. But in some cases, e.g. when the mixture is lean

or the combustion starts late, the slow flame propagation of CH_4 can be problematic and may need to be augmented by, for instance, increasing charge turbulence levels. Furthermore, the resultant differences in the energy conversion rate from burning CH_4 and petroleum fuels should be taken into account when the engine operation parameters are to be set.

Although CH_4 has higher energy density per unit mass (i.e. LHV_f) than diesel and gasoline, its energy density per unit volume is undesirably lower as a result of the light molecules of CH_4. As a matter of fact, at the same level of energy content, natural gas pressurized to 20.7 MPa still occupies about five times the volume of diesel and four times the volume of gasoline [62]. This could put natural gas at a disadvantage in terms of fuel transportation, onboard fuel storage and engine fuel supply systems (e.g. natural gas injectors and compressors), for which specialized design, or adaptation, and increased total energy consumption are inevitable.

1.3.2 SI stoichiometric natural gas engines

Fundamentals and fuel compatibility

An ideal SI IC engine works according to the Otto cycle, wherein the air and fuel are introduced into the cylinder to form a mixture, compressed to a higher thermodynamic state till the vicinity of the top dead center (TDC), and followed by the combustion initiated by an electric discharge provided by the spark plug, hence the name spark ignition [11]. The distinctive characteristic of SI engine combustion process is the flame propagation, often turbulent, from the ignition sites near the spark plug outwards throughout the then premixed air-fuel mixture. The mixture in most cases is composed of air and fuel at the stoichiometric ratio so that the engine-out HC, CO and NO_X emissions can be substantially reduced by three-way catalytic converters that function most efficiently at stoichiometry.

Accordingly, natural gas is highly compatible with the working principles of SI engines as a gasoline substitute. In fact, any existing gasoline engines on the current market can be converted to a bi-fuel or dedicated CNG one with fair ease. And most of the current CNG vehicles in operation are retrofitted from gasoline ones [63].

One good compatibility of natural gas-fueled SI operation is the formation of a premixed air-fuel mixture that is facilitated by the intrinsic gaseous state of natural gas. In addition, the use of gaseous fuel avoids wall wetting on intake ports and cylinder liner especially during cold start thanks to the absence of evaporation and enrichment issue, which improves cold startability and reduces the engine-out total HC (THC) emissions below the corresponding levels of gasoline baseline engines [64]. Further reduction in THC emission is attainable due to the lower dissolvability of light CH_4 molecules in oil film and therefore less adsorption-desorption-related HC emissions than gasoline fueling [65].

The other, and most advantageous, compatibility is that CH_4 is inherently more

knock-resistant, enabling the adoption of higher compression ratios which normally elude gasoline fuel. Compression ratio can be safely risen from about 9:1, normally adopted by gasoline engines, to 13:1 or even up to 15:1 without engine knocking, depending on gas quality, which allows natural gas engines to operate at enhanced engine thermal efficiencies above that of gasoline baseline by the order of 5-10% [33][66][67][68]. Equivalently, engines running on natural gas permit higher levels of supercharged or turbocharged boosts that are, in combination with downsizing, a key enabler to extract more power from a given engine displacement for higher specific power and improved fuel economy [69].

Performance

As mentioned earlier, the process and outcomes of fuel combustion is largely affected by the physicochemical attributes of the fuel. Accordingly, with respect to performance, the brake specific fuel consumption (BSFC) of natural gas engines is always below that of gasoline engines throughout the speed range at full load [27] [43][70][71], which can be rationalized from the definition of BSFC and the 8% higher LHV_f of natural gas compared to gasoline, provided that the engines work under similar operating conditions.

The engine power, au contraire, shows the opposite trend. It has been generally observed in experimental studies that SI engines retrofitted to CNG fueling are subject to a 15% to 20% decrease in brake power across the operating ranges in comparison with their respective baseline versions running on gasoline under similar operating conditions (e.g. with the same compression ratios) [43][44][63] [70][71][72][73][74][75]. Indeed, the brake power loss has been the major obstacle to be overcome for the development of SI natural gas engines. Several factors have been identified which act and contribute together to the engine power and efficiency losses.

Despite the higher combustion enthalpy of natural gas, the stoichiometric fuel-to-air ratio, i.e. the reciprocal of $(A/F)_{st}$, of natural gas is about 14.5% lower compared to gasoline. And it is actually the product of $LHV_f(F/A)_{st}$, an indication of the energy content in stoichiometric mixtures, that determines the total fuel effect on the power output of engines operating with stoichiometric combustion. In this regard, the higher caloric value of natural gas is offset by its lower $(F/A)_{st}$, leading to a net disadvantage of around 7.7% to natural gas against gasoline.

After the fuel effects, the amount of fuel in the mixture that is inducted into the engine comes into play. The gaseous state gives natural gas an advantage over liquid fuels for the air-fuel mixing process, but its lower density (or molar mass) requires a larger volume to be occupied by natural gas and therefore has an adverse effect on the volumetric efficiency, by displacing a proportionally larger volume of air that would otherwise be available for combustion. This argument can be explained approximately by applying the ideal gas equation and making several simplifying assumptions. Assuming that the air and fuel are well premixed before entering the

cylinder, that gasoline in the mixture is fully evaporated, and that the temperature and pressure of the mixtures are the same for both fuels, the same displaced volume accessible to the mixtures, V_d, can be expressed (in terms of inducted air volume, V_{air}, and fuel properties) as

$$\begin{aligned} V_d &= \frac{m_{air}}{\rho_{air}} + \frac{m_{fuel}}{\rho_{fuel}} \\ &= \frac{m_{air}}{\rho_{air}}\left(1 + \frac{m_{fuel}}{m_{air}}\frac{\rho_{air}}{\rho_{fuel}}\right) \\ &= \frac{m_{air}}{\rho_{air}}\left(1 + \frac{1}{(A/F)_{st}}\frac{\frac{p\mathrm{M}_{air}}{RT}}{\frac{p\mathrm{M}_{fuel}}{RT}}\right) \\ &= V_{air}\left(1 + \frac{1}{(A/F)_{st}}\frac{\mathrm{M}_{air}}{\mathrm{M}_{fuel}}\right) \end{aligned} \quad (1)$$

where M is the molecular mass, R the universal gas constant, p the pressure, T the temperature, and V the volume. By rearranging Equation (1), the volume occupied by the inducted air, V_{air}, in a stoichiometric mixture is then given by

$$V_{air} = \frac{V_d}{1 + \frac{1}{(A/F)_{st}}\frac{\mathrm{M}_{air}}{\mathrm{M}_{fuel}}} \quad (2)$$

By inserting 28.9 [g/mole] as the molecular mass of air and the corresponding values for CNG and gasoline presented in Table 1.3 into Equation (2), it is clear that the effect solely due to the difference in molecular mass of the two fuels, both at gaseous state, reduces the volumetric efficiency of a natural gas engine by 7.5% compared to a gasoline one. This result is admittedly an illustrative estimate since the actual values depend on additional variables according to the engine design and operation. One such additional variable, for example, is the fact that the simplified assumption about fully evaporated liquid fuel does not represent the real situation. Actually, in the case of port injection (PI), a portion of the fuel remains as liquid particles only to evaporate later inside the cylinder, leaving more volume available for the air than the amount calculated according to Equation (2).

Another variable omitted in the reasoning above is the evaporation undergone by liquid fuels and the corresponding effect of charge cooling associated with the latent heat. The lack of evaporation of natural gas prevents the increase in mixture density by cooling and thus further reduces the volumetric efficiency by about 3%

compared to gasoline fueling [64].

In summary, the overall volumetric efficiencies of natural gas engines operating with premixed stoichiometric combustion and methods of fuel induction outside the cylinder (e.g. PI) are reduced by between 10% to 15% depending on the engine optimization [45][65][73][76][77][78][79], and a corresponding decrease in engine torque by 16% is also noticed [44], in comparison with their gasoline counterparts.

The lower volumetric efficiency is the main culprit responsible for the reduced power output from natural gas-fueled SI engines, but a few other factors of smaller contributions influence the engine power as well.

Apart from cooling the charge, the evaporation phenomenon of inducted liquid fuels has another beneficial effect of increasing pressure inside the cylinder at the beginning of the compression stroke as part of the liquid fuel droplets are still to evaporate inside the cylinder after the intake valve closing. Therefore, natural gas that remains constantly in the gas phase has the disadvantage of lacking such boost to the effective inlet pressure of the engine cycle [36].

Another noteworthy combustion-related attribute of natural gas is the low flame speed relative to gasoline, which is particularly critical at the early stage of flame development when the flame is almost laminar due to limited reaction as well as preheated zones [80], and in general affects the turbulent flame propagation. As a consequence, two impacts on the engine power output are due. First, the slow flame propagation lengthens the combustion duration. Although the resultant slow heat release rate reduces the peak combustion temperature, the lengthened combustion still rises the temperature high enough to cause prolonged heat transfer. A reduction in engine power output by 5-10% is attributable to such thermal losses [72]. Second, to avoid unfavorable effects of excessively retarding the combustion past TDC (e.g. bulk quenching), advanced spark timing is normally applied to natural gas engines to accommodate the slow burning rates. The spark advance may be set up to 10 crank angle degrees (degCA) earlier than gasoline fueling, depending on engine speed [70]. Earlier combustion onset during the compression stroke rises the charge pressure against the piston and hence increases the work transfer required from the piston in order to compress the charge, which reduces the net work the natural gas engine is able to do throughout the engine cycle, compared to a gasoline engine with shorter combustion duration and later spark timing at the same operating point.

Finally, since natural gas has lower value of $LHV_f(F/A)_{st}$ and displaces larger volume of air compared to gasoline, natural gas engines in general operate with less air flow restriction at all loads by roughly 10% [81], using either wider throttle or higher intake valve lifts. Less restricted intake flow reduces inlet pressure drop with beneficial effect on volumetric efficiency. Pumping work losses are decreased as well. However, these effects are favorable to a lesser extent and are overwhelmed by all the aforementioned unfavorable factors.

There are several methods that are adopted to overcome the power output losses

for natural gas engines, most of which aim to compensate for the low volumetric efficiency. To eliminate the drawback of intake air volume displacement, direct injection (DI) has long been widely implemented to gasoline engines [82]. DI of natural gas is particularly advantageous since natural gas would occupy even more volume otherwise available for air than gasoline would at the same temperature and pressure. Therefore, DI increases the amount of inducted air that in turn increases the amount of fuel to be properly oxidized, thus enhancing the total energy content of the cylinder charge. Forced induction, i.e. boost by means of supercharging or turbocharging [83], is also an effectual method that increases the density of the inducted air, hence directly increasing the engine power output [68][77]. Moreover, the volumetric efficiency can also be improved by optimizing throttling or intake valve timing and lift profiles with specific respect to natural gas [64], i.e. reducing the intake flow restriction, especially at part loads, due to the lower energy content of stoichiometric air-natural gas mixtures compared to air-gasoline mixtures, as previously mentioned.

Apart from remedying the weakness in volumetric efficiency, the high knock-resistance of natural gas can also be exploited for which increasing the compression ratios is viable [33], thus making the engine more thermally efficient and generate higher power. Whereas a naturally aspirated natural gas engine generally has lower torque output than its gasoline counterpart, the combination of forced induction and increased compression ratio, which would push the natural gas engines to operate near the knocking limits as what has been done for gasoline engines, suffices to significantly boost the engine torque output above the baseline gasoline engine [84]. Furthermore, the boost levels and compression ratios of natural gas engines can be elevated beyond the normally acceptable values for gasoline engines, owing to the higher knock-resistance of natural gas.

Exhaust emissions

The major motivation behind the continuous interest in CNG as an alternative transport fuel is from the perspective of its clean combustion and thereby reduced environmental impacts. It is obvious that raw engine-out PM is negligibly minimal for the simple CH_4 molecules. All the other exhaust emissions, namely CO_2, NO_X, HC and CO, from properly calibrated natural gas engines are in general lower than those from comparable gasoline engines as well [85][86].

When the fuel properties are concerned in general, natural gas has lower carbon intensity and hence produces less CO_2 on both mass and energy basis compared to gasoline, as explained previously. Specific to stoichiometric engine operation, the potential of natural gas for reducing CO_2 emissions can be revealed by calculations similar to Equation (1) and (2). By applying the ideal gas equation and assuming that the air and fuel are premixed before entering the cylinder, that the gasoline in the mixture is fully evaporated, and that the temperature and pressure of the mixture are the same for both fuels, the same displaced volume accessible to the mixtures,

V_d, can be expressed (in terms of fuel mass and properties) as

$$
\begin{aligned}
V_d &= \frac{m_{air}}{\rho_{air}} + \frac{m_{fuel}}{\rho_{fuel}} \\
&= \frac{m_{fuel}}{\rho_{fuel}}\left(\frac{m_{air}}{m_{fuel}}\frac{\rho_{fuel}}{\rho_{air}} + 1\right) \\
&= \frac{m_{fuel}}{\frac{pM_{fuel}}{RT}}\left((A/F)_{st}\frac{\frac{p\mathrm{M}_{fuel}}{RT}}{\frac{p\mathrm{M}_{air}}{RT}} + 1\right) \\
&= \frac{m_{fuel}}{\frac{pM_{fuel}}{RT}}\left((A/F)_{st}\frac{\mathrm{M}_{fuel}}{\mathrm{M}_{air}} + 1\right) \qquad (3)
\end{aligned}
$$

where M is the molecular mass, R the universal gas constant, p the pressure, T the temperature, and m the mass. By rearranging Equation (3), the mass of fuel, m_{fuel}, and the corresponding amount of substance, n_{fuel}, in the inducted stoichiometric mixture is then given by

$$
m_{fuel} = \frac{V_d\frac{pM_{fuel}}{RT}}{(A/F)_{st}\frac{\mathrm{M}_{fuel}}{\mathrm{M}_{air}} + 1} \qquad (4)
$$

$$
n_{fuel} = \frac{V_d\frac{p}{RT}}{(A/F)_{st}\frac{\mathrm{M}_{fuel}}{\mathrm{M}_{air}} + 1} \qquad (5)
$$

Then by introducing the chemical stoichiometry of ideal complete combustion of fuels, the mass of CO_2, m_{CO_2}, as the combustion product is given in the form of carbon balance as

$$
\begin{aligned}
m_{CO_2} &= n_{fuel}xM_{CO_2} \\
&= \frac{V_d\frac{p}{RT}}{(A/F)_{st}\frac{\mathrm{M}_{fuel}}{\mathrm{M}_{air}} + 1}xM_{CO_2} \qquad (6)
\end{aligned}
$$

where x is the number of carbon atoms in one fuel molecule. By substituting x = 1

for natural gas (represented by CH_4), $x = 8$ for gasoline (represented by C_8H_{18}, i.e. iso-octane), and the corresponding values for CNG and gasoline presented in Table 1.3 into Equation (6), it is found that a natural gas engine produces 33.7% less CO_2 than a gasoline engine does if the same volume of stoichiometric mixtures is burned to completion.

Obviously, the energy contents in the same volume of stoichiometric air-natural gas and air-gasoline mixtures differ. The mass of ideal-combustion-produced CO_2 on the basis of energy contained in the air-fuel mixture, a better indicator of specific emissions, is then given by

$$\frac{m_{CO_2}}{m_{fuel}LHV_{fuel}} = \frac{n_{fuel}xM_{CO_2}}{m_{fuel}LHV_{fuel}} = \frac{1}{M_{fuel}LHV_{fuel}}xM_{CO_2} \quad (7)$$

Again, by substituting corresponding values into Equation (7), the results are still 20.5% lower for natural gas than for gasoline. Based on the simplification that the natural gas and gasoline engines are comparable, i.e. having the same thermal and mechanical efficiencies, it is implied that the brake specific CO_2 emissions can be reduced by around 20% by switching the fuel from gasoline to natural gas. Of course, this argument is on a simplified and purely theoretical basis. In reality, the combustion processes in IC engines are much more complicated, and therefore the actual CO_2 emission advantages of natural gas engines may vary. Nevertheless, reduction in CO_2 emissions from SI natural gas engines have been experimentally confirmed in general [44][86][87].

NO_X formation during combustion process depends directly on two factors, i.e. the temperature and the concentration of reactants. In engine context, the lack of excess air in stoichiometric SI operation creates an environment of much lower reactant concentrations for the oxidation of N_2 in comparison with lean-burn SI or diesel operations. For this reason, NO_X emissions are normally of little concern for stoichiometric gasoline engines. Moreover, NO_X formation is further suppressed in natural gas engines by the lower charge temperature during combustion [60][78], due to the slower burning rate and the lower adiabatic flame temperature of CH_4 as mentioned previously.

With respect to the other pollutants, HC and CO emissions depend on various factors, e.g. the actual combustion quality which in turn depends on the individual engine optimization. Nevertheless, SI stoichiometric natural gas engines in general produce lower CO and non-methane HC emissions than gasoline engines do [36] [44][86]. The THC emissions vary on a case-by-case basis, of which, however, the vast majority is unburned CH_4 [86][88][89]. It is worth pointing out, nevertheless,

that in most cases the observed increases in unburned fuel emissions are typical of end-user converted gasoline engines to run on natural gas without optimization of engine tuning (e.g. spark and injection timing) [44]. As already mentioned, a spark timing as retarded as for the gasoline version, for instance, is likely to excessively postpone the combustion phasing of natural gas and to end up causing charge quenching during the expansion stroke. Otherwise, the THC emissions from natural gas engines stay low [65].

The main focus of contemporary development of SI stoichiometric engines is in general on rectifying their lower thermal efficiency than those typically observed in lean-burn SI or diesel engines. A common practice to improve fuel economy is to introduce exhaust gas recirculation (EGR) that lowers the charge temperature due to the dilution effect and increased heat capacity, with the additional benefits of further reducing PM and NO_X emissions. However, engine-out THC emissions, as the consequence of less stable combustion, tend to increase with increasing EGR rates [90]. Natural gas engines are more sensitive to EGR rates in terms of the risk of unstable combustion leading to excessive unburned HC emissions or losses of engine power, since the dilution effect of EGR slows down the flame propagation which for natural gas is already slow to begin with and the thermodynamic effect of EGR lowers the already low combustion temperature. Therefore, the use of EGR for natural gas engines has to be controlled with more caution than for gasoline.

1.3.3 SI lean burn natural gas engines

Fundamentals and fuel compatibility

The essence of lean burn concept is to control the charge energy contents and thus the engine load, through variation of the inducted fuel quantity while keeping the amount of inducted air nearly unchanged, i.e. engine load shift through varying lambda as opposite to the traditional throttling for stoichiometric lambda control.

There are two principal implications of such combustion system. First, the air-fuel ratio of the actual cylinder charge varies over a certain range on the lean side of the stoichiometry, and hence the consistent presence of excess air influences the combustion and pollutant formation processes. Second, intake air flow restriction at part loads, which is otherwise used to adjust the amount of air according to loads so as to always maintain stoichiometric operation, is substantially reduced. In this way, the fuel economy can be considerably improved above that of stoichiometric operating modes thanks to the increase in thermal efficiency and to the mitigation of pumping losses [60][62][91]. These two implications are the core aspects around which investigations of lean-burn SI engines have been motivated.

In terms of fuel effects, natural gas is in a rather advantageous position for lean burn applications. On the credit side, natural gas has wider flammability range than most liquid hydrocarbon fuels, and is therefore more flexible and amenable to lean

combustion operations. On the other side of the coin, the relatively low flame speed and flame temperature of natural gas are critical and call for particular caution as to how much the mixtures can be practically leaned out for them to be burned properly under engine-relevant boundary conditions, before the slower flame propagation of leaner mixture takes its toll on combustion stability.

Aftertreatment systems

The lean mixture provides abundant oxygen that facilitates complete oxidation of the fuel and various intermediate species during combustion, which substantially inhibits the formation of CO and HC. In fact, lean-burn natural gas engines under proper operating conditions produce 50-90% less CO and up to 55% less unburned HC emissions compared to gasoline engines, depending on the adopted equivalence ratio [44][86]. With extremely lean mixture, however, the CO and HC emissions rise abruptly as the combustion quality deteriorates.

The influence of lean mixture on NO_X formation is less straightforward. It is clear that the intrinsic slow heat release of natural gas combustion decreases peak charge temperature, and hence favors less the formation of NO_X than comparable gasoline and diesel engines do [92]. Two additional competing factors act within the lean-burn system. The formation of NO_X is inhibited by the lower combustion temperature as the mixture becomes leaner, but is at the same time promoted by the presence of excess oxygen. In general, the excess oxygen offsets the effect of lower temperature up to around equivalence ratio $\phi = 0.9$ and the later predominates at further leaner mixtures [11]. As lean-burn natural gas engines usually work in the range $\phi < 0.9$, NO_X emissions are lower than those from stoichiometric operations. Higher compression ratios and intake boost are commonly implemented for natural gas engines in order to compensate for the disadvantage of engine torque and power due to lean operation, and to increase thermal efficiency and power density. Those factors tend to encourage NO_X formation above the level of gasoline engines. Raw NO_X emissions from lean-burn engines, which may even be at lower levels (but still higher than the regulated values), are more problematic for exhaust treatment than those from stoichiometric engines.

In SI stoichiometric engines, the three-way catalytic converters are a reliable and cost-effective tool to simultaneously reduce NO_X, CO and HC emissions, with a reduction efficiency of over 90% [11]. However, three-way catalytic converters reply on very low concentration of oxygen to function properly, as the excess air in the exhaust stream creates an unfavorable oxidative environment for efficient NO_X reduction. Thus, for lean-burn engines the three-way catalytic converter works only as an oxidation catalyst, oxidizing HC and CO but not reducing NO_X. The resultant untreated tailpipe NO_X emissions thus pose a limiting factor for lean-burn engines.

If NO_X emissions from lean-burn operations are to be handled by aftertreatment systems, sophisticated diesel-like technologies such as ammonia-based selective reduction catalysts (SCR) or lean-NO_X traps have to be implemented [93]. But in

practice, these aftertreatment systems suffer from design complexity, high costs and difficulties of maintenance [94]. Moreover, the preference of SI engines over diesel engines, mainly for their cleanness, would be no more logically justifiable if the same aftertreatment systems for diesel engines are also needed for SI engines in order to comply with stringent emission regulations.

Since THC emissions from lean-burn natural gas engines are mostly unburned CH_4, a further complication stems from the inefficiency of conventional oxidation catalysts at oxidizing CH_4. Apart from the fact that CH_4 is the most stable and hence the most difficult hydrocarbon to be oxidized, the exhaust temperatures of natural gas engines, below 750K in many lean-burn operating points, constitute additional inconvenience for exhaust aftertreatment [95][96][97]. The mechanism governing the different oxidation efficiencies between stoichiometric and lean combustions is linked to the availability of CO in the exhaust gas. The catalytic oxidation reaction of CO has a lower light-off temperature and is exothermic which heats the active catalyst surface up to the much higher light-off temperature of the catalytic CH_4 oxidation reaction [98]. As lean-burn exhaust contains significantly less CO, CH_4 removal efficiency correspondingly declines below acceptable level. The remaining non-methane HC and CO emissions raise no particular concerns for conventional catalytic conversion [99].

Consequently, it is in general preferable to reduce the raw engine-out pollutant emissions, especially NO_X, by controlling the combustion process itself, rather than counting heavily on aftertreatment systems.

Combustion stability

In the case of moderately lean mixtures, the wider flammability limits of natural gas outweigh its low flame propagation rate. For example, natural gas engines could run on leaner mixtures than gasoline engines (ϕ = 0.7 versus 0.9) while maintaining the same level of combustion stability with 4% coefficient of variation (CoV) in the indicated mean effective pressure (IMEP) [100]. However, running moderately lean mixtures is seldom the case in which lean-burn natural gas engines are operated. In line with the motivations behind lean combustion concept, being to suppress NO_X formation and to improve fuel economy as much as the engine operations permit, the mixture is typically leaned out close to the lean misfire limits.

Under the critically lean conditions, the resultant flame propagation throughout the charge is much slower than that under stoichiometric conditions. Consequently, the heat release rate is decreased and the overall combustion duration prolonged, which in turn increases heat transfer losses to the combustion chamber walls [101]. And the expected improvement in thermal efficiency from lean-burn operations is not completely fulfillable.

The low heat release rate of extremely lean mixtures also results in perceivable combustion instability shown as poor combustion phasing and high cycle-to-cycle variations (CCV) in both peak pressure and IMEP. Moreover, in order to further the

reduction in engine-out NO_X emission, a common operation for lean-burn natural gas engines is to introduce diluents (e.g. EGR) whereby the flame speed is lowered [102][103], and the issue of combustion instability then becomes even more critical. When the combustion becomes unstable and the flame propagation is so slow that the flame is extinguished before all the mixture is burned, incomplete combustion or misfire cycles may occur in the end gas zone, bringing about drastic increases in HC emissions, engine roughness and poor drivability [62][104][105].

Stabilization of the combustion process is therefore of crucial importance to the engine control of lean-burn operations. Above all, a well-known method to enhance combustion stability for SI engines is to accelerate the spherical flame propagation by introducing adequately high levels of turbulence into the flowfield [106][107], with respect to the characteristic regimes of turbulent combustion [108][109][110] [111]. Proper design of combustion chamber, intake ducts and valve lift profiles can control the fluid flow and increase the coherent charge motion, e.g. the tumble motion in SI engines. The coherent motion then gradually dissipates towards the end of the compression stroke and subsequently increases the turbulence level there, which has been verified to increase burning rate, improve combustion quality and decrease cyclic variability [112][113]. In addition, the elevated compression ratios typical of natural gas engines, the high energy ignition systems required by lean mixtures at high pressure, and catalytic coatings on the combustion chamber, all contribute to stabilizing the combustion process [60]. Moreover, as the mixtures are ideally as lean as almost at misfire level, precise control and distribution of air-fuel ratios by means of PI or DI can prevent unwanted combustion abnormalities due to air-fuel ratio errors, e.g. misfire if the mixtures are leaner than desired [96][100] as well as occasional high NO_X emissions if the mixtures are richer. Finally, more sophisticated methods such as mixture stratification have been conceived. Mixture stratification is artificially stratifying the lean mixture so as to create a relatively richer mixture in the vicinity of the ignition source and leaner mixture in the outer regions, as opposite to forming a homogeneous mixture. This approach is able to strengthen the flame kernel and thus shorten the overall combustion duration, but the flame propagation speeds are not significantly increased, since the flame front, albeit strong at the beginning, still has to travel outwards throughout the remaining, even leaner mixture [105][114].

With the general objective to achieve high thermal efficiency and low pollutant emissions, the major challenge for the development of lean-burn natural gas engines resides in the definition of the air-fuel ratios for the optimum compromise between NO_X formation, combustion stability (hence CH_4 emissions), and fuel economy, for each operating point on the engine map and given fuel compositions.

Despite the necessity of fine-tuning the air-fuel ratios, lean-burn engines are in principle not restricted to stoichiometric combustion for the aftertreatment system, and can thereby employ skip fire at low loads to further improve fuel economy [74].

1.3.4 CI natural gas engines

Fundamentals

Engines working with the Diesel cycle, or compression ignition (CI), have long enjoyed popularity by reason of their superb thermal efficiencies, torque output and durability. The attractiveness of diesel engines, nevertheless, has been increasingly overshadowed by growing concerns over the hazardous impacts and regulations of their high PM and NO_X emissions as a result of the characteristic high-temperature high-equivalence ratio combustion path [115][116]. Various advanced combustion strategies have been proposed to remedy the emission issues of diesel engines, such as premixed charge compression ignition (PCCI), partially premixed compression ignition (PPCI) and homogeneous charge compression ignition (HCCI). Naturally, it is appealing to incorporate the emission advantages of natural gas as an alternative into diesel operations in order to attain both high efficiency and low emissions.

However, the high octane number of natural gas belies its intuitive applicability in CI engines since the compressive heating alone is certainly not sufficient to cause its spontaneous ignition. In fact, experimental study has shown that, under similar diesel engine conditions, the ignition delay of natural gas exceeds 5ms and is highly variable [117], while typical diesel ignition delay is about 1ms and repeatable [118]. The energy demand for natural gas autoignition, if provided only by compression, necessitates a compression ratio as unrealistically high as 38:1 [36]. Consequently, alternative igniting sources are in need for converting diesel CI engines to natural gas fueling.

A common approach is the dual-fuel combustion system [47][119][120] that falls into the category of reactivity controlled compression ignition (RCCI) concept. Essentially, RCCI is utilizing the combination of a high-cetane number fuel and a high-octane number fuel (hence "dual-fuel") to realize fuel reactivity stratification for engine control purposes [121]. In this way, the high-cetane fuel (with high CI reactivity) is ignited spontaneously by the compression and in turn serves as the igniting source for the high-octane fuel (with low CI reactivity). The terms "dual-fuel" and "RCCI" may differ according to the method and timing of the high-cetane fuel introduction, the ratio between the two fuels and the combustion objective, yet no concrete distinguishing definition has been provided and therefore they are often used interchangeably.

Specific to natural gas dual fueling, diesel is the high-cetane fuel and natural gas the high-octane fuel. Typically, natural gas is injected in the manifold or intake ports to form a homogeneous mixture before inhaled into the combustion chamber, or injected with high pressure in the combustion chamber directly, then followed by the well-timed direct injection of diesel as the pilot fuel at the vicinity of TDC. The injected diesel then auto-ignites by the compressive heating, which provides sufficient energy for the subsequent autoignition of the air-natural gas mixture. Therefore, in-use diesel engines can be conveniently converted into dual-fuel ones

without major modifications. Even in the case of natural gas DI, a single integrated injector for both diesel and natural gas can be easily mounted on the cylinder head to replace the original diesel injector [122].

Engine control is realized by the injection timing of the pilot diesel fuel and the portion of total energy content which is provided by natural gas, i.e. the substitution rate or the gas-diesel blend ratio. The pilot injection timing control is in principle similar to conventional diesel engines with minor adjustment in the dual-fuel mode. The difference resides in the slightly delayed autoignition of the injected pilot diesel as the radicals during the ignition accumulation stage are in part consumed by the low-reactivity natural gas [27]. Meanwhile, the engine load is mainly controlled by varying the substitution rate. Starting from the idle condition where the engine tend to exclusively operate on diesel, the substitution rate increases up to 60-90% as the engine load ramps up.

In this regard, the term "CI natural gas engine" is not technically rigorous as natural gas per se is not exactly "compression-ignited" and, more importantly, the engine runs on fuels with variable proportion, sometimes even none, of natural gas. Based on the relative distribution of energy content between the two fuels and the major combustion pattern, it can be better termed simply dual-fuel engine, or, more specifically, "natural gas-assisted diesel engine" at low loads and "diesel-assisted natural gas engine" at high loads. The "assistance" is derived from the fact that, at high loads, the replacement of diesel by natural gas avoids the high-equivalence-ratio diesel combustion that is the main cause of NO_X and soot formation, while, at low loads, the combustion instability issue of natural gas lean burn is circumvented by instead using diesel combustion, in addition to the autoignition energy supplied by pilot diesel. Moreover, combustion resulting from the autoignition of air-nature gas mixture at multiple points in the combustion chamber, which is enabled by the autoignition of dispersed diesel fuel, is supposed to be more stable, yet noisier, than the SI flame propagation process. Hence one fuel covers the drawbacks of the other whereas the benefits of both are retained, in theory.

Performance and emissions

Partially reallocating the charge energy content from diesel to the overall-lean premixed air-natural gas mixture, which is characterized by low heat release rate, high hydrogen-to-carbon ratio and simple molecular structure, leads to significantly reduced NO_X and PM emissions in dual-fuel mode compared to conventional diesel operation [123][124]. And such emission reduction is particularly noticeable when natural gas is the primary fuel and diesel the pilot fuel only for ignition [125][126][127], which is most likely attributable to the replacement of the high injected diesel mass and thus the alteration of combustion pattern from the high-equivalence-ratio-then-high-temperature diesel pathway to the premixed low-temperature one. This alteration of combustion pattern is conceptually similar to PCCI or HCCI systems, with a different, cleaner fuel in place and wider load ranges.

Substantial reductions in NO_X and PM emissions through dual-fuel operations come at the cost of deteriorating combustion process. Even though the overall-lean air-natural gas mixture is auto-ignited thanks to the pilot diesel autoignition, the flame propagation in dual-fuel mode is still by nature slow at CI-engine temperature typically lower than SI engines, leading to incomplete natural gas combustion with consistently higher HC and CO emissions than in neat diesel mode [123][128][129]. And the low flame propagation rate as the limiting factor is particularly problematic at low and intermediate loads [130][131], since the temperature is even lower and the air-natural gas mixture leaner. The incomplete natural gas combustion also leads to lower thermal efficiency and hence higher BSFC compared to diesel mode, as the pilot diesel fuel apparently fails to ignite most of the natural gas under those load conditions [132][133][134]. Additional source of HC emissions in dual-fuel mode is the air-natural gas mixture trapped in and late released from the crevices, unburned, which is absent in diesel operation. And the lower oxygen level available for diesel oxidation in dual-fuel mode than in neat diesel mode may also contribute to increased CO emissions, since in the former mode diesel and natural gas compete for oxygen for complete oxidation.

Whilst low charge temperature gives rise to particular difficulties at part loads, full-load thermal efficiencies in dual-fuel mode are similar to [135] or could even be higher than [136] those in normal diesel operations, provided that proper engine tuning and natural gas induction systems are implemented. CCV in IMEP does not seem to be affected by the change from diesel mode to dual-fuel mode, remaining at the level of 1% [137], suggesting that the combustion stability of lean air-nature gas mixtures is to some extent enhanced by the multi-spot diesel autoignition.

It is obvious that the most important control parameter peculiar to the dual-fuel operation is the substitution rate which shows profound impacts on both emissions and performance [138]. The optimum trade-off between reducing NO_X emissions and retaining the attractive thermal efficiencies of diesel engines (in particular the combustion efficiency) needs to be defined for each engine operating point, while HC and CO emissions have to be kept at reasonably low levels. For example, even if higher natural gas proportion at high loads is more desirable for NO_X and soot reduction, a minimum diesel amount of about 10% as pilot fuel should still be used so as to maintain reliable ignition and combustion stability of the overall lean air-natural gas mixture [139].

Introducing uncooled EGR may be an effective solution to the problematic low charge temperature in order to ameliorate the low-to-intermediate-load combustion. In addition, high-pressure diesel injection, increased number of diesel injector holes whose orifice diameter is smaller than standard diesel application, and proper diesel spray angles and injection timings optimized for particular substitution rates and engine loads can all improve atomization and penetration of the pilot diesel fuel in the air-natural gas mixture, providing more ignition spots and enhancing natural gas combustion stability with noticeably reduced HC and CO emissions and increased

combustion efficiencies [140][141].

1.4 Final remarks on natural gas fueling

The achievement of a commercially and technically applicable vehicle fueling option encompasses much more aspects than just the development of an optimized combustion system. After the proposal of one out of all the plausible combinations of ignition types and mixture characteristics, additional aspects, like fuel production and delivery, refueling infrastructure, fuel storage [142], fuel price and system costs as well as future perspectives have to be considered.

1.4.1 A proposal for engine solution

A viable proposal for natural gas combustion systems is the stoichiometric SI engines. Working with cooled EGR and three-way catalytic converters, this engine type produces the lowest exhaust emissions well below the levels of the current and near-to-mid-term-future stringent emission regulations (e.g. post-Euro VI).

The most significant drawback is efficiency penalties in comparison with diesel and lean-burn SI engines, although efficiency is still higher than equivalent gasoline engines. However, the advantages in terms of regulated pollutant emissions are too appealing to relinquish. Soot and treated tailpipe NO_X emissions are undoubtedly negligible compared to the troublesome levels from diesel engines. Moreover, NO_X and THC emissions are 96-99.9% and 90-97% lower, respectively, than lean-burn operations, thanks to EGR and three-way catalytic converters [90][143][144][145]. CO emissions, however, tend to increase in stoichiometric operations compared to lean-burn operations equipped with oxidation catalysts, as a result of less available oxygen in the stoichiometric combustion. But the emission levels are well within certification limits. In addition, stoichiometric natural gas engines do not relay on sophisticated and cost-ineffective aftertreatment systems that may compromise fuel economy due to the need of catalysts regeneration, thermal management or carrying additional reductants. For instance, in order to provide adequate performance for practical vehicles, lean-burn engines with EGR fail to suppress raw NO_X emissions below compliance standards, and SCR is thereby mandatory [39], whereas cooled EGR with the help of three-way catalytic converters can significantly reduce NO_X emissions for stoichiometric engines [146][147].

Incremental efficiency gains are likely to continuously shrink the gap between natural gas SI engines and diesel engines. Future demand from legislative bodies and customers will also squeeze engine efficiency, performance and affordability to the utmost so that even small improvements that were previously considered not worth pursuing may acquire renewed importance [148]. Being part of the SI family,

natural gas engines are expected to enjoy the same efficiency improvement as their gasoline homologues, including downsizing, turbocharging, increased compression ratio, high-EGR-tolerance configurations and use of Miller cycle [149][150][151] [152]. In addition, optimizations specific to natural gas fueling can promise further efficiency gains and fully derive the potential of natural gas. For example, spark advances, in general higher than gasoline engines, should be appropriately adjusted according to engine loads which determine charge temperatures and therefore flame propagation speed. And a proper combination of higher compression ratio, higher boost pressure and higher cooled EGR rate than future gasoline engines [153] may be applicable.

Engine efficiency influences not only fuel consumption but also CO_2 emissions. Results of a well-to-tank (WTT) and tank-to-wheels (TTW) analysis are presented in Figure 1.6, comparing the current and estimated beyond-2020 horizon total GHG emissions from stoichiometric SI CNG-fueled vehicles with conventional gasoline and diesel ones performing the New European Driving Cycle (NEDC). Currently, both the total and TTW GHG emission levels of CNG vehicles lie between gasoline and diesel. And the situation for CNG vehicles improves over time.

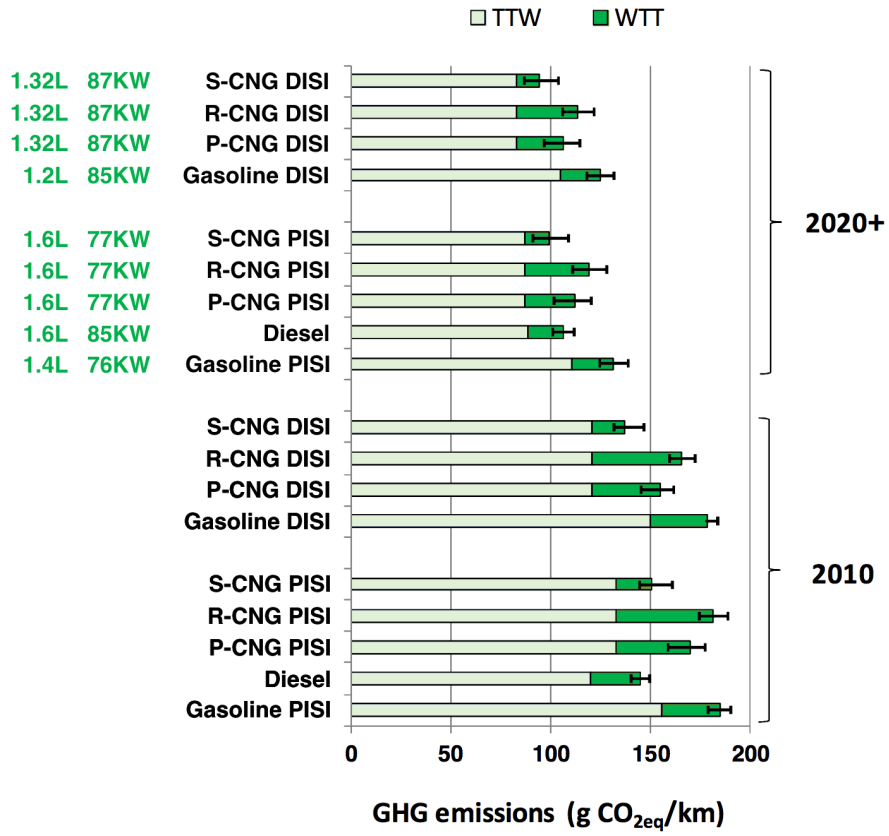

Figure 1.6 Total GHG emissions from conventional and CNG vehicles, adapted from [149]
P-CNG – pipeline CNG
R-CNG – remote liquefied natural gas
S-CNG – shale gas extracted within Europe

As far as direct CO_2 emissions are concerned, the lower carbon intensity grants natural gas a perceivable advantage over gasoline, with similar engine efficiencies. And the TTW emissions from diesel vehicles stay low as diesel engines enjoy a net advantage with respect to engine efficiency. As for the short-term projection, TTW emissions from both PISI and DISI CNG vehicles are lower than diesel, owing to efficiency improvements and lower fuel carbon intensity. It is worth noting that the estimated emissions for CNG vehicles are derived by assuming the same efficiency improvement for all SI engines, and therefore slightly larger displacements are used for CNG to obtain the same engine power of gasoline (see engine information in Figure 1.6). As a consequence, further actual TTW emission reduction is attainable should optimizations specific to natural gas are implemented which would drive natural gas engine efficiency higher than gasoline. On the other hand, CNG origin and supply pathway cause the variation in WTT emissions which depend on future gas resource exploration and infrastructure deployment.

Apart from direct CO_2 emissions, another major driving factor of total GHG emissions for CNG vehicles is identified as methane leakage both from vehicle end use and supply chain [154], since methane, with a global warming potential (GWP) over 20 and 100 years of 86 and 34 respectively, is a much more potent GHG than CO_2. The slightly higher total GHG emissions of CNG vehicles compared to diesel is mainly due to upstream sources such as fuel transmission and delivery, whereas the tailpipe emissions of CNG vehicles are actually lower [155]. However, when crankcase emissions are considered, methane contained in blowby gas from engines without closed crankcase system increases the vehicle-based total GHG emissions by an amount comparable with the tailpipe CO_2 emissions [156]. Accordingly, it is imperative to curtail the well-to-wheels methane leakage, or fugitive emissions, for CNG vehicles to immediately beget climate benefits [157].

The likelihood is high that stoichiometric SI natural gas engines are one of the viable solutions to a carbon-efficient, (hopefully diesel-like) energy-efficient, and sustainable future transport.

1.4.2 Sources and supplies

Fossil fuels are fast dwindling resource. The current reserve-to-production ratio of oil amounts to 50.6 years and natural gas between 52.5 and 60.8 years, depending on the data sources [158][159]. Moreover, oil is forecast to remain the absolute lead fuel in the energy mix up to 2040 [20], whereas the natural gas demand growth is stymied by stronger-than-expected competition from coal, nuclear and renewables, as the flip side of its unparalleled versatility across the energy system to generate electricity, heat and mobility. Therefore, natural gas is as staple as oil, if not more, ready to meet the future energy demand together.

In addition to the proven reserves, most explorationists accept that it is easier to find more gas resources than oil, as the remaining technically recoverable natural

gas resources are estimated to be several times more abundant [159]. Conventional natural gas is either found on its own or as a by-product of oil production (i.e. the associated gas). The discovery of new gas fields and the expansion of gas-rich tight-oil production partially contribute to the estimated large resources. And there is a growing recognition that unconventional gas sources, such as shale gas, tight gas and coalbed methane, will contribute a significant proportion to future gas supplies as technologies evolve [160]. Coalbed methane in the US, Canada, Australia and China is playing a more important role in those markets than originally envisaged. Moreover, the expanding exploration of shale gas in the US and Canada, enabled by gradually mature technologies of horizontal drilling and high-volume hydraulic fracturing, has proven a significant success. In particular, ever since the US shale gas revolution took off in the late 2000s, the rapid increase in shale gas output with an annual growth rate averaged 27% has reshaped the US, the largest gas consumer worldwide, into the largest gas producer as well (even before Russia and Iran). And such success has stimulated other regions, e.g. Europe and Asia, to re-evaluate their gas resources.

In fact, out of the estimated amount of world natural gas resources, around 45% is accounted for by unconventional gas (see Table 1.4). Opposite to the situation of oil that more than half of the reserves are located in regions with frequent political turmoil leading to price fluctuation or supply disruption, as much as is conventional gas, one important feature of unconventional gas is geographical diversity. Deposits are more evenly distributed among regions, which helps stabilize natural gas supply and price. Whilst natural gas is a fossil (hence non-renewable) fuel, methane can be produced in renewable and sustainable ways which further reduce carbon intensity. An intensely studied renewable methane is biogas or landfill gas, a gaseous mixture that is the by-product of anaerobic decomposition of biomass and consists of at least 50% CH_4 and up to 50% CO_2. Biogas can be used for generating power and heat, or as fuel [149][161][162][163], but has to undergo cleaning and upgrading before being used as the equivalent of natural gas. Another route to renewable methane is

Table 1.4
Remaining technically recoverable natural gas resources by regions, end-2016 (unit: trillions cubic meters, or tcm), adapted from [159]

	Resources			Reserves
	Conventional	Unconventional	Total	
Middle East	103	20	123	80
Eurasia	134	38	172	74
Asia Pacific	45	94	139	20
Africa	51	50	101	17
North America	51	79	130	12
Central & South America	28	56	84	8
Europe	19	28	47	5
World	**432**	**365**	**796**	**216**

creating synthetic or substitute natural gas (SNG) from renewable electricity, water and captured CO_2 [164] then with final upgrading. Moreover, there are also massive gas deposits such as methane clathrates, or natural gas hydrate (NGH), offshore in sediment or onshore at high latitudes, which are not yet technically or economically extractable [165]. Biogas, SNG from renewable electricity and NGH all currently assume a minor role due to process complexity or technological limitation, but have the potential to ensure long-term natural gas supply.

Apart from the diversity of natural gas sources, gas supply and trading patterns have also become increasingly flexible. Traditionally, natural gas trading involves capital-intensive infrastructures, which are vital to and cost-effective at transporting large volume from major exporters to importers, but at the same time rigid in terms of long-term bilateral agreements and trade rules (e.g. take-or-pay clauses) between suppliers and customers. The gas market liquidity is being intensified by the recent rapid-growing availability of liquefied natural gas (LNG) [166] mainly due to new liquefaction capacities in the US and Australia. In general, LNG largely benefits remote regions that are not served by pipelines and small market entrants for which constructing pipelines is not economically justifiable. Furthermore, LNG increases the attractiveness and encourages the production of moderate-scale unconventional gas resources that are not readily reached by existing gas grids. Following this trend, offshore in-situ gas liquefaction technology (floating LNG) is being deployed by fuel industry to tap remote gas fields where undersea pipelines are not applicable. The vessel-carried liquefaction facilities are by nature fast to deploy and redeploy, and require much less sunk capital than onshore plants, which further increases the flexibility of gas market. In summary, the increasingly active LNG trading together with reliable pipeline networks enables short-term procurement, enhances security and diversity of supply, increases the range of potential suppliers, and helps to shape a benchmark-based gas pricing that reflects the supply-demand balance [159].

Despite the versatile role of natural gas across the energy system, road transport remains a territory mostly dominated by oil and relatively uncharted for natural gas. But the booming gas market is providing a great opportunity and environment for the road transport sector to enrich engine portfolio, which reduces the dependency of transport on crude oil and, vice versa, mitigates the depletion of oil by transport.

1.4.3 Costs

The abundant and flexible availability of natural gas, especially unconventional gas resources, ensures sufficient future supply and reins in prices. In fact, CNG has a net advantage of price over conventional as well as other major alternative fuels. For example, in the US market, CNG is absolutely cheaper, either on per equivalent gallon basis (the unit in which it is typically sold) or when normalized to an equal energy contents basis, than other fuels (see Table 1.5). In addition, while the prices of gasoline and diesel (and consequently biodiesel blends) considerably vary in the

Table 1.5
Nationwide average fuel retail prices, tax included (unit: US dollars), adapted from [167][168]
GGE – gasoline gallon equivalents; DGE – diesel gallon equivalents;
MBtu – million British thermal units

	per gallon		per GGE		per DGE		per MBtu	
	2014	**2017**	**2014**	**2017**	**2014**	**2017**	**2014**	**2017**
Gasoline	3.34	2.49	3.34	2.49	–	–	28.95	21.78
Diesel	3.89	2.76	–	–	3.89	2.76	30.26	21.45
CNG	–	–	2.09	2.17	2.33	2.45	18.09	18.99
Ethanol (E85)	3.04	2.10	4.29	2.73	4.79	3.08	37.22	31.16
Propane	3.12	2.78	4.31	3.82	4.81	4.29	37.35	45.75
Biodiesel (B20)	3.97	2.68	3.62	2.41	4.04	2.73	31.40	19.07
Biodiesel (B99-B100)	4.28	3.38	4.22	3.31	4.70	3.72	36.53	28.27

two quoted years due to global crude oil price fluctuation (2014 is the last year of a continuing high oil price period and 2017 is in the middle of a low oil price period), CNG remains stably inexpensive. The downward pressure on gas price is the steady and plentiful supply of indigenous shale gas and is likely applicable to other regions in the world thanks to the geographically diversified distribution of unconventional gas deposits. Finally, for natural gas to secure a foothold in the transport sector, it is of crucial importance to remain commercially attractive by keeping the price gap to other fuels.

Nevertheless, fuel price is but a portion of the total costs associated with a fair degree of market penetration of natural gas vehicles. Another major cost division is fuel provision. Conventional liquid fossil fuels have the advantages of storing and delivering large amount of energy with consistently high efficiency. Natural gas on the other hand is more difficult to store and transport due to its low energy density per unit volume. Therefore, CNG requires dedicated infrastructures for distribution and refueling. For a road fuel market penetration up to 10%, the exiting gas pipeline grids that are currently serving domestic, commercial and industrial customers are believed to have sufficient capacity for supplying additional natural gas demand to refueling stations [149]. For areas that are not readily served by gas grids, transport demand alone is unlikely to justify extensive pipeline construction, but LNG trade and local regasification may be an option. The remaining infrastructure issues are primarily related to refueling stations. Firstly, a ratio of 1:300 between fuel stations and natural gas vehicles is recommended [169], implying the necessity of building more fuel stations than the current status to widely promote natural gas as a fueling candidate. Secondly, natural gas delivered by pipeline grids is at an entry pressure of the order of 1 bar and has to be pressurized to at least several tenths times higher when refueling vehicles, requiring additional equipment and energy. Operating and manufacturing costs of refueling hardware are therefore incurred.

At vehicle level, there are incremental costs associated with natural gas as well.

Unlike liquid fuels, the lack of evaporation latent heat of natural gas leaves piston, valves, valve seats and cylinder walls uncooled, and gaseous jets do not provide the same lubrication and cleaning as liquid sprays do. Furthermore, natural gas engines in general have to withstand high in-cylinder pressure, especially peak combustion pressure, as a result of elevated compression ratios and intake boosts. Consequently, robust engine component design with suitable materials and surface treatment [170] [171][172] is needed to guarantee reliability and durability. Finally, additional costs of fuel storage tanks that are specifically designed for highly pressurized CNG have to be included in the equation.

In summary, incorporating natural gas fueling into the transport sector requests initial investment that, from the perspective of individual end users, is expected to be reimbursed by the lower-than-conventional-fuel retail price as well as lower fuel consumption. As a matter of fact, the payback period has to be short enough, ideally within 3 to 4 years, to justify the investment, which may be assisted by government incentives [173]. From a broader and longer-term perspective, the capital costs are to be returned over time by the reduction in GHG and air pollutant emissions which benefits the entire general public.

1.4.4 A viable gas future

A question mark is explicitly intended at the end of the title.

Being both gas fuels, natural gas may play a synergetic or even transitional role towards hydrogen with respect to combustion in general and IC engine applications. The laminar flame speed of hydrogen is 7-10 times higher than methane and, as a consequence, combustion of hydrogen-methane blends is speeded up [174][175] [176], which is particularly favorable to natural gas engines for the major drawback of slow flame propagation is resolved by hydrogen enrichment [177]. And the early almost laminar flame development stage benefits more from hydrogen addition than later turbulent combustion wherein the flame is largely assisted by turbulence [178]. The promoting mechanism of hydrogen enrichment is mainly attributable to kinetic effects, with minor contribution from thermal effects and negligible from diffusion [179][180][181]. Hydrogen admixture introduces high concentration of hydrogen atoms (H) which in turn promotes the production of hydroxyl radical (OH) through the reaction $H + HO_2 \rightarrow 2OH$. Since OH is of significant importance for hydrogen abstraction reaction in fuel oxidation process, the reactivity of methane is increased in hydrogen-enriched flames. The increase in H concentration accompanying the addition of hydrogen sensitizes methane to oxidation to a greater extent for lean mixtures than for stoichiometric ones, as in the former case reactant concentrations are lower and benefit more from the promoted OH production [182]. Furthermore, the combustion of heavier hydrocarbons, when blended with hydrogen, is enhanced to a lesser extent than the combustion of methane-hydrogen blends is [183], which is reasonable considering that methane is the most stable and least reactive of all

hydrocarbon fuels.

As a result of the afore-described promoting mechanism of hydrogen-methane blends, several immediate improvements for engines running on hydrogen-enriched compressed natural gas (HCNG) are obtainable. First and foremost, while methane is the lowest carbon-intense hydrocarbon fuel, hydrogen per se as a fuel is carbon-free. Engine-out CO_2 emissions are therefore further reduced. In addition, shortened combustion duration allows the spark timing to be set closer to TDC which favors engine cycle expansion work over compression work. Moreover, OH concentration boosted by hydrogen partially compensate the dilution effect of EGR by enhancing the combustion, granting HCNG engines higher EGR tolerance than CNG engines [184]. Similarly, hydrogen addition partially offsets the detrimental impacts of lean-burn operations on combustion stability, and is shown to extend flammability range of air-methane mixtures and boost lean-burn features in burners [185][186] as well as in HCNG engines [187][188][189][190]. Hydrogen-induced increase in methane reactivity leads to more stable and complete combustion and in general reduces HC and CO emissions, but meanwhile NO_X emissions tend to increase due to faster and hotter combustion. Under certain operating conditions, it is possible to utilize ultra-lean operations together with hydrogen addition to suppress all recorded emissions thanks to the hydrogen-enhanced lean-burn capability [94][191][192]. Also, with deNO_X aftertreatment devices, hydrogen enrichment can help lean-burn natural gas engines decrease NO_X emissions to extremely low levels and even reach equivalent zero-emission vehicle (EZEV) standards [189].

The relationship between natural gas and hydrogen can go beyond the HCNG that is limited to a mere fuel-blend application. Since both gas species feature high energy content on a mass basis but low density due to the absence of carbon chains that compact molecular structures, engine platforms developed for natural gas have long been demonstrated to run on HCNG [193][194] with little modifications. And this argument is applicable to hydrogen fuel as well, considering that the proportion of hydrogen in HCNG may be gradually increased. In addition, fuel provision and storage systems for natural gas can be synergized with or repurposed for hydrogen-based fuels with minor technological difficulties [195]. Therefore, natural gas could serve as a bridge to HCNG and then to hydrogen, ultimately towards a carbon-free future transport and economy. This is particularly true for the transport sector, and such bridge is projected to be a much longer one, since cost-efficient renewable alternatives are less readily available than for other energy systems [159].

In this regard, the development of natural gas engines actually plays an active double role in decarbonizing the society, since, on the one hand, natural gas as an alternative fuel lowers the transport carbon emissions relative to conventional liquid fuels, and on the other hand, natural gas paves a pathway towards green hydrogen.

Hydrogen, the most abundant element in the universe, is rarely available in the molecular form and requires other energy sources for production, hence considered

as an energy carrier rather than energy source. The use of hydrogen as a combustion enhancer in fuel blends or as fuel in IC engines [196] is consequently dependent on future advancement of renewable hydrogen mass-production technologies utilizing biomass gasification, biological hydrogen, and water splitting by thermochemical pyrolysis and photoelectrolysis [197][198][199].

Progressive incorporation of alternative or renewable energy into the IC engine technology, starting from CNG and so forth, is also an effective way of facilitating market penetration of those energy forms for other prospective propulsion modes like fuel cells, hybridization or electrification, thus accomplishing the multifaceted long-term roadmap to address the multifaceted challenges confronting the transport industry. For this reason, it is not a completely implausible scenario that the future transport is to stand, whether mostly or partially, upon the pillars of natural gas and hydrogen, and that a viable gas future is parked around the corner.

Technologically, natural gas is a promising alternative fuel solution to emission reduction, efficiency improvement and energy sustainability. However, technology is but one integrated factor that determines market participation and penetration of natural gas vehicles. There are far more social and economic factors such as subsidy for purchase, regulative mandates, fuel price regulation, standards for safety and fuel quality, tax reduction from government, financing mechanism, and coordinated development of natural gas vehicles and infrastructure. In summary, successful and fairly popular introduction of natural gas into the transport sector requires political, legal, regulatory, financial as well as technological variables to be simultaneously tackled [40][200][201].

The internationally agreed Sustainable Development Goals (SDGs) [202] for the first time dedicates one specific goal to energy. The seventh SDG, in particular, requires the efforts to ensure universal access to affordable, reliable, sustainable and modern energy, and to double the global rate of energy efficiency improvement by 2030. In addition, the SDG urges clean energy research and technology wherein advanced and cleaner fossil fuel is included. Natural gas accordingly fits well in the scenario for the future.

In conclusion, natural gas fueled IC engines bear eminent prospects of making appreciable contribution to an environmentally, economically and technologically sustainable future transport.

Chapter 2

PISI Natural Gas Engine

Despina can be reached in two ways: by ship or by camel. The city displays one face to the traveller arriving overland and a different one to him who arrives by sea.

When the camel driver sees, at the horizon of the tableland, the pinnacles of the skyscrapers come into view, the radar antennae, the white and red wind-socks flapping, the chimneys belching smoke, he thinks of a ship; he knows it is a city, but he thinks of it as a vessel that will take him away from the desert…

…In the coastline's haze, the sailor discerns the form of a camel's withers, an embroidered saddle with glittering fringe between two spotted humps, advancing and swaying; he knows it is a city, but he thinks of it as a camel from whose pack hang wine-skins and bags of candied fruit, date wine, tobacco leaves, and already he sees himself at the head of a long caravan taking him away from the desert of the sea…

…Each city receives its form from the desert it opposes; and so do the camel driver and the sailor see Despina, a border city between two deserts.

— Italo Calvino

"Le città invisibili"

2.1 Background

In this chapter, the work related to numerical study of the gas fuel injection and air-fuel mixture formation processes, by means of multidimensional computational fluid dynamic (CFD) simulations, in a PISI CNG engine is presented.

2.1.1 Port injection of natural gas

Stoichiometric SI natural gas engines have been proposed as a viable solution to the adoption of natural gas as an alternative fuel for the transport sector. And this combustion system is further divided into two categories according to fuel delivery methods, namely PI and DI. Despite the most pronounced drawback of the reduced engine power due to low volumetric efficiency, PI CNG engine-powered vehicles are absolutely more popular in the current market than DI ones. In fact, most car manufacturers that produce natural gas vehicles opt for PI engines. The advantages associated with PI CNG engines are the reason for the preference that may outweigh the drawbacks.

Although PI CNG engines are not efficient at air admission, the full benefits of volumetric gains from DI are not always attainable when the start of injection (SOI) is set before the intake valve closing (IVC) [203] which is often unavoidable at high loads and high speeds. And in general, the allowable air-fuel mixing windows for DI are considerably shorter than for PI, which necessitates shorter injection duration. As a consequence, DI CNG engines require high-pressure and high-volume-flow-rate injection systems. In fact, a conventional production gasoline PI injector is far less than sufficient for creating stoichiometric mixture in DI natural gas engines due to the difficulty in achieving required flow rates [204]. Specialized injector designs are therefore mandatory for DI applications and are technically challenging in terms of size, materials and tribology, owing to the drastically lower density and viscosity of natural gas than liquid fuels. For example, sealing failures in the nozzle, the lack of natural injector cooling and lubrication, and plunger bouncing at injector opening and closing pose unprecedented challenges for direct injector design. Moreover, to achieve an adequate and reliable mixing process is an imperative task, since it is generally observed that DI produces higher THC emissions than PI, regardless of

engine load conditions as a result of mixture inhomogeneity [205]. Further research and development are still necessary for DI engines to reach a massive commercial stage. DI natural gas vehicles accordingly suffer from high manufacturing costs and complexity mainly owing to the fuel supply lines, which in turn makes PI natural gas vehicles a commercially appealing option to exploit the multi-fuelability of IC engines.

Gasoline-CNG bi-fuel vehicles (alternatively termed bi-fuel or flexible-fuel CNG vehicles) have firstly and long witnessed vast popularity in the market. As a matter of fact, the size of the global natural gas vehicle fleet has increased by an order of magnitude over the last decade [173], and most CNG engines are retrofitted from gasoline ones [63]. The main reasons are fueling flexibility with respect to range and fueling infrastructure availability, relatively low conversion costs, and low fuel prices. Any existing gasoline SI engine can be retrofitted to CNG fueling with the equipment of a low-pressure gas PI system and a storage tank, which is economical and leaves the original engine intact to retain gasoline operation mode. Bi-fuel CNG taxis are typical applications in many cities as an effort to mitigate urban air pollution. The conversion of taxi engines is particularly advantageous as the initial conversion costs are reimbursed rapidly by the price difference between CNG and gasoline, given the high mileages traveled. Such enduring popularity has prompted continuing research activities pertaining to, for instance, the modeling of performance and emission characteristics [206], experimental driving-cycle bench tests [207] as well as real-world emission measurement [208] of bi-fuel PI CNG engines and vehicles. Despite the fact that optimization for bi-fuel CNG engines is compromised in order to accommodate the properties of both fuels, the introduction of bi-fuel vehicles is actually beneficial since it relaxes the close coupling of vehicle adoption rates and infrastructure expansion rates, which assists a gradual transition to and preparation for a more profound future market penetration of dedicated CNG vehicles [209].

The inherent emission reduction potentials of stoichiometric SI CNG engines along with the technological convenience of natural gas PI systems that operate at low pressure (typically $\leq$ 1MPa) have led to the growing interest in dedicated PISI CNG engines. And absent the constraint of maintaining gasoline compatibility, the performance gap to comparable gasoline engines can be partially rectified by CNG-specific optimization with, for example, higher CRs and intake charge boosts. PISI engines dedicated to CNG fueling have hence attracted extensive research effort to date for a variety of applications such as on-road and marine propulsion, and power plants. An analytical optimization methodology based on empirical and numerical models has been developed to expedite cost-effective conversion of diesel engines into dedicated PISI CNG engines by evaluating alternatives regarding combustion chamber design and engine control parameters [210]. And the combustion process of natural gas inside a diesel-converted PISI optical engine has been observed [211] to assess the influences of typical diesel combustion chamber. It was found that the

combustion was stable and knock-free at medium load, and flame winkling due to the re-entrant piston bowl was occasionally observed. Conversion of diesel engines to PI CNG is generally feasible, and involves the replacement of the diesel injector with a spark plug, the addition of a port injector, and a decrease in CR. No major modifications are implemented to the original cylinder head. Another compatibility is that diesel engines are mechanically more robust than gasoline ones, which fits well the CNG fueling with higher-than-gasoline CRs and resultant peak combustion pressures. The emission advantages of natural gas are thus immediately obtainable. Based on similar considerations, a stationary generator diesel engine converted into PISI running on CNG, biogas, and CNG-enriched biogas has been experimentally tested for performance comparison [212]. In addition, CNG PI has been exploited in a supercharged high-CR (21:1) HCCI engine for the application of decentralized combined heat and power (CHP) generating plant [213]. And the combination of a relatively high CR and low boost pressure could raise the generating efficiency to the typical level of large-scale plants. In general, high-pressure fuel supply system and storage tank are not economically and technically applicable to those small gas engines, and PI is a promising candidate. PM emissions from LDVs powered by PISI CNG and diesel engine have been measured [214] by which CNG was found to produce lower PM than diesel particulate filter (DPF) -equipped diesel but higher particle number (PN) performing the Federal Test Procedure (FTP) -75 and the Highway Fuel Economy Test (HWFET) cycles. Experimental measurement of NO_X emissions from a PISI CNG engine has been conducted [215] to individualize each EGR component and its associated thermal and diluent effects on combustion and NO_X formation. Numerical and experimental analyses have been applied to piston and combustion chamber optimization in a small diesel-derived PISI and gasoline-like PISI engines, respectively [216][217], with the aim of enhancing in-cylinder charge motion and turbulence level to sustain the relatively slow flame propagation of natural gas and thus to improve combustion stability. Wavelet analysis has been used to study the IMEP fluctuation dynamics and to identify the dominant spectral modes under different operating conditions of a PISI CNG engine [218], which was a useful insight into the engine pressure variability for developing control strategies. Statistical analysis of the IMEP data and numerical simulations of chemical species distribution have also been performed to examine the hidden rhythms and dynamics of the natural gas combustion system with different injection timings and to identify possible sources of combustion instabilities in a premixed PISI CNG engine [219]. The influence of injector design on CCV has been investigated in a large-bore PISI engine wherein the fuel was delivered to intake valve seats with different types of injector elbows [220], by which extended injection duration was found favorable to mixture quality leading to low CCV. The gaseous jet emitted from a production PI injector has been examined in detail by means of schlieren photography [221]. Both free and impinging natural gas jets were visualized in order to reflect realistic PI conditions, wherein the axial and radial penetration and the overall targeting profile were assessed. The relationship between nearfield shock structure and farfield jet

evolution has been studied with different pressure ratios and nozzle diameters [222], wherein it was found that increases in pressure ratio and hence in Mach disc width resulted in larger nearfield jet angle and promoted spatial distribution and turbulent mixing. In order to improve the thermal efficiency, a PISI CNG engine using late IVC (LIVC) Miller cycle has been experimentally investigated [223] wherein the geometric CR and thereby the expansion ratio were elevated and LIVC was used to maintain the effective CR within knock limits. The net indicated thermal efficiency was improved by 2% and thermodynamic analysis was employed to reveal positive and negative effects associated with the Miller cycle operation combined with EGR. Furthermore, PISI in a premixed-charge side-ported rotary engine intended as range extender for hybrid electric vehicles has been numerically studied with respect to the injection and mixing process [224][225]. PI has been found highly applicable to rotary engines, thanks to the low requirement on injection system and simplified housing design as well as intrinsic short windows for mixture formation inside the combustion chamber. The potential of natural gas fueling has been experimentally and theoretically proven by converting a gasoline engine into a dedicated PISI CNG engine [226] whereby, with optimization of downsizing, compression ratio, EGR rate and spark timing tailored for CNG, reductions in specific CO_2 emissions of 25-34% at part load and 42-45% at full load would be achievable.

An important share of current dedicated PISI CNG vehicle fleet is accounted for by HD applications that had been exclusively occupied by diesel engines in the past decades, and the trend is rapidly growing. This is especially true for the captive HD fleet (e.g. transit and school buses, refuse and delivery trucks) in urban locations where concerns over air quality are more significant than other factors and refueling stations are guaranteed on fixed service routes. Therefore, many HD CNG engines are built around a diesel block with a simple incorporation of the PI fueling system, and meanwhile an increasing number of specifically optimized PISI CNG engines are being introduced to the market [39]. As to complying with emission standards, PISI CNG engine with a single three-way catalytic converter is a substantially more economical alternative to its diesel-fueled counterpart that has to resort to a series of NO_X and PM aftertreatment devices. And the generally observed durability issue of CNG engines within the trucking industry is compensated by the aftertreatment maintenance costs and management of additional reductive agents for diesel. PISI CNG engines running with homogeneous charge offer almost soot-free combustion that forgoes particulate filters. And the superb NO_X reduction capability of three-way catalytic converters significantly lowers distance-specific NOx emissions over a variety of vehicle operating conditions [143][227][228][229]. Besides the major benefits in terms of pollutant emissions, CNG as a low-carbon alternative to diesel also reduces GHG emissions. As a result of the balance between lower fuel-carbon intensity and lower engine efficiency of CNG relative to diesel, PISI CNG vehicles in HD fleet have been found to produce comparable [230], around 13% less [231] and 20-30% less [87] CO_2 emissions than diesel vehicles. With emissions of CO,

methane, and N_2O from SCR [232] and cold-start three-way catalytic converters all considered, the overall tailpipe GHG emissions from PISI CNG HDVs were found to be 6% lower than diesel ones [233], whereas the total life-cycle CO_2eq emissions were found to be approximately 24% lower [234].

In addition to conventional combustion systems, PI of natural gas has also been extensively applied to various advanced combustion concepts.

To exploit the benefits of hydrogen addition to natural gas in terms of further fuel carbon content reduction and flame speed promotion, hydrogen enrichment has emerged as a captivating technology for natural gas engines. SI engine fueled with HCNG blends with varying hydrogen fractions has experimentally demonstrated clear carbon emission reduction potentials [235]. As a result of the extremely light hydrogen molecules, HCNG has even lower density and viscosity than CNG, and thus the technical difficulties in manufacturing CNG direct injectors with adequate injection pressure and volume flow rate apply to HCNG as well. Consequently, PI is commonly adopted in HCNG engines [236][237][238][239][240]. Similarly, PI has also been employed in engines fueled with biogas-derived hydrogen-enriched synthetic gases [241].

CNG PI has also been the staple fuel delivery method for dual-fuel, or RCCI, engines [127][141][242]. To avoid insufficient CI or diesel knock due to the long ignition delay of natural gas, pilot injection of a high-cetane fuel, typically diesel, is utilized whose autoignition serves as the igniting energy source for the premixed air-natural gas mixture. A gas PI system is normally added to a diesel engine so that CNG is delivered as the main fuel in dual-fuel mode, whereby the emission benefits of natural gas is conveniently included with CI-like engine efficiency. Experimental tests have demonstrated the potential of PI CNG-diesel dual-fuel mode to reduce NO_X and PM emissions, and to improve performance and fuel economy compared to conventional diesel mode, especially at medium and high loads [243]. Moreover, CNG PI has been integrated in a pre-combustion chamber RCCI engine, showing drastic decrease in NO_X emissions as well [244]. In addition to CNG and diesel, the combination of gas PI and pilot DI has been widely applied to other alternative fuels for dual-fuel mode such as biogas, hydrogen, DME and biodiesel [245][246][247] [248][249]. CNG with n-heptane has also been proposed for HCCI operation [250].

Another combustion concept of SI engine running simultaneously on gasoline and CNG (i.e. a fuel blend thereof) has recently attracted much research attention. Essentially, such combustion system adopts the configuration of a typical retrofitted bi-fuel CNG-gasoline engine, but works on the principle of dual-fuel operation in the sense that both fuels are burned together instead of separate combustion of each fuel at a time. The idea is to overcome the volumetric efficiency losses of PISI CNG engines through the synergy between a high-octane fuel and a high-energy-density liquid fuel whose evaporative charge cooling further benefits volumetric efficiency. The fuel blends are realized by independently controlled injection of both CNG and

gasoline, termed concomitant injection, by means of either two port injectors [251] [252][253] or the combination of a gas port injector and a gasoline direct injector [254][255][256]. And experimental researches have suggested that improvement in engine efficiency and emissions with little sacrifice of power output is obtainable. In addition, gas PI technology has been applied to similar combustion systems with different fuel blends that are composed of LPG-gasoline [257], hydrogen-gasoline [258][259], and DME-methanol [260] for the prospective combined benefits from both fuels in terms of knock resistance, cold startability, combustion stabilization, power density and, more importantly, emissions.

In summary, PI of natural gas, or gaseous fuels in general, is still quite relevant to the recent development of IC engines. And the present work attempts to provide a useful insight into gaseous PI operation that is important on its own regarding gas-fueled engines as well as essential for other combustion concepts which involve the injection of various gaseous fuels.

2.1.2 Underexpanded gas jet

Although modeling turbulent liquid spray and two-phase fluid flow is avoided since both the fuel, CNG, and the medium, air, are in gaseous state throughout the process, gaseous fuel injection more often than not results in sonic underexpanded jets which are numerically challenging. Ratio between the fuel rail pressure and the backpressure is usually elevated far beyond the critical condition so as to realize backpressure-independent accurate fuel metering and, more importantly, to achieve adequate mass flow rates compensating for the low fuel density. Such high pressure ratio is bound to induce sonic nozzle flow and proximate underexpanded jet.

Underexpanded jet appears in a variety of applications from rocket propulsion systems to leakage of high-pressure gas containers, and its highly complex behavior has been extensively studied by, for instance, the famous names in scientific history, including Barré de Saint-Venant [261], Mach with physicist-photographer Peter Salcher [262], Prandtl [263] and Courant with Friedrichs [264]. In essence, the occurrence of underexpanded jet is determined by the relative magnitude between the pressure at which a fluid is released from a device exit and the ambient pressure. When the exit pressure is higher than the ambient one, which happens at sonic speed and thus the downstream ambient fluid is unable to equalize the pressure upstream, equilibrium is achieved outside the device wherein the fluid further expands to the ambient pressure and thereby accelerates to supersonic state.

Depending on specific fields, the pressure conditions are designated by various notations. The ratio between the exit pressure, P_e, and the ambient pressure, P_a, P_b or P_∞, is equivalently termed jet pressure ratio (JPR), exit pressure ratio, or exit-to-ambient pressure ratio. If the device is a nozzle or an equivalent thereof, the relation is then extended to the nozzle inlet. And the ratio between the inlet total pressure or the stagnation pressure, P_0, and the ambient pressure is equivalently referred to as

nozzle pressure ratio (NPR), overall (or total) pressure ratio, or supply-to-ambient pressure ratio. Given the same value of P_e/P_a that specifies the jet flow conditions, the ratio P_0/P_a is dependent on the fluid properties as well.

The flow pattern of an emitted jet is therefore fundamentally governed by the ratio P_e/P_a. Obviously, $P_e/P_a = 1$ discriminates the subsonic and underexpanded regimes [265]. When $P_e/P_a = 1$, subsonic jet emerges from the exit and the flow is slow enough to adjust to, and thereby depend on, the downstream conditions. For this reason, the gas injectors for engine applications always work in underexpanded regimes to circumvent the jet dependence on the continuously varying downstream pressures. When P_e/P_a is above 1, the jet becomes supersonic and underexpanded. The extent of underexpansion intensifies as the pressure ratio rises, and the resultant flow structures have been well documented [266][267][268]. The flow regime of an underexpanded jet is analytically complicated and is in general divided into the nearfield region and the farfield region with a transition in between. Moreover, the nearfield flow region is further divided into two distinct parts, i.e. the inner potential core and the outer mixing layer that envelopes the core.

Potential core

In the potential core, the flow by its supersonic nature is isolated from ambient fluid by shock waves and the flow structure within is dominated by compressible effect (hence the name gas-dynamic region). The flow is mainly inviscid since no significant viscous effect occurs, and undergoes isentropic expansion. The potential core is generally stationary for a given pressure ratio, and characterized by standing shock structures. Nevertheless, the shock structures assume different patterns as the pressure ratio varies.

For pressure ratios approximately in the range $1.1 \leq P_e/P_a \leq 3$ [265][269][270], the jet is considered to be moderately underexpanded (see Figure 2.1). Immediately downstream of the exit, the fluid undergoes expansion in the form of the Prandtl-Meyer expansion fan propagating towards the jet boundary. When the supersonic expansion waves arrive at the convex constant-pressure streamline that is equal to the ambient pressure, they are reflected back as converging compression waves that coalesce into an oblique shock (termed intercepting shock), owing to the pressure difference between the jet core and ambient gas. The intercepting shock is reflected on the jet centerline, being the axisymmetry boundary, into an outbound reflected shock that then arrives at and is reflected again by the constant-pressure line into a new expansion fan from whose coalescence a new intercepting shock emerges. The cell-like shock patterns are thus replicated along the jet axis.

For higher pressure ratios approximately in the range $2 \leq P_e/P_a \leq 4$ [265][269][270][272][273][274][275], the jet is considered to be highly underexpanded (see Figure 2.2a). In this case, the expansion fan and the reflected compression waves are stronger due to higher pressure difference. And the resultant intercepting shock

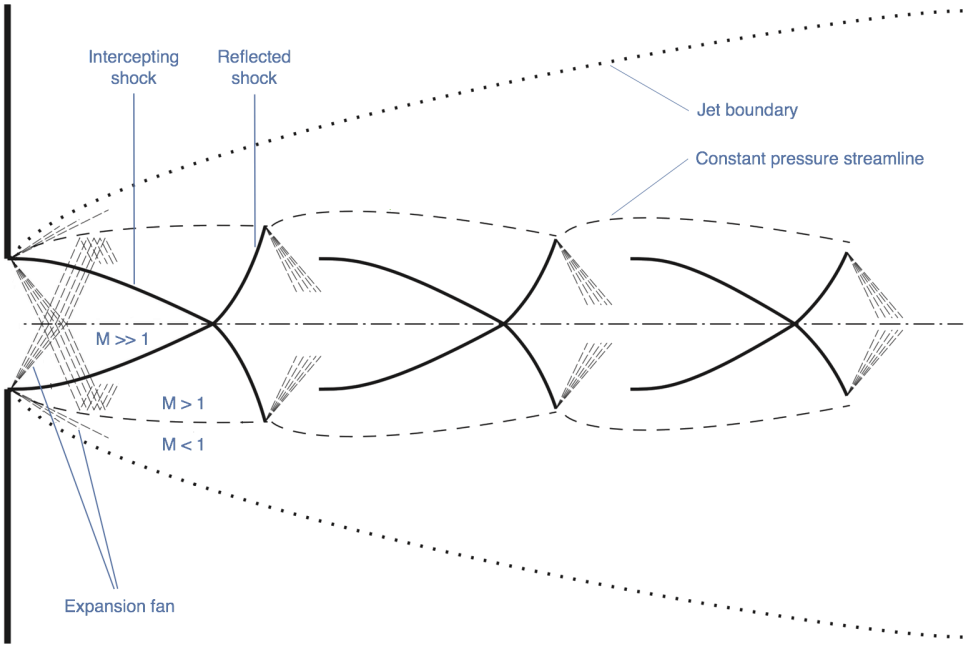

Figure 2.1 Nearfield structure of moderately underexpanded jet, adapted from [271]

has a different angle and assumes the characteristic shape termed barrel (or bottle) shock. Regular reflection of the intercepting shock on the jet axis is instead replaced by a singular reflection which in turn leads to the formation of a normal shock. The normal shock, termed Mach disk, is the signature shock structure that characterizes highly underexpanded jets, and has been extensively studied [266][276][277][278][279][280]. Despite being quantitatively unclear the mechanism that underlies the transition (i.e. the tipping point) from regular reflection to the occurrence of Mach disk, the location of the Mach disk has been universally acknowledged to correlate predominantly with the pressure ratio (or the exit Mach number for supersonic flow issuing from convergent-divergent nozzles) and to be independent, or at the most a weak function, of the fluid [266][269][270][274][276][278][279][281][282][283][284][285][286]. The triple point is formed at the intersection of the barrel, normal, and reflect shocks. A slipstream, which is an embedded shear layer, emanates from the triple point, and separates the subsonic core downstream of the Mach disk from the supersonic outer flow downstream of the reflect shock [287]. The subsonic core flow is reaccelerated to supersonic state through the triple point, physically similar to a convergent-divergent nozzle, and passes smoothly to the supersonic outer flow region. The space between the exit and the Mach disk is encapsulated by the barrel and normal shocks (hence sometimes called the zone of silence), and the isolated flow within undergoes inviscid isentropic expansion, which constitutes the physical background for many analytical approaches.

When the pressure ratio is further elevated to the range $P_e/P_a \geq$ 3-4 [272][274], the jet is considered to be very highly underexpanded (see Figure 2.2b). The shock structure, apart from the first one up to the Mach disk, begins to diminish. The first shock cell is elongated as the location of the Mach disk correlates with the pressure

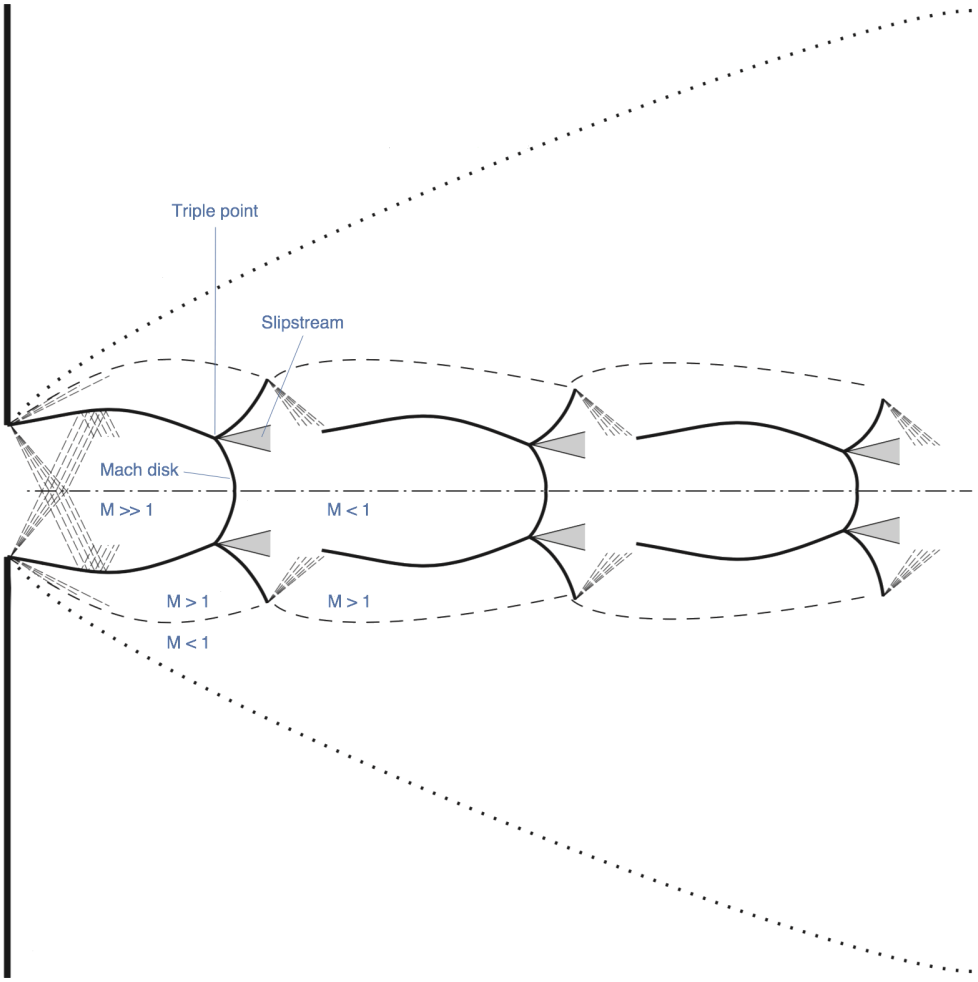

(a) Highly underexpanded jet

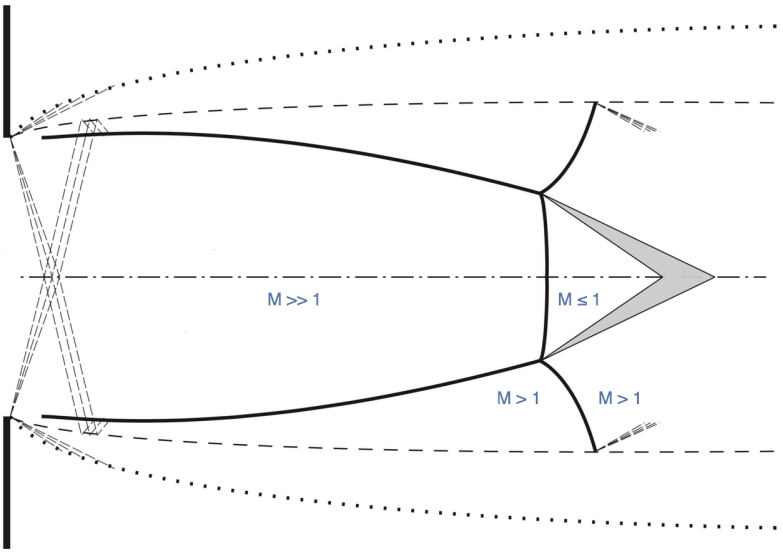

(b) Very highly underexpanded jet

Figure 2.2 Nearfield structure of highly underexpanded jets, adapted from [271]

ratio whereas its diameter shrinks due to intense momentum exchange with ambient fluid, all together leading to increasingly long plume as P_e/P_a rises. For sufficiently

high pressure ratio, the slipstream emanating from the first Mach disk converges on the jet centerline and encloses the subsonic core flow downstream of the Mach disk, and the expansion fan no more coalesce into intercepting shock. Consequently, the potential core is characterized by a unique, long and narrow shock cell.

For gaseous fuel injection application in IC engines, the range of interest of the pressure ratio in general corresponds to the highly and very highly underexpanded jets, with the accompanying barrel shock and Mach disk structures being observed.

Mixing Layer

Opposite to the inviscid potential core, the flow in the surrounding mixing layer between the potential core and jet boundary is significantly influenced by viscous effects and is subjected to large shear, as a result of considerable differences in flow velocity. Therefore, the flow contains large-scale turbulent structures which affect the exchange phenomena between the jet and ambient fluid (hence the name mixing layer) and the jet development [288].

The turbulence is associated with two types of hydrodynamic instabilities in the mixing layer. The first type, Kelvin-Helmholtz instability, is the direct result of the large radial velocity gradient between the supersonic flow close to the intercepting shock and the subsonic flow around the jet boundary (see Figure 2.2). The Kelvin-Helmholtz type instabilities in the shear layer generate the typical wave-like small recirculation that evolves into large-scale vortex rings in the longitudinal direction and involves the entrainment of ambient fluid [289][290]. The second type, Taylor-Görtler instability, results from the conjunct effect of the centrifugal forces and the radial velocity gradient, giving rise to flow non-uniformities and resultant counter-rotating streamwise vortex pairs [291]. The centrifugal forces exerted on the fluid in the mixing layer are connected with the streamline curvature that in turn depends on the strong expansion as well as the inner nozzle boundary layer.

Apart from the shear-induced instabilities, highly underexpanded jets are also affected by shock-induced turbulence. The shock-related Richtmyer-Meshkov type instability arises when two fluids with different density are impulsively accelerated into each other by a traversing shock wave [292]. The strong shock waves involved in a highly underexpanded jet initially cause small-magnitude perturbations which then evolve into chaotic regimes. Such shock-induced instabilities may eventually disturb the shock interfaces, resulting in turbulent mixing and the disappearance of subsequent shock cells downstream of the Mach disk. The triple point as well as the point at which the outbound reflected shock intersects with the constant-pressure streamline are identified as the main instability-inducing sources [293].

All the instabilities exert substantial impacts on the underexpanded jet structure due to perturbating interaction with the shock waves, and are primarily responsible for the highly unsteady behavior of the jet and jet noise (e.g. the vortex pair-induced Mach waves).

Farfield flow region

The outer viscosity-dominated mixing layer grows, starting from the exit as the supersonic jet continuously exchanges momentum with ambient fluid and decays, eventually reaching the jet centerline and completely replacing the inner potential core. The nearfield region is thus terminated.

In the farfield region, the jet is perfectly expanded and the flow fully developed into the shape of a quasi-steady conical stem led by a spherical vortex head. The jet far field is in pressure equilibrium with the ambient fluid despite higher velocity, with its radial and axial penetration achieving self-similarity. Radial profiles of the mean flow variables, i.e. pressure, velocity and temperature, assume the same laws, which is similar to the farfield region of an ideally expanded jet and can actually be treated as one supplemented with proper parameter scaling. This observation serves as the physical basis of many phenomenological jet models that describe the farfield asymptotic region of an underexpanded jet as a fully expanded jet issuing from a corrected pseudo-source [294].

2.1.3 RANS and turbulence modeling

A variety of computational methods have been employed to numerically study underexpanded jet. Given the inviscid compressibility-dominated nature of the core flowfields, the hyperbolic partial differential Euler equations have been reduced to ordinary differential equations by the application of method of characteristics and analytical approaches, in order to investigate various shock phenomena [287][295]. The compressible two-dimensional or axisymmetric Euler equations have also been numerically solved by finite element [296] and finite difference methods [297][298] for the nearfield shock-containing region of underexpanded jets. However, in order to investigate the mixing behaviors of highly underexpanded fuel jets wherein the effects of molecular diffusion and turbulent transport may play a significant role, the hyperbolic-parabolic Navier-Stokes equations have to be applied.

Fundamental physical conservation laws of classical Newtonian mechanics in their original forms are defined for a mass system (or for a material control volume varying in time). Through the application of the Reynolds transport theorem and divergence theorem, the conservation laws are universally formulated for a Eulerian control volume fixed in space, stating that the rate of change of a generic extensive property is the consequence of the interaction between the control volume and its surroundings. Accordingly, by considering momentum as the extensive property, the general strong conservative form of the Navier-Stokes equation, also termed the momentum equation, can be derived from Newton's law of motion applied to a fluid element (to determine its interaction with the surroundings) [299][300] and written in Cartesian tensor notation (with Einstein summation convention) as

$$\frac{\partial}{\partial t}(\rho u_i) + \frac{\partial}{\partial x_j}\left(\rho u_i u_j - \tau_{ij}\right) + \frac{\partial p}{\partial x_i} = 0 \tag{8}$$

where ρ is the density, p the pressure, x_i the Cartesian coordinate, u_i the velocity component in the corresponding coordinate direction, and $\boldsymbol{\tau}$ the stress tensor.

In the Navier-Stokes equation, the viscous stress tensor $\boldsymbol{\tau}$ for a Newtonian fluid is determined according to the Stokes hypothesis that is the extension of the linear dependence of stress on strain rate formulated for one-dimensional flow by Newton. The three assumptions made by Stokes are: (1) the stress tensor is a linear function of the strain rate tensor; (2) the fluid is isotropic; (3) divergence of the stress tensor, $\boldsymbol{\nabla} \cdot \boldsymbol{\tau}$, must vanish for a fluid at rest so that correct hydrostatic pressure results. The resultant stress tensor is given by the Stokes constitutive relations as

$$\tau_{ij} = \mu\left(2S_{ij} - \frac{2}{3}S_{kk}\delta_{ij}\right) \quad = \mu\left[\left(\frac{\partial u_i}{\partial x_j} + \frac{\partial u_j}{\partial x_i}\right) - \frac{2}{3}\frac{\partial u_k}{\partial x_k}\delta_{ij}\right] \tag{9}$$

where S_{ij} is the strain rate tensor, μ the molecular (dynamic) viscosity, and δ_{ij} the Kronecker delta that equals zero when $i \neq j$ and equals 1 otherwise. In conjunction with the constitutive relations in Equation (9), the momentum equation is complete and describes the exact motion of viscous fluid, laminar or turbulent, as long as the fluid can be regarded as a continuum. When the system is more discrete than being a continuum, the Navier-Stokes equation is not applicable and other mathematical formulation is necessary (e.g. the Boltzmann equation).

The instantaneous Navier-Stokes equation, given in Equation (8), is a nonlinear second-order partial differential equation. Specifically, it is in fact the convection-diffusion equation for momentum, which involves the rate of change of momentum in time, the convection of momentum being the first derivative of the nonlinear term $\rho u_i u_j$ with a hyperbolic nature, and the viscous diffusion of momentum being the second derivative of velocity field with a parabolic nature. Although the solution to the momentum equation, together with accompanying conservation of mass (or the continuity equation), conservation of energy (in terms of total energy or enthalpy), closed with an equation of state, provides a precise depiction of the flowfield, the existence and smoothness of analytical solutions in three-dimensional space remain one of the most important open problems in mathematics. Even solving the equation sets numerically is rarely feasible, given the Reynolds numbers typically present in practical applications and the consequent length scales that require computationally expensive spatial and temporal resolution. Accordingly, modeling the turbulence scales entirely or partially is a common practice.

In many engineering applications, the mean flowfield is of greater interest than

the chaotic turbulence fluctuations, and the Reynolds decomposition is applied that separates the mean flow from the fluctuations around it. For unsteady problems, the mean flow variables are obtained by means of ensemble rather than time averaging. For a generic dependent variable ϕ, its Reynolds decomposition is defined as

$$\phi(\boldsymbol{x},t) = \bar{\phi}(\boldsymbol{x},t) + \phi'(\boldsymbol{x},t) \tag{10}$$

$$\bar{\phi}(\boldsymbol{x},t) = \lim_{n\to\infty} \frac{1}{n}\sum_{i=1}^{n} \phi_i(\boldsymbol{x},t) \tag{11}$$

where $\bar{\phi}$ and ϕ' are the ensemble mean and corresponding fluctuation, respectively. Furthermore, for compressible flows, the Favre averaging, i.e. the density-weighted Reynolds averaging, is applied so as to take into account the effects of fluctuations in density as well, and is defined as

$$\phi = \tilde{\phi} + \phi'' \tag{12}$$

$$\tilde{\phi} = \frac{\overline{\rho\phi}}{\bar{\rho}} \tag{13}$$

where the overbar "$\bar{}$" denotes the Reynolds-averaged ensemble mean and the tilde "$\tilde{}$" the Favre-averaged mean. Note that with the definitions given in Equation (10-13), $\overline{\phi'} = 0$ but $\overline{\phi''} \neq 0$, and meanwhile $\overline{\rho\tilde{\phi}} = \bar{\rho}\tilde{\phi} = \overline{\rho\phi}$ so $\overline{\rho\phi''} = 0$. In addition, the averaging operation is by definition interchangeable with linear operations but not with nonlinear ones. Accordingly, for two generic flow variables ϕ, ψ and two constants A, B, the following important property of the Favre averaging holds,

$$\begin{aligned}\bar{\rho}\widetilde{\phi\psi} &= \bar{\rho}\tilde{\phi}\tilde{\psi} + \bar{\rho}\widetilde{\tilde{\phi}\psi''} + \bar{\rho}\widetilde{\phi''\tilde{\psi}} + \bar{\rho}\widetilde{\phi''\psi''} \\ &= \bar{\rho}\tilde{\phi}\tilde{\psi} + \overline{\rho\phi''\psi''}\end{aligned} \tag{14}$$

The momentum equation is studied here as an example since, first, it represents the general feature of the Navier-Stokes equations which is also applicable to other conservation equations, and, second, the closure problem of turbulence modeling is approached starting with the momentum equation to which a physically meaningful reasoning is provided. By introducing the Reynolds decomposition to density and pressure, and the Favre decomposition to velocity, and finally by applying ensemble averaging to the entire instantaneous Equation (8), the resultant Reynolds-averaged

momentum equation writes

$$\frac{\partial}{\partial t}(\bar{\rho}\tilde{u}_i) + \frac{\partial}{\partial x_j}\left[\bar{\rho}\tilde{u}_i\tilde{u}_j - \left(\tilde{\tau}_{ij} - \overline{\rho u_\iota'' u_j''}\right)\right] + \frac{\partial \bar{p}}{\partial x_i} = 0 \tag{15}$$

wherein an additional term $-\overline{\rho u_\iota'' u_j''}$ appears as the direct result of the nonlinearity of the Navier-Stokes equation, specifically the nonlinear convection term, which is demonstrated in Equation (14). In addition, by writing $\tilde{\tau}_{ij}$, the fluctuating term of the stress tensor, $\overline{\tau''}_{ij}$ consisting of second derivatives of the velocity fluctuations, is implicitly neglected due to its negligible magnitude compared to the mean stress tensor, i.e. $\left|\overline{\tau''}_{ij}\right| \ll \left|\tilde{\tau}_{ij}\right|$, which is true for virtually all flows. The fluctuations in the molecular viscosity μ is also neglected in $\tilde{\tau}_{ij}$ according to Equation (9).

The nonlinear convection-induced additional term in Equation (15), $-\overline{\rho u_\iota'' u_j''}$, introduces the correlations of velocity fluctuations as, by symmetry, six additional unknowns to the otherwise closed set of Navier-Stokes equations, but no additional equations are provided, hence the closure problem of turbulence. It has been proven that multiplying the Navier-Stokes equation by the fluctuating velocities and then averaging the product always generates more unknown correlations than equations [301], due to the nonlinear nature of Equation (8). Accordingly, approximations for the unknown correlations in terms of known flow variables are necessary. The term $-\overline{\rho u_\iota'' u_j''}$ is known as the (turbulent) Reynolds stress and physically interpreted as the mean rate of transport of momentum by the fluctuating velocity field. Based on the analogy between the effects of turbulent motion on the mean flow and molecular gradient diffusion in laminar flow, i.e. the Boussinesq approximation, the Reynolds stresses are directly linked to the gradients of the averaged flowfield in the similar manner to the laminar stress tensor [302][303]. The linear constitutive relation, the simplest form and the closest to Equation (9), for instance, is given by

$$-\overline{\rho u_\iota'' u_j''} = \mu_t\left[\left(\frac{\partial \tilde{u}_i}{\partial x_j} + \frac{\partial \tilde{u}_j}{\partial x_i}\right) - \frac{2}{3}\frac{\partial \tilde{u}_k}{\partial x_k}\delta_{ij}\right] - \frac{2}{3}\rho k \delta_{ij} \tag{16}$$

where μ_t is the turbulent viscosity, and $k = \widetilde{u_\iota u_\iota}/2$ the turbulence kinetic energy. The last additional term in Equation (16), relative to the definition of laminar stress tensor, is necessary in the strict sense to ensure proper trace of the Reynolds stress tensor. The effects of the thus-defined Reynolds stress on the mean flow are akin to those of the total laminar stress, $\left(\tau_{ij} - p\delta_{ij}\right)$, with the first part being similar to the viscous stress and the last part to the pressure. Accordingly, the overall effect of the modeled turbulent motion can be considered as an increase in the fluid viscosity on

the basis of the molecular viscosity, hence the name eddy viscosity model (EVM).

The turbulent viscosity μ_t is determined by a characteristic turbulence velocity scale and a length scale. It is in fact the choices for those two characteristic scales that define various EVMs. The same averaging principles are also applied to other conservation or transport equations (of mass, energy and, optionally, species). And based on the same eddy viscosity assumptions, the nonlinearity-induced correlation terms, associated with the turbulent transport of energy (or enthalpy) and species, are modeled in an analogous way to their respective laminar fluxes in terms of linear gradient diffusion through coefficients based on μ_t, which act as an increase in the fluid diffusivity caused by turbulence. The complete method of Reynolds-averaged Navier-Stokes equations (RANS) is thus formulated that provides an approximate mean solution of the flowfields, when supplemented with an equation of state and a turbulence model.

RANS is an extensively used and validated numerical approach with reasonable computational costs for many gas-phase fluid flows and engine-related engineering applications [304][305][306].

2.2 Engine configuration

The engine investigated in the present work is intended specifically for high-performance urban mobility solution that incorporates the immediate pollutant and GHG emission benefits of natural gas fueling in order to alleviate air quality issues in traffic-dense regions with practical gas distribution network.

Specifically, the prototype is a downsized two-cylinder PISI water-cooled CNG engine which is turbocharged with intercooling. Variable valve actuation (VVA) is implemented to the intake valvetrain. The main engine parameters are presented in Table 2.1. Being a dedicated CNG engine, the CR is raised from a gasoline baseline up to 13:1 by modifying the piston crown, in order to take advantage of the knock-resistance of natural gas. A Bosch single-hole injector is mounted to the intake port of each cylinder and supplied by a high-pressure CNG storage tank along with two pressure regulating valves. A gasoline port injector is mounted at the conventional position closely behind the intake valves and a reduced-capacity liquid fuel tank is retained for emergency use only.

The prototype engine is experimentally tuned with respect to injection timing, and numerically investigated for diagnostic purposes of providing explanations for the optimum timing that has been identified by experiments, and of understanding in detail the influences of different PI injection timings on air-fuel mixing process, fuel distribution among cylinders, volumetric efficiency and flowfields that may in turn affect combustion quality and pollutant formation.

Table 2.1
Natural gas engine specifications

	Item	Unit	Value
General Info.	Engine	–	SI CNG
	Cylinder	–	Straight twin
	Cylinder head	–	Pent-roof
	Air induction	–	Turbocharge, intercooler
	Turbocharger	–	Wastegate controlled
Crank Train	Bore	mm	72
	Stroke	mm	84
	Connecting rod	mm	128
	Displacement	cm^3	685
	Compression ratio	–	13:1
Valve Train	Valves per cylinder	–	4
	Valve train intake	–	FIAT MultiAir VVA
	Valve train exhaust	–	Fixed cams
Fuel Inject.	Injection system	–	Multipoint port injection
	Fuel rail pressure	bar	5 – 10 (9 used herein)
	Injector type	–	Single hole
	Hole diameter	mm	1.5

2.3 Numerical model description

A three-dimensional CFD analysis of the engine cycle including gas injection is performed in the environment of a finite-volume commercial CFD solver, Star-CD (version 4.20) along with the parameterized grid generation tool Es-ICE.

2.3.1 Computational domain

The computational domain used in the present work encompasses the complete engine geometry including the combustion chamber, intake and exhaust ports which are extended up to the respective collecting manifold (see Figure 2.3), consisting of hexahedral finite-volume cells. The target cell size in the majority of the volume is imposed at 1mm, and local mesh refinements are allowed to resolve critical engine geometries. In particular, cells between the valves and corresponding seats are set in the range of 0.2-0.4 mm, considering the high flow velocity during gas exchange phases. Such choice of spatial resolution has been widely validated in terms of grid sensitivity, for example in [307][308], and accepted to be sufficient for non-reacting engine flow studies. Moreover, several layers of gradually coarsened extrusion cells are imposed on the inlet and outlet pressure boundaries to improve accuracy and to attenuate possible boundary-induced perturbation and wave reflection thanks to the

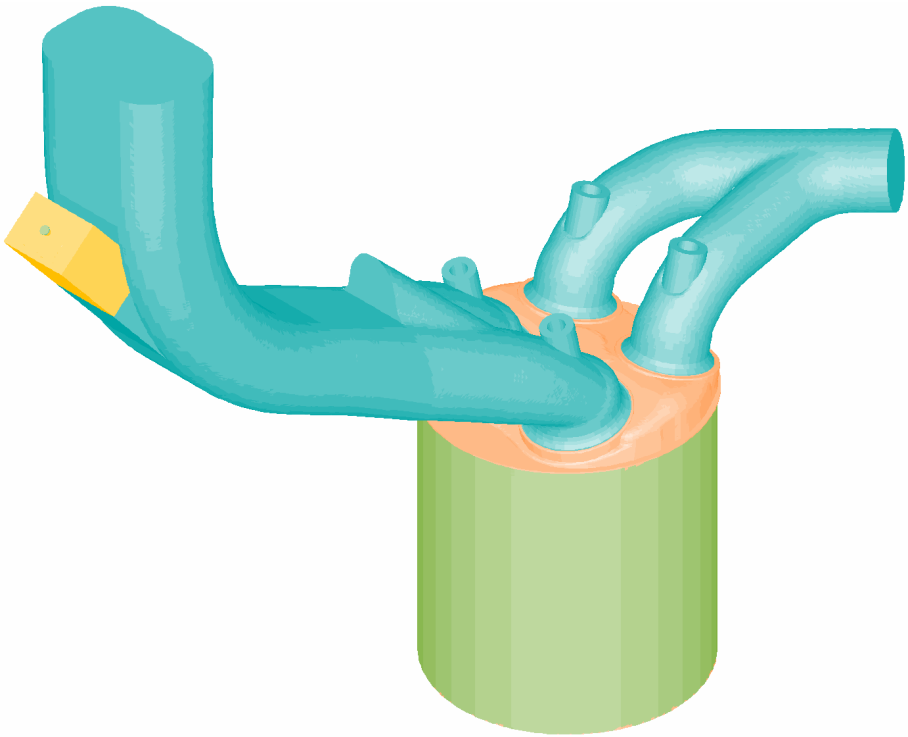

Figure 2.3 Overview of the engine geometry and computational domain
(Intake on the lefthand side; Exhaust on the righthand side)

artificially increased numerical dissipation.

Besides an accurate representation of the engine geometry, the computational grids are variable with moving surfaces that faithfully reproduce the movement of valves and piston, such that full four-stroke engine-cycle simulations are enabled.

A manually built grid of the injector and housing thereof with regularly spaced orthogonal hexahedral cells is incorporated into the engine volume (see the yellow grid block in Figure 2.3), including the PI injector nozzle in the same position as in the actual engine. The grid is manually built so as to have a good control over the mesh quality and spatial resolution inside and in the near downstream region of the injector nozzle. A gradual multi-layer transition zone from the refined cell sizes of the injector grid to the ~1mm cell size of the main engine grid is realized.

2.3.2 Numerical modeling strategies

The three-dimensional time-dependent turbulent flowfields are solved by the RANS approach together with the RNG k-ε two-equation turbulence model. RANS is selected to approximate the mean flowfields so that reasonable requirements on the spatial and temporal resolutions are to be satisfied, especially considering the underexpanded jet that would induce large mean flow gradients and thereby a wide range of turbulence scales. The RNG k-ε model is derived from a renormalization group analysis of the Navier-Stokes equations and accounts for effects of different

scales of turbulent motion [309][310], which is supposed to improve the prediction of complex flowfield involving, for instance, swirling and rapid strain changes. The model has also been corrected for compressibility effects and is thus appropriate to compressible flows [311]. RANS with RNG k-ε model has been a staple choice for numerical analyses of various reacting and non-reacting engine flows [225][244] [312][313][314][315] as well as specifically of underexpanded gas jets issuing into quiescent gaseous medium in constant-volume chambers [316][317][318][319] and of gas fuel injection in engines [320][321][322][323], which were all validated. In addition, it has been pointed out that different turbulence model variants within the k-ε family (e.g. the standard, RNG and realizable models) have limited influences on the predicted structure of underexpanded gas jets [317][324][325]. Finally, the RANS equations are supplemented with the ideal gas model in the present work as it has been shown that the real gas effects are significant for gas pressure above at least 10MPa that is far beyond the injection pressure investigated herein [326][327].

An experimentally calibrated model of the same engine using the system-level simulation tool GT-Power provides crank angle-resolved pressure and temperature profiles at the intake and exhaust manifolds which are then used to set the boundary conditions at the same locations in the three-dimensional CFD model. Pressure and temperature data inside the combustion chamber are also utilized to initialize the thermodynamic state at the beginning of the simulations. In particular, the start of simulation is set at 90 degCA before exhaust valve opening (EVO), and the initial condition is calculated from a hypothetical polytropic expansion according to the experimental data, so that the in-cylinder pressure and temperature are the same at EVO as those in a realistic expansion stroke likely with ongoing combustion. Such initialization strategy, rather than directly setting the pressure and temperature at or after EVO when the combustion is certainly finished, is crucial to the imposition of a correct velocity field inside the combustion chamber. Actually, due to the large pressure difference between the fluid inside the cylinder and the exhaust ports, the strong blowdown in conjunction with the asymmetric exhaust port geometry (see Figure 2.3) causes a significantly different flowfield than an otherwise symmetric piston-driven one. For the same reason, the entire engine geometry instead of a half thereof is included in the computational grid.

All geometrical boundaries of the engine are treated as adiabatic walls since the temperature difference between the working fluids and walls, and the variations in fluid temperature are insignificant without the combustion process. Standard wall function, wherein the assumed distribution of velocity, temperature, and turbulence kinetic energy k and dissipation rate ε are represented by algebraic formulae [328], is applied to cells lying in the logarithmic region of the boundary layer where the molecular and turbulence effects are of comparable magnitude. Convective fluxes in the finite-volume discretized RANS conservation equations are approximated by a second-order accurate differencing scheme, the MARS (monotone advection and reconstruction scheme), which depends on a first-step calculation of cell-face flow

properties and gradients through a second-order accurate total variation diminishing (TVD) scheme (the reconstruction step) and a second-step calculation of the cell-face fluxes through a monotone second-order upwind scheme (the advection step). The thus computed cell-face-centered variables are also used to approximate the diffusion terms. The MARS scheme of second-order accuracy is preferred for the spatial discretization of the momentum equation over the first-order upwinding one in order to avoid excessive numerical dissipation and to capture the large gradients associated with the fuel injection, even though the latter is convergence-wise better. The second-order accurate central differencing (CD) scheme is instead applied to the continuity equation. The advancement of the discretized equations in each time step, the time marching procedure, is handled by an implicit scheme that is based on the unconditionally stable implicit first-order Euler scheme and explicit deferred correctors, leading to a formal accuracy between the first and second order. Finally, the computational difficulty associated with the velocity-pressure coupling in the momentum equation is solved by the predictor-corrector PISO (pressure-implicit with splitting of operators) algorithm [329][330] wherein the mass and momentum conservation laws are satisfied, in an approximate sense, by alternately solving the temporarily operator-split (i.e. variable-decoupled) momentum equation and the pressure correction equation that is derived from and hence enforcing the continuity equation. In the present work, subsequent to the first predictor stage, the provisional velocity and pressure fields are refined by more than the originally proposed two corrector stages, based on the splitting error, in order to enhance the reliability and numerical accuracy.

2.3.3 Injector model

A particular injector model, the source cell method, is applied to the manually built injector grid that includes a part of the injector nozzle geometry. Specifically, the injected fuel is introduced into the computational domain as additional source terms in the form of

$$s_\phi = \dot{m}'''\phi \tag{17}$$

where $\dot{m}'''$ is the injected mass flow rate per unit volume, ϕ a generic flow variable attributed to the injection stream. A proper source term is provided at the selected cluster of cells for each finite-volume equation solved, i.e. the mass flow rate itself ($\phi = 1$) for the continuity-derived pressure equation, the three velocity components for the momentum equation, and the information of temperature and mass fraction for the energy and species transport equations. The prescribed variable values are calculated from the upstream stagnation condition in the fuel rail, according to the nozzle theory and position of the source cells relative to the actual injector.

The method has similar effect to a fixed inlet boundary condition but eliminates the necessity of imposing an actual boundary and the corresponding inner injector geometry leading up to the inlet. Nevertheless, it has to be noted that this modeling method is fundamentally different from many phenomenological injection models such as notional nozzles with corrected diameters or fictive gas droplets that bypass the underexpansion and related shock waves. The source cell method introduces the gas flow within the injector nozzle and therefore allows the physical phenomena of an underexpanded jet to be numerically described.

2.4 Results of injector modeling

Different implementations of the source cell method and hence a generalization thereof for the numerical analysis of gas fuel injection are presented in detail. Pure CH_4 is hereinafter used as the surrogate fuel for natural gas.

2.4.1 Source cell locations

The effects of different locations of the cell cluster wherein the source terms in Equation (17) are introduced are first examined. Three locations relative to the inner injector geometry are selected for inspection (see blue-colored cells in Figure 2.4). The near-tip flow passage of the actual injector is conceptually a convergent nozzle with the exit being the critical section. A conical nozzle with ~30° convergent angle and the same exit diameter as the actual injector nozzle is implemented in the first case, called case "nozzle" hereinafter, and the source cells are located at a distance from the critical section with known cross-section diameter. The velocity (in terms of Mach number) and temperature for the source cells are calculated as

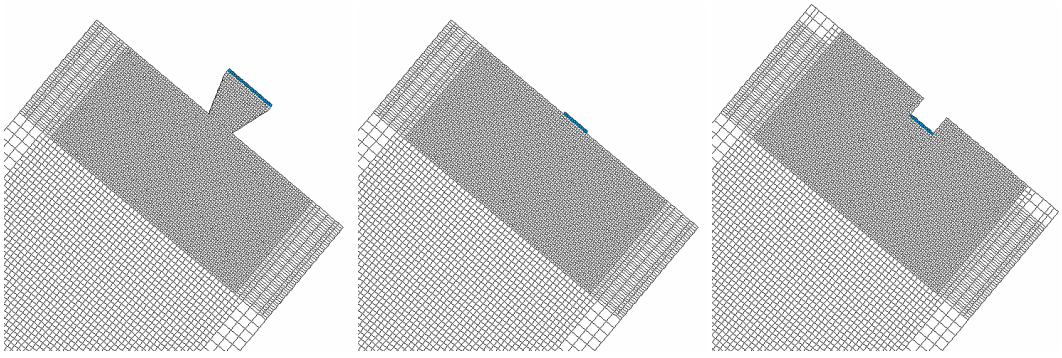

(a) Nozzle **(b)** Upstream of nozzle **(c)** Downstream of nozzle

Figure 2.4 Different locations of source cells

$$\frac{A}{A^*} = \frac{1}{M}\left(\frac{1+\frac{\gamma-1}{2}M^2}{\frac{\gamma+1}{2}}\right)^{\frac{\gamma+1}{2(\gamma-1)}} \tag{18}$$

$$\frac{T_0}{T} = 1+\frac{\gamma-1}{2}M^2 \tag{19}$$

where A is the cross-section area where the source cells are located, A^* the critical section area, T_0 the stagnation temperature in the fuel rail, T the temperature of the source cells, γ = 1.32 the specific heat ratio for CH_4, and M the Mach number.

In the second and third cases, the source cells are directly at the critical section and, since a geometrical section could not be represented by finite-volume cells, the second case has the source cells immediately upstream of the critical section, hence called case "upstream of nozzle" hereinafter, whereas the third case at immediate downstream, called case "downstream of nozzle". An extrusion of the surrounding grid is built in the third case but the critical section is in the same position as in the other two cases. The critical temperature is calculated according to Equation (19) (inserting M = 1) and the velocity corresponds to the local speed of sound since the injector is always chocked. The aim is to understand if different flow structures and mixing behaviors would result from the two source cell locations that should have both otherwise been located at the exact critical section if not for the limiting finite-volume discretization.

As mass flow rate per volume is a parameter to be specified for the source term, all the three cases have equal total mass flow rate. Case upstream and downstream of nozzle have the same per-volume value, different from case nozzle as the latter has a larger source cell volume. In order to compare the effects of locations isolated from other factors, the entire manually built injector mesh and the cells inside the nozzles have exactly identical mesh topology, cell size and refinement transition.

The underexpanded gas jets issuing from the source cell-modeled injector are presented in Figure 2.5. Examples of the jet development shown as mass fraction contours of CH_4 at 50 μs after SOI, corresponding to 0.6 degCA at 2000 rpm, and for the fully developed jets are presented in Figure 2.5 (a) and (b), respectively. It is observed that all three cases predict the same overall jet development with case nozzle showing a slight difference in the head vortex structure at SOI. However, the fully developed underexpanded jet structures in the nearfield region are almost identical in terms of both fuel distribution and Mach number. In Figure 2.5 (c), the predominant first shock cell structure, barrel shock wave and the Mach disk, typical of highly underexpanded jet, are clearly discernable. Furthermore, high momentum regions, distributed along the envelope of the annular potential core downstream of the Mach disk, are captured in the same manner by all three cases. Mixing occurs exclusively in the outer mixing layers, whereas the inner potential cores are isolated

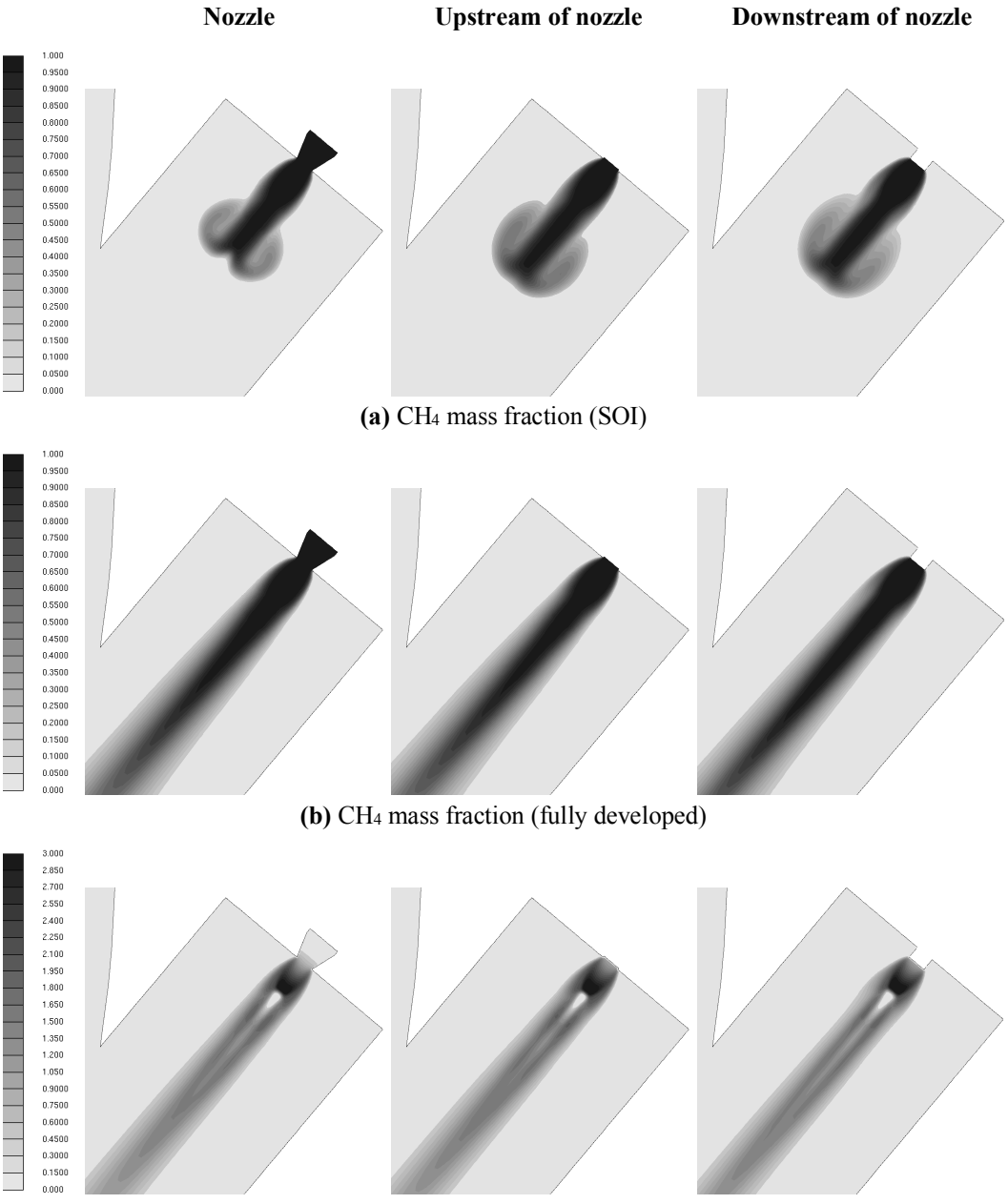

(a) CH_4 mass fraction (SOI)

(b) CH_4 mass fraction (fully developed)

(c) Mach number (fully developed)

Figure 2.5 CH_4 mass fraction and Mach number contours for different locations of source cells

from the ambient fluid by shock waves and hence the fluid inside is pure methane, as shown in Figure 2.5 (a) and (b).

To present a quantitative description of the nearfield shock structures, the Mach numbers along the injector centerline for the three cases are presented in Figure 2.6 with the abscissa representing the distance x from the nozzle exit normalized by the nozzle diameter D. Case nozzle exits at a subsonic speed, indicating that the values calculated from isentropic nozzle evolution and imposed in the source terms are an underestimation, which may be explained by the decrease in discharge coefficient caused by the curvature of converging streamlines upstream of the nozzle exit and

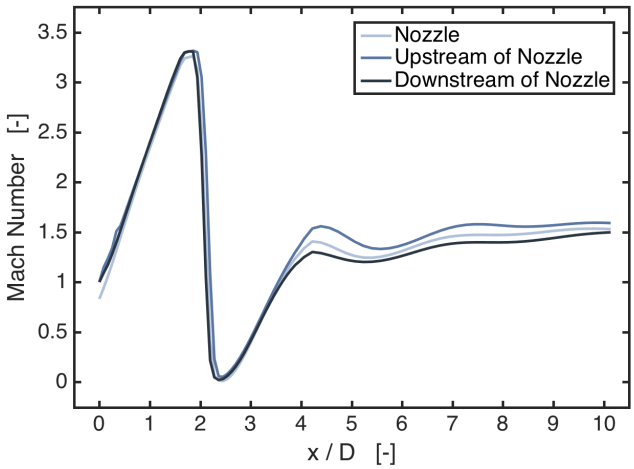

Figure 2.6 Mach number distribution along injector axis for different locations of source cells

by the viscous effects and a consequent transition in the boundary layer [271]. Then, despite being initially subcritical, the flow reaccelerates to supersonic state shortly downstream. And eventually all three cases achieve the same first-shock structure. This is the reason that, in Figure 2.5 (a), case nozzle develops a weaker head vortex at the initial stage, but exhibits the same jet structure as the other two cases when fully developed. Differences in Mach number appear from $x/D = 4$ onwards. The discrepancies are nonetheless considered less of a concern since, firstly, the Mach disk and the first shock cell, which are typically dominant in highly underexpanded jets, are identically predicted. And more importantly, the overall jet development, as shown in Figure 2.5 (b) and (c), is not perceivably influenced.

It has to be clarified that the objective of the injector modeling is to identify a suitable method for the analysis of mixture formation in the combustion chamber, and therefore an accurate description of the complex shock waves appearing in the underexpanded jet is beyond the scope of the present work. To this end, the air-fuel mixing process is further investigated. For the reason of clarity, the convention of crank angles is such that the firing TDC is at 0 degCA, or periodically 720 degCA, and accordingly 360 degCA corresponds to the valve-overlapping TDC, which is consistently used throughout the present work.

From the perspective of engine operation, the mixture at the spark timing is of the most interest which significantly affects the combustion in terms of ignitability, stability, flame propagation rate, heat release rate and pollutant formation process. Accordingly, the probability distribution of the fuel mass with respect to the relative air-to-fuel ratio (RAFR, or lambda λ) at the spark timing (in this case at 690 degCA, or 30 degCA before firing TDC), in the range $\lambda = 1 \pm 0.06$, is presented in Figure 2.7 as an overview of the mixture homogeneity. The probability distributions are derived by statistically analyzing the instantaneous CH_4 mass fraction values from all the finite-volume cells at the given crank angle. All the three cases result in the

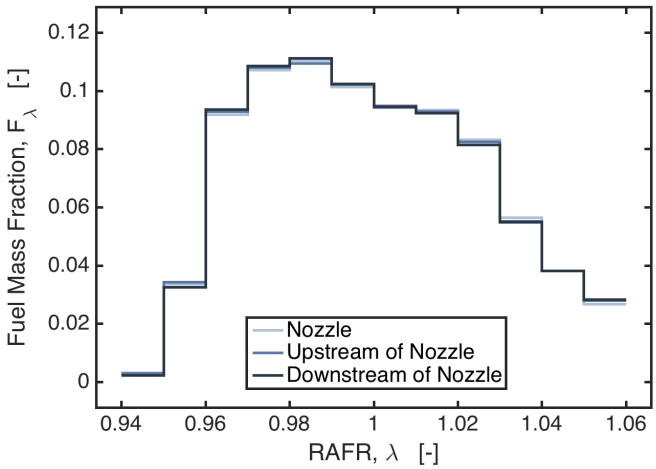

Figure 2.7 Fuel mass probability distribution for different locations of source cells

same final mixture distribution, further confirming that the differences in the minor shock cells posterior to the Mach disk has insignificant influences on the mixing in the combustion chamber.

Besides the statistical presentation of the final mixture, the spatial information on the mixing process is also investigated. The fuel distributions in terms of RAFR contours inside the combustion chamber are presented in Figure 2.8 at three typical engine cycle phases including the intake stroke, intake bottom dead center (BDC) and spark timing near the firing TDC. Starting from the intake phase when the air-fuel mixture is being inducted up to the end of the compression stroke, the mixture formation process predicted by the three cases shows extremely subtle differences. In particular, at the spark timing, the three cases result in the same statistical as well as spatial distribution of the injected fuel.

In conclusion, positioning the source cells between the critical section and some section upstream within the injector nozzle results in slightly different minor shock cell structures towards the rear end of the underexpanded potential core. However, the first shock cell, Mach disk, jet evolution and mixing process remain the same, regardless of whether the nozzle flow is simulated from upstream or directly at the critical section, as long as the local spatial resolution is adequate which is addressed in the next two subsections.

2.4.2 Grid dependence

In view of the independence of principal underexpanded shock structures and mixing process from the source cell locations, the case upstream of nozzle is then used hereinafter for the fuel injector modeling.

The grid dependence studied in the present work focuses on spatial resolution, i.e. the finite-volume cell sizes, in the proximate region downstream of the injector

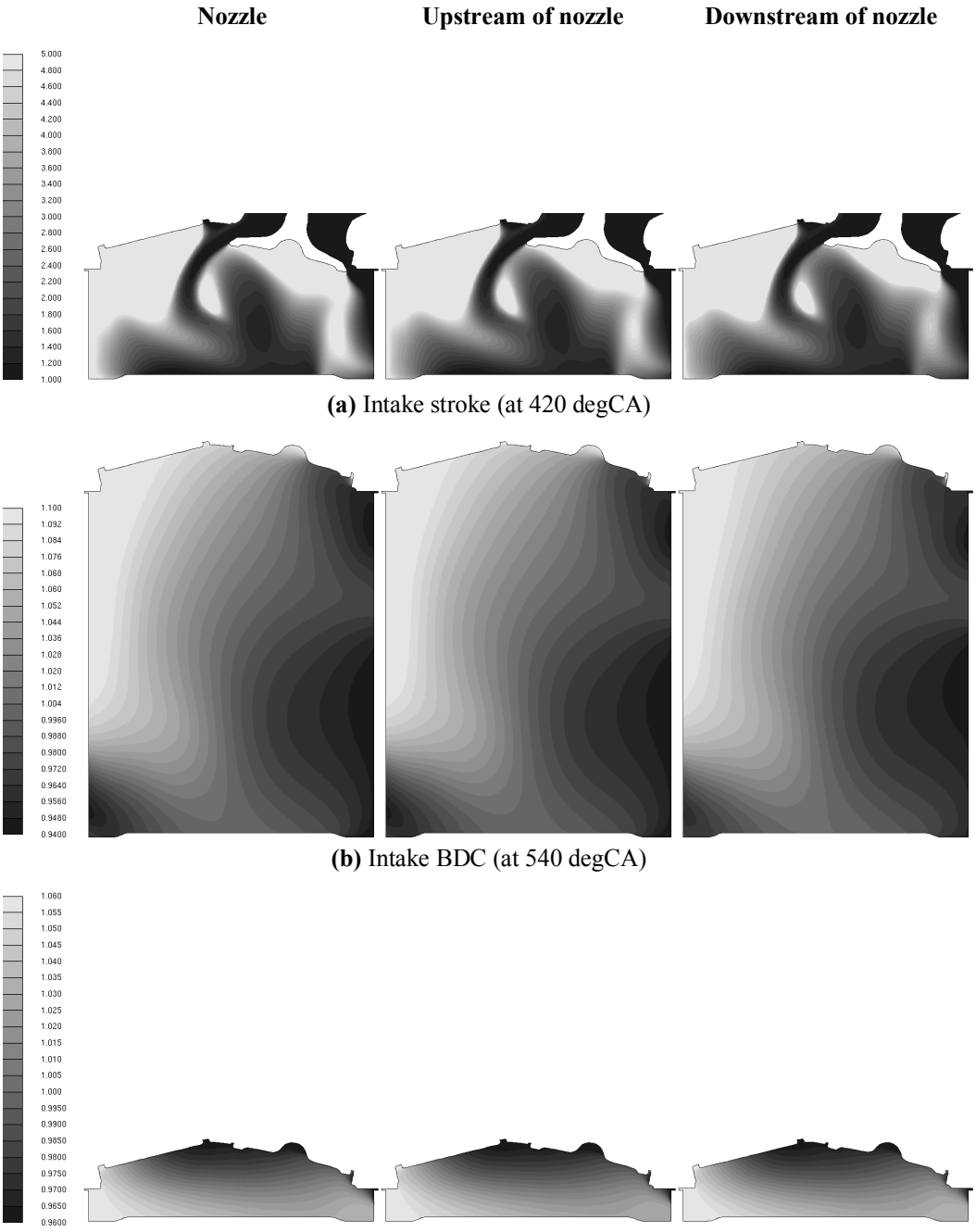

(a) Intake stroke (at 420 degCA)

(b) Intake BDC (at 540 degCA)

(c) Spark timing (at 690 degCA)

Figure 2.8 RAFR contours for different locations of source cells

exit, relative to the cell size in the nozzle. The number of cells, and thereby the cell size, used to resolve the nozzle is instead fixed and the validity is discussed in the next subsection, since there have been numerous numerical studies on nozzles and underexpanded jets which provide useful guidance. Specifically, 12 cells across the 1.5 mm nozzle diameter (as reported in Table 2.1) which lead to 0.125 mm cell size, are placed inside and in the immediate downstream of the nozzle. And level-wise transition (i.e. multiplied by 2) is realized towards the bulk engine grid with a cell size ~1 mm. Accordingly, three refinement zones with cell sizes of 0.125, 0.25, and

0.5 mm are imposed for a gradual transition and conformal nodal connection.

The grid dependence study herein is to understand the necessary extension of each refinement zones for an acceptable description of the underexpanded injection and mixing process, acceptable in the sense of an acceptable compromise between result fidelity and computational overhead. Three refinement cases are examined for this purpose (see Figure 2.9). In common, the finest 0.125 mm zone covers the initial distance of $x/D \leq 4$, which is essential to capturing the high underexpansion and the first shock cell. In case refinement 1, this finest refinement zone is further extended up to $x/D = 20$, whereas in case refinement 2 that same range is covered by the next refinement level of 0.25 mm. In case refinement 3, a rapid transition of 4 layers for each remaining refinement level after the initial range is implemented that in total span the range of $x/D \leq 6$ from which the bulk engine grid then starts. The case refinement 2 in fact coincides with case upstream of nozzle in the previous subsection, and the consequently same results are presented for comparison.

The predicted underexpanded injection jets are presented in Figure 2.10 for the three refinement cases. First of all, it is obvious that the refinement zone extension in case refinement 3 is insufficient since the numerical dissipation associated with the coarse mesh disrupts the still supersonic flow regime causing an overestimated spreading. As for case refinement 1 and 2, the jet development and fully developed jet structure are identical. In Figure 2.10 (c), whereas the jet boundary is the same for both cases, case refinement 1 shows a more potent alternate pattern of subsonic and supersonic regions downstream of the Mach disk than case refinement 2, as a result of numerical dissipation of the latter case attenuating the shock-induced large velocity gradients. However, the transition from the initial finest refinement region to the next double-sized level in refinement 2 constitutes no disturbance to the core flows as the transition location is not identifiable, indicating that the 0.25 mm cell size is fine enough to resolve the underexpanded flow regions downstream of the Mach disk without causing substantial numerical dissipation.

The influences of grid refinement on the nearfield shock structure are shown in Figure 2.11 quantitatively, wherein the Mach numbers along the injector centerline are presented. The three cases describe the first shock cell in exactly the same way

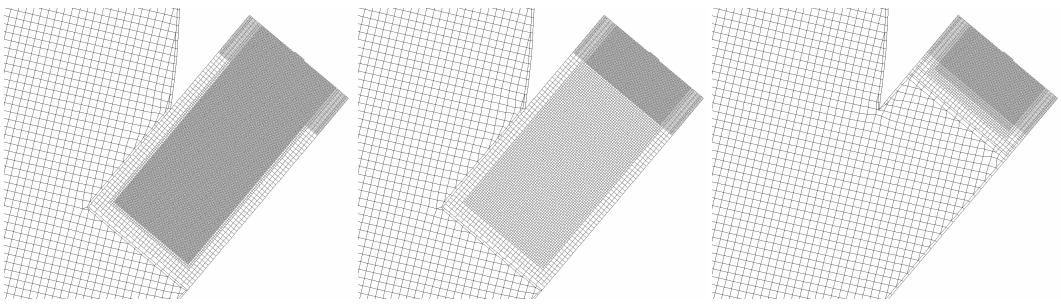

(a) Refinement 1 **(b)** Refinement 2 **(c)** Refinement 3

Figure 2.9 Different mesh refinement levels for grid dependence study

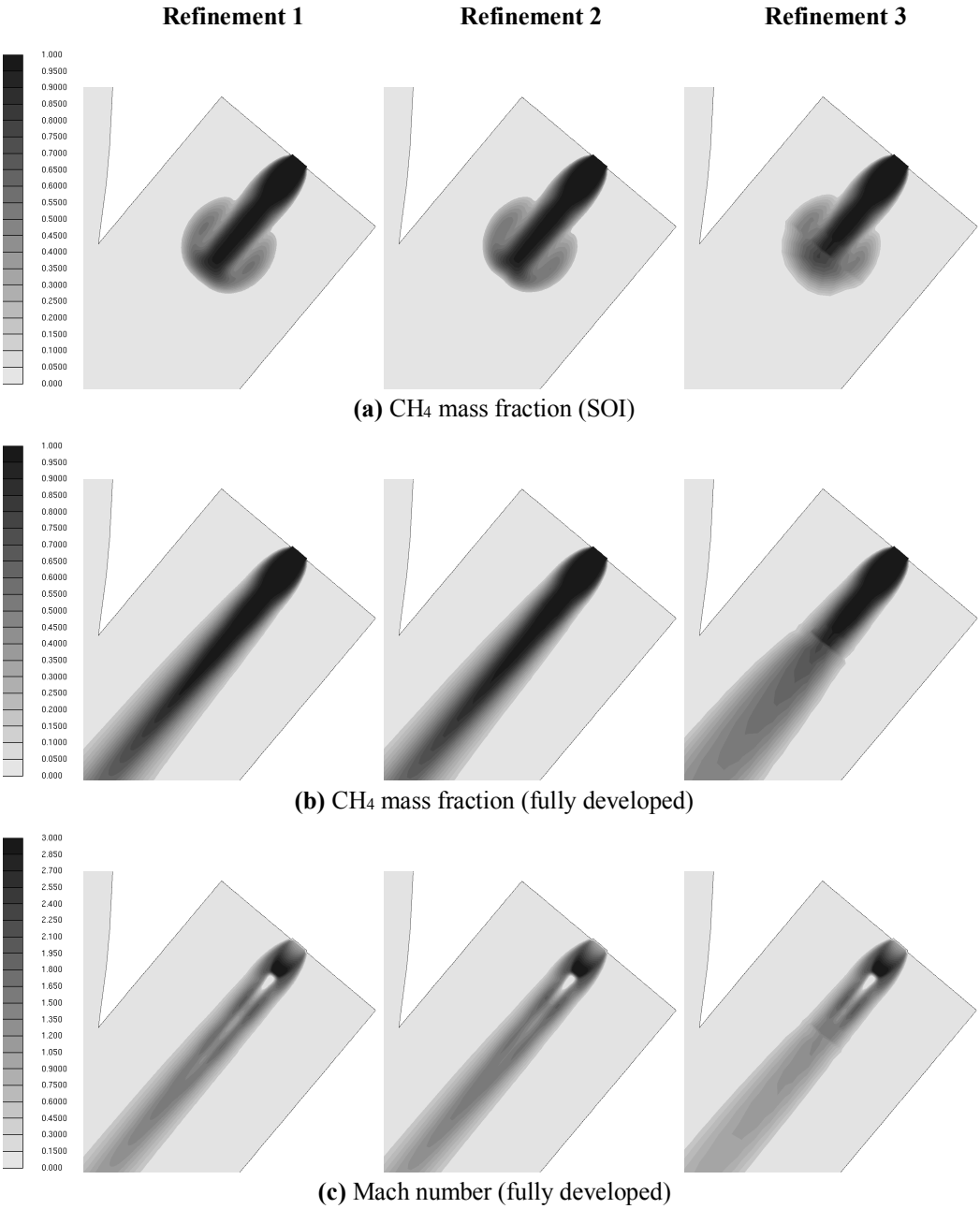

(a) CH_4 mass fraction (SOI)

(b) CH_4 mass fraction (fully developed)

(c) Mach number (fully developed)

Figure 2.10 CH_4 mass fraction and Mach number contours for different grid refinement levels

due to the commonly imposed initial refinement zone up to $x/D = 4$, regardless of the downstream refinement levels. From this aspect, the numerical simulations are physically plausible in that the first shock cell by its supersonic nature is supposed to be unaffected by downstream grid structures that are blocked by the shock waves. Furthermore, the bulk engine grid proves to be excessively coarse for capturing the minor shock cells, as in case refinement 3 the periodicity is lost immediately after the rapid refinement transition zones. The multiple minor shock cells are described in both case refinement 1 and 2, with the latter case having a lower amplitude due to doubled cell size than the former. The wavelengths are nonetheless the same, and the differences in wave amplitude are small. The periodic structures downstream of

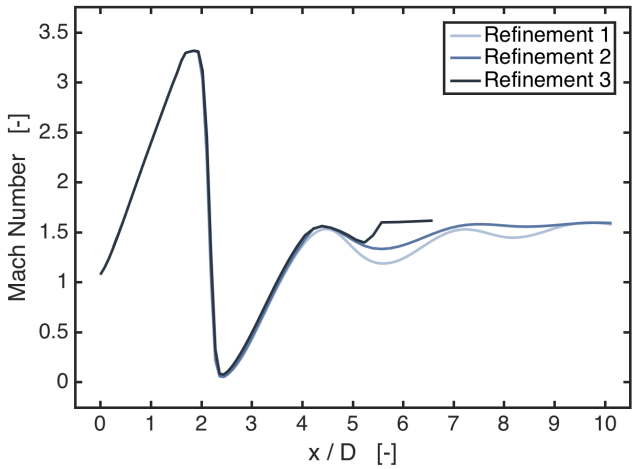

Figure 2.11 Mach number distribution along injector axis for different grid refinement levels

the Mach disk, as captured by case refinement 1 and 2, are expected. The pressure ratio for the fuel injection in the present work lies exactly on the ambiguous border of the transition ranges from highly to very highly underexpanded jets, ambiguous in that the range criteria have been on an empirical basis and the transition itself is more gradual than distinct. Therefore, the underexpanded jet is predominantly but not exclusively characterized by the first shock cell. Downstream periodic structure, weak but existent, is discernable with diminishing wavelengths similarly obtained by case refinement 1 and 2. In addition, the small difference in the minor part of the potential core between case refinement 1 and 2 produces very limited influences on the overall jet structure in terms of fuel distribution as shown in Figure 2.10 (b).

To investigate the specific effects of different grid refinement levels on mixture homogeneity, the statistical probability distribution of the fuel mass with respect to RAFR at the spark timing is presented in Figure 2.12. Consistent with the previous

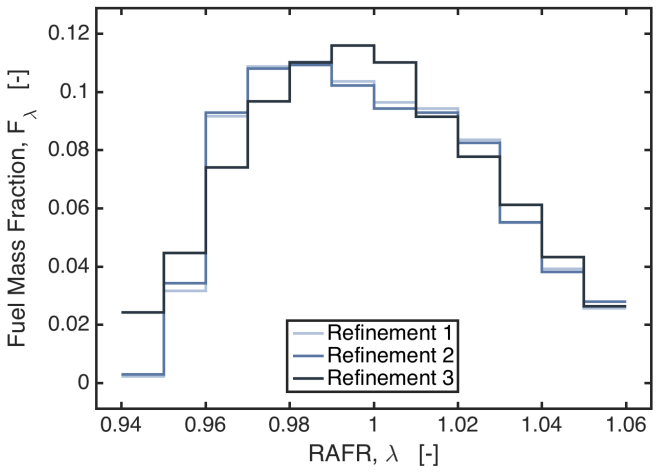

Figure 2.12 Fuel mass probability distribution for different grid refinement levels

observations in Figure 2.11, the excessive numerical dissipation of case refinement 3 overestimates the jet spreading and mixing rate, and the effects are carried over into the combustion chamber as the final mixture is more homogeneous than the other two cases (appearing as a narrower probability distribution around RAFR = 1). In the meanwhile, the final mixtures obtained from case refinement 1 and 2 are nearly identical, indicating that the small differences in minor shock cell description have very limited impacts on the mixing process. And this conclusion is consistent with the one drawn from the cases with different source cell locations.

The detailed mixing processes resulted from different refinement cases are also presented in Figure 2.13 as RAFR contours inside the combustion chamber. From the perspective of a PI engine, the main influences of differently modeled injection reside in the air-fuel premixing in the intake ports prior to intake charge admission. Naturally, as case refinement 3 has an artificially enhanced mixing due to numerical dissipation, the inducted charge is more uniformly premixed which is demonstrated by the bulkier (and hence less concentrated) fuel-rich pockets, especially visible in Figure 2.13 (b) and (c), compared to the other two cases. On the contrary, the RAFR contours for case refinement 1 and 2 are indistinguishable, as being concluded that the differences in minor shock cells do not perceivably affect mixing process.

In conclusion, a refinement zone of sufficient extension covering the potential core is as much necessary as is an initial refinement zone with the same cell size as that across the nozzle to cover the dominant first shock cell. A reasonably refined grid in the exit proximate region is essential to describing the underexpanded jet for two reasons: first, the core flow, albeit inviscid and non-mixing, contains complex shock waves and requires high resolution to predict the resultant structures (e.g. the Mach disk); and second, the mixing layer is subjected to vast shear, generating large gradients to be resolved. In terms of mixing behaviors, case refinement 1 and 2 are considered equivalent, which indicates the achievement of grid independence from the specific perspective of mixing. And case refinement 1 is superior in predicting the minor shock cells downstream of the Mach disk, although the differences from case refinement 2 are very small.

Accordingly, case refinement 2 is finally selected for the subsequent PI engine investigations, as it fits well the scope of the present work. In fact, as a result of the extensive highly-refined zone, the injector grid alone in case refinement 1 contains ~1.9 million cells, comparable with the ~2.1 million cells of the remaining engine grid which is already a refined mesh by RANS standards. Case refinement 1 hence incurs significant computational overhead but largely diminished improvement in the mixing process predictability, especially at the combustion onset.

2.4.3 Injector model validation

As mentioned earlier, the choice of resolving the injection orifice with 12 cells across the diameter is considered sufficient and valid by referring to available grid

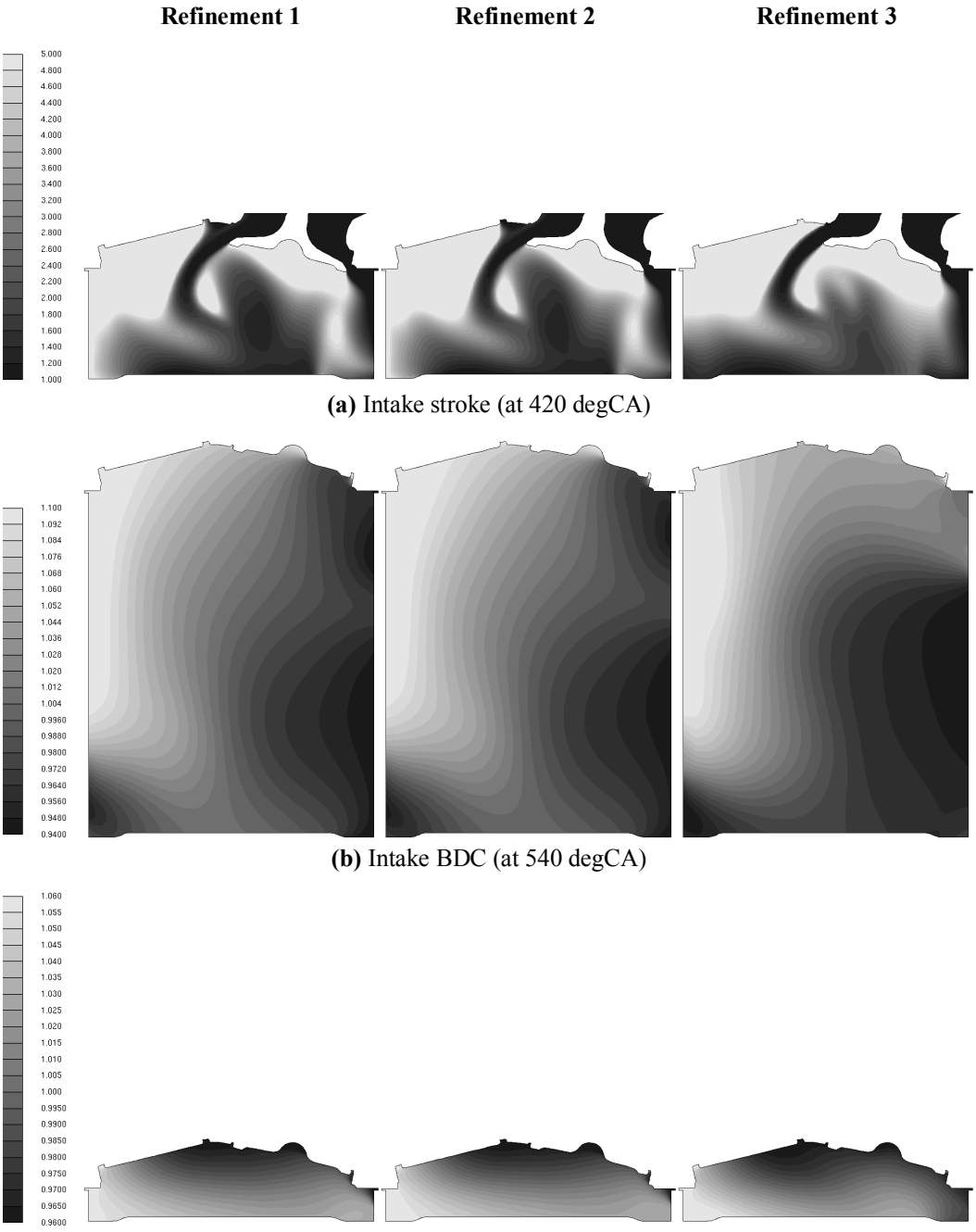

(a) Intake stroke (at 420 degCA)

(b) Intake BDC (at 540 degCA)

(c) Spark timing (at 690 degCA)

Figure 2.13 RAFR contours for different grid refinement levels

dependence studies on gaseous fuel injection process from circular nozzles, which are pertinent to the present work. Specifically, it has been verified that from 10 cells upwards the grid sensitivity of fluid flows near the nozzle is largely reduced [331], and using more than 10 cells across the nozzle brings about little effects on the jet development, penetration and consequent mixing behaviors [332]. Furthermore, the combined effects of spatial resolution and discretization schemes have been studied in [324], arguing that 20 diameter-wise cells with the first-order upwind scheme are sufficient for a fully grid-independent description of the time-variable jet evolution

and mixing process, whereas equivalent results are achievable with 10 cells and the second-order accurate MARS scheme which also provide a good prediction of the typical underexpanded shock structure. Given 10 cells proven to be the convergence point, 12 cells are accordingly imposed for an extra safety margin and considered methodologically validated. In addition, pressure ratios involved in all the reference studies are much higher than that in the present work, and theoretically less than 10 cells may suffice. Based on the universal similitude of the circular nozzle geometry and flowfield, detailed grid dependence study of the required number of cells across the orifice is therefore not repeated here.

Nevertheless, considering that all the different source cell models investigated herein result in identical characterization of the singular barrel shock reflection and the normal shock formation with proximate subsonic flow zone, comparison of the predominant shock-relevant Mach disks is discussed. Above all, the consensus has long been reached that compressibility-governed flow phenomena in the potential core are primarily dependent on the pressure ratio. The injection pressure is 9 bar, and the ambient pressure inside the intake ports corresponding to the crank angle in Figure 2.6 and 2.11 is about 0.85 bar (a specific crank angle has to be referred to since the pressure during an engine cycle varies continuously), resulting in p_0/p_a ≅ 10.59, typical value to generate very highly underexpanded jets.

The Mach disk position is discussed here. In fact, Mach disk location is the only parameter that has been extensively studied with well-documented reliable relations for pressure ratio correlation, in comparison with other parameters (e.g. Mach disk diameter) that may be predicted by case-specific expressions with fair uncertainties. An empirical relation based on a collection of experimental measurements has been proposed in [267] for the correlation between normalized Mach disk position and pressure ratio, and is reported in Equation (20). Another similar experiment-derived relation, reported in Equation (21), has been proposed in [277][333] with a different coefficient. Both relations imply that the Mach disk position is insensitive to factors other than the pressure ratio. Alternatively, the correlation has been formulated as a weak function of γ in addition to pressure ratio by using theoretical analysis based on dimensional group [334] so as to consider the thermodynamic effects of the gas species, as reported in Equation (22). Mach disk positions obtained from the various relations are slightly different from one another yet no verdict has been provided, although Equation (20) and (21) have been referred to more often in the literature

$$2.4\left(\frac{x_{MD}}{D}\right)^2 = \frac{p_0}{p_a} \tag{20}$$

$$\frac{x_{MD}}{D} = 0.67\sqrt{\frac{p_0}{p_a}} \tag{21}$$

$$\frac{x_{MD}}{D} = \frac{1}{2}\sqrt{\gamma}\left(\frac{\gamma+1}{\gamma-1}\right)^{\frac{1}{4}}\sqrt{\frac{p_e}{p_a}} \tag{22}$$

where x_{MD} is the position of Mach disk along the jet centerline from the exit.

The Mach disks predicted by the injector model in the present work (see Figure 2.6 and 2.11) are slightly more inclined than a vertical step-like discontinuity, which is attributable to several factors. First, in the transition from a highly to a very highly underexpanded jet as the pressure ratio increases, substantial curvature of the Mach disk is observed and local discontinuities no longer feature a normal shock interface [271]. Second, owing to the same transition, the Mach disk thickens, appearing as simultaneous diffusions in both directions from its continuum position [335]. Third, oscillation in Mach disk positions has been experimentally observed [336]. Finally, apart from the physically based explanations, the local cell sizes are purposely not optimized for capturing detailed complex shock structures, and numerical diffusion unavoidably tends to smooth out sharp gradients. Accordingly, the average position between the maximum and minimum Mach numbers, which is shortly upstream of the position where $M = 1$, is chosen to represent the Mach disk location, since Mach disk curving, thickening and oscillation have seldom been considered in empirical quantitative correlations. The comparison is presented in Table 2.2. The numerical results obtained in the present work closely reproduce the two empirical relations, and is about 4.6% lower than the analytical formulation using $\gamma = 1.32$ for methane, indicating that the numerical model is reasonably valid.

The Mach disk position is compared with two additional correlation studies as presented in Figure 2.14. The experimental measurements are cited from [279]. And the numerical results have been obtained in [298] by solving the axisymmetric Euler equations with a third-order TVD finite-difference shock-capturing scheme [337]. An as good agreement with the references as in Table 2.2 is shown, with the present work falling very close to the relation range of the experimental results and slightly above that of the numerical results.

The comparisons of Mach disk positions also imply that the injector modeling by means of source cells is able to predict consistent underexpanded jet structures that are equivalent to the results obtained by conventional modeling approach using

Table 2.2
Comparison of the Mach disk positions

p_0/p_a	p_e/p_a	x_{MD}/D			
		Present	Equation (20)	Equation (21)	Equation (22)
10.59	5.74	2.154	2.100	2.180	2.258
		0	+ 2.6%	- 1.2%	- 4.6%

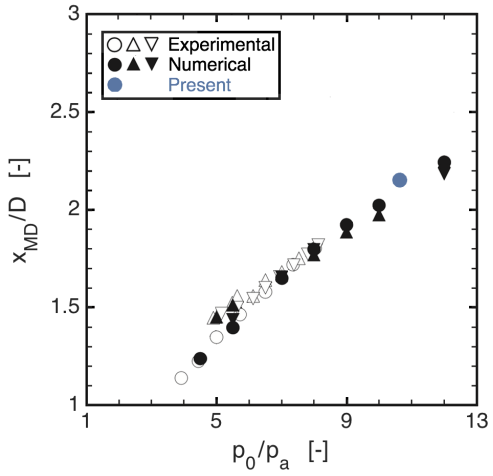

Figure 2.14 Comparison of the Mach disk positions, adapted from [298]

boundary conditions at the upstream nozzle inlet, substantiating the same argument made in [324].

2.5 Results of mixture formation

In view of the source-cell location sensitivity and grid dependence studies on the in-cylinder mixture formation as well as of the methodological and analytical validation, the injector model with the configuration of case upstream of nozzle and case refinement 2, is considered appropriate to the air-fuel mixing investigations in realistic engine operations.

2.5.1 Injection timing and inter-cylinder fuel distribution

The numerical model is employed as a diagnostic tool to investigate in detail the mixing mechanism and determinative factors thereof that elude experimental testing on the prototype engine. Specifically, an injection sweep over the entire 720 degCA engine cycle for the operating point 2000 rpm low part load is undertaken on the test bench, in order to identify the effects of injection timing. This particular operating point is chosen for two reasons: first, the close-to-low-end engine speed would largely hinder the in-cylinder charge motion and the consequent mixing; and second, the VVA-enabled short intake valve opening window and small lift, typical of part-load operations, could be problematic for charge induction.

End-of-injection (EOI) at 270 degCA has been identified as the optimum timing according to standard engine calibration procedures in terms of fuel consumption and emissions, with operational abnormalities occurring at other timings. To reveal the underlying mechanisms, the injection sweep is reproduced through a system-

level engine simulation. The RAFR distribution between the two cylinders, together with the valve lift curves, is presented in Figure 2.15 with respect to all investigated EOI timings. The VVA-reduced intake valve profiles indeed pose a constraint on charge induction, as a small fraction of the engine cycle, from ~150 to 420 degCA, is usable for EOI variation to produce an even inter-cylinder fuel distribution. For EOIs outside the range, the symmetric patterns of RAFR distribution indicate that fuel crossing from one cylinder to another occurs. Six injection timings (see filled dots in Figure 2.15) are selected for further CFD analysis, among which the early and late EOIs (60 and 510 degCA) are for understanding the fuel crossing and four EOIs within the usable window (150, 270, 360 and 420 degCA) for detailed mixture formation mechanisms.

The definition of earliness and lateness for PI is different from DI engines. For the latter, injection timings are termed relative to the spark timing but for the former to IVC. Accordingly, EOI 510 degCA is actually the earliest among all the selected injection timings and 420 degCA effectively the latest.

2.5.2 Two-stage mixing process

Two phenomena are revealed by CFD simulations utilizing the injector model developed and validated before. Firstly, the injected fuel, accumulating in the intake ports, is drawn reversely into the intake manifold due to pressure drop caused by the intake phase of the other cylinder. An example is presented in Figure 2.16 for case EOI 60, wherein reverse flow of the rear end of the injected fuel occurs while the front end is moving towards the then-closed intake valves. The same situation appears for case EOI 510 since the fuel residing time is even longer. Therefore, the injection timing cannot be set throughout the entire 720 degCA range to make full use of the hypothetical long mixing time of PI engines. Instead, a threshold exists

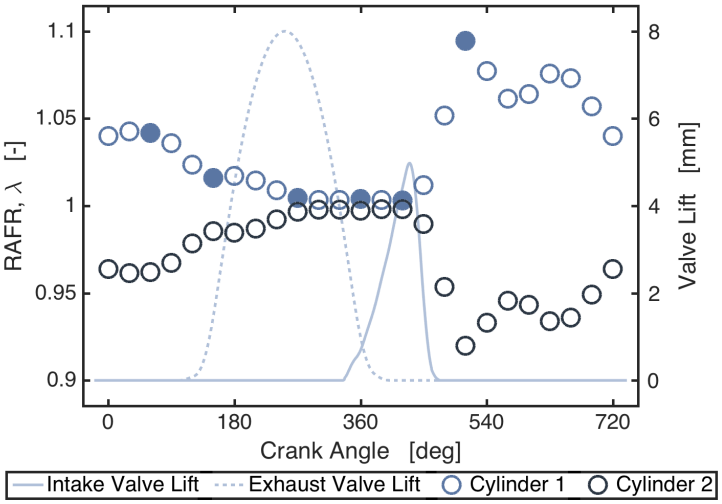

Figure 2.15 Injection sweep results for different EOI timings (with 30 degCA interval)

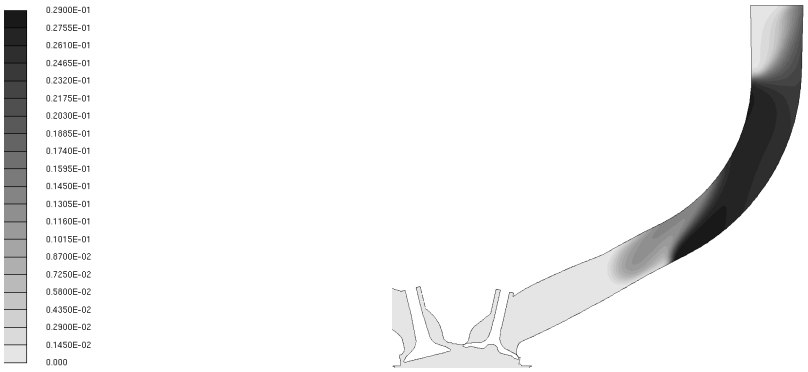

Figure 2.16 Fuel crossing for case EOI 60 degCA, occurring at 170 degCA

for gas-fueled PI engines, earlier than which fuel crossing is inevitable.

The second, more peculiar phenomenon is the two-stage mixing process. Fuel injected before IVO of each engine cycle is in fact partially inducted and burned in the same cycle. And a portion of the total injected quantity is left in the intake ports after IVC. Consequently, except for the first cycle, the fuel inducted in the cylinder consists of residual fuel from the previous cycle and injected fuel from the current cycle. From the perspective of numerical simulations, the residual fuel distribution inside the intake ports has to be considered for initialization, in order to reflect the actual mixing processes. An example is presented in Figure 2.17 for case EOI 270. Figure 2.17 (a) shows the residual fuel distribution from the previous engine cycle, used for flowfield initialization, and Figure 2.17 (b) the residual from the currently simulated cycle. A steady state is clearly reached, for which the two-stage mixing process is detectable in neither experiments nor system-level simulations.

The two-stage mixing process is influenced by injection timings. Figure 2.18 shows the differences in inducted fuel mass between simulations with and without initialization of intake port residual fuel, for the four investigated injection timings. By comparison between the two groups (with or without initialization), two distinct induction stages are identifiable. Initially, due to limited fuel traveling speeds from the injection site to intake valves, induction occurs much later than IVO for cases

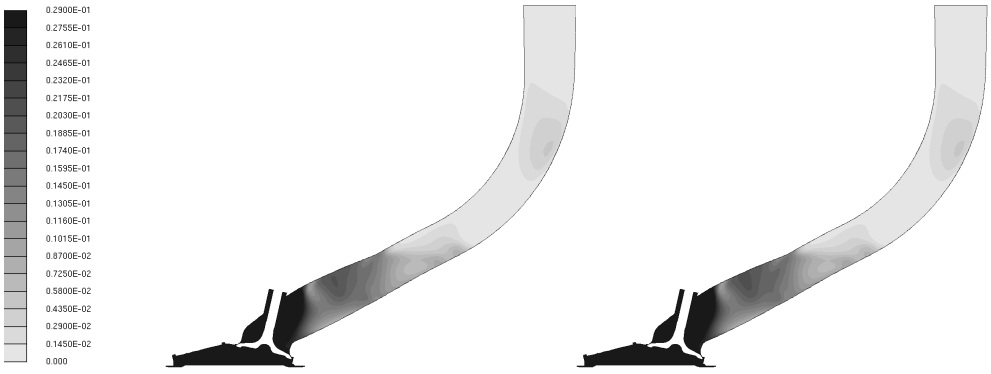

(a) At 0 degCA **(b)** At 720 degCA

Figure 2.17 Fuel mass fraction contours inside the intake ports, case EOI 270

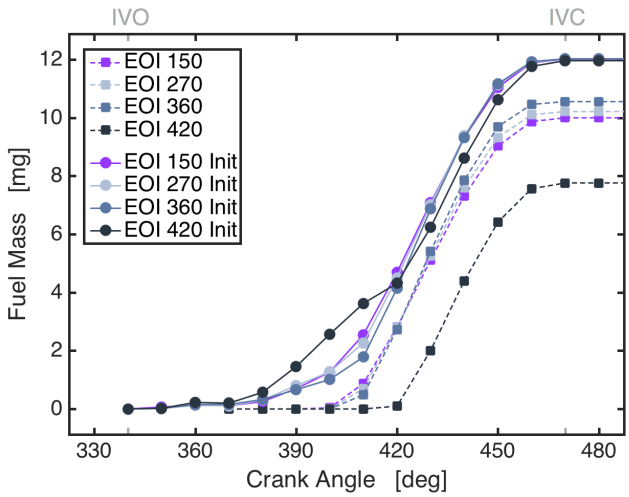

Figure 2.18 Cumulative fuel mass present in the combustion chamber for different EOI timings

without residual fuel. For the other group with initialization, the first empty window is covered by induction of the residual fuel. Such distinction not only influences the amount of fuel eventually present in the cylinder after IVC, but, more importantly, discloses two mixing stages, i.e. the mixings of initially inducted residual fuel and of freshly injected fuel that arrives later (hence termed two-stage mixing process).

Accordingly, injection timing has a two-fold impact on the mixing mechanisms of an actual engine (always with intake port residual fuel). The amount of time for the freshly injected fuel to arrive at the intake valves and thereby the amount of fuel involved in the second mixing stage may vary with the injection timing. Moreover, later injection may result in more residual fuel that partakes in the first mixing stage of the succeeding engine cycle. The two-stage fuel induction process is detailed in Figure 2.19 by comparing the cases with and without residual fuel initialization so as to individualize the first and second stages (as the figures are for qualitative and illustrative purposes, colormaps are omitted for simplicity and the scale is the same across each of the three shown crank angles). Figure 2.19 (a) clearly demonstrates the empty window of intake phase prior to the arrival of injected fuel and the first-stage induction of residual fuel which in turn depends on the injection timing. For instance, case EOI 420 has the highest amount of residual fuel and correspondingly more fuel is inducted and mixed in the combustion chamber during the first stage than the other three cases. Then, as shown in the upper rows in Figure 2.19 (b) and (c), the fresh fuel reaches the intake valves and the second-stage induction begins subsequently. It is observed that the first-stage induction does not affect the second-stage one, as the cases without initialization show the same inducted charge flows as cases with initialization. The sole differences are the preexistent mixture inside the combustion chamber in the latter cases. Nevertheless, depending on the relative phasing between the arrival of freshly injected fuel and intake valve lift profile, the combined results of the two mixing stages are different. Specifically, as shown in Figure 2.19 (b), delaying the injection event leads to more fuel flowing through the

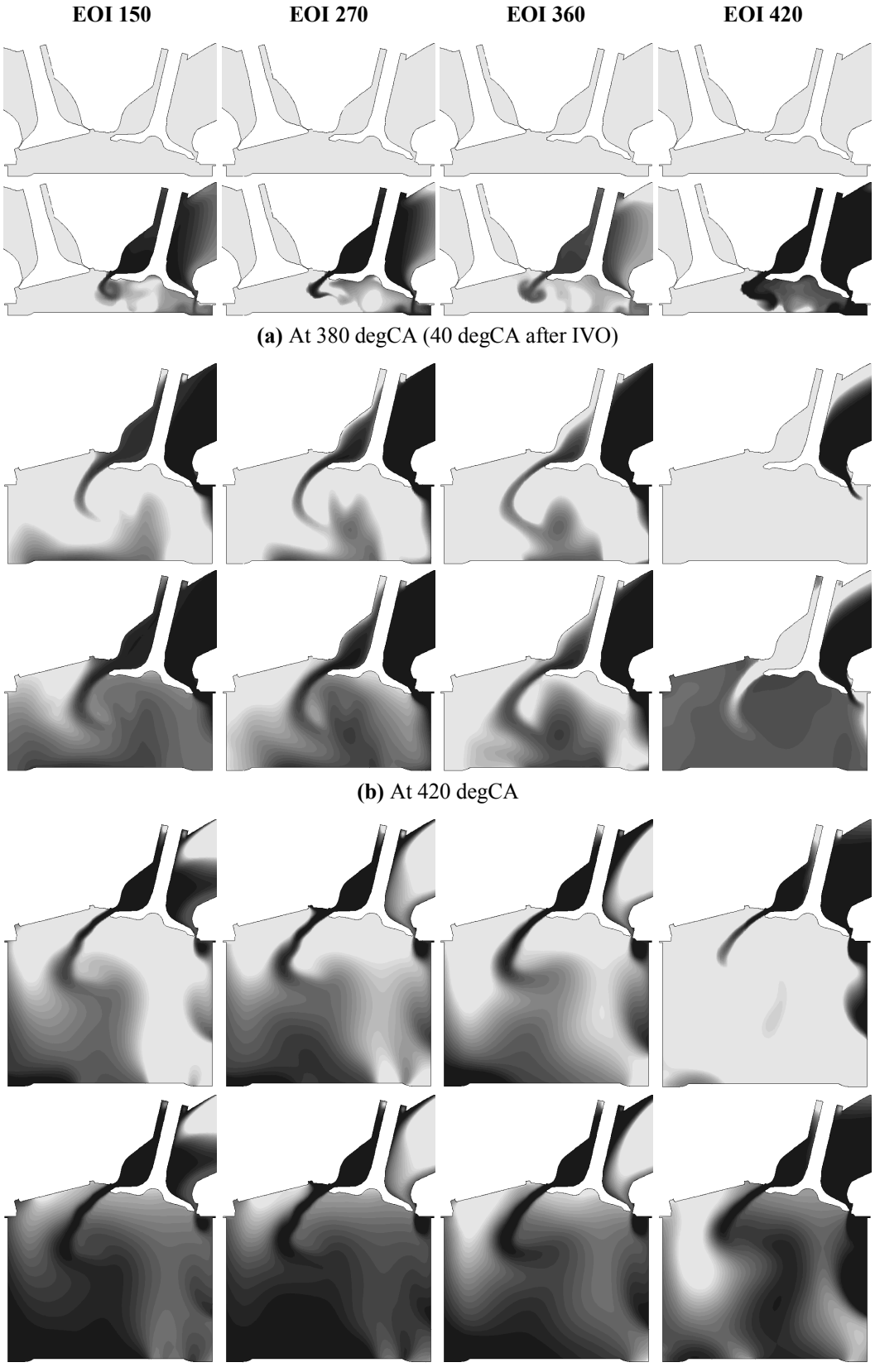

(a) At 380 degCA (40 degCA after IVO)

(b) At 420 degCA

(c) At 450 degCA (20 degCA before IVC)

Figure 2.19 RAFR contours for different EOI timings
Each crank angle: upper row = without residual fuel, lower row = with residual fuel initialization
Grayscale: darker = higher fuel mass fraction, lighter = lower fuel mass fraction

righthand section of the intake valves and less through the lefthand section. As a consequence, pure air may be inducted for the intervening duration between the end of first-stage induction and the start of second stage, which is especially evident for case EOI 360 and 420. Since the inducted charge, albeit partially premixed inside the intake ports, remains relatively rich, the distribution of fuel-rich pockets in the combustion chamber upon the completion of charge intake phase is fundamentally determined by the particular induction sequences of the residual fuel, injected fuel and pure air, if any, which is illustrated in the lower row in Figure 2.19 (c).

In summary, the effect of gas injection timing on in-cylinder mixture formation is vastly complicated by the two-stage mixing mechanism, peculiar to PI of gas fuel and absent for example in gasoline engines, which depends on the total injected fuel quantity, the proportion thereof inducted in the first and second stages, and the time that the injected fuel spends traveling from injector to intake valves.

2.5.3 Injection timing and mixture formation

The results of mixing process inside the combustion chamber for different EOI timings are presented in Figure 2.20, quantified statistically as the CoV in fuel mass fraction distribution across the whole flow domain and the mass of fuel included in flammable mixtures. The flammable fuel mass fraction is evaluated by summing up fuel mass found in all finite-volume cells whose cell-wise RAFR lies between 0.7 and 1.7, the flammability range of natural gas established according to experimental data on CNG engines [338][339], divided by the total in-cylinder fuel mass.

The principal mixing process occurs during the charge induction phase as the CoV decreases most rapidly during that period. Moreover, the flammable fuel mass fraction already reaches unity at IVC, indicating flammability of the entire mixture upon the completion of charge induction. Both observations correspond well to the typical behaviors of a PI engine.

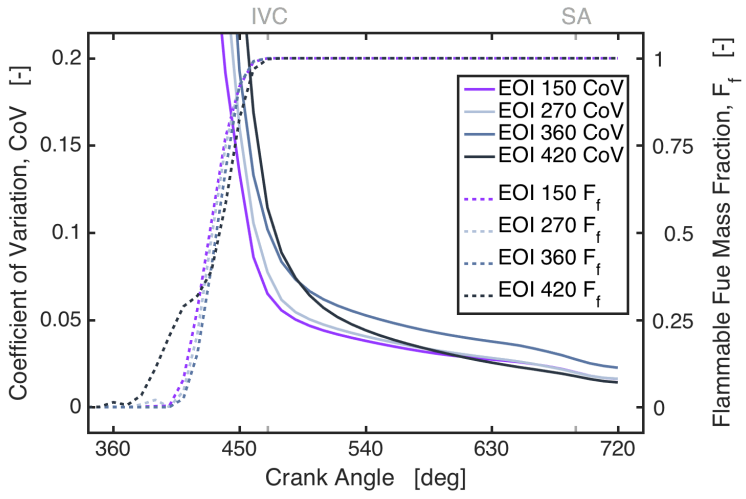

Figure 2.20 Mixing process inside the combustion chamber for different EOI timings

However, combustion and pollutant formation processes depend further on the mixture homogeneity and detailed fuel distribution at the spark timing which in turn rely on the continuous air-fuel mixing during the remaining intake and compression strokes. Mixing inside the combustion chamber is generally a complex phenomenon involving the interactions between coherent charge motion, chamber geometry and piston movement, which in the case of natural gas PI is in addition complicated by the two-stage mixing mechanism. Mixing rates after IVC for all EOI timings are significantly lower than in the preceding phase, as a result of low engine speed for which the present investigation is specifically purposed. Furthermore, the declining rates of individual CoV curves differ among the four cases, and no general trends appear to correlate the differences with EOI timings. With the injection event 120 degCA later, case EOI 270 exhibits extremely similar mixing rate to case EOI 150, whereas the mixing rate for case EOI 360 is notably lower even though the injection is delayed by a lesser 90 degCA relative to case EOI 270. And case EOI 420, despite being the latest injection, shows the highest mixing rate.

The resultant final mixture quality at the spark timing of the most interest is characterized by the same trend. Figure 2.21 presents the probability distribution of fuel mass with respect to RAFR at the instant of spark timing. And in Figure 2.22 fuel mass fraction as a function of deviation η of the local mixture RAFR from the stoichiometric ratio 1 is presented, i.e. the fraction of fuel mass enclosed in mixtures whose RAFR is $1 \pm \eta$. Both are statistical metrics indicating mixture homogeneity. Case EOI 150 and 270 result in mixtures that are equivalently homogeneous, with the later injection timing being slightly more so. As a result of low mixing rate, case EOI 360 produces notably less homogeneous mixture, with local RAFR spreading over a larger range. Mixture from the latest timing, case EOI 420, has the highest homogeneity thanks to the highest mixing rate. Again, there seems to be no general trend that correlates the final mixture quality with injection timings.

The apparent decoupling between mixing and injection timing is in fact found

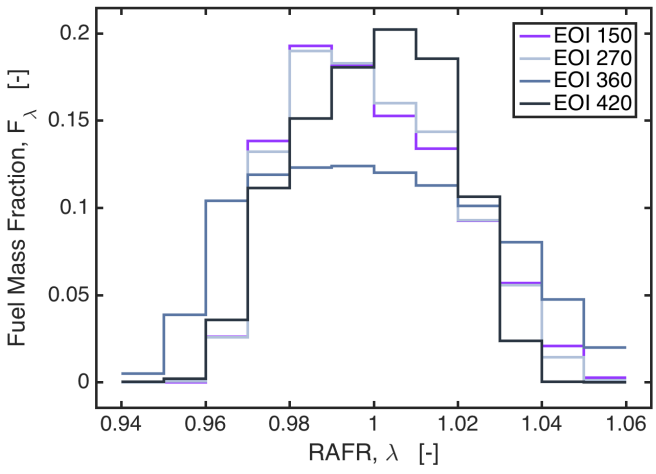

Figure 2.21 Fuel mass probability distribution for different EOI timings

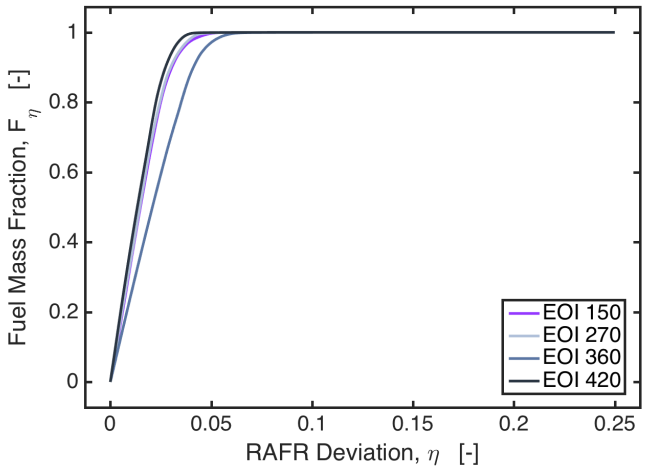

Figure 2.22 Fuel mass fraction as a function of RAFR deviation for different EOI timings

to be the consequence of two counterbalancing effects caused by the same variation in EOI timing. On the one hand, advancing the injection event expectedly promotes the air-fuel premixing prior to the intake phase. This trend by nature is a monotonic correlation with injection timing, and evidenced by the part of CoV curves before IVC in Figure 2.20. On the other hand, postponing the injection event gives rise to larger amount of residual fuel to partake in the first-stage mixing of the succeeding cycle as the arrival of injected fuel is delayed relative to the intake phase. For the same total quantity of inducted fuel in each engine cycle, evening the fuel subtotals between the two mixing stages enhances the subsequent mixing process inside the combustion chamber by increasing the number of local fuel-rich mixing sites. This is obvious in particular for case EOI 420 as the first-stage residual fuel accounts for one third of the total inducted fuel (see Figure 2.18), which explains its high mixing rate. In addition, as pointed out earlier, largely postponing the injection event (EOI close to IVC) introduces an empty window between the end of first-stage and the start of second-stage induction during which no fuel but pure air enters. The amount of air inducted during this period also contributes to a special distribution of fuel-rich pockets and may affect the mixing process.

Figure 2.23 details the in-cylinder mixing process by presenting the fuel spatial distribution at three crank angles during the late intake and compression stroke. The two counterbalancing effects of injection timings are demonstrated in Figure 2.23 (a) in that earlier injection timings result in broader fuel-rich pockets (hence better out-of-cylinder premixing) but the fuel-rich zones are meanwhile more restricted in space (hence more predominant second-stage induction). The particular patterns of fuel distribution determine the subsequent mixing process during the compression stroke till the spark event as shown in Figure 2.23 (b). Furthermore, the fuel spatial distribution reveals that, for case EOI 360, the spreading of fuel between the two induction stages appears to be insufficient for the marginal first stage to compensate for the less premixed second stage. For this reason, the mixing rate of case EOI 360

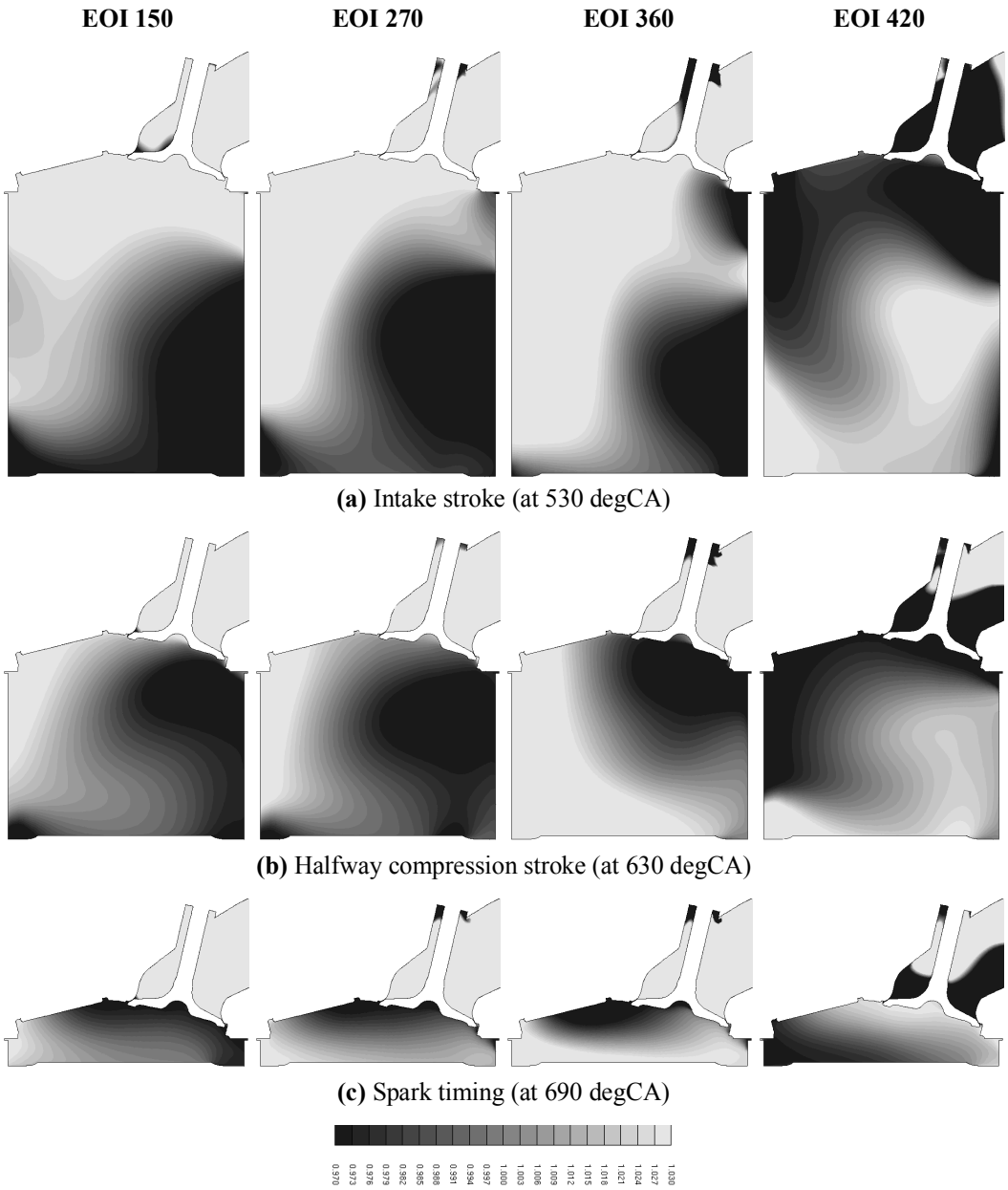

(a) Intake stroke (at 530 degCA)

(b) Halfway compression stroke (at 630 degCA)

(c) Spark timing (at 690 degCA)

Figure 2.23 RAFR contours for different EOI timings

is low relative to both the more premixed cases with earlier injection events and the later timing with two comparable fuel-rich zones spread at a distance by intervening air induction.

In conclusion, the otherwise intuitive correlation between mixture homogeneity and injection timing, i.e. earlier injection most likely leads to better air-fuel mixing, is profoundly obscured by the two-stage mixing (or induction) mechanism. And the resultant mixing process for a PI engine running on gaseous fuels is complicated.

From the perspective of mixture homogeneity, case EOI 420 is supposed to be the best according to the statistical evaluations presented in Figure 2.21 and 2.22. The experimental engine calibration nevertheless pinpoints case EOI 270 to be the

optimum timing, which is justified by the numerical investigation. Despite that the final mixture at spark timing is statistically less homogeneous to a small extent, the local fuel distribution as shown in Figure 2.23 (c) favors the flame propagation from spark plug spherically outwards to the largest extent among all investigated timings. And case EOI 420, albeit having the most favorable mixing process, results in the exactly opposite fuel distribution. The relatively lean mixture in the upper region is supposed to adversely impact flame kernel stability and early quasi-laminar flame propagation, whereas the rich mixture near the piston may increase crevice-trapped fuel mass and HC emissions. Case EOI 360 has similar fuel distribution to case EOI 270 but the homogeneity is less ideal.

2.5.4 Injected fuel traveling

The injected fuel, due to relatively low momentum of gas jet limited by nozzle sonic speed and density, arrives at intake valves after a perceivable delay. The finite fuel traveling speed plays a crucial role in the two-stage mixing mechanism, since it determines the start of second-stage induction and the amount of residual fuel for the first stage. In general, fuel jet is propelled by the ongoing injection event as well as the intake flow due to piston movement which is in turn directly linked to engine speed. To further investigate the injected fuel traveling, five cases, divided into two groups, are designed. The parameters and resultant fuel traveling of the cases are presented in Figure 2.24. Specifically, the previous case EOI 270 and 420 (at 2000 rpm) are retained as references to which three cases at doubled engine speed (4000 rpm) are added. Apart from injection timings and engine speeds, all other engine parameters remain the same. In particular, the injected fuel quantity is identical, and cases at 4000 rpm have double the injection duration in terms of crank angle due to the doubled engine speed. The fuel front position designates the distance along the intake ports from the injector tip whereat the farthest front of injected fuel is located, normalized by the total distance from injection site to intake valves.

In the first group, all three injection events are completed prior to IVO, and the two additional cases at 4000 rpm have either the same SOI or EOI as the reference case 2000 rpm EOI 270. Since the intake valves remain closed, the initial portion of fuel penetration is solely energized by the injection event and thereby scaled with absolute time instead of crank angle. This is confirmed by the equal slopes of the two 4000 rpm cases EOI 270 and 324. Actually, case 2000 rpm EOI 270 has double the slope that would be the same as the other two cases when expressed in unit time. Another peculiar feature is that the fuel penetration stalls at the position where the intake pipe branches into two leading to the intake valves (at approximately the 0.7 position into the intake ports), likely ascribable to pressure buildup that acts against the incoming fuel flow. The fuel penetration then resumes upon IVO. This feature of fuel stagnation profoundly influences the charge induction and mixing process. First of all, for a certain injection timing with which the fuel penetrates exactly into the branch at IVO, the expected faster fuel traveling to intake valves by advancing

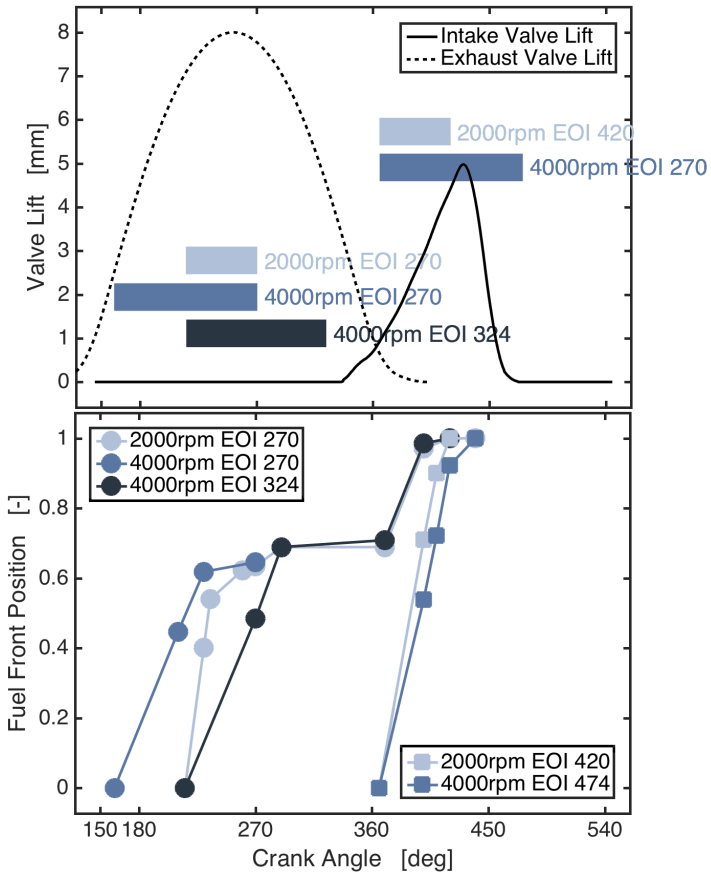

Figure 2.24 Case setup and results for fuel traveling investigation

injection events beyond it would simply be negated, explaining the reason that the previously investigated case EOI 150 and 270 feature almost identical start of the second-stage induction (see Figure 2.19 (b)) despite a difference of 120 degCA in injection timing. In addition, the injected fuel accumulates in the upstream segment of intake ports and therefore is prone to fuel crossing. The resumed fuel penetration, without being energized by ongoing injection, assumes the same rate in crank angle for all three cases, implying that the driving force is the piston movement that scales with crank angle instead of time.

In the second group, the two injection events occur completely within the intake phase, and the jet penetration is consequently under the joined influences of piston movement and injection energization. Therefore, the two cases exhibit very similar slopes as the piston speed scales with crank angle, whilst the case at 2000 rpm is slightly but not twice faster than the case at 4000 rpm indicating the existent but not dominant driving effect of injection. No fuel penetration stalling occurs since the intake valves remain open. Furthermore, it is observed that the injected fuel in case 2000 rpm EOI 420 arrives at intake valves with a noticeable delay, nearly halfway through the valve opening window, which explains its especially pronounced first-stage induction in previous investigations (see Figure 2.18 for example).

In conclusion, on the basis of two-stage mixing mechanism, the mixing process in a PI gas-fueled engine is further complicated by the relative phasing between the injection event and intake valve lift profile, which determines the different driving forces and occurrence of fuel flow stalling.

2.6 Comparison with premixed simulation

Conventionally, most numerical simulations of PI engines have been done with perfectly premixed charge in either intake ports or combustion chamber, presuming the assurance of PI to form homogeneous mixtures without the need of simulating the actual injection process. In view of the mixing mechanism and different mixture qualities found in previous investigations, a comparative study of simulations with injection and premixed charge is conducted to understand any possible differences. Specifically, a case with homogeneous stoichiometric mixture preset in intake ports is compared with the four cases at 2000 rpm in the injection timing investigation, with all other engine parameters remaining unchanged.

2.6.1 Intake mass flow rate

Given the fundamental role of the two-stage mixing mechanism in determining the mixing process, the variable most closely connected with charge induction, the mass flow rates through intake valves, are considered first and presented in Figure 2.25. The annular opening section of intake valves is conceptually divided into two halves by a plane passing through the centerlines of the two intake valves. The half section on the exhaust side is responsible for the formation of typical tumble motion in pent-roofed SI engine cylinders, and the other half on the intake side facing the adjacent liner admits minor intake flows (corresponding to the left and right flows in Figure 2.19, respectively). Investigating mass flow rate through individual halves is based on the observation that the freshly injected fuel for increasingly postponed injection events tends to be inducted more through the intake-side half and more air through the exhaust-side half (see Figure 2.19(b)). Furthermore, assuming that the volume flow rate through intake valves follows the same pattern across all the cases, differences in mass flow rate can be interpreted as changes in fuel mass contained in the intake flow, given the fact that the density of CH_4 is about 0.55 of that of air at the same pressure and temperature.

Due to pressure differences, the same impulsive inflows occur initially through both half sections followed then by a backflow whereby an insignificant amount of charge is admitted. The first-stage induction starts at 370 degCA, during which the differences in mass flow rate are subtle as a result of differences in the amount of residual fuel and premixing level thereof with local air which in turn determine the instantaneous fuel concentration in the intake flows and total duration of first-stage

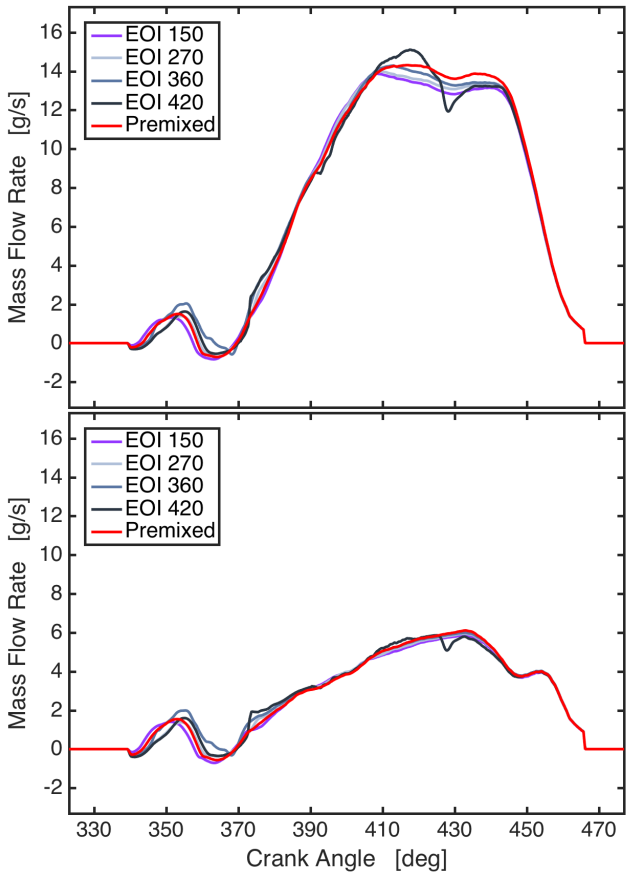

Figure 2.25 Mass flow rate through half intake valve sections
Upper: exhaust half of intake valves; Lower: intake half of intake valves

fuel induction. Corresponding to Figure 2.18, appreciable differences in mass flow rate appear at 410 degCA when the second-stage induction starts for the three earlier EOI cases and at 430 degCA for case EOI 420. Due to different injected fuel arrival time, more air is being inducted through the exhaust-side half valve section for more postponed injection timings, represented by higher mass flow rate. And mass flow rate of the premixed case lies above the three earlier EOI cases but below case EOI 420 wherein pure air is being inducted, indicating that the earlier cases are far from being perfectly premixed. This trend continues till the rapid closing phase of intake valves, except for case EOI 420 whose later and much less premixed second-stage induction drastically decreases its mass flow rate. The differences in mass flow rate through the intake-side half section are milder, especially the overshoot of case EOI 420 at 410 degCA, as fuel-rich mixture is being admitted more consistently without distinct intervening pure air induction. Nevertheless, the exhaust-side half plays a more significant role with respect to the proportion of total inducted charge and the intensity of main coherent flow motion established inside the combustion chamber than the intake-side half does.

2.6.2 Volumetric efficiency

Table 2.3 compares the volumetric efficiency, λ_V, resulting from the five cases. Incorporating injection process with various timings leads to different volumetric efficiencies than the premixed case, which is the direct consequence of discrepancy in mass flow rate. Specifically, mass flow rates of the injection cases are on average lower than that of the premixed case during the critical period of intake phase when the intake valve lift is around the maximum (see Figure 2.25), owing to the second-stage induction of fuel-rich charge that coincides in time. In other words, the high-volume flow rate window of the intake phase for the injection cases is occupied by charges with lower-than-stoichiometric-mixture density (i.e. richer in fuel). This is a feature peculiar to gas-fueled engines as the gaseous fuels often have low densities, whereas the admission of liquid fuel coincident with the maximum lift window may actually increase volumetric efficiency thanks to charge cooling by latent heat.

The pure air induction before second-stage induction for case EOI 420 partially compensates the loss in flow density during the maximum intake phase, and thereby its volumetric efficiency is negligibly impaired. As for case EOI 360, its flow rate is not as much lower than the premixed case as case EOI 150 and 360 are. Together with constantly higher mass flow rate during the first-stage induction of leaner than premixed mixture, the resultant volumetric efficiency is marginally augmented in comparison with the premixed case. Reduction in volumetric efficiency is slightly more evident for case EOI 150 and 270. In particular, since case EOI 270 has been experimentally confirmed as the optimum injection timing, the decrease of 2.1% in volumetric efficiency and consequently in total energy content may perhaps lead to discrepancies in heat release and pressure profiles between numerical simulations and experimental data, if the premixed case is used instead of injection. Considering that increasingly high precision has been required from combustion simulations in terms of burning rate and combustion phasing, differences in volumetric efficiency for the currently investigated engine operating point and for many others may not be neglected. Nonetheless, the differences found in the present work are not deemed to be significant, and the final assessment of influences on combustion process is dependent upon the complicated interactions of more than one variable.

Again, no monotonic correlation is found between volumetric efficiency and injection timing over the investigated range, as a consequence of the complications pertaining to the two-stage mixing and fuel traveling. However, given the similarity between case EOI 150 and 270 in that both have dominant second-stage induction

Table 2.3
Comparison of volumetric efficiency

Case	EOI 150	EOI 270	EOI 360	EOI 420	Premixed
λ_V	0.4253	0.4260	0.4370	0.4315	0.4351
Δ%	-2.3	-2.1	0.4	-0.8	0

and fuel stalling in intake ports, it is deduced that the volumetric efficiency would decrease in an asymptotically diminishing way with advanced injection timing from EOI 270 backwards, until fuel crossing unacceptably impairs operability.

2.6.3 Turbulence level and flow motion

Turbulence is an influential parameter in SI combustion systems, helping speed up the slow flame propagation of natural gas and thus stabilize the combustion. The underexpanded jet of fuel injection is a well-established source of local turbulence due to the presence of large-gradient shearing zones both embedded in and around the jet core flow. For this reason, the influences of injection events or lack thereof on the turbulence level are investigated for the injection and premixed cases.

Figure 2.26 presents the turbulence kinetic energy both in the entire intake ports and in the immediately upstream region of intake valves. Such distinction is made in order to explicate the extent to which local turbulence effects caused by injection can be retained and propagate further downstream. Local increases in turbulence kinetic energy are comparable for all injection cases. The two later injection cases, especially the latest case EOI 420, produce slightly lower turbulence, likely owing

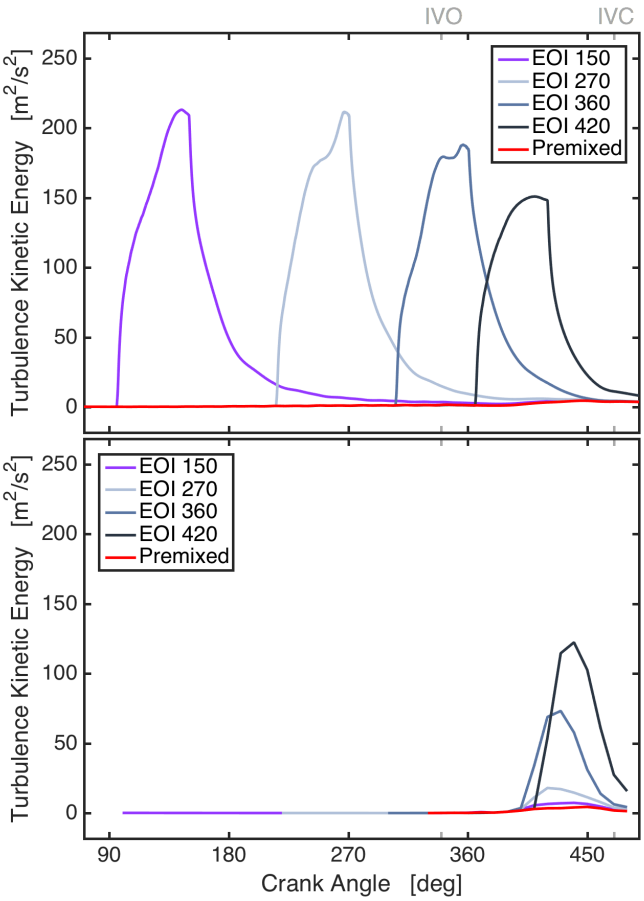

Figure 2.26 Turbulence kinetic energy in intake ports and valves
Upper: in entire intake ports; Lower: near intake valves

to the interference of intake flows imposing a nonnegligible ambient fluid velocity that reduces local velocity gradients. The premixed case, devoid of injection event, shows no sign of enhanced turbulence. However, due to finite fuel traveling speed and in particular mixture stalling at intake port branch, local increases in turbulence level in the upstream region close to intake valves occur almost concurrently despite different injection timings. In addition, turbulence energy created by injection is dissipated to a greater extent for earlier injection, as a result of longer delay between injection events and mixture arrival at intake valves. Accordingly, there is a clear correlation that advancing the injection event provides no benefits to the phasing of turbulence enhancement upstream of intake valves but may instead lead to decrease in transported turbulence energy downstream, with very early timings granting little turbulence increase relative to no injection at all.

The eventual effects of turbulence enhancement inside the combustion chamber are presented in Figure 2.27 along with the coherent tumble motion, given the close connection between the two phenomena and the fact that both are likely influenced by fuel injection. The tumble motion, namely the dominant large-scale vortical flow structures typical of and often purposely established in SI engines, is quantified by the dimensionless tumble number, expressed relative to the instantaneous geometric

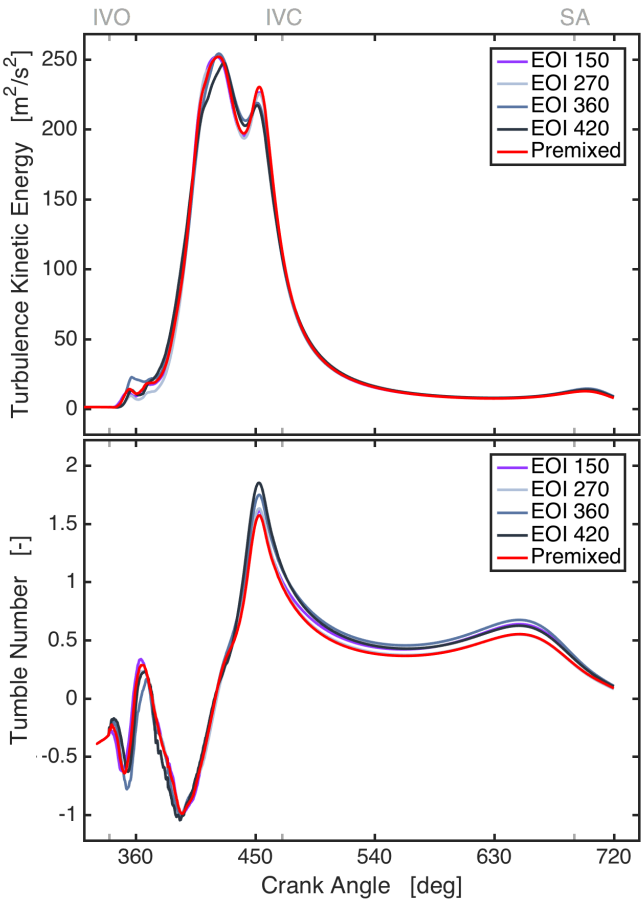

Figure 2.27 Turbulence kinetic energy and tumble number inside the combustion chamber

volume center of the combustion chamber and, by definition, in the vertical plane of symmetry (xz-plane in the present work). The tumble number is essentially the normalized mass-weighted magnitude of the total planar rotation defined as

$$Tumble\ number = -\frac{\sum m_i[w_i(x_i - X_V) - u_i(z_i - Z_V)]}{\frac{2\pi N}{60}\sum m_i[(x_i - X_V)^2 + (z_i - Z_V)^2]} \tag{23}$$

where m_i is the mass of cell i, x_i and z_i the x and z-coordinate of cell i, X_V and Z_V the x and z-coordinate of cylinder volume center, u_i and w_i the x and z-component of velocity, and N the engine speed in revolution per minute. Positive value denotes counterclockwise rotation in Figure 2.19 and 2.23.

Oscillations in turbulence kinetic energy and tumble number initially appear at around 360 degCA due to impulsive charge inflows and subsequent backflows. The principal phase of turbulence buildup and tumble establishment corresponds to the main charge induction, both first and second-stage, starting at 370-380 degCA. The first peak of turbulence energy occurs when the intake valves are at maximum lift with the highest mass flow rate, in accord with Figure 2.25. The turbulence declines as the intake flow, the main turbulence source, diminishes towards IVC. The second peak occurs owing to intensified tumble motion in the mid intake stroke when the piston movement is rapid. Then both turbulence and tumble abate in the absence of intake flows. Despite the correlation between local turbulence levels upstream of intake valves and injection timing found in Figure 2.26, the intake-governed major turbulence enhancement phase (from 370 degCA till the decline of the first peak of turbulence kinetic energy) inside the combustion chamber shows little differences among all the cases. In particular, the premixed case, devoid of injection-induced turbulence, has comparable turbulence buildup with the injection cases. In addition, the turbulence kinetic energy well preserved from injection site to intake valves for case EOI 420 warrants no apparent advantage inside the combustion chamber. On the contrary, its relatively low intake mass flow rate during the high valve lift period impairs the turbulence creation near the first turbulence peak at about 420 degCA, corresponding well to Figure 2.25. Therefore, it is concluded that the direct effects of port fuel injection on in-cylinder turbulence level are insignificant regardless of the proportion of injection-induced turbulence transported downstream to the intake valves backs. Instead, the upstream turbulence information is lost when the charge passes through the intake valves at high velocity, and the turbulence buildup in this phase is associated with intake flow rates.

Perceivable differences in turbulence kinetic energy take place near IVC when the valves are rapidly closed by the VVA system. Accordingly, such differences are likely attributable to the combined influences of remaining inflow-created kinetic energy and accelerated mean-flow tumble motion. Nevertheless, all the turbulence,

built up either by high-velocity intake flows or by coherent fluid motion, is quickly dissipated after IVC and further during the rest of the intake stroke. In addition, the accompanying discrepancies disappear across the cases with or without injection, since their direct influences through charge induction cease and the flowfield is then driven by piston movement that in turn slows down towards intake BDC. This trend expectedly coincides with the deceleration of tumble motion.

At the spark advance (SA) and towards the firing TDC, the extremely similar turbulence curves of the investigated cases diverge, following the reinforcement of tumble motion by the rapid upward piston movement during the mid-compression stroke. In general, tumble motion in SI engines is purposely established by proper combustion chamber design in order to enhance turbulence at firing TDC through the transfer of kinetic energy from coherent mean-flow motions to turbulent eddies, which is demonstrated by the mismatch in time between the tumble number peak (at 650 degCA) and turbulence peak (at 700 degCA) in Figure 2.27. The divergence of transferred turbulence level is supposed to stem from the differences in tumble intensity. Specifically, tumble numbers remain mostly equal in the charge induction phase until shortly before IVC, implying that intake mass flow rate is not the major cause for the different tumble intensities. A plausible explanation appears to be the relative distribution of fuel mass fraction inside the combustion chamber. Given the much lower density of CH_4 than air, different spatial distribution of fuel amounts to different distribution of mass relative to the instant center of tumble rotation. This speculation is evidenced by the remarkable agreement between the tumble numbers in Figure 2.27 and the CoV in fuel mass fraction distributions in Figure 2.20 in that, starting from 450 degCA (shortly before IVC), high tumble intensity corresponds to high mixture inhomogeneity. For instance, case EOI 420 initially has the highest CoV as well as the highest tumble number, and the CoV then declines rapidly below the other cases with the tumble number following the same trend. For the premixed case with perfectly homogeneous mixture, its tumble number is hence expected to stay below all the injection cases.

Based on the proposed correlation between mixture inhomogeneity and tumble intensity, the tumble-generated turbulence is supposed to be intrinsically different for all the investigated cases. However, energy transfer from mean-flow motion to turbulence and turbulence dissipation are complicated phenomena, especially near TDC wherein the coherent vortical flow structure is confined by irregular geometric surfaces and significantly deformed. The turbulence kinetic energy may not follow exactly the same trend as tumble number. To put things into perspective, turbulence kinetic energy at the crank angle corresponding to its peak value (700 degCA) are presented in Table 2.4. The differences at the crank angle relevant to the combustion onset may be considered nonnegligible between the various injection cases and the premixed case, taking into account the effects of turbulence on flame propagation.

Table 2.4
Comparison of turbulence kinetic energy (TKE)

Case	EOI 150	EOI 270	EOI 360	EOI 420	Premixed
TKE	13.09	12.42	14.06	13.24	12.11
Δ%	8.1	2.6	16.1	9.3	0

In summary, incorporating gas injection process into the numerical analysis of PI engines provides additional pertinent information to what is usually captured by premixed simulations, including mixture homogeneity, spatial distribution of fuel, volumetric efficiency and turbulence kinetic energy. Depending on specific engine design, operating points and modeling approaches, differences in these parameters combined may prove combustion-significant, or may alternatively provide insights into the interpretation of discrepancies between numerical and experimental results. Tuning of model coefficients for premixed simulations may also be elucidated. For example, given the similar fuel distribution patterns with the mixture progressively leaning out from the spark plug in case EOI 270 and 360 (see Figure 2.23 (c)), the former has been experimentally identified as the optimum timing, implying that its higher homogeneity outbalances the turbulence advantage of the latter case for the studied engine and operating point.

Chapter 3

Direct Gas Injector

The purpose of computing is insight, not numbers.

— Hamming Richard

"Numerical methods for Scientists and Engineers"

3.1 Background

In this chapter, the work related to an experimental and numerical study of gas jet structures and mixing characteristics of a natural gas direct injector is presented. The experimental study consists in performing the schlieren visualization technique and the numerical study three-dimensional CFD simulations. The gas injector under investigation is later incorporated into the development of a high-performance DISI CNG engine.

The necessity of such an isolated study is twofold. Firstly, from the perspective of component design, the studied direct gas injector is characterized by an outward-opening poppet valve with an annular inner passage and exit. However, the injected gas is designed to develop a concentrated shape that collapses onto the injector axis rather than forming a conventional conical umbrella-shaped jet. Therefore, the set of design parameters including needle lift, needle seat geometry and overall nozzle diameter needs to be verified experimentally with the injector prototype. Secondly, structures and mixing characteristics of underexpanded jet issuing from an outward-opening conical nozzle have been scarcely documented. And a suitable numerical model is therefore required to understand the injection process, which, after being validated, is instrumental in accessing the mixture formation in engine context.

3.2 Schlieren flow visualization

In general, informative non-intrusive techniques with high spatial and temporal resolutions are desirable to visualize and study phenomena that involve transparent media such as gas injection into gaseous environment. Such techniques have to be adequately sensitive to changes of the target variable and do not interfere with the studied process on the physical scale of interest. In this regard, a multitude of optical diagnostic techniques have been extensively employed to study underexpanded gas jets, including for instance particle image velocimetry (PIV) [340][341][342], laser Doppler anemometry (LDA) [274][343], laser Rayleigh scattering [344][345], laser Mie scattering [346][347], and laser-induced fluorescence (LIF) [348][349].

In addition, optical techniques that exploit the refraction of light beam passing through inhomogeneous media, namely interferometry, shadowgraph and schlieren, have enjoyed enduring popularity in studying gas dynamic systems. In particular, schlieren imaging has been the most widely used refractive index-based technique. Depending primarily on geometric rather than wave optics, schlieren imaging has simpler instrumentation and is less sensitive to extraneous factors such as vibrations than differential interferometry [350], whereas analysis of schlieren images for field information of refractive index is less intimidating than shadowgraph that involves (often numerically) solving a governing Poisson equation [351].

Specifically, schlieren imaging has been routinely implemented to investigate underexpanded sonic jets, both in the nearfield region for detailed shock structures like barrel shock and Mach disk [222][265][352][353][354][355], and in the farfield region for transient time-dependent macroscopic behaviors such as axial and radial penetration length, penetration speed and jet cone angle [204][319][356][357][358] [359][360][361]. In the present work, schlieren technique has been utilized to study the transient evolution of an underexpanded jet as a result of fuel injection from an outward-opening injector which has proven to bring about complex flowfields.

3.2.1 Fundamentals of schlieren optics

Schlieren, which literally means "streak"-like appearances in German (singular "Schliere"), designates optical inhomogeneities present in transparent media which appear in the form of local light path alterations and thereby cause spatial variation in light intensity that renders the inhomogeneities, normally eluding naked human eyes, optically detectable. The German term is credited to German physicist August Toepler who reinvented the sensitive knife-edge test developed by French physicist Léon Foucault, devised a functional apparatus and procedure for schlieren imaging, and spearheaded real-time observation of generic "Schlieren" in fluid flows [362]. For this reason, the epitaph of Toepler reads "He was the first who saw sound" (with sound being actually referred to his pioneering schlieren imaging of weak acoustic waves). Whilst German nouns are always capitalized, the capitalization is dropped for the technical term "schlieren" in English.

The physical basis for schlieren imaging is light refraction in a field of variable refractive index. Due to continuous repetitive scattering and rescattering of photons by electrons, the apparent phase velocity of lightwave propagating through a dense medium is reduced below its counterpart in vacuum, which is collectively indicated by refractive index $n = c/v$ where c is the speed of light in vacuum and v the local phase velocity of light [363]. Refraction is the macroscopic result of light traveling in medium at varying phase velocity. One way of explaining refraction is that, when propagating in any direction but the same as the refractive index gradient, one side of the wavefront in the high refractive index region slows down more than the other side in the low refractive index region. To preserve wavefront continuity, the whole

wavefront pivots towards the slower side. Alternatively, refraction can be explained by Huygens's principle. The secondary spherical wavelets emitted from wavefront points in the high refractive index region cover a shorter distance than those in the low refractive index region, and the resultant new wavefront, as the envelope of the wavelets, appears to pivot towards the smaller spherical wavelets. Accordingly, the light rays, defined as orthogonal trajectories of wavefronts, bend in the presence of refractive index variation.

The working principle of schlieren imaging technique resides in the refraction of light rays by variable refractive index and the consequent deflection from their continuous path. The information recorded by schlieren images is the cumulative angle of refraction of the light rays passing through a test section, as a function of coordinates in the plane normal to the light ray propagation direction [364][365]. The refraction angle is derived from geometric (or ray) optics. Considering a test section with positive refractive index gradient in the vertical direction ($\partial n/\partial z > 0$) (see Figure 3.1), a planar lightwave (i.e. a group of horizontal light rays), after a small time interval Δt, covers a small distance Δy, and the light rays are refracted upwards through a small angle $\Delta\varepsilon$. As the local phase velocity of light is a function of refractive index that in turn is a function of coordinate z, the distance is given by

$$\Delta y = (c/n)\Delta t \tag{24}$$

Furthermore, by applying the small angle approximation, the refraction angle $\Delta\varepsilon$ of the light rays is determined by geometric relation as

$$\Delta\varepsilon \approx \frac{\frac{c}{n_z}\Delta t - \frac{c}{n_{z+\Delta z}}\Delta t}{\Delta z} \tag{25}$$

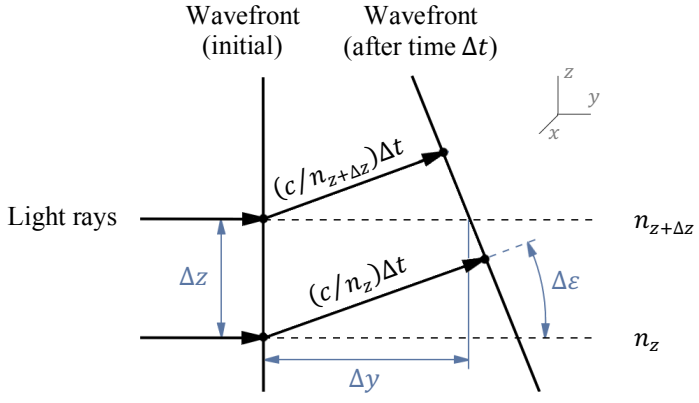

Figure 3.1 Deflection of light ray by a vertical refractive index gradient $\partial n/\partial z > 0$

By inserting Equation (24) into Equation (25) for Δt, and considering the limiting case by letting all finite difference terms Δ approach zero, the elementary refraction angle along the light ray propagation direction is expressed as

$$\begin{aligned}\Delta\varepsilon &= \frac{c\left(\frac{1}{n_z}-\frac{1}{n_{z+\Delta z}}\right)\Delta y\frac{n}{c}}{\Delta z} \\ &= \frac{n}{n_z n_{z+\Delta z}}\frac{n_{z+\Delta z}-n_z}{\Delta z}\Delta y \\ \frac{d\varepsilon}{dy} &= \frac{1}{n}\frac{\partial n}{\partial z}\end{aligned} \tag{26}$$

It is noted from Equation (26) that the light ray deflection detected by schlieren imaging is associated with the refractive index gradient rather than refractive index itself. The cumulative angle of refraction over the span of the inhomogeneous test section is derived from integration of Equation (26) along the direction of light ray propagation (y-axis). By assuming that the reciprocal of refractive index, $1/n$, does not vary significantly throughout the test section, which is applicable to virtually all cases of gaseous media ($n \approx 1$), the vertical deflection angle is then given by

$$\begin{aligned}\varepsilon_y &= \int \frac{1}{n}\frac{\partial n}{\partial z}dy \\ &\approx \int \frac{\partial n}{\partial z}dy\end{aligned} \tag{27}$$

In standard schlieren imaging application, a knife-edge cutoff is placed at the plane onto which the deflected light emerging from the test section is focused by optical lens or mirror, before being imaged by an intensified charge-coupled device (ICCD) camera. The knife edge is in general positioned perpendicular to both the light ray propagation direction and the direction of the to-be-investigated refractive index gradient (x-direction in Figure 3.1). In the absence of inhomogeneities within the test section, the light intensity is uniformly reduced by the cutoff. In the presence of vertical refractive index gradient and corresponding vertical light ray deflections, the emerging beam of light focuses irregularly and the light that has been focused in the cutoff area is blocked, thus augmenting the imaged contrast between upward and downward deflection. The use of such an explicit cutoff saliently differentiates schlieren from other associated techniques (e.g. shadowgraph).

The light intensity after the cutoff is then measured by an ICCD camera whose image sensor, within saturation limits, functions as a linear device and yields pixel

intensity in direct proportion to incident local illumination. Therefore, the contrast corresponding to the schlieren imaging system, according to Equation (27), is given by

$$contrast = \frac{I - I_0}{I_0} = S \int \frac{\partial n}{\partial z} dy \tag{28}$$

where I is the measured pixel intensity from inhomogeneity-containing test section, I_0 the pixel intensity with the same cutoff but uniform test section, S the schlieren system sensitivity [365] that depends on the focal length of the converging optical component focusing the light to the cutoff behind the test section and on the light field height unobstructed by the cutoff.

For gases, there exists an experimentally established unique linear relationship between refractive index (very close to unity) and density [363], expressed as

$$n - 1 = K\rho \tag{29}$$

where ρ is the gas density and K the Gladstone-Dale constant that depends on the gas species and light wavelength. By combining Equation (28) and (29) to substitute refractive index with gas density, the imaged contrast is written as

$$\frac{I - I_0}{I_0} = SK \int \frac{\partial \rho}{\partial z} dy \tag{30}$$

which is the governing equation in a schlieren imaging system, devised to probe the density distribution in the test section of interest.

3.2.2 Experimental setup

A Z-type monochrome schlieren system is constructed for flow visualization in the present work, schematically shown in Figure 3.2. A halogen metal vapor lamp is utilized to provide illumination for the entire system. Light from the lamp is then focused by a condenser lens onto a slit so as to obtain a well-defined homogeneous light source that minimizes astigmatism and intensifies luminosity taking the cutoff into account. A pair of equisized parabolic focusing mirrors are positioned in front of (Φ = 150 mm, f = 600 mm) and behind (Φ = 150 mm, f = 1141 mm) the injector test section respectively, and tilted at the same angle but opposite to each other. The Z-type configuration is preferred for two major advantages associated with the use

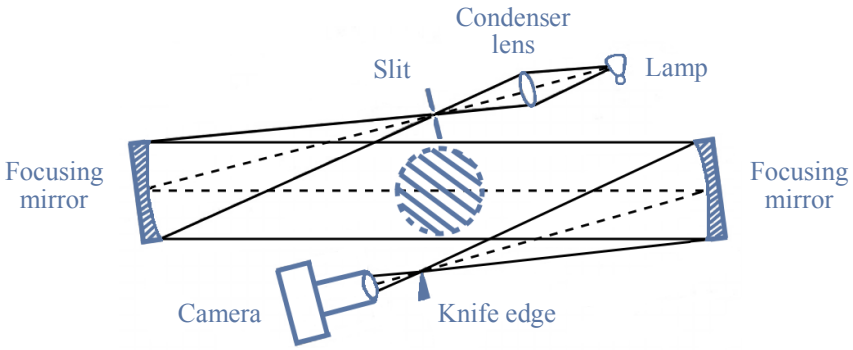

Figure 3.2 Schematic of the Z-type schlieren experimental setup

of mirrors rather than optical lenses. Firstly, the mirrors simplify the procedure for aligning all the optical components on a common centerline and thus eliminate the optical aberration known as coma [365]. Secondly, focusing mirrors are more cost and space-efficient at providing a large field of view than focusing lenses, therefore maximizing the useful height to image jet evolution. The diverging light emerging from the slit is directed to and collimated by the first focusing mirror. The bundle of collimated uniform light, passing through the test section and being deflected by the density gradient, falls onto the second focusing mirror, the decollimator, and is in turn focused onto the plane of knife edge. The knife edge is oriented horizontally, perpendicular to both the optical centerline and the to-be-observed vertical density gradient. The cutoff is set to approximately 50% for an equal measuring range in both vertical directions of deflection.

A high-speed ICCD camera records the schlieren image behind the knife-edge cutoff. The camera frame rate is set to 40,000 frame per second, leading to a high temporal resolution of 25 μs. At this frame rate, resolution of the image sensor is cropped to 732 × 764 pixels, which in combination with the optical system results in a spatial resolution of 7 pixel per mm (or equivalently ~0.14 mm per pixel). The imaged intensity values of undisturbed background are about in the middle of the sensor dynamic range, allowing for an equal recording range of brighter and darker schlieren and hence equal contrast capability according to Equation (28).

The injector tip is positioned at the center of the circular field illuminated by the focusing mirror-collimated light. Helium is used as the surrogate medium for natural gas. In particular, helium provides three advantages for practical schlieren imaging. Firstly, being chemically inert and most importantly inflammable, helium is safe to handle. Secondly, helium is a non-toxic benign gas species. Thirdly, under the same conditions, the difference in refractive index between air and helium is greater, albeit to a minor extent, than that between air and methane. Nonetheless, it has been pointed out that such minor difference enhances signal sensitivity to small density variations and thereby measurement certainty [319][359][366]. Helium is injected directly into the quiescent air in a controlled laboratory room. The absence of optical windows confining the test section avoids light scattering and refraction

prior to the second focusing mirror and the knife edge. The testing room is optically insulated to eliminate extraneous light contamination. The injection pressure is 16 bar, the same nominal value for DI engine operations. The injection pulse width is set to 2 ms that represents a typical injection duration in engine context and allows for a complete jet evolution up to a steady state within the observable field of view. Quiescent air in the room is at standard pressure 1 atm, resulting in a pressure ratio of $p_0/p_a \approx 16$ that typically induces highly underexpanded jet.

3.2.3 Image processing

A raw image obtained from schlieren technique is in general an array of bright and dark pattern that corresponds to the deflection direction of light passing through the probed density gradient and the cutoff. Flow structures are normally identifiable directly from unprocessed raw images thanks to the optical principles of schlieren imaging technique. Raw schlieren images are also further processed for additional information to be extracted. For example, the undisturbed background images were subtracted from raw injection images to recover changes in light intensity owing to inhomogeneous density distribution [359][361]. An edge detection algorithm [367] was then applied to the difference images so that jet boundaries were isolated from background for penetration measurement. Alternatively, the background image was first normalized by its mean value. The injection images were in turn divided pixel-wise by the normalized background [357]. The corrected images were subsequently converted into binary images by imposing a threshold that amounted to an artificial increase in the original schlieren contrast. Image segmentation methods (e.g. edge detection and thresholding) have often been implemented to schlieren images for the purpose of jet boundary augmentation thus enabling precise measurement of the radial and axial fuel penetration.

In the present work, a companion numerical study is undertaken which directly yields the corresponding density field to be compared with the schlieren experiment results. Therefore, the contrast of incident light intensity according to Equation (28) is derived from each recorded image as

$$intensity\ contrast = \frac{I - \bar{I}_{BG}}{\bar{I}_{BG}} \tag{31}$$

where I represents the instantaneous injection image and $\bar{I}_{BG}$ the mean background image. In particular, 10 undisturbed background images are taken prior to SOI and averaged out in order to minimize irregular features like random background noise and camera dark current. No additional artificial image treatment is introduced, and the optically probed information on density distribution is intact.

In the formulation of Equation (31), subtracting the background image from the

instantaneous raw image serves the purpose of removing constant undisturbed light intensity and hence of isolating the net intensity changes caused by injection event, as well as eliminating constant illumination irregularities such as leaked extraneous light or impurities present in the optical system. In addition, nonuniform gains and nonlinear response of the camera sensor [368] are implicitly corrected by dividing the net intensity changes by the background image (i.e. flat-field correction through dividing both the numerator and denominator by the signal gain matrix that cancels out). This operation meanwhile converts net intensity changes to intensity contrast.

The procedure of image processing is demonstrated in Figure 3.3. A grid with uniform 10 mm intervals is embedded in the captured schlieren images and added to experimental and numerical results presented hereinafter. The circular light field realized by the focusing mirrors is exhibited in Figure 3.3 (a). Due to the purposely designed collapsing shape, the entire jet is well confined within a limited portion of the field of view (422 × 700 pixels out of the original 732 × 764 pixels) that is hence extracted from the original images for processing, as shown in Figure 3.3 (b). The derived light intensity contrast is presented in Figure 3.3 (c) wherein roughly equal range of positive and negative contrast relative to the zero background is observed, as expected from schlieren optics. The background is not uniformly at zero contrast due to the disturbance of spherical acoustic waves originating from the injector tip, which are not present in and therefore cannot be corrected by the background image. Relatively high light intensities near the top center and low light intensities towards the lower right corner, as well as sporadic black spots, in Figure 3.3 (b) are corrected in Figure 3.3 (c) by the processing procedure.

3.2.4 Schlieren imaging results

The jet structure and evolution imaged by the schlieren system are presented in Figure 3.4, shown as the processed results of schlieren intensity contrast at selected time instants. SOI corresponds to 225 μs as the first appearance of visible jet, which

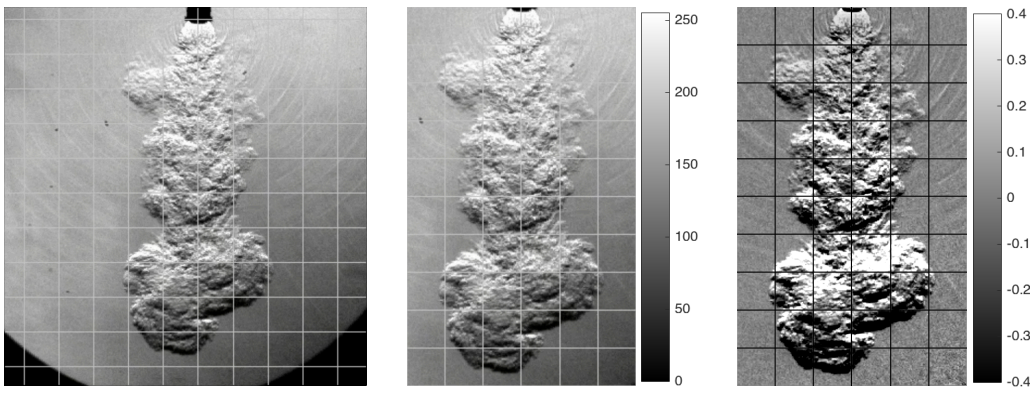

Figure 3.3 Schlieren image processing for contrast evaluation
(a) Original raw image at 1200 μs; **(b)** Raw image with useful field of view; **(c)** Intensity contrast

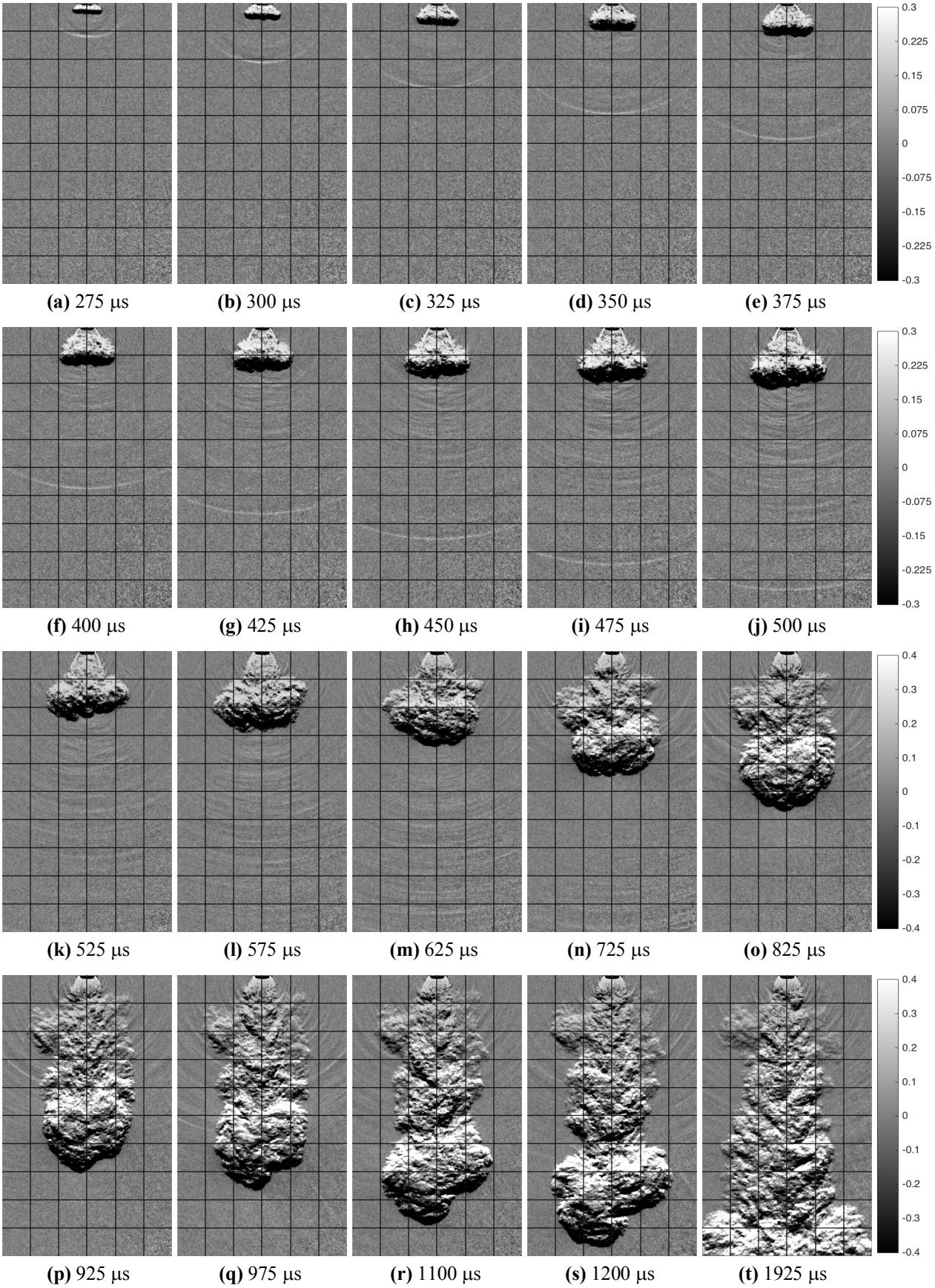

(a) 275 μs **(b)** 300 μs **(c)** 325 μs **(d)** 350 μs **(e)** 375 μs

(f) 400 μs **(g)** 425 μs **(h)** 450 μs **(i)** 475 μs **(j)** 500 μs

(k) 525 μs **(l)** 575 μs **(m)** 625 μs **(n)** 725 μs **(o)** 825 μs

(p) 925 μs **(q)** 975 μs **(r)** 1100 μs **(s)** 1200 μs **(t)** 1925 μs

Figure 3.4 Jet structure and evolution from the outward-opening injector shown as intensity contrast
SOI = 225 μs; Grid interval = 10 mm

is consistently used henceforth to differentiate between electrical and mechanical SOI. A narrower contrast range is applied to the first two rows than the last two in order to enhance visibility of the initially limited jet volumes.

A unique high-contrast spherical wavefront originates immediately after SOI from the injector tip, as shown from Figure 3.4 (a) to (j). Based on an approximate graphical calculation, the wavefront travels at about 400 m/s through the quiescent ambient air at standard temperature (across on average one interval of 10 mm in 25 μs between every two consecutive images in the first row in Figure 3.4), which is most likely a shock wave initiated by the abrupt poppet valve opening and the large pressure difference. The shock wave is followed by a series of slower and weaker spherical acoustic waves responsible for the disturbed background whose intensity contrast oscillates around instead of being exactly zero. Moreover, unlike the shock wave being symmetric about the central gridline (i.e. the injector axis), the acoustic waves are not precisely concentric at a single origin, which is particularly evident for fairly developed jet (see Figure 3.4 (f) to (k)). The potential core associated with the highly underexpanded jet is accordingly supposed to be the source.

The overall jet evolution is characterized by three distinct stages (shown in the first and second rows, the third row, and the fourth row in Figure 3.4, respectively). The initial stage features a hollow cone jet structure typical of an outward-opening poppet valve injector with annular flow passage and exit. The emerging annular jet coils inwards to form a toroidal vortex structure that grows in size with increasing needle lift (hence the name hollow cone). The hollow cone structure fundamentally differs from the circular jet issuing from a single-hole injector or an axisymmetric orifice in general. The peculiar initial vortex ring structure plays an essential role in determining the subsequent jet evolution, and is therefore presented at the same frame rate of the high-speed camera from Figure 3.4 (a) to (j).

The inward side of the growing toroidal vortex ring eventually reaches the jet centerline and establishes a region of large-scale recirculation filling up the hollow cone (see Figure 3.4 (k) and (l)). Radial jet expansion ceases upon the conversion of the toroidal vortex into the recirculation region, and the second jet development stage commences. A major portion of the injected gas flows past the envelope of the recirculation region and then converges downstream on the jet centerline. The overall jet structure in the second stage appears apparently similar to a circular jet headed by a spherical vortex [269][369] (see the third row in Figure 3.4). However, in the third stage, the further developed jet exhibits highly unsteady behaviors. In particular, the conical jet stem sustaining the head vortex is far from quasi-steady state as generally observed in a circular jet. Instead, peculiar large-scale instabilities appear in the form of alternate helical patterns, resembling the three-dimensional vortex shedding (von Kármán vortex street) phenomenon (see the last row in Figure 3.4). In addition, the head vortex deviates from a symmetric spherical shape, as the left half advances more than the right half, which coincides with the same trend of asymmetry in the upstream recirculation region in Figure 3.4 (p) and (q). Given the

correspondence between the peculiar jet structures and the asymmetric recirculation zone, it is believed that the fully-developed jet from an outward-opening injector is governed by the toroidal vortex ring-converted nearfield recirculation flow region and hence fundamentally different from the well-studied circular jet with stationary shock cell structures that cover the initial flow core and are governed primarily by compressibility rather than viscosity effects.

The jet stem, albeit featuring three-dimensional large-scale vortex structures, shows a coherent conical boundary, indicating self-similarity in this region. After the continuously changing head vortex moves completely outside the field of view, the imaged jet boundary reaches a quasi-steady state, shown in Figure 3.4 (t) as an example at 1925 µs.

3.3 Numerical modeling of transient injection

A three-dimensional CFD investigation of the transient injection process from the outward-opening injector is performed to provide further details about the flow structures and underlying mechanisms. Unlike hour-long steady-state jets typical of aerospace applications, the engine fuel injection is practically of pulsed intermittent feature in the millisecond-order. The transient flow behavior is therefore as crucial as steady-state structures. The numerical model is developed in the environment of a commercial finite-volume-based CFD solver, AVL FIRE (version 2014).

3.3.1 Outward-opening injector model

To precisely control the fuel injection event, valve needles are routinely utilized in engine injectors that are categorized into two main types, i.e. inward and outward opening. Inward-opening injector is widely used for gasoline DI (GDI) as well as gas fuel applications, which conceptually works as the well-studied circular nozzle. Outward-opening injector is involved in some aerospace [370][371] and GDI [304] [372] applications to exploit the nozzle geometry variation and flow characteristics that noticeably differ from axisymmetric orifice.

Specific to DI of gas fuels, outward-opening injector is of practical interest due to its characteristic larger flow cross section and corresponding higher volume flow rate than inward-opening injector under the same supercritical conditions, since gas flow rate is considerably limited by local speed of sound at the throat section which is unlikely for liquid fuels. The requirement on injection pressure is thus reduced, and so are the manufacturing complexity and costs of fuel supply systems. Whereas detailed jet structures and penetration correlations have been well documented for circular jet [357][369], studies on hollow cone jet issuing from an outward-opening injector are however comparatively scarce.

An essential challenge for numerically modeling direct gas injection consists in

the supercritical nozzle pressure ratio and the substantial geometric scale separation between the injector exit section and the combustion chamber usually of two orders of magnitude. Specifically, the typical supersonic flow regimes and shock structure formation associated with highly underexpanded jet have been acknowledged to be computationally problematic. A variety of modeling approaches to the investigation of gas fuel injection have been employed. The complicated underexpanded jet flows have been circumvented, either by conceiving an equivalent fully expanded jet with the same momentum and corrected nozzle diameter or by introducing part of the jet downstream of the Mach disk through local inflow boundaries [369][373]. Fictive gas droplets (or gaseous spheres) analogous to the dispersed multiphase modeling of liquid sprays have also been developed to represent the gas jets [374][375][376] [377]. These phenomenological injection models handle the underexpanded gas jet without resolving the injector geometry and shock waves, which remarkably reduce computational costs and have proven effective in predicting jet penetration. In order to investigate the influences of nearfield shock structures on air entrainment and jet development, the gas fuel injection process, along with the underexpanded jet, has been numerically simulated with pressure or mass-flow boundaries at or upstream of the injector exit [225][319][322][332]. The main focus of these studies has been on the circular jet issuing from inward-opening injectors or equivalent thereof that correspond to axisymmetric orifices.

The injection process resulting from an outward-opening poppet valve injector features a distinctive hallow cone jet that, depending on the injector geometry and pressure ratio, may shortly collapse onto the injector axis, maintain its conical shape onwards or attach to adjacent walls [378][379][380]. The hallow cone jet has been experimentally investigated by means of schlieren [361][381], planar laser-induced fluorescence (PLIF) [380][382] and X-ray radiography [316][317], specifically for engine gaseous fuel DI applications. It has been substantiated by those experimental studies that the hollow cone jet structures and underlying flow characteristics, as a result of the special annular opening, fundamentally differ from the universal well-defined circular jet from axisymmetric orifice. Therefore, many numerical studies have investigated the transient hollow cone jet by means of computational grids that were dedicated to replicating the annular flow passage of outward-opening injectors with the poppet valves fixed at corresponding maximum lift [320][321][324][325] [332][378]. It has been found in consequence that the choice of initial conditions to mimic the transient needle opening significantly affected the gas jet formation and subsequent mixing [325] and, similarly, that the injector flow initialization through gradual increase in inlet boundary pressure during the transients was crucial to the numerical model predictability [379]. In the meanwhile, difficulties in defining a proper parameter variation to reproduce the actual transient behaviors with a static injector flow passage have been recognized [322]. In addition, the absence of valve needle movement in the numerical models during the initial transient phase resulted in mismatches of jet penetration and velocity between experimental and numerical

results [319][321][325][379]. Moreover, it has been pointed out that air-fuel mixing might occur within the slipstream regions [383], for which the initial establishment of the underexpanded jet and associated shock structures may be important for fuel concentration prediction.

In view of the nearfield toroidal vortex structure and the subsequent formation of recirculation region observed in the schlieren images and their effects on both jet development and fully-developed jet structure, the injector transients are considered critical to determining the flowfield. In fact, the injector valve movement induces a complex geometric change in the annular flow passage in that both the nozzle cross-sectional area and location of the critical section vary continuously. To improve the fidelity of the numerical model, the time-dependent variation of the injector nozzle geometry is retained in the present work by a dedicated manually built mesh with hexahedral cells (see Figure 3.5). The injector model consists in a two-block grid, namely an axisymmetric block realized by rotating a two-dimensional mesh and a central block to avoid rotational singularity and small-angled cells along the injector axis. The poppet valve needle (see blue-colored surface in Figure 3.5) is movable according to imposed lift curve and thus adapts the mesh to the real nozzle geometry at every time instant. Therefore, no artificial treatment for the nozzle inlet boundary is required to take into account the build-up phase during transients. Examples of the injector model at closed and maximum-lift open position are presented in Figure 3.5 (b) and (c) in cutaway view, respectively. The complete moving injector model encompasses the annular nozzle passage, a portion of the internal fluid path leading upstream to the inlet boundary (partially shown in Figure 3.5), and a portion of the volume immediately downstream of the nozzle exit wherein a high cell density is necessitated by the underexpanded jet in order to resolve with reasonable accuracy the expansion, compression and shock waves inside the potential core as well as the large gradients in the surrounding mixing zones. Since the nozzle passage cannot

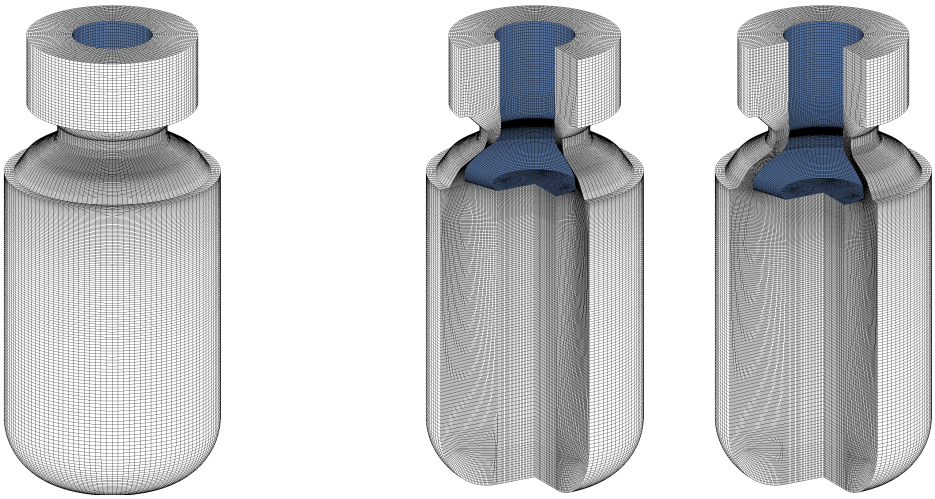

(a) Complete injector model **(b)** Closed position **(c)** Open position

Figure 3.5 Manually built moving injector model (complete and cutaway view)

be physically closed with finite-volume discretization, the closed injector position corresponds to a needle lift of 15 µm that, on the basis of a preliminary study, is sufficiently small relative to the maximum lift of ~370 µm to be considered virtually closed, provided that the start of simulation is aligned with the mechanical SOI and excludes the actuation delay of 225 µs as discussed in the schlieren images.

3.3.2 Computational domain

The moving injector model is integrated into a cylindrical volume featuring a structured axisymmetric grid with hexahedral cells. A cutaway view of the overall computational domain and a schematic showing the dimensions (normalized by the valve seat diameter d = 6mm) and domain boundaries are presented in Figure 3.6. The region near the moving injector model is locally refined to the same cell sizes ranging from 0.03 to 0.05 mm, in order to guarantee sufficient spatial resolution for the toroidal vortex and recirculation regions and a smooth transition from the nozzle area. The cell sizes are then gradually expanded radially up to ~0.8 mm and axially ~1.2 mm near the domain boundaries. The z-axis of the Cartesian coordinate system coincides with the vertical direction along which the density gradient is probed by the schlieren imaging system.

To replicate the schlieren experiment of injection into quiescent air at standard condition (20 °C and 1 atm) in a controlled open environment, open boundary is imposed on the upper, lateral and lower surfaces of the cylindric volume, i.e. zero-gradient condition for outflow and fixed ambient pressure for inflow. A sufficiently long internal fluid path upstream of the nozzle is included to minimize influences

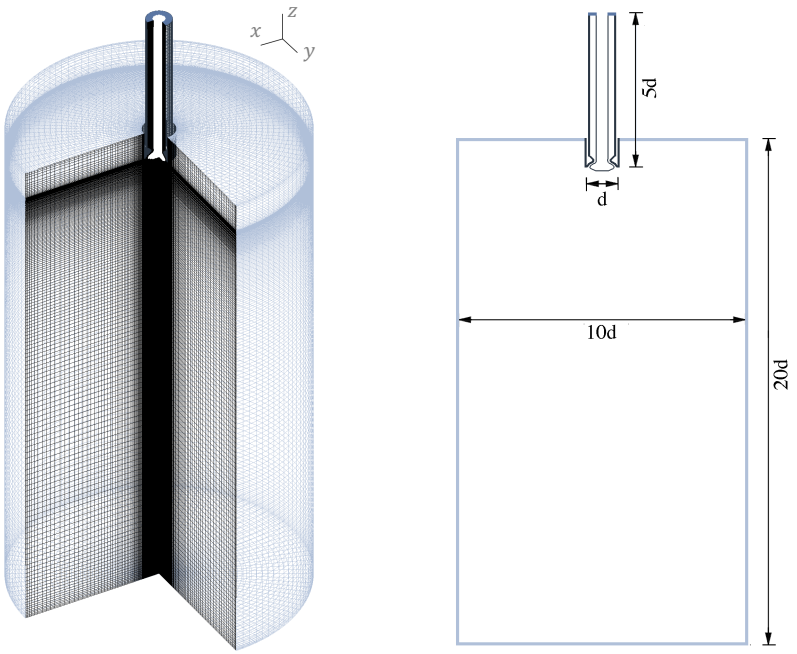

Figure 3.6 Overview and schematic of the computational domain and boundaries
– Inlet pressure boundary, – Open boundary, – Injector wall boundary

of the annular nozzle passage and to achieve vertical laminar flow close to the inlet boundary. The time-dependent inlet fuel pressure is derived from an experimentally calibrated one-dimensional CFD model of the injection system that monitors flow variables at the same boundary position. The injector wall and poppet valve surfaces represent the real geometry rather than a hypothetical nozzle, and are hence treated as adiabatic no-slip wall boundaries. In particular, the poppet valve is configured as wall boundary with mesh movement according to laser-measured needle lift curves. The time-dependent inlet pressure and needle lift for the investigated injection case of 2 ms pulse width are presented in Figure 3.7 wherein the curves are shifted by 225 μs leftwards corresponding to the mechanical SOI delay. In fact, the local inlet pressure drops by around 3.6 bar below the nominal upstream supply pressure of 16 bar during the injector opening transient, and remains at the reduced level for the entire steady-state operation, as a result of relatively low flow velocity and high compressibility of the gaseous fuel inside the supply line. Being an electromagnetic solenoid injector often with longer transients than piezoelectric injectors, the effects of gradual needle opening and pressure drop are especially important for accurate jet behavior predictions.

3.3.3 Numerical modeling strategies

The three-dimensional time-dependent turbulent flowfields are solved by the RANS approach together with the k-ζ-f formulation of the eddy-viscosity model for turbulence closure. Despite recent growing popularity of large-eddy simulation (LES) in studying underexpanded jets, the applications have been limited to single-hole orifice featuring fixed nozzle geometry [384][385][386][387][388][389][390]. Applying LES to the complex flowfields generated by the annular flow passage of an outward-opening injector with time-dependent geometry would be prohibitively cumbersome. Therefore, RANS is employed to approximate the mean flowfields,

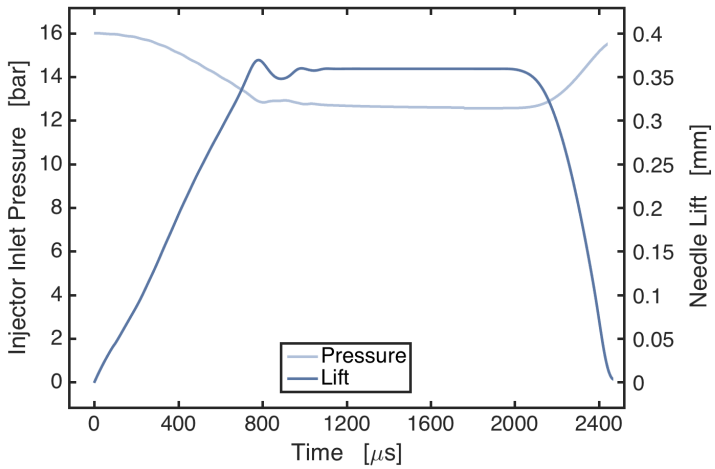

Figure 3.7 Time-dependent inlet pressure and needle lift for the injector model

which fits the scope of characterizing coherent flow structures and air-fuel mixing in the present work at reasonable computational costs. The k-ζ-f turbulence model, similar to the $\overline{v^2}$-f model, involves an elliptic equation for the relaxation function f based on the elliptic relaxation concept [391][392] and the transport equation of a velocity scale, in addition to the transport equations of turbulence kinetic energy k and dissipation rate thereof ε. By solving for the velocity scale ratio $\zeta = \overline{v^2}/k$ (a normalization) rather than the velocity scale $\overline{v^2}$ and introducing near-wall damping to the turbulence production coefficient in the ε equation, computational robustness and tolerance to grid nonuniformities are enhanced [393]. The k-ζ-f formulation is coupled with a hybrid near-wall treatment [394] that, extending the description of temperature distribution in fully turbulent boundary layers [395] to all turbulence properties, provides the results of low Reynolds number integration-up-to-the-wall models [396] or of the standard wall function [328], depending on whether the wall-nearest grid centroids lie within the viscous sublayer and the buffer zone or in the logarithmic region. This complete approach of turbulence modeling is accordingly considered suitable for complex flow domain and a priori unknown partition point between near-wall layer and fully turbulent region. Finally, the RANS turbulence modeling is closed with the equation of state of ideal gas for the moderate pressure range involved.

Convective fluxes in the set of finite-volume discretized RANS conservation equations are approximated by a TVD scheme that is based on the MINMOD flux limiter [397] for boundedness and consists in a piecewise combination of the linear upwind and central differencing schemes in the monotonic range, amounting to a second-order accuracy with refined numerical grids. The thus calculated cell-face-centered variables are also used to approximate the diffusion terms. The velocity-pressure coupling problem of the momentum equation is tackled by the SIMPLE (semi-implicit method for pressure-linked equations) algorithm [398] wherein the mass and momentum conservation laws are satisfied, in an approximate sense, by updating the velocity and pressure fields calculated from the momentum equation with the pressure correction that is derived from and hence enforces the continuity equation. The provisional velocity and pressure fields are corrected once, and thus the splitting error is reduced iteratively within each time step. Density correction is introduced and coupled with pressure correction through the equation of state [399] [400] to extend the SIMPLE algorithm to compressible flows. The advancement of the discretized equations through each time step, the time marching procedure, is handled by the unconditionally stable implicit first-order Euler scheme that assumes linear variation of variables between two time steps. An alternative is the second-order scheme with quadratic relation across three time steps whose formal accuracy is however strictly preserved for constant-density non-moving mesh cases, and is therefore not adopted. The time steps in the present work, ranging from 4×10^{-7} to 8×10^{-7} s, are considered sufficiently small to limit temporal truncation errors for the unsteady RANS solutions during transient phases.

The relevant properties of helium, a non-routine gas species for fluid machine applications, are not readily available in the built-in library and thereby supplied to the solver by means of the CHEMKIN-compatible database format [401] that is consistent with the NASA complex chemical equilibrium code [402]. In particular, the thermodynamic properties are prescribed by a fourth-order polynomial fit to the specific heat at constant pressure, c_p, expressed as a function of temperature on the assumption of ideal gas

$$\frac{c_p}{R} = a_1 + a_2 T + a_3 T^2 + a_4 T^3 + a_5 T^4 \tag{32}$$

where R is the universal gas constant and T the absolute temperature. Accordingly, the expressions of specific enthalpy, h, and entropy, s, whose standard-state values are both defined as zero at 298.15 K for helium, are derived from the corresponding relations with the specific heat as

$$\begin{aligned} \frac{h}{R} &= \int_0^T \frac{c_p}{R} dT \\ &= a_1 T + a_2 \frac{T^2}{2} + a_3 \frac{T^3}{3} + a_4 \frac{T^4}{4} + a_5 \frac{T^5}{5} + a_6 \end{aligned} \tag{33}$$

$$\begin{aligned} \frac{s}{R} &= \int_0^T \frac{c_p}{RT} dT \\ &= a_1 \ln T + a_2 T + a_3 \frac{T^2}{2} + a_4 \frac{T^3}{3} + a_5 \frac{T^4}{4} + a_7 \end{aligned} \tag{34}$$

where a_6 and a_7 are two integration constants, in addition to the five coefficients, a_1 to a_5, introduced together with the polynomial for c_p. The functions in Equation (32), (33) and (34) are least-squares fitted simultaneously. The fitting temperature range from 200 to 6000 K is split into two intervals with a breakpoint at 1000 K. Therefore, the thermodynamic properties of a gas species are uniquely determined by the molecular mass and a total of 14 coefficients, i.e. a_i $(i = 1,2,\dots,7)$ for the upper and lower intervals respectively. The transport properties include molecular viscosity, diffusion coefficients and thermal conductivity, which are determined in general by the kinetic theory of gases involving Chapman-Enskog solutions of the Boltzmann equation with respect to binary molecular collisions in the presence of macroscopic gradients in bulk velocity, composition and temperature. In particular, the pure-substance viscosity, η, and diffusion coefficients in a binary mixture, D_{12}, obey a principle of corresponding states for monatomic and polyatomic gases alike,

and can therefore be evaluated by a set of collision integrals along with respective molecule-specific scaling parameters, σ and ε, for intermolecular potentials [403]

$$\eta = \frac{5}{16}\frac{\sqrt{\pi M k_B T}}{\pi\sigma^2\Omega^{(2,2)^*}} \tag{35}$$

$$D_{12} = \frac{3}{16}\frac{\sqrt{2\pi k_B^3 T^3\left(\frac{1}{M_1}+\frac{1}{M_2}\right)}}{p\pi\sigma_{12}^2\Omega^{(1,1)^*}} \tag{36}$$

where M is the molecular mass, k_B the Boltzmann constant, T the temperature, and p the pressure. The reduced collision integrals, $\Omega^{(1,1)^*}$ and $\Omega^{(2,2)^*}$, are obtained by a quadratic interpolation of the tabulated Stockmayer potentials [404] as a function of the reduced temperature T^* and reduced dipole moment μ^* which, in the case of Equation (35) for pure substance, are in turn given by

$$T^* = \frac{k_B T}{\varepsilon} \tag{37}$$

$$\mu^* = \frac{1}{2}\frac{\mu^2}{\varepsilon\sigma^3} \tag{38}$$

where ε is the Lennard-Jones potential well depth, σ the Lennard-Jones collision diameter, and μ the dipole moment. In the case of Equation (36) for binary mixture, the parameters in Equation (37) and (38) are replaced by binary forms, i.e. ε_{12}, σ_{12} and μ_{12}, which, depending on polarities of the collision pair, are given by

Polar-polar or nonpolar-nonpolar	Polar-nonpolar	
$\varepsilon_{12} = \sqrt{\varepsilon_1\varepsilon_2}$	$\varepsilon_{12} = \xi^2\sqrt{\varepsilon_1\varepsilon_2}$	(39)
$\sigma_{12} = \frac{1}{2}(\sigma_1+\sigma_2)$	$\sigma_{12} = \frac{1}{2}(\sigma_1+\sigma_2)\xi^{-\frac{1}{6}}$	(40)
$\mu_{12}^2 = \mu_1\mu_2$	$\mu_{12}^2 = 0$	(41)
	$\xi = 1+\frac{1}{4}\frac{\alpha_{np}}{\sigma_{np}^3}\frac{\mu_p}{\sqrt{\varepsilon_p\sigma_p^3}}\sqrt{\frac{\varepsilon_p}{\varepsilon_{np}}}$	(42)

where α is the polarization, and the subscript p and np denote polar and nonpolar molecule in the collision pair, respectively. Equation (35) and (36) are in fact first-order approximations and neglect the effects of inelastic collisions of polyatomic molecules due to their rotational and vibrational degrees of freedom, amounting to an overall error not more than a few percent [403]. However, thermal conductivity of polyatomic gases is considerably influenced by inelastic collisions, and applying the principle of corresponding states is consequently of poor accuracy. The thermal conductivity, λ, is normally assumed to be the sum of translational, rotational and vibrational contributions, and the formulation is given by [405]

$$\lambda = \frac{\eta}{M}\left(f_{trans}C_{v,trans} + f_{rot}C_{v,rot} + f_{vib}C_{v,vib}\right) \tag{43}$$

wherein an extended Eucken correction is introduced to the simplified assumptions that the translational function equals that of monatomic gases and the rotational and vibrational (i.e. the internal) energy is transported at the same rate as the molecules themselves by diffusion

$$f_{trans} = \frac{5}{2}\left(1 - \frac{2}{\pi}\frac{C_{v,rot}}{C_{v,trans}}\frac{A}{B}\right) \tag{44}$$

$$f_{rot} = \frac{\rho D}{\eta}\left(1 + \frac{2}{\pi}\frac{A}{B}\right) \tag{45}$$

$$f_{vib} = \frac{\rho D}{\eta} \tag{46}$$

where ρ is the density derived from the ideal gas equation, and the "self-diffusion" coefficient, D, the two correction functions, A and B, are given by

$$A = \frac{5}{2} - \frac{\rho D}{\eta} \tag{47}$$

$$B = Z_{rot} + \frac{2}{\pi}\left(\frac{5}{3}\frac{C_{v,rot}}{R} + \frac{\rho D}{\eta}\right) \tag{48}$$

$$D = \frac{3}{16}\frac{\sqrt{2\pi k_B^3 T^3/M}}{p\pi\sigma^2\Omega^{(1,1)^*}} \tag{49}$$

where Z_{rot} is the rotational relaxation collision number that in turn is temperature-dependent [406][407]. A reference value at 298 K is provided to calculate the values

at other temperatures as

$$Z_{rot}(T) = Z_{rot}(298)\frac{F(298)}{F(T)} \tag{50}$$

$$F(T) = 1 + \frac{\pi^{3/2}}{2}\left(\frac{\varepsilon}{k_B T}\right)^{1/2} + \left(\frac{\pi^2}{4} + 2\right)\left(\frac{\varepsilon}{k_B T}\right) + \pi^{3/2}\left(\frac{\varepsilon}{k_B T}\right)^{3/2} \tag{51}$$

and the molar heat capacities at constant volume for each contribution depends on geometric configurations of the gas molecule

Monatomic	Linear	Nonlinear	
$C_{v,trans} = \frac{3}{2}R$	$C_{v,trans} = \frac{3}{2}R$	$C_{v,trans} = \frac{3}{2}R$	(52)
$C_{v,rot} = 0$	$C_{v,rot} = R$	$C_{v,rot} = \frac{3}{2}R$	(53)
$C_{v,vib} = 0$	$C_{v,vib} = C_v - \frac{5}{2}R$	$C_{v,vib} = C_v - 3R$	(54)

where the pure-substance molar heat capacity at constant volume, C_v, is obtained on the basis of Equation (32) and Mayer's relation of heat capacities. In summary, the thermodynamic and transport properties of a gas species of interest are uniquely specified by a system consisting of the molecular mass, 14 polynomial coefficients, the Lennard-Jones potential well depth and collision diameter, the dipole moment, the molecule polarization and the rotational relaxation collision number. The values of corresponding parameters for helium are quoted from datasets in the literature [408][409] and are presented in Table 3.1.

In addition, the ambient air is assumed to be composed of 76.8% nitrogen and 23.2% oxygen by mass. The thermodynamic and transport properties of nitrogen and oxygen are prescribed in the same form as helium, and the various parameters are available in the built-in library assuming the standard values commonly used in numerical physicochemical analysis [410][411][412].

3.3.4 Transport of species

Apart from addressing transient turbulent flowfields and underexpanded sonic jet, correctly describing the distribution of various species is an important aspect of studying the injection and mixing process.

According to the numerical setup, a ternary system of gas-phase mixing results.

Table 3.1
Specifications of thermodynamic and transport properties of helium

Molecular mass [g/mol]	4.0026			**Molecule geometric configuration**	Monatomic	
Thermodynamic properties: upper temperature interval (1000-6000 K)						
$\boldsymbol{a_1}$	$\boldsymbol{a_2}$	$\boldsymbol{a_3}$	$\boldsymbol{a_4}$	$\boldsymbol{a_5}$	$\boldsymbol{a_6}$	$\boldsymbol{a_7}$
2.5	0	0	0	0	-745.375	0.928723974
Thermodynamic properties: lower temperature interval (200-1000 K)						
$\boldsymbol{a_1}$	$\boldsymbol{a_2}$	$\boldsymbol{a_3}$	$\boldsymbol{a_4}$	$\boldsymbol{a_5}$	$\boldsymbol{a_6}$	$\boldsymbol{a_7}$
2.5	0	0	0	0	-745.375	0.928723974
Transport properties:						
$\boldsymbol{\varepsilon}$ [K]		$\boldsymbol{\sigma}$ [Å]	$\boldsymbol{\mu}$ [Debye]	$\boldsymbol{\alpha}$ [Å^3]		$\boldsymbol{Z_{rot}}$
10.200		2.576	0.000	0.000		0.000

The local mass fraction of each species is predicted by a transport (i.e. conservation) equation in a hyperbolic-parabolic convection-diffusion form similar to the Navier-Stokes equation, which, for the i-th species without chemical reaction, is expressed in the scalar differential form as

$$\frac{\partial}{\partial t}(\rho Y_i) + \nabla \cdot (\rho \boldsymbol{u} Y_i) + \nabla \cdot \boldsymbol{J_i} = 0 \tag{55}$$

where Y_i is the mass fraction and $\boldsymbol{J_i}$ the diffusive mass flux vector that arises from the concentration gradient. The ordinary mass diffusion in turbulent flows is often modeled by the phenomenological Fick's law [413] as

$$\boldsymbol{J_i} = -\left(\rho D_{i,m} + \frac{\mu_t}{Sc_t}\right)\nabla Y_i \tag{56}$$

where μ_t is the turbulent viscosity defined by the turbulence model, Sc_t = 0.7 the turbulent Schmidt number, and $D_{i,m}$ the diffusion coefficient of the i-th species in the mixture. While Fick's law provides a reasonable approximation of the diffusion process in binary mixtures, the formulation with one effective diffusion coefficient per species and with direct proportionality between flux and concentration gradient of the concerned species alone is sometimes debatable [414][415]. In fact, applying Equation (56) to multicomponent system leads to some nonconservation of species mass, i.e. non-vanishing sum of diffusive fluxes over all species and the sum of all species mass fractions different from unity.

Diffusion in multicomponent gaseous mixture is accurately described by the Maxwell-Stefan theory for transport phenomena [416][417] which is based on the binary reciprocal interaction between gas molecules. In particular, diffusion process

by nature is associated with relative motion as a result of differences in the average velocities of constituent chemical species. Molecules of one species are accordingly subjected to drag exerted by the other species, analogous to the drag from a tube to the fluid flowing through. The Maxwell-Stefan theory in essence hypothesizes local equilibrium between the frictional and driving forces. In general, frictions between diffusing particles are proportional to the relative velocity and mole fraction of the other species. And driving forces for ordinary diffusion process, assuming the same external forces (e.g. gravitational and electric fields) on all species and neglecting net-pressure diffusion, are the gradient of partial pressure of the concerned species in the mixture, whereby for ideal gas the mole fraction is explicitly involved. The Maxwell-Stefan equation for the i-th species in an ideal gas mixture is [418]

$$\nabla X_i = \sum_{\substack{j=1 \\ j \neq i}}^{N} \frac{X_i X_j}{D_{ij}} \left(\boldsymbol{V_j} - \boldsymbol{V_i} \right) \tag{57}$$

where N is the number of gas species, X the mole fraction, $\boldsymbol{V}$ the diffusion velocity, and D_{ij} the Maxwell-Stefan diffusion coefficient that for ideal gas equals the binary diffusion coefficient defined in Equation (36). It is convenient to deduce an explicit expression for diffusive mass flux instead of diffusion velocity, given $\boldsymbol{J_i} = \rho_i \boldsymbol{V_i}$

$$\begin{aligned} \nabla X_i &= \sum_{\substack{j=1 \\ j \neq i}}^{N} \frac{1}{D_{ij}} \left(\frac{X_j}{\rho_j} X_i \boldsymbol{J_j} - \frac{X_i}{\rho_i} X_j \boldsymbol{J_i} \right) \\ &= \sum_{\substack{j=1 \\ j \neq i}}^{N} \frac{M}{\rho D_{ij}} \left(\frac{X_i}{M_j} \boldsymbol{J_j} - \frac{X_j}{M_i} \boldsymbol{J_i} \right) \end{aligned} \tag{58}$$

where ρ is the density of the mixture and M the mixture-averaged molar mass that is in turn given by definition in terms of mole fraction, X or mass fraction Y as

$$M = \sum_{i=1}^{N} X_i M_i = \left(\sum_{i=1}^{N} \frac{Y_i}{M_i} \right)^{-1} \tag{59}$$

Applying Equation (58) to each of the N species in the gas-phase mixture leads to a system of N linearly-dependent equations. The linear dependence resides in the

conservation of species mass, i.e. the sum of the N Maxwell-Stefan equations must vanish, which is expressed by either of the two equivalent closure conditions

$$\sum_{i=1}^{N} \boldsymbol{J_i} = 0 \tag{60}$$

$$\sum_{i=1}^{N} X_i = \sum_{i=1}^{N} Y_i = 1 \tag{61}$$

Therefore, $N-1$ independent equations results. In general, explicit expressions of diffusive mass fluxes as a function of mass fraction gradients are requested for the species transport equation (Equation (55)) to be solved. Given the relation between mass and mole fractions and by taking the gradient of Equation (59), mole fraction gradient is converted into mass fraction gradient by

$$X_i = Y_i \frac{M}{M_i} \tag{62}$$

$$\begin{aligned} \nabla X_i &= \frac{M}{M_i}\nabla Y_i + \frac{Y_i}{M_i}\nabla M \\ &= \frac{M}{M_i}\nabla Y_i + \frac{X_i}{M}\left(-M^2 \sum_{j=1}^{N} \frac{\nabla Y_j}{M_j}\right) \end{aligned} \tag{63}$$

wherein the mass fraction of the N-th species, Y_N, is dependent and to be eliminated by applying the closure condition in Equation (61)

$$\begin{aligned} \nabla X_i &= \frac{M}{M_i}\nabla Y_i + X_i M\left(-\frac{\nabla Y_N}{M_N} - \sum_{j=1}^{N-1} \frac{\nabla Y_j}{M_j}\right) \\ &= \frac{M}{M_i}\nabla Y_i + X_i M\left(\sum_{j=1}^{N-1} \frac{\nabla Y_j}{M_N} - \sum_{j=1}^{N-1} \frac{\nabla Y_j}{M_j}\right) \\ &= M\left(\frac{X_i}{M_N} + \frac{1-X_i}{M_i}\right)\nabla Y_i + \sum_{\substack{j=1 \\ j\neq i}}^{N-1} X_i M\left(\frac{1}{M_N} - \frac{1}{M_j}\right)\nabla Y_j \end{aligned} \tag{64}$$

The lefthand side of Equation (58) is thus transformed in the mass reference frame, from N dependent mole to $N-1$ independent mass fraction gradients. Similarly, the corresponding diffusive flux of the N-th species, $\boldsymbol{J_N}$, is dependent and has to be eliminated from the righthand side of Equation (58) through the closure condition in Equation (60)

$$\sum_{\substack{j=1\\ j\neq i}}^{N} \frac{M}{\rho D_{ij}}\left(\frac{X_i}{M_j}\boldsymbol{J_j} - \frac{X_j}{M_i}\boldsymbol{J_i}\right)$$

$$= -\frac{M}{\rho}\left(\frac{\boldsymbol{J_i}}{M_i}\sum_{\substack{j=1\\ j\neq i}}^{N}\frac{X_j}{D_{ij}} - X_i\sum_{\substack{j=1\\ j\neq i}}^{N}\frac{\boldsymbol{J_j}}{M_j D_{ij}}\right)$$

$$= -\frac{M}{\rho}\left[\frac{\boldsymbol{J_i}}{M_i}\sum_{\substack{j=1\\ j\neq i}}^{N}\frac{X_j}{D_{ij}} - X_i\left(\frac{\boldsymbol{J_N}}{M_N D_{iN}} + \sum_{\substack{j=1\\ j\neq i}}^{N-1}\frac{\boldsymbol{J_j}}{M_j D_{ij}}\right)\right]$$

$$= -\frac{M}{\rho}\left\{\frac{\boldsymbol{J_i}}{M_i}\sum_{\substack{j=1\\ j\neq i}}^{N}\frac{X_j}{D_{ij}} - X_i\left[-\left(\frac{\boldsymbol{J_i}}{M_N D_{iN}} + \sum_{\substack{j=1\\ j\neq i}}^{N-1}\frac{\boldsymbol{J_j}}{M_N D_{iN}}\right) + \sum_{\substack{j=1\\ j\neq i}}^{N-1}\frac{\boldsymbol{J_j}}{M_j D_{ij}}\right]\right\}$$

$$= -\frac{1}{\rho}\left[M\left(\frac{X_i}{M_N D_{iN}} + \frac{1}{M_i}\sum_{\substack{j=1\\ j\neq i}}^{N}\frac{X_j}{D_{ij}}\right)\boldsymbol{J_i} + \sum_{\substack{j=1\\ j\neq i}}^{N-1} X_i M\left(\frac{1}{M_N D_{iN}} - \frac{1}{M_j D_{ij}}\right)\boldsymbol{J_j}\right] \tag{65}$$

In accord with Equation (58), the $N-1$ independent equations are transformed into the matrix form $[\boldsymbol{A}]\{\boldsymbol{J}\} = -\rho[\boldsymbol{B}]\{\nabla Y\}$ wherein $\{\boldsymbol{J}\}$ and $\{\nabla Y\}$ are the diffusive mass flux and mass fraction gradient vector, respectively, with dimension $N-1$, and $[\boldsymbol{A}]$ and $[\boldsymbol{B}]$ are $(N-1)\times(N-1)$ matrices whose elements are defined by Equation (65) and (64) respectively as

$$A_{ii} = M\left(\frac{X_i}{M_N D_{iN}} + \frac{1}{M_i}\sum_{\substack{j=1\\ j\neq i}}^{N}\frac{X_j}{D_{ij}}\right) \tag{66}$$

$$A_{ij} = X_i M\left(\frac{1}{M_N D_{iN}} - \frac{1}{M_j D_{ij}}\right) \tag{67}$$

$$B_{ii} = M\left(\frac{X_i}{M_N} + \frac{1-X_i}{M_i}\right) \tag{68}$$

$$B_{ij} = X_i M \left(\frac{1}{M_N} - \frac{1}{M_j} \right) \tag{69}$$

As the $N-1$ equations are independent, matrix $[\boldsymbol{A}]$ is invertible. The system of coupled non-linear Maxwell-Stefan equations is recast into a Fickian formulation that is substituted for the diffusion fluxes in the transport equation of species

$$\boldsymbol{J_i} = -\sum_{j=1}^{N-1} \left(\rho \mathcal{D}_{ij} + \frac{\mu_t}{Sc_t} \delta_{ij} \right) \nabla Y \tag{70}$$

where $\mathcal{D}_{ij} = [\boldsymbol{\mathcal{D}}] = [\boldsymbol{A}]^{-1}[\boldsymbol{B}]$ are the generalized Fickian diffusion coefficients and δ_{ij} is the Kronecker delta. Mass fraction of the N-th species, normally the species with the highest overall mass fraction to minimize numerical error, is calculated by species mass conservation from Equation (61).

It is noted that in turbulent flows laminar diffusions are in general overwhelmed by turbulent diffusions. The difference in specifying properties of laminar diffusion by means of the single-gradient Fick's law in Equation (56) or the coupled Maxwell-Stefan multicomponent formulation Equation (70) may therefore be insignificant. The magnitude of non-Fickian phenomena is small compared to turbulent transport. Nevertheless, the multicomponent diffusion modeling is incorporated in the present work for completeness of the problem formulation. Specifically, the ternary mixture is solved by two transport equations for helium and oxygen with $[\boldsymbol{\mathcal{D}}]_{2\times2}$ from the generalized Fick's law for the diffusion coefficients.

3.4 Numerical results and discussion

Three computational grids with 10, 15 and 20 cells across the radial opening of the injector annular flow passage, respectively, (called case 1, 2 and 3 hereinafter) are implemented to investigate the injection process. The numerical results and the schlieren images are compared.

3.4.1 Jet penetration

The axial jet penetrations are measured from the schlieren images and the three numerical cases as the maximum distance in the direction of jet centerline between the injector tip and the jet boundary. The jet boundaries are identified as contour of contrast visibly discernible from the background in schlieren images, and as contour

of density 5% below the ambient air in numerical results. Due to the considerable difference in molecular weight between helium and air, the identifying criterion of density as 1%, 2% or 5% leads to a tiny variation in axial penetration measurement within 1-2 mm based on a preliminary test. Similar findings about the jet boundary identification criteria in terms of mass fraction have also been reported [323][325]. Furthermore, the frequent jet asymmetry in both experimental and numerical cases is considered by taking the average of penetration lengths of the left and right half jet, divided by the jet centerline, as the jet penetration at each time instant.

The measured axial jet penetrations are presented in Figure 3.8 for comparison. The total range of length measurement corresponds to the observable light field in the schlieren images (100 mm). The penetration length is obviously underestimated by the coarsest grid of case 3, and resolving the flow passage with 10 cells thereby proves inadequate. The refined grids in both case 1 and 2 predict the jet penetration lengths in close agreement with the experiments. Moreover, the difference between the two cases is slight, implying much weakened grid dependence towards the finest case 3. Therefore, it is concluded that, with respect to jet penetration, 15 cells across the annular flow passage is the minimum resolution requirement and increasing the number of cells to 20 brings further, albeit slight, improvement.

Another observation is that the experimentally measured jet penetration shows an S-shaped trend whereas the numerically predicted penetration lengths are more rectilinear (case 2 and 3). The differences between the numerical and experimental curves are nevertheless insignificant, likely due to asymmetry of the instantaneous flowfield and associated measurement uncertainties.

3.4.2 Jet structure comparison

In theory, further detailed comparison of jet structure between experimental and numerical results is viable. As suggested by Equation (30), for the schlieren system

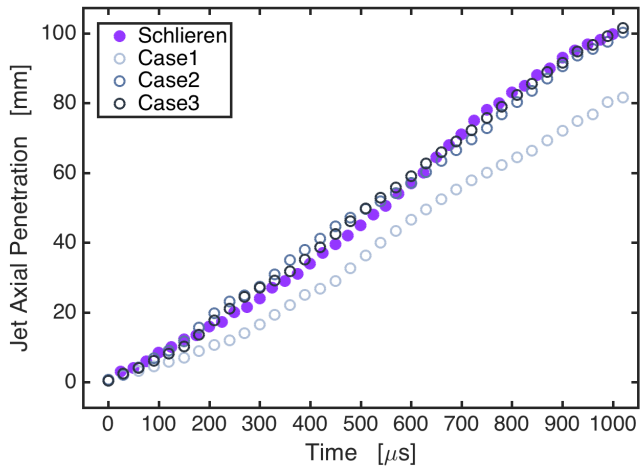

Figure 3.8 Axial jet penetration measured from experimental and numerical results (SOI = 0 μs)

employed in the current work, there exists a definite relationship between recorded images and jet density fields.

However, as a transillumination (or line-of-sight) technique, schlieren imaging consists in the projection of three-dimensional information onto a two-dimensional plane. The embedded mathematical operations on flow variables, i.e. the light path-integrated density gradient, make the comparison between schlieren and numerical results in terms of numerically predicted tomographic fields or iso-surface of mass fraction or density, as often adopted in the literature, physically counterintuitive. In recent experimental studies, background-oriented schlieren (BOS) [419][420] has been utilized to probe quantitative density distribution in a flowfield. Nevertheless, the application of tomographic reconstruction methods has been limited to cases of axisymmetric flows to which inversion of the Abel or Radon integral transform is applied [421][422][423], or to asymmetric flows whereby several BOS projections obtained along different viewing directions (either by using multiple synchronized cameras or by rotating a single camera setting for stationary or periodic flows) are necessitated for computed tomography [424][425][426]. Whereas processing BOS images yields the flow density fields with reasonable accuracy, the applicability of BOS and associated reconstruction computations to the large-scale complex gas jet issuing from an outward-opening injector with curved underexpanded structures is largely restricted. Alternatively, in view of the companion numerical investigation, it is unnecessary to extract density distribution from the experimental data. Rather, the schlieren and numerical results are processed to yield intermediate comparable quantities, which fits the purposed of jet morphology comparison herein.

Specifically, the result processing is based on Equation (30) that describes the governing equation of schlieren imaging system. The lefthand side of Equation (30) corresponds to the schlieren contrast that is applied by Equation (31) to all schlieren images as shown in Figure 3.3. The righthand side is connected with the integration in a horizontal direction of the density gradient in the vertical direction, which is in turn derivable from the numerical results. The equality then dictates that the thus-obtained lefthand and righthand-side quantities are directly comparable.

In particular, mathematical operations on the finite-volume-discretized density field are required to evaluate the righthand-side quantity. The computational grid is mostly axisymmetric and hence curvilinear. The cell-centered flow variables cannot be directly used to perform the partial differentiation and integration that, according to the optical principle of schlieren, are along rectilinear paths. Consequently, the numerical density fields are interpolated (or remapped) onto a regularly spaced grid. The cuboid query grid contains $422 \times 422 \times 700$ points in correspondence with the schlieren image resolution of 422×700 pixels. The interpolation is performed by a two-step linear triangular (tetrahedral for three-dimensional case) method. The first step involves the construction of an interpolant through tetrahedrization of the set of scattered finite-volume cell centers, which is based on the Delaunay triangulation [427][428]. The geometric properties of Delaunay triangulation guarantee that the

circumscribed sphere of each underlying tetrahedron simplex encompasses no other point of the known set and hence no other tetrahedron (i.e. the Delaunay condition of empty interior) and that the minimum angle of each triangle is the largest among all possible triangulations (i.e. the "maxmin" angle criterion), thus rejecting sliver-shaped triangles [429][430]. The resultant single-valued interpolant is a continuous tetrahedrization structure, which is divided by triangular facets joined along edges and equivalent to a three-dimensional generalization of a piecewise linear function in one dimension, and forms a convex hull of the known point set. The second step involves evaluation of the interpolant at each query point within the convex hull by traversing the tetrahedrization structure to find the enclosing tetrahedron. The query value is then determined by the linear barycentric interpolation as the weighted sum of values of the four vertices. As the query grid is cubic and the computational grid cylindrical, the nearest-neighbor extrapolation is applied to the $(4-\pi)/4$ portion of query points located outside the convex hull. To achieve the same resolution as the schlieren images, the query grid contains ~98 million points in the cylindrical volume as compared to ~3.6 million cells in the computational grid. Therefore, the linear interpolation method is expected to well preserve the numerical density field. To validate the interpolation procedure, the numerically predicted and interpolated density fields in two orthogonal symmetry planes (xz and yz-plane) are compared in Figure 3.9 whereby it is verified that no detectable modification is introduced to the solution fields by the interpolation.

Partial differentiation and subsequent integration of the numerical solution are evaluated on the basis of the interpolated results. According to the schlieren system setup, it is unambiguous that partial derivative in the vertical direction (with respect to z-coordinate) corresponds to the probed density gradient. On the contrary, given the axisymmetric boundaries and unsteadiness of the problem, the specific direction in which the collimated light passes through the flowfield for the schlieren imaging is indeterminable with respect to the coordinate system of the numerical model, and the integration can be evaluated in any arbitrary horizontal direction depending on which the results may differ (see Figure 3.9 as an example of the flow asymmetry).

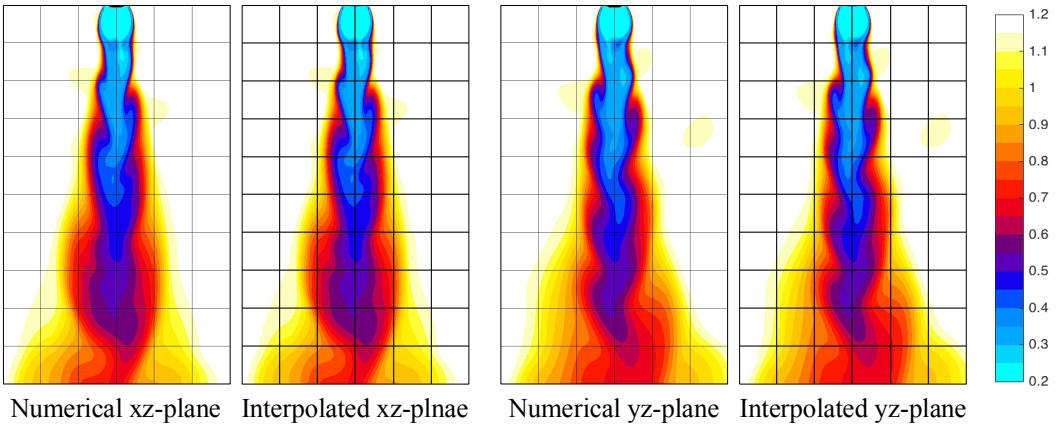

Figure 3.9 Comparison between numerically predicted and interpolated density fields at 1300 μs

Consequently, at each presented time instant, two processed numerical results are obtained by integrating the vertical density gradient along two mutually orthogonal directions (x and y-axis) respectively, for the purpose of comparing the jet structure from experimental and numerical results.

Figure 3.10 presents the comparison of results at 975 µs when the field of view is fully exploited to show a complete jet structure. The injector reaches steady-state operation with the maximum needle lift from this time instant on. Some jaggedness appears in the processed numerical results due to the vertical partial differentiation since by definition the Delaunay triangulation and linear barycentric interpolation are C^1 continuous. Higher-order continuity is hardly achievable for the construction of interpolant function and the subsequent interpolation method for scattered three-dimensional data. Furthermore, detailed surface corrugation caused by small-scale turbulence in the schlieren image is not captured by the RANS simulations. In this respect, schlieren images in general are equivalent to individual LES realizations as the finite sensor resolution can be considered as subgrid-scale averaging. And the RANS result therefore represents the ensemble average over multiple instantaneous schlieren images at the same time instant. Neither are the spherical acoustic waves perturbating the background in schlieren image captured by the numerical nature of the RANS model. As reported in Figure 3.8, case 1 notably underestimates axial jet penetration whereas the predictions from case 2 and 3 are similarly accurate. Radial

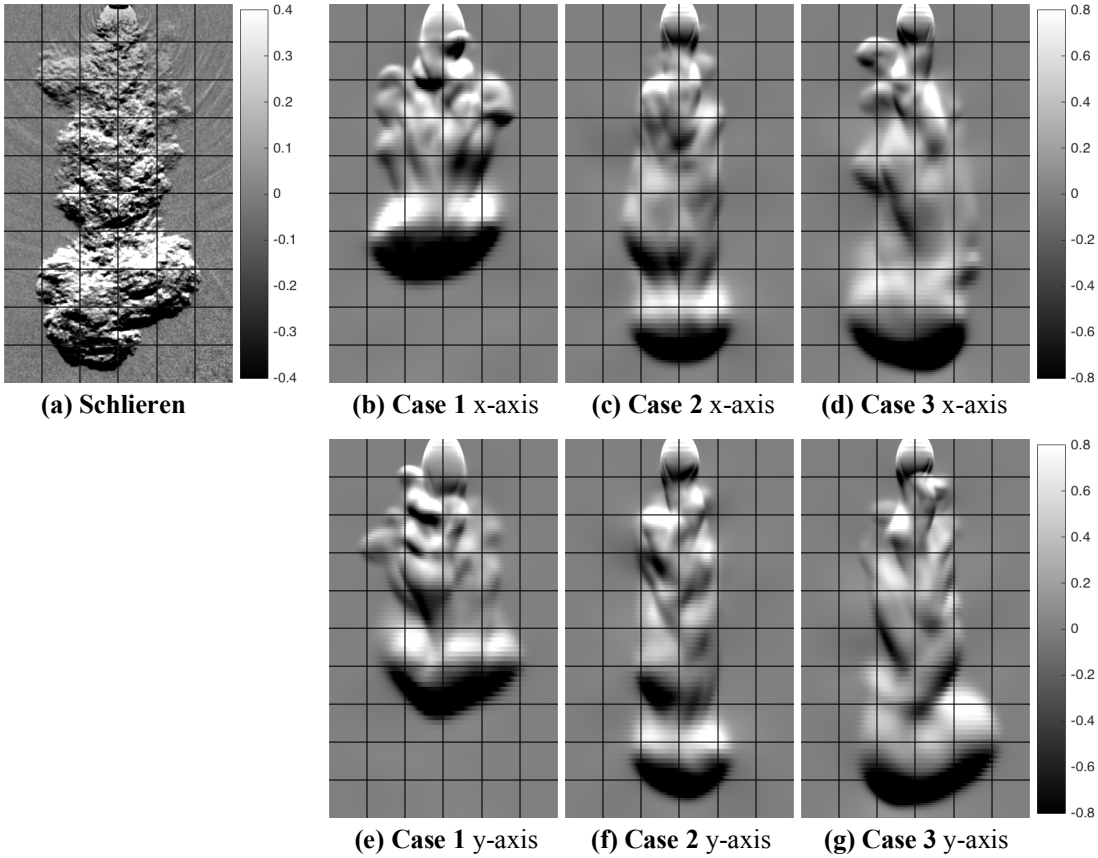

(a) Schlieren **(b) Case 1** x-axis **(c) Case 2** x-axis **(d) Case 3** x-axis

(e) Case 1 y-axis **(f) Case 2** y-axis **(g) Case 3** y-axis

Figure 3.10 Comparison between the schlieren contrast and numerical result at 975 µs

spreading of the jet, especially in the middle section, is overestimated by case 1 but slightly underestimated by case 2 and 3, with case 3 to a lesser extent.

With respect to jet structure, the three major morphological characteristics, i.e. the recirculation zone established by collapse of the initial toroidal vortex ring, the conical jet stem and the head vortex, are all captured by the three numerical cases. Except for the recirculation zone that is enclosed by the underexpanded supersonic flow regime, the jet is highly unsteady and far from axisymmetric. In particular, the recirculation zone predicted by case 1 is more radially extended and thus converges at a lower point along the jet centerline, forming a larger hollow cone, compared to the schlieren and the other two numerical cases. Furthermore, there appears to be a trend that the ellipsoid-shaped recirculation zone is more elongated when the grid is coarser, with case 3 providing the closest result to the experiment. And similar to the conclusion on axial jet penetration, the difference between case 2 and 3 is much smaller than that between case 1 and 2, indicating reliable grid independence. The highly unsteady jet stem with large-scale mean-flow instabilities and periodic three-dimensional vortex shedding pattern is faithfully depicted by the numerical model, especially by case 2 and 3. Volume of the asymmetric head vortex is underestimated by all three cases, which is most likely attributable to the common fact that RANS-based mean-flow solutions tend to predict reduced diffusion. Overall, the flowfield resulting from case 3 is comparatively the best among the three cases, and shows a reasonably good agreement with the schlieren image.

To further identify the underlying mechanism for the differences in jet structure described by the numerical cases, the initial injection phase is presented in Figure 3.11. Investigating the initial phase is of crucial importance since, first, the toroidal vortex ring and the resultant recirculation zone are speculated to determine the jet development and fully-developed jet structure based on the schlieren experiment in Figure 3.4, and, second, the primary difference between the numerical cases resides in the number of cells across the annular flow passage whose most direct influence would be on the nearfield flow. In addition to the transilluminated view of schlieren imaging, density contours (color images in Figure 3.11) in the corresponding plane of symmetry along y-axis (i.e. the xz-plane) are presented to provide a tomographic perspective.

The different jet structures are ascribable to the initial establishment of hollow cone which in turn is affected by grid resolution as expected. At 250 μs, the toroidal vortex ring in case 2 and 3 collapses onto the jet centerline to form a recirculation zone due to the low pressure inside the hollow cone, and the injected gas continues forwards in the vertical direction with a leading outward-rotating head vortex ring. In case 1, the initial toroidal vortex ring maintains the course of a conical umbrella-like shape instead of converging and forming large-scale flow recirculation filling the hollow cone (see Figure 3.11 (e)), thereby overpredicting the hollow cone angle and underpredicting the axial jet penetration in comparison with the schlieren image. It is in addition observed that the integrated density gradient along the two axes is

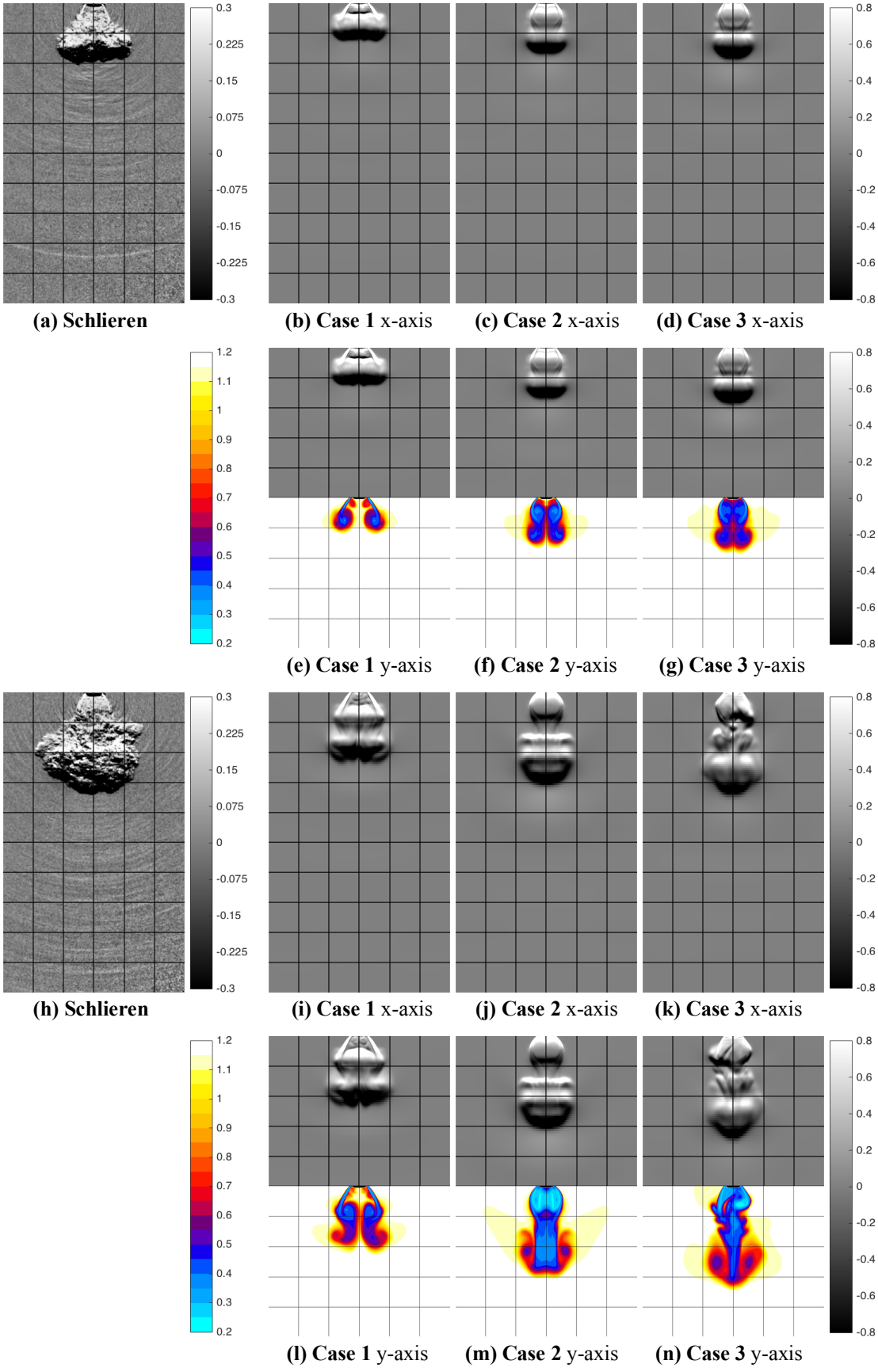

Figure 3.11 Comparison between the schlieren contrast and numerical results
(a) to (g) at 250 µs; (g) to (n) at 400 µs

identical in each numerical case, implying that the jet is currently axisymmetric like the geometric boundary and thus the flowfield is dominated by the compressibility-dependent potential core of underexpanded jet. The umbrella-shaped jet collapses at 400 µs in case 1, about 150 µs later than the other two cases (see Figure 3.11 (l)). Due to the relatively small cone angle of the flow passage, the poppet valve contour design for opportune flow detachment, and the low-pressure zone formed beneath the injector tip, the jet is after all prone to collapse. However, the postponed collapse of gas jet predicted by case 1 leads to overextension of the initial vortex ring that in turn affects both subsequent jet development and overall jet structure. In conclusion, the influence of spatial resolution of the numerical grid across the flow passage of injector nozzle is through the different predicted timing of transition from the first to the second jet development stage (i.e. the collapse of toroidal vortex ring and the formation of recirculation zone). More refined, less numerically dissipative grid is likely to resolve better the flowfield details and unsteadiness that are important and intrinsic characteristics of the complex hollow cone jet, and thereby results in more realistic predictions. For instance, the jet in case 3 with the finest grid already starts to deviate from axisymmetry caused by the unsteady recirculation zone (see Figure 3.11 (k) and (n)) which is not yet captured by the other two coarser cases as a result of the numerical dissipation of the latter cases which tends to attenuate detailed flow structures for unsteadiness to appear.

The radial jet penetration in Figure 3.11 is in general underestimated by all the numerical cases, which, as mentioned earlier, is due to the difference between more chaotic flowfields recorded in schlieren images and mean flow solved by numerical schemes, and to the typical tendency of diffusion underestimation of RANS models.

The structures of fully developed jet are compared in Figure 3.12. In particular, as the jet contour attains a steady-state conical shape after the head vortex advances beyond the field of view, the average of 25 consecutive schlieren images is derived (see Figure 3.12 (e)) to represent the mean jet outline. Despite the differences during the injector transient, the ellipsoid-shaped recirculation zone predicted by the three numerical cases is identical and in good agreement with the schlieren images when the jet is fully developed. And the trend that coarser grid leads to larger recirculation zone disappears, especially for case 1. Moreover, the unsteady von Kármán vortex pattern of the conical jet stem is similarly described by all cases. Nevertheless, as a result of different transient history of nearfield flow behavior, the jet contours differ, with case 1 to a greater extent and case 2 a lesser extent from case 3. And the shape of jet boundary predicted by case 3 is comparatively in the best agreement with both the instantaneous and averaged schlieren images.

For the purpose of more detailed comparison of the unsteady jet flowfield, on the one hand the vortex shed in the instantaneous schlieren image (see Figure 3.12 (a)) is obscured by the chaotic turbulent flowfield and therefore less distinguishable than that in the RANS-solved mean flow. The main reason is the high flow velocity and large velocity gradient, inducing large turbulent fluctuations and perturbations

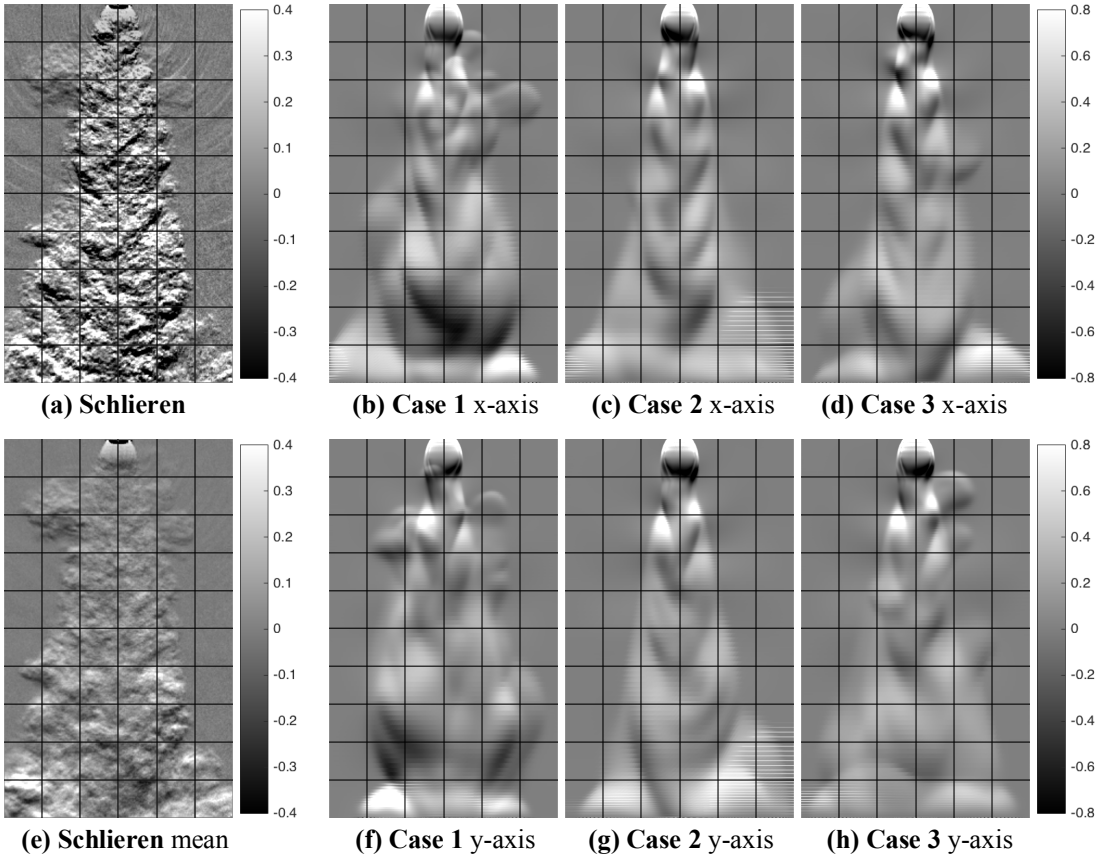

(a) Schlieren **(b) Case 1** x-axis **(c) Case 2** x-axis **(d) Case 3** x-axis

(e) Schlieren mean **(f) Case 1** y-axis **(g) Case 2** y-axis **(h) Case 3** y-axis

Figure 3.12 Comparison between the schlieren contrast and numerical result at 1800 µs

to the mean-flow vortex shedding pattern that would otherwise be easily discerned in instantaneous images (e.g. for low-speed gas or more-viscous liquid flows). On the other hand, averaging over 25 consecutive schlieren images, the same minimum number of individual LES solutions for first-order flow variables to converge [431], abates local maxima and minima of the noisy jet flowfield and verifies that the jet boundary shape is stationary and consistent with the numerical cases. Nonetheless, except for the upper part of the recirculation zone that is supposed to be dominated by supersonic flows, the mean-flow vortices are canceled out by the time-averaging due to their unsteady nature. And even if ensemble-averaging over multiple images at the same time instant can in theory provide proper mean flowfields for unsteady problems, experimentally repeating the injection process to yield coherent vortex shedding patterns is physically implausible. It is therefore considered to be difficult for experiments to calibrate numerical simulations in terms of the alternate unsteady vortex structure inside the jet stem, which is in line with the findings in [375].

In conclusion, despite the infeasibility to quantitatively calibrate the instability-associated vortex shedding characteristics (e.g. time and length scales), comparison of the jet penetration length and overall structure suggests that resolving the annular flow passage with 20 cells is methodologically reliable. In fact, this conclusion is consistent with the outcome of available similar grid-dependence studies about gas fuel injection applications with outward-opening poppet valve injectors. It has been

argued in [324] that, with the first-order upwind scheme being utilized to discretize convective fluxes, 16 cells across the injector nozzle at the maximum valve lift were sufficient to describe fuel distribution and hence the mixing process, and increasing up to 32 cells brought about small and localized differences in the periodic nearfield shock structure. The grid-dependence study in [320] has verified that the finest grid featuring a cell size of 40 µm across the injector opening, in combination with the second-order MARS scheme for convective flux discretization, led to satisfactory results with reference to experiments. Adaptive mesh refinement that automatically increases grid resolution in regions of large gradients has been applied in [316][317] from which the minimum cell size of 31.25 µm resulted. The stand-alone injection process from a similar outward-opening injector has been numerically investigated by means of LES in [325] wherein the use of 10-20 hexahedral cells with 5 prism near-wall layers across the nozzle gap was experimentally validated. Moreover, the nozzle pressure ratio encountered in the present work ($13 \leq p_0/p_a \leq 16$) is lower than the values in the aforementioned studies, implying that lower spatial resolution may suffice. Therefore, the numerical method implemented here, i.e. imposing 20 cells across the flow passage with an average cell size below 18 µm at the maximum lift and further dwindling during injector transient together with the less dissipative second-order MINMOD scheme for jet-related large gradients, is methodologically pertinent to the intended study of gas injection and mixing process. Such minuscule cell size is attributed to the typically small needle lift and hence narrow flow domain of outward-opening injectors, albeit with large total opening area, which necessitate refined grid to resolve the corresponding flow structures and diffusion scales. As a matter of fact, due to the peculiar geometry formed by the outward-opening poppet valve, the local cell size in the nozzle region is comparable with [334][432][433] or smaller than [434][435] the values used for LES of underexpanded circular jet from single-hole nozzles. This distinction further substantiates the differences in flow-mechanical and numerical characteristics between the circular and hollow cone jets.

3.4.3 Nearfield underexpansion structure

Nearfield shock structures of the underexpanded jet issuing from the outward-opening gas injector are presented in Figure 3.13, shown as Mach number contours at an early vortex-ring formation stage and the steady-state operation stage. Apart from the three previous cases with moving grid and different spatial resolutions, a fourth case with static grid fixed at the maximum nozzle opening from the start of simulation and otherwise the same grid of case 3 is added, in order to illustrate the underlying mechanism of potential issues when the complete injection process with transient is simulated by means of static meshes.

As concluded previously from the comparison between schlieren and numerical results, the influence of varying the local grid resolution on predicted jet flowfield appears to be the timing at which the initial toroidal vortex ring collapses and forms the recirculation zone. Comparing the Mach number contours of case 1 to 3 at 100

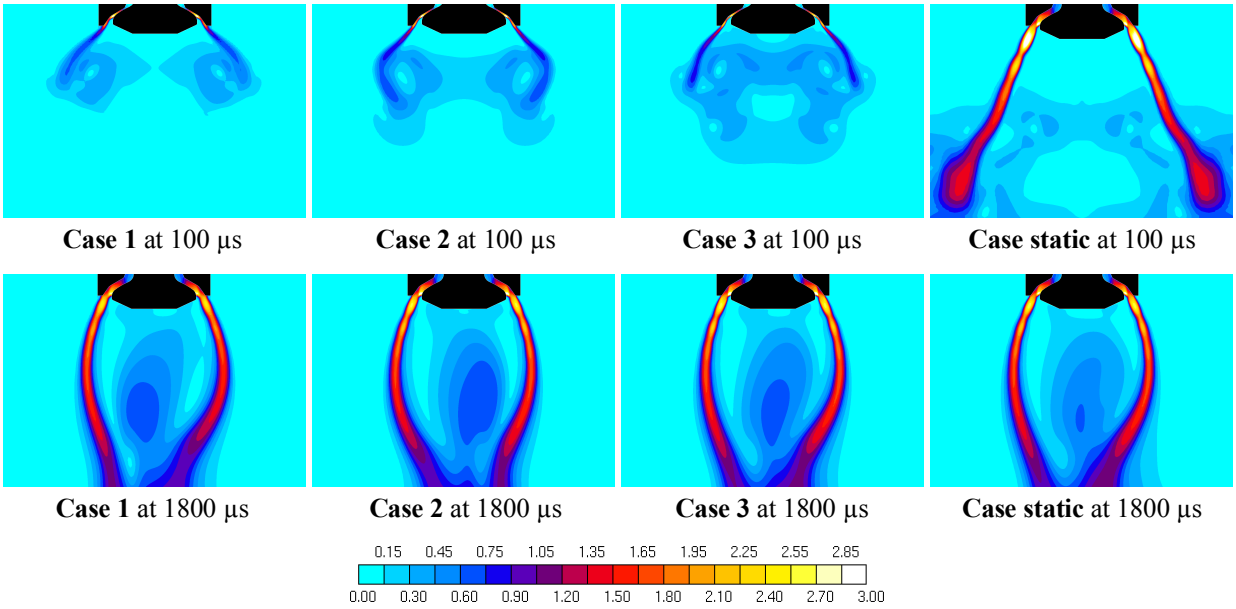

Figure 3.13 Nearfield shock structure of the underexpanded hollow cone jet shown as Mach number contours in the symmetry plane (xz-plane). Black regions denote the injector geometry.

µs indicates that the supersonic flow immediately downstream of the nozzle exit is very similar with regard to both cone angle and flow structure. The main differences occur in the farfield where the jet momentum is diffused by shear exchange and the subsonic flow convolves into a toroidal vortex ring towards the low-pressure zone. In addition to diffusion caused by large velocity gradients, the gas jet is further more dissipated numerically by coarser grid, whereas more refined grid tends to preserve jet momentum and resolve shock-induced local fluctuations better. In particular, the coarsest grid of case 1 dissipates the jet momentum to the greatest extent, and as a consequence the vortex ring and the depression in the center are the weakest. The flow velocity, within both the underexpanded jet boundary and the vortex ring, is the highest in case 3 with the sufficiently refined grid. And detailed flow structures, such as multiple vortices involved in the hollow cone and a central stagnation zone, are captured, which contribute to the higher-velocity and lower-pressure zone inside the hollow cone and accordingly explain the stronger tendency for the vortex ring to collapse than the less refined cases. Therefore, it is noted that, as a result of the minuscule flow passage during the transient, the effect of numerical dissipation on the initial jet flow with small dimension can be of perceivable significance, and the flowfield is thus computationally demanding in terms of spatial resolution. In line with the conclusion from Figure 3.12 that grid resolution exacts nearly negligible impact on the ellipsoid-shaped flow recirculation zone when the injector operation reaches steady state, the nearfield shock structure in Figure 3.13 is not qualitatively changed among the cases. The sole difference is that the variation in Mach number of the shock structure along the jet stream direction is slightly more attenuated by coarser grid.

The Mach number contour of the additional case static at 100 µs illustrates the

generally encountered issue of the overestimation of axial jet penetration when the complete injection event including transient phases is simulated with static injector grid. The absence of gradual nozzle opening alters both the instantaneous mass flow rate and the geometrical length scales of the gas jet. The result is often that a larger quantity of gas is encompassed in the supersonic flow and the corresponding higher jet momentum is dissipated further downstream where the vortex ring is formed, in comparison with moving-grid cases. In addition, the geometrical peculiarity of an outward-opening injector poses difficulties in finding a proper boundary condition that mimics the transient behavior with a static (usually the wide-open) annular flow passage. Specifically, the gas jet during transient undergoes two changes, i.e. a drop in the supply pressure (as shown in Figure 3.7) and an increase in flow area, which exert opposite effects on mass flow rate. Calibration of such an effective boundary condition may be thereby more complicated for an outward-opening injector than for an inward-opening one, and is beyond the scope of the present work. Upon the completion of injector transient, the nearfield structure under steady-state operation is predicted in the same way whether the grid is moving or static, as the geometrical and boundary conditions are identical among the cases. Whereas static grid suffices to study jet structures under constant conditions, describing the transient behaviors with accuracy, especially for solenoid actuated injectors, entails artificial treatment for the inlet boundary. And reproducing the actual needle movement arguably suits the pulsed intermittent nature of engine fuel injection that consists of a fair portion of transient phases.

Some general nearfield characteristics of the underexpanded jet are observed in Figure 3.13. First, the flow passage shaped by the poppet valve and the seat thereof typically includes a divergent part prior to the exit. The flow is thus accelerated to supersonic state and the first shock cell already appears at some position within the nozzle gap, impeding the application of simplified injector models by imposing the flow state at the exit section that is often adopted for circular jet cases. Second, a series of cell-like shock structures embodying the oblique intercepting and reflected shocks that result from alternate coalesced expansion and compression waves in the potential core is observed, which in general characterizes underexpanded jets. The peculiarity is that the underexpanded potential core in this case is distributed in a hollow cone in accord with the annular flow passage, instead of concentrating along the injector axis to fill up the central region as in the case of a circular jet. Third, as the noise generation mechanism of supersonic jets has been long recognized to be largely dependent on high-Mach-number-induced turbulence structures [436], the annularly distributed potential core is supposed to be responsible for the sources of the non-concentric acoustic waves observed in the background of schlieren images (see Figure 3.4). To further study the acoustic behaviors numerically, turbulence-resolving methods (e.g. LES) are needed. Fourth, despite being underexpanded, the jet cross section, in this case regarded as thickness of the supersonic annular cone, does not immediately enlarge downstream of the nozzle exit. The limited transverse

expansion is likely attributed to the converging streamlines (i.e. the vena contracta) when the flow approaches the abruptly narrowed nozzle gap from the injector inlet (see Figure 3.5) [354], which is further exacerbated by the expansion fan that causes flow detachment from the poppet valve. From the viewpoint of inward-opening fuel injector, flow contraction is to be avoided since the barrel shock growth determines jet cone angle and thus air-fuel mixing efficiency for circular jet. On the contrary, cone angle and cross-sectional area of a hollow cone jet do not directly depend on shock cell dimension, and therefore converging streamlines are less problematic for outward-opening injector.

3.4.4 Transient jet development

In addition to the transilluminated schlieren images, a tomographic presentation provides detailed information on jet development and underlying interior structures. Figure 3.14 presents the flow streamlines at various time instants during the injector transient. The initial formation of the hollow cone and the toroidal vortex ring are shown in Figure 3.14 (a), denoting the first jet development stage. As an increasing amount of gas is injected and exchanges momentum with the ambient air, a strong low-pressure zone results beneath the injector tip by which the growing vortex ring is drawn towards the centerline and converted into a large-scale recirculation zone.

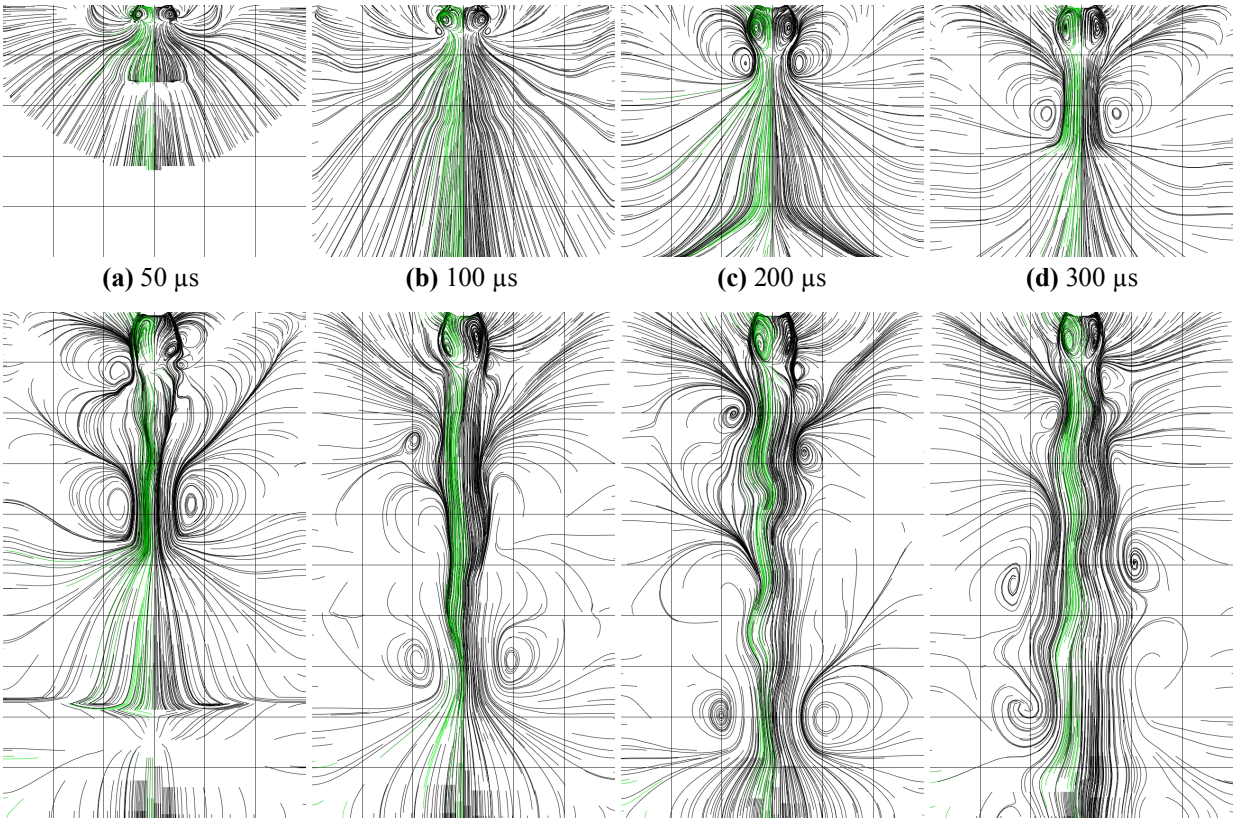

(a) 50 µs **(b)** 100 µs **(c)** 200 µs **(d)** 300 µs

(e) 400 µs **(f)** 600 µs **(g)** 700 µs **(h)** 1000 µs

Figure 3.14 Flow streamlines during injector transient in the symmetry plane (xz-plane)

The ellipsoid-shaped recirculation zone is elongated by the high-momentum jet as the injector opens, whereas the radial expansion is constricted by the low-pressure center. The second development stage commences in Figure 3.14 (c), during which the injected gas proceeds in the form of a head vortex ring that is observed as a pair of vortices in symmetric locations advancing downwards in the subsequent figures, sustained by a quasi-steady stem. If the upstream recirculating flowfield is ignored, the jet development at this stage is very similar to a circular jet, which is consistent with the observation in schlieren images (see Figure 3.4 (k) to (o)). When the needle lift is sufficiently high, the entire jet, up from the recirculation zone, becomes highly unsteady from about 400 µs onwards, corresponding to the third and also the main development stage that ensues the two momentary stages of early injector transient and characterizes the majority of the injection process.

In fact, the unsteady flowfield is phenomenologically as well as conceptually analogous to bluff body wakes [437] that have been well known to feature complex dynamic Reynolds-number-dependent vortical structures. In particular, the hollow cone jet resembles the canonical case of wake flows around a semicircular cylinder [438][439][440] in that the flow separation and reattachment are directly associated with the blunt edge. It is observable in the fully-developed jet (see Figure 3.14 (e) to (h)) that the flow recirculation behind the bluff body shows dynamic asymmetric behaviors accompanied by the formation of undulating vortices alternately on each side of the oscillating jet stem upwind of the head vortex ring. And this observation is consistent with the coherent pattern of periodic shedding and rolling-up of large-scale von Kármán vortices. Moreover, the supersonic flow around the bluff body in the near-wake region up to the reattachment point (see Figure 3.13), with the shock waves, and the intrinsic three-dimensionality of the bluff body geometry and hence the vortex structure introduce additional complexity to the wake-like flowfield. For instance, vortex shedding initiated in the recirculation bubble, i.e. the periodic shift of relatively dominating role of the vortex in one angular section, and oscillation of the entire flow in general are much less pronounced than in typical low-Reynolds-number modes, which is attributable to the high flow velocity and the stabilization of underexpanded potential core enclosing the recirculation zone with shock waves. The result is that the recirculation zone mostly maintains its ellipsoidal shape with mere internal vortex dynamics, and that the jet stem is not segmented into the usual discontinuous appearance of a von Kármán vortex street.

It is therefore obvious that the development and structures of a hollow cone jet is fundamentally different from a circular jet. While both being underexpanded, the standing shock of a circular jet stabilizes the jet core to a sizable distance before the entire jet becomes highly unsteady, and a hollow cone jet features unsteadiness up from the poppet valve face. And in addition to the Kelvin-Helmholtz and Taylor-Görtler type instabilities in the mixing layer and shock-related Richtmyer-Meshkov type instability that underlie non-linear behaviors of underexpanded jet in general, hollow cone jet is subjected to mean-flow large-scale vortex shedding that interacts

with those instability mechanisms, especially the Kelvin-Helmholtz type [441], and alters the overall transition-to-turbulence and mixing characteristics. Accordingly, the peculiarities of outward-opening poppet valve injector are worth detailed study.

3.4.5 Mixing characteristics

The jet overall has a regular conical shape and the jet centerline coincides with the injector axis, despite the large-scale oscillation and turbulent mixing layers. The outward-opening injector design is therefore able to achieve the directionality and targeting profile equivalent to a circular nozzle, which is an important requirement of engine design parameter for air-fuel mixing and the purpose of fast jet collapsing.

Air entrainment characteristics associated with various regions of the gas jet is presented in Figure 3.15. The jet volume fraction denotes the volume of jet whose local mass fraction of helium, Y_{He}, is higher than a given threshold, normalized by the total volume of the open cylindrical chamber. The mass fraction thresholds of 0.001, 0.002 and 0.005 are commonly used in the literature to indicate boundary of the jet, which, as shown in Figure 3.15, slightly differ from one another in a linear way with mass fraction but feature the same general trend throughout the injection

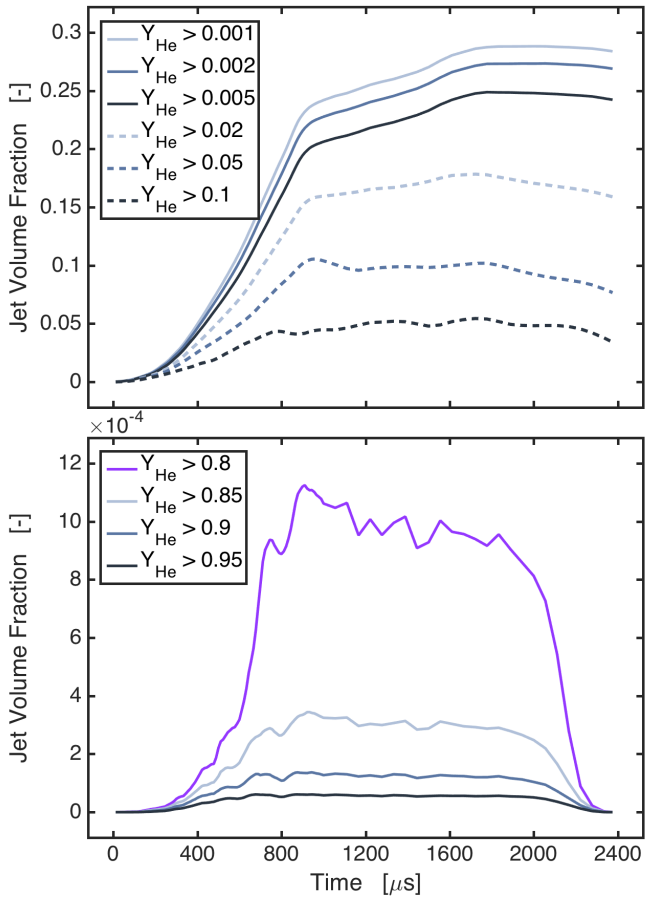

Figure 3.15 Volumes of the gas jet with different mass fraction of injected helium

process. The other higher mass fraction thresholds are adopted to visualize how the air entrainment levels evolve in a cascade of representative regions of the jet.

Three distinctive parts of the curves are recognizable. The first part corresponds to the injector opening transient in which volumes of all mass fractions increase as a concave function of time apparently different from the linear needle lift curve (see Figure 3.7). In particular, increases in the jet volumes are relatively slow during the first jet development stage of toroidal vortex ring formation, implying insignificant air entrainment capability of the small initial injector opening and the hollow cone formed by free propagation of the underexpanded jet. The jet volumes then grow at an increasing rate subsequent to the vortex ring collapse and the recirculation zone establishment, owing to the combined effects of linear enlargement of nozzle flow area and large-scale air entrainment enhancement by flow recirculation and vortex shedding in addition to turbulent mixing within the outer jet boundary.

The volume fraction curves bend at the end of the first part, and the second part spans from about 800 to 2000 μs, corresponding to the injector steady state. In this part however, the curves differ not only in absolute values as in the first part but in trend. Specifically, the entire jet volume identified by $Y_{He} > 0.001$, 0.002 and 0.005 continues to rise linearly, less rapidly than in the first part. The lowered growth rate is attributed to the fact that, firstly, one of the promoting effects owing to enlarging flow area ceases to exist, and secondly, the jet reaches the opposite boundary of the computational domain at around 1000 μs (see Figure 3.10) and thus the jet volume is no longer counted entirely. For the latter reason, the computed overall jet volume becomes constant from 1700 μs onwards, which is consistent with the observation in previous experimental and numerical results that the jet boundary attains a quasi-steady conical shape after the head vortex ring advances beyond the domain. For higher mass fractions, the curves remain nearly constant throughout the second part, indicating that the high-mass-fraction portion of the jet is in a mixing equilibrium and does not grow with jet penetration as the injection proceeds. Furthermore, the curves in this part bear fluctuations of varying degrees. The volume fluctuation is limited for $Y_{He} > 0.95$ and 0.9 that are likely associated with the standing potential core of the underexpanded jet. And the fluctuation is the maximum for $Y_{He} > 0.8$, for which the high-mass-fraction mixture involved in the periodic vortex shed from the recirculation zone appears to be responsible. Fluctuations due to local unsteady structures of vortex shedding contribute collectively to the overall mixing process whose volumes (for $Y_{He} > 0.1$ and other lower values) in turn remain decreasingly fluctuating.

The fact that only mixtures of relatively low mass fractions grow in volume and that the growth rate is limited, especially during the principal steady-state operation, suggests that additional assistance to the mixing process (e.g. by means of ambient fluid flow or jet impingement) would be necessary in order to achieve an adequate mixing rate for fuel injection applications.

3.4.6 Jet unsteadiness and asymmetry

The high flow unsteadiness of both the outer mixing layer and the inner jet core of a hollow cone jet constitutes a problem with the approximate assumption of flow symmetry, notwithstanding the apparent axisymmetry of numerical and geometric boundary conditions. In particular, even if RANS modeling numerically cancels out instantaneous turbulence-induced fluctuations, the aforementioned jet unsteadiness due to vortex shedding is a mean-flow variation and the resultant coherent flowfield oscillations are intrinsically three-dimensional. Artificially treating the flowfield as being symmetric is likely to introduce significant inaccuracy.

The asymmetry problem is demonstrated in Figure 3.16 by showcasing Mach number contours in the horizontal plane (xy-plane) at some representative positions along the vertical z-axis. Figure 3.16 (a) and (b) compare numerical results obtained with a full and a half computational grid at two time instants. It is observed that the core flow and surrounding mixing layers of the jet predicted by the full model vary in a non-axisymmetric way. And the incapability of the half model to accommodate the oscillatory displacement and deformation in the direction normal to the assumed symmetry interface of the jet is obvious. In fact, the symmetry boundary condition, i.e. null velocity component in the normal direction, acts like a slip wall when the flowfield is not symmetric about it. Similar problem with a quarter model and two symmetry interfaces is shown in Figure 3.16 (c) and (d) wherein the jet appears to spread over the two orthogonal "slip walls". Since the asymmetry problem is related to the mean-flow unsteadiness, no obvious difference in the predicted recirculation zone close to the injector tip (e.g. z = -5 mm, see Figure 3.16 (e)) occurs as the near-wake flow is bounded by the annularly distributed standing shock structures.

Therefore, in addition to the intrinsic three-dimensionality of turbulence, the coherent three-dimensional mean-flow unsteadiness of vortex shedding has also to be considered to improve the accuracy in predicting hollow cone jets.

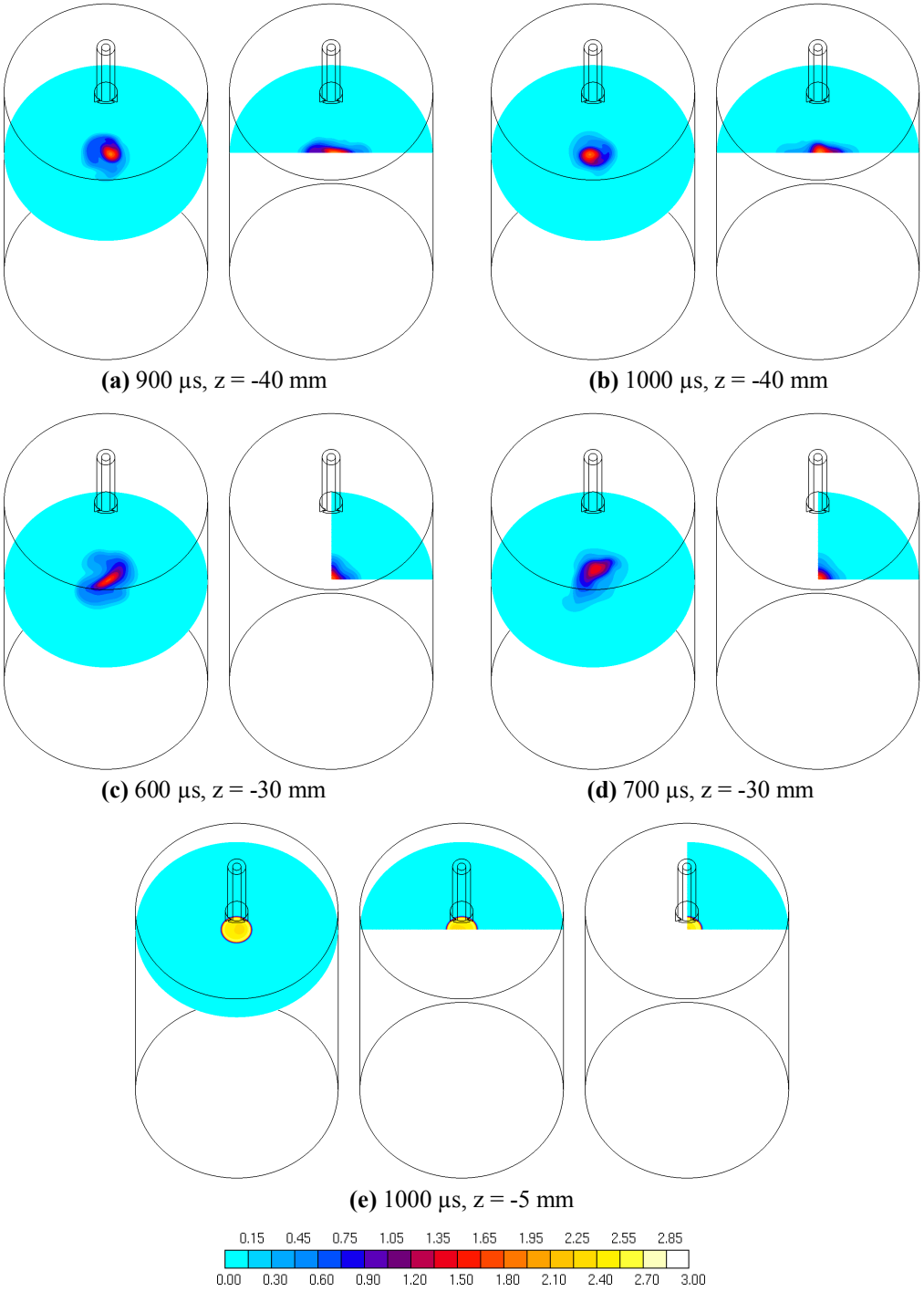

(a) 900 µs, z = -40 mm

(b) 1000 µs, z = -40 mm

(c) 600 µs, z = -30 mm

(d) 700 µs, z = -30 mm

(e) 1000 µs, z = -5 mm

Figure 3.16 Mach number contours in horizontal planes obtained with a full, a half and a quarter computational grid

Chapter 4

DISI Natural Gas Engine

Who looks outside, dreams;
Who looks inside, awakes.

— Carl Gustav Jung

4.1 Background

In this chapter, the work related to an experimental and numerical analysis of combustion chamber design and fuel injector implementation of a DISI natural gas engine is presented. Specifically, the overall mixture formation process is inspected experimentally through planar laser-induced fluorescence (LIF) in a single-cylinder optical engine, and the corresponding combustion data are collected. Further details on gas injection, interaction thereof with charge motion and geometrical bounding walls, the resultant air-fuel mixing process, and mixture homogeneity are provided by three-dimensional CFD simulations with the developed moving injector model. Finally, performance of the investigated combustion system is optimized by bench-testing a multi-cylinder prototype engine with reference to a target GDI engine.

Currently, the vast majority of on-road CNG vehicles, especially the LDVs, are powered by bi-fuel engines originally designed to run on gasoline wherein the CNG mode consists in the inclusion of a natural gas PI system. Whereas the usual choice of retaining gasoline compatibility is mainly attributable to the insufficiency of gas refueling infrastructure, the CNG operating mode of bi-fuel engines is subjected to perceivable compromise on engine parameters and thereby performance compared with CNG-optimized counterparts. To fully exploit the benefits of CNG fueling, a number of researches focusing on combustion system, catalytic aftertreatment, gas extraction facility, transport network and onboard gas storage have been promoted on a global scale. The overall objective of the present work is to develop a mono-fuel downsized turbocharged CNG engine, equipped with advanced variable valve actuation (VVA) MultiAir system and direct gas injector, which is able to comply with post-Euro VI emission regulations and post-2020 CO_2 emission targets taking into account new homologation driving cycles and real-world driving conditions.

On the basis of the promising physicochemical properties of natural gas as an alternative fuel mainly in terms of vehicular emissions and knock resistance, DI that has been routinely employed in gasoline SI engines [82][442][443] can be utilized to further improve efficiency and power performance of CNG-fueled engines [444][445][446][447]. PI is currently the predominant fueling method for CNG engines wherein the injected gaseous fuel displaces a portion of air otherwise available for combustion, thus diminishing the effective charge energy content. Adopting DI can

therefore bring forth the benefit of volumetric efficiency and hence proportionally engine torque and power density [32][44][444][448][449]. Moreover, without the premixed intake charge, DI engines have the flexibility of injection timing and may thus take advantage of more effective clearance-volume scavenging through valve overlapping, resulting in further increase in volumetric efficiency and optimization of compressor working point especially at low engine speeds. Directly injected gas jet, in addition, shows potential for speeding up combustion process and extending lean-burn operation limits by enhancing the turbulence level [203][374][449][450]. Direct gas injection, despite the advantages, poses a critical challenge to obtaining adequate control of air-fuel mixing for the development of natural gas combustion systems, mainly due to the fuel being constantly in gaseous state with relatively low density and hence momentum than liquid [321][374][451][452]. However, mixture quality has well-known crucial influences on the ignition reliability and combustion stability, and hence on fuel oxidation rate, energy release efficiency and formation of pollutant emissions.

In pursuit of establishing guidelines pertaining to the challenge of DI for CNG engine applications, many researches, both experimental and numerical, have been undertaken. In particular, the spatial and temporal mixing characteristics are the key factor in DI engines and determined primarily by injector parameters such as nozzle type, internal geometry, supply pressure and protrusion [375][378][379][381]. The effect of medium-range rail pressure on CNG engine performance has been studied in [453]. It was argued that higher rail pressure led to better engine performance at lower engine speed due to the predominant effect of volumetric efficiency whereas lower rail pressure (hence longer injection event) was preferable at higher speed as air-fuel mixing rate was the limiting factor. The dependence of jet penetration and mixture distribution on gas species and jet underexpansion level has been examined through numerical modeling of methane and nitrogen jets in a cylindrical chamber, suggesting optimization specific to fuel and pressure ratio [385]. An experimental study of the influence of injection timing on combustion characteristics and engine performance has been conducted at a given engine speed with fixed ignition timing and fuel quantity in [450] whereby the drawbacks of over-retarded injection due to insufficient mixing time and the existence of optimum timing at that specific speed in terms of both burning rate and HC emission were verified. Likewise, the need to advance injection timing with increasing engine speed for adequate mixing time has been stressed by an experimental investigation on a stoichiometric single-cylinder CNG engine at various engine speeds [454]. The effects of injector type, injection timing and pressure on mixture formation inside a constant-volume chamber and an engine sector have been numerically investigated in [320]. The results suggested that injection timing had considerable impact on mixing rate and the overall mixing mechanism was highly case-dependent. A DI CNG engine, converted from a diesel core and operating with homogeneous stoichiometric combustion, has been studied experimentally and numerically in [321], wherein the late injection with late spark

timing was found to increase both volumetric efficiency and burning rate compared to PI engine. A comparative study of PI and DI CNG engine performance [203] has shown that early DI before IVC interfered with intake air quantity in a way similar to PI, and the advantages of DI in volumetric efficiency and torque were noticeable for injection timing near or after IVC with the accompanying increase in turbulence level and in resultant combustion rate and efficiency. The beneficial effects of late injection timings after IVC on supporting early flame development and shortening overall combustion duration have been experimentally verified in DI CNG engines with side [374] and centrally mounted [449] injector, which were based potentially on case-specific mechanism of transferring jet kinetic energy to turbulence kinetic energy and improved especially low-speed high-load performance.

It has been experimentally revealed that, whereas retarding the injection event often resulted in increased combustion speed regardless of engine load, the mixture homogeneity might deteriorate for late DI due to limited mixing time and distance [205]. The generically problematic air-fuel mixing process of late injection during compression stroke has also been observed for partially stratified operation at low-to-medium loads in DISI CNG engines [455][456][457] in that the turbulence level augmented by late injection stabilized combustion but the mixing rate to eliminate local rich mixtures was critical. The difficulty in achieving proper mixing with late injections [445] has experimentally proven to be the source of high CoV in IMEP and diffusion soot-forming burn in fuel-rich regions by emission spectrum analysis and soot luminescence in an optical engine [458].

Moreover, the process and underlying mechanism of air-fuel mixing inside an engine involve complicated interaction between the underexpanded gas jet and in-cylinder fluid flow, combustion chamber geometry and other engine variables (e.g. piston speed and valve actuation). Therefore, it is important to place injection study into the perspective of the dynamic engine environment, in addition to stand-alone gas jet characterizations. The necessity of matching combustion chamber geometry, injection timing, injector type and location for combustion system optimization has been emphasized by a numerical study of mixture preparation in a CNG engine for different piston bowls, cylinder head shapes and hole configurations of a centrally mounted injector [332]. The mixing process resulting from the interaction between tumble motion with possible intake backflow, injector configuration with potential angle-dependent occurrence of the Coandă effect, injection timing and gas jet has been investigated in [375][459] to understand the problematic phenomena. The jet evolution at different pressures has been visualized by PLIF in [349], implying that pulsed short injection events and large variation in in-cylinder backpressure would make the injection process highly dynamic and complicated in DI engines. And the corresponding prospect of injection pressure optimization relative to timings, with proper hardware support, has been proposed in [205]. The dominant importance of speeding up combustion at low engine speed with late injection and of guaranteeing mixing time for homogeneity at high engine speed with advanced injection has been

identified for the design of DI engine parameters [450][454].

Apart from SI engines, DI of natural gas is implemented in and have significant impacts on other combustion systems. Dual-fuel (or RCCI) engines with diffusion flame of pilot diesel and premixed, fully or partially, flame of natural gas has shown efficiency close to diesel engines [460]. Given the recent development of integrated high-pressure diesel-gas injector, direct sequential injection of diesel and CNG has witnessed widespread applications wherein the available mixture formation time is largely curtailed and air-fuel mixing plays a vital role in combustion optimization [461][462][463][464]. For instance, PM emissions have proven a challenge to dual-fuel engines with DI of the low-reactivity fuel [465][466], as a result of diffusion burn of fuel-rich pockets [467] of both diesel and natural gas. And the combustion of natural gas in the diesel spray zone constitutes particular difficulties in providing reliable ignition for the entire natural gas mixture at low loads and in avoiding both diesel knock and end-gas SI knock at high loads, of which mixture formation of the directly injected gas is a crucial factor. Another application of natural gas DI is hot surface-assisted CI, wherein the injection timing and duration-dependent presence of premixed and mixing-controlled combustion of natural gas entails insights into the air-fuel mixing characteristics [468][469]. The dual-fuel SI combustion system with port-injected gasoline and direct-injected natural gas, as a measure to combine the flame speed, knock resistance and energy density benefits of both fuels, requires injection and mixing controls similar to mono-fuel CNG engines [470][471]. Gas injection and in-cylinder mixture formation are important aspects to be investigated in DI engines running on other alternative gaseous fuels such as hydrogen-enriched CNG [190][472] and hydrogen [473][474].

Therefore, the study of direct gas injection and resultant air-fuel mixing within the dynamic flow environment bears broad scope for a multitude of engine-related applications. And despite the available researches, in-depth understanding of these processes in CNG engines remains scarce in the literature. The present study hence seeks to provide a detailed fluid-dynamic characterization of the mixture formation from the perspective of a DISI CNG engine by experimental and numerical means. Furthermore, as optimum combustion process results from the combinative effects of various operating parameters, the current work aims to shed light on combustion system development as a whole by thoroughly investigating the interaction between gas injection, coherent charge motion and combustion chamber geometry at several engine speeds and loads.

4.2 Engine configuration

The studied engine is derived from a 1.4-litre four-cylinder GDI engine block and dedicated to CNG fueling with the homogeneous stoichiometric SI combustion

system that permits the use of three-way catalytic converter to efficiently meet the Euro VI emission regulations. The main engine parameters are presented in Table 4.1. The small engine displacement, together with turbocharged intercooled intake, allows considerable downsizing for increases in efficiency and power density. The MultiAir VVA system is introduced to de-throttle the engine and perform cylinder scavenging when necessary. Moreover, the specific intake valve lift profile at each operating point is optimized to support the turbocharger with sufficient engine flow to deliver requested boost, and to improve the compressor working point and hence its efficiency.

Another important feature is the engine architecture of high structural strength able to sustain high combustion peak pressures (up to 150 bar for a limited period), in order to fully exploit the knock resistance of natural gas. Being considerably less prone to knocking, CNG engines relax the constraint of delaying the spark advance (SA) from the maximum-brake-torque timing practiced in gasoline engines, and in general adopt more advanced SA that leads to decreased specific fuel consumption. In addition to SA optimization, the robust engine structure accommodates margins for increase in CR, hence further improving thermal efficiency and performance by favoring peak pressures for rated torque and power. Accordingly, the piston design

Table 4.1
Prototype DISI natural gas engine specifications

	Item	Unit	Value
General Info.	Engine	–	SI CNG
	Cylinder	–	Four-in-line
	Cylinder head	–	Pent-roof
	Air induction	–	Turbocharge, intercooler
	Turbocharger	–	Wastegate controlled
Perform.	Maximum torque	Nm	250 (at 1500 rpm)
	Maximum BMEP	bar	22.96
	Rated power	kW	103 (at 5000 rpm)
	Rated BMEP	bar	18.07
Crank Train	Bore	mm	72
	Stroke	mm	84
	Connecting rod	mm	128
	Displacement	cm^3	1368
	Compression ratio	–	13:1
Valve Train	Valves per cylinder	–	4
	Valve train intake	–	FIAT MultiAir VVA
	Valve train exhaust	–	Fixed camshaft
Fuel Inject.	Injection system	–	Direct injection
	Fuel rail pressure	bar	6 – 16 (16 used herein)
	Injector type	–	Outward-opening
	Hole diameter	mm	6.5

is modified to raise the CR from the GDI baseline 9:1 to 13:1, a suitable value for knock-free operations with a reasonable trade-off between efficiency benefits and emission penalties [475].

With respect to DI, the gas injector with outward-opening poppet valve is side-mounted rather than positioned in the center. From the perspective of cylinder head design, side-positioning minimizes interference of the injector housing with valves and spark plug, thereby simplifying component arrangement and more importantly enhancing mechanical strength of the combustion chamber. Furthermore, without severe impact on structural integrity, a relatively large injector tip that is generally required for sufficient volume flow rate of gaseous fuels can be feasibly integrated in the side position.

The pent-roof shaped cylinder head, including the side-mounted injector niche between the intake valves and the centrally mounted spark plug, and the redesigned piston, featuring a reduced shallow bowl for CR increase, are schematically shown in Figure 4.1. The objective is to achieve the performance equivalent to the boosted baseline GDI engine with the same displacement. Furthermore, an improvement in fuel economy by 20% is expected in comparison with the FIAT in-production PISI CNG engine that has been installed on B-segment natural gas vehicles since 2014. And upon the completion of calibration on the prototype engine, demo vehicles will be available for comprehensive assessment.

4.3 PLIF Experiment

The in-cylinder mixture formation process is experimentally investigated in an optically accessible single-cylinder engine by means of PLIF. Non-intrusive in-situ diagnostic techniques with high spatial and temporal resolutions are widely applied to the study of engine-related physical and chemical processes. LIF in particular is an informative way of remotely detecting gas-phase transport phenomena without the insertion of interfering probes, and has several advantages. First, fluorescence

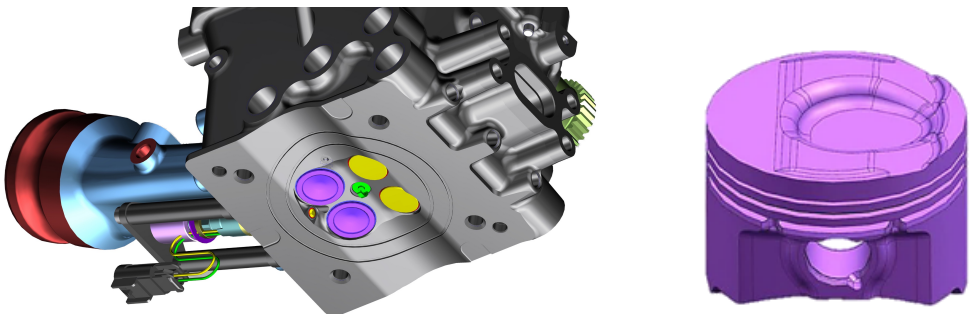

(a) cylinder head (intake on the lefthand side) **(b)** piston

Figure 4.1 Combustion chamber geometry of the developed DISI CNG engine

induction is typically faster than the time scale of turbulent mixing and thus freezes the to-be-observed transient motion. Second, a given chemical species in a specific quantum state can be selectively excited by wavelength tuned to the corresponding absorption spectrum not overlapping with the others in the same system. Third, LIF signal is observed against dark background, providing high signal-to-noise ratio and sensitivity. Fourth, LIF affords excellent detection efficiency and is able to detect minute amount of species down to nanomolar concentration levels (in the order of 10^2 atoms/cm^3 [476]). The use of planar light sheets for excitation, hence PLIF, is a constructive method for tomographic representation of three-dimensional field of species concentration and therefore offers a detailed interior perspective. PLIF has been implemented to analyze underexpanded gaseous fuel jets in constant-volume pressure chamber for nearfield shock structures such as barrel shock and Mach disk [349][477] and for farfield macroscopic air-entrainment behaviors and morphology [318][374][375][380][382][478][479], and to study mixture formation process for the application of DI gas engines fueled with hydrogen [322][459][480][481][482] [483] or with CNG [324][360][455][484].

4.3.1 Fundamentals of LIF photophysics

LIF is a spectroscopic technique that involves the excitation of target molecule to a higher electronic energy level populated by selective absorption of a photon in the laser pulse followed, in a few nanoseconds, by the subsequent spontaneous de-excitation through the emission of another photon with longer wavelength forming a red-shifted electromagnetic radiation, i.e. the fluorescence [485][486][487][488]. "Fluorescence" denotes such phenomenon of light wavelength shift, a term coined analogously from opalescence by Irish physicist Sir George Stokes to describe the change over light spectrum from absorbed invisible ultraviolet to re-emitted visible blue by fluorite (mineral calcium fluoride, CaF_2) [489]. The absorption wavelength to excite a molecule usually increases with the size of its fluorophore, i.e. the active part of the compound responsible for fluorescence, analogous to chromophore for color. Therefore, providing the incident exciting light by laser is preferable for its unique wavelength tunability, capable of delivering large amount of energy within extraordinarily narrow spectral range, and directionality. Excimer lasers, the pulsed lasers with well-characterized ultraviolet wavelengths and high pulse repetition, are typically utilized for LIF experiments. Fundamental knowledge of the underlying photophysics facilitates interpretation of measured LIF signal intensity.

Two opposite processes, namely excitation and de-excitation (or relaxation), are involved in LIF. An orbital electron, upon the absorption of a photon in a certain spectral range, transitions from its ground-state orbital to another orbital according to the selection rules that are determined by electronic wavefunction configuration (symmetry and spatial overlap), magnetic dipole moment and angular momentum of the participating molecular orbitals, and interaction thereof with intra-molecular vibration. The absorbing fluorescent molecule is thus excited to a higher electronic

energy state above thermal equilibrium.

The electronic energy state of a molecule is associated with the total spin of its constituent electrons. Electronically neutral organic molecules for LIF applications typically have covalent-bound electrons and thereby closed shells. The ground state corresponds to total spin $S = 0$, i.e. each electron (with half-integer spin $S = 1/2$) is paired with an anti-parallel spin electron occupying the highest bonding π, σ or non-bonding neutral n orbitals. Upon excitation, a single electron transitions to the lowest unoccupied anti-bonding π^* or σ^* orbitals, and the participating orbitals in the transition (π-to-π^*, n-to-π^*, n-to-σ^* or σ-to-σ^*) depends on the selection rules and specific electronic configurations. At excited state, the two resultant unpaired electrons are allowed to be either parallel (total spin $S = 0$) or anti-parallel ($S = 1$) and, according to the spin multiplicity, the two states are classified as singlet (S) or triplet (T) respectively. Therefore, S_0 denotes the (singlet) ground state, T_1 the first excited triplet state, S_1 the first excited singlet state and S_2 the second excited singlet state, with increasing energy. At the same excitation level, e.g. T_1 and S_1, triplet is systematically lower in energy than singlet, based on Hund's rule of maximum spin multiplicity. The excitation transition usually occurs between S_0 and higher singlet states, since S-T transition is theoretically spin-forbidden for orthogonal electronic wavefunctions (no spatial overlap) and the enabling mechanism involving orbital angular momentum is weak for LIF-relevant organic molecules.

Population of electronically excited states is temporary, and within an interval of a few nanoseconds to microseconds, the excited molecule relaxes by a variety of competing pathways, radiative and non-radiative [488][490], that are summarized by the Jabłoński diagram and schematically presented in Figure 4.2. The vibrational ground states of each electronic energy state are indicated with thick horizontal iso-energy lines, and higher vibrationally excited states with thinner lines. Transitions are indicated with differently colored arrows, horizontal for nil total energy change and vertical otherwise.

Radiative relaxation processes consist in the spontaneous photon re-emissions which are particular forms of photoluminescence, and, as the opposite process of photoexcitation, have to satisfy the same selection rules. The spontaneous radiative emission leading to the S_1-S_0 transition is fluorescence and depopulates the excited state within an effective lifetime of 1-100 ns. The spin-forbidden spontaneous T_1-S_0 transition, the phosphorescence, occurs on a typical timescale of milliseconds, several orders of magnitude longer than fluorescence, and is therefore insignificant for LIF signal detection. Electronic transitions of non-radiative relaxations involve intra-molecular vibrational (and rotational for gas-phase systems) energy transfer. Specifically, the non-radiative process is termed intersystem crossing (ISC) in the case of transition between energy states with different spin multiplicity, and internal conversion (IC) in the case of the same multiplicity. ISC and IC are both constant-energy vibronic transitions, i.e. a transition involving simultaneous changes in the electronic (redistribution of electron) and vibrational (nuclear motion) energy states

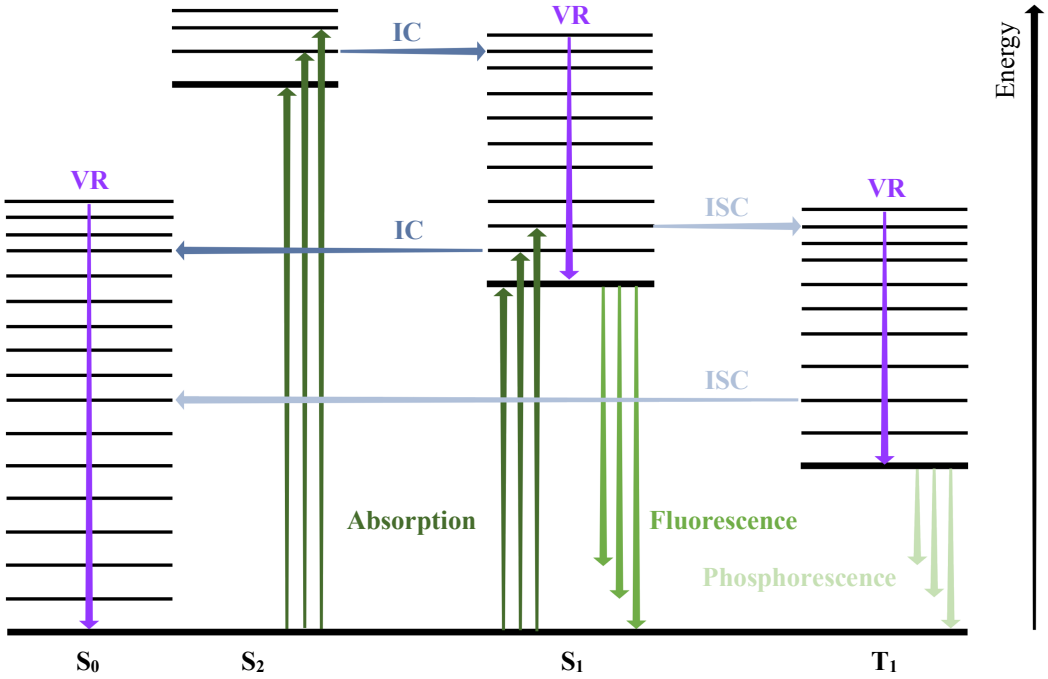

Figure 4.2 Jabłoński diagram of the LIF photophysical processes of excitation and relaxation of organic molecules in the ground state and three excited electronic states
IC – internal conversion, ISC – intersystem crossing, VR – vibrational relaxation

of the molecule whereas the total energy is conserved. The relative significance of non-radiative relaxations to fluorescence is anchored in quantum mechanics by the Franck-Codon principle [491] stating that the transition is most probable when the vibrational wavefunction of the final upper vibronic state most resembles the bell-shaped gaussian of the vibrational ground state of the initial lower electronic state. The probability is quantified by the overall electric dipole transition moment which increases with the overlap of the vibrational wavefunctions of the two participating vibrational states in their respective electronic states, the Franck-Codon factor. In general, the overlap is greater between two vibronic states closer in energy, and the energy spacing in turn decreases with energy level for most organic molecules (see Figure 4.2). Non-radiative ISC and IC decay between excited states are therefore preferred to radiative relaxation between the electronic ground and excited states.

Inter-molecular energy transfers through collision with surrounding molecules in addition contribute to the non-radiative de-excitation, which are further divided into two types, i.e. vibrational relaxation through non-quenching collisions (VR) and collisional quenching. The excited molecule during VR intensifies vibration of colliding molecules at the expense of its own excess energy. The Franck-Condon principle is appropriately extended from its canonical form applicable to vibrational state changes in the course of an electronic state change to inter-molecular VR. The usually clustered vibrationally excited states accordingly allow fast VR towards the vibrational ground state of each electronically excited state (hence non-quenching, see Figure 4.2). In general, a range of vibrationally excited states of upper electronic

states are temporarily populated upon absorbing photons. Molecules in these upper excited vibronic states, with considerable wavefunction overlap, rapidly relax to the lowest vibrational state of the lowest electronic state through a combination of IC, ISC and VR prior to the onset of corresponding radiative emissions. As a result of the subsequent much greater energy gaps back to the ground state, both IC and ISC are inefficient. Fluorescence is hence kinetically competitive with the non-radiative pathways and the partially de-excited molecules start to fluoresce. The observable outcome is that fluorescence is expected in appreciable yield exclusively from the lowest excited state (i.e. S_1-S_0 transition for most organic molecules, Kasha's rule), or, equivalently, that the yield and wavelength of a generic photoluminescence are independent of the excitation wavelength (Vavilov's rule) [492].

Non-radiative inter-molecular decay through collisional quenching depopulates the excited states specifically by three dynamic mechanisms. The first is the Förster resonance [493] due to electronic dipole-dipole interaction. Dipole oscillation of an excited molecule induces oscillation in the ground-state colliding molecule without direct physical contact. This mechanism thereby enables electronic energy transfer over the distance of several molecule diameters and obeys the selection rules. The second mechanism of short-range electronic energy transfer is the Dexter electron exchange [494] between the colliding pair, relying on direct contact and the spatial overlap of molecular orbitals. Those two mechanisms are frequent and important in liquids and solids. The third mechanism is quenching by molecular oxygen that is common in gas-phase systems containing air. Oxygen molecule, or dioxygen, has a pair of fully-filled π and half-filled π^* molecular orbitals, leading to an electronic configuration with two unpaired electrons in the half-filled anti-bonding π^* orbital of equal energy [495] and hence a triplet electronic ground state. The unusual triplet ground state of oxygen facilitates the formation of intermediate triplet exciplex, i.e. excited-state complex, with the organic molecule that has closed valence shell and is in the first excited singlet state, through partial charge transfer and spin-pairing. This process is allowed if the S_1-T_1 energy gap of the organic molecule exceeds the energy required to induce T_0-S_1 excitation in oxygen [496]. The exciplex exists as a transition state and dissociates to produce the organic molecule in a triplet state. The presence of molecular oxygen may significantly promote the otherwise spin-forbidden ISC and be therefore efficient at quenching fluorescence, depending on electronic energy states of the organic molecule.

The various non-radiative relaxation pathways often occur on similar timescale and dynamically reduce the fraction, termed fluorescence quantum yield, of excited organic molecules that actually fluoresce. In particular, ISC, IC and VR all involve transferring part of the absorbed photon-energy to vibrational energy, essentially dissipating the excess energy to heat. Those thermal-decay processes are therefore responsible for the loss of photon energy and the resultant red-shift of the emission spectrum since the effective fluorescing state is mostly the vibrational ground state of S_1, which is figuratively represented by the lengths of the differently green-toned

vertical arrows in Figure 4.2. Moreover, the fluorescence quantum yield is affected by local oxygen concentration due to oxygen quenching, and such dependence can be exploited to probe more constructive information on air-to-fuel ratio rather than fuel concentration for engine diagnostics.

The LIF signal of a specific organic species excited by a given laser wavelength is governed by the absorption cross-section and fluorescence quantum yield which in turn depend in its own characteristic way on temperature and pressure [497][498][499][500][501][502][503]. The absorption cross-section is temperature-dependent and increases with temperature since higher vibrational energy, and corresponding quantum states, relaxes the selection rules. The fluorescence quantum yield on the contrary decreases with increasing temperature that raises the vibrational excitation levels and, according to the Franck-Condon principle of wavefunction overlap, the transition probability of competing rapid ISC de-excitation. The dependence of LIF quantum yield on pressure is case-specific. In general, inter-molecular collisions, quenching or non-quenching, intensify with pressure. Furthermore, relaxing excited molecules fully to vibrational ground state through VR in gas-phase systems occurs on a longer timescale than fluorescence and is usually incomplete. For species on which oxygen quenching has negligible influences due to small S_1-T_1 energy gap, increasing pressure facilitates the population of lower vibrational states within the lowest excited electronic state, favoring fluorescence lifetime and thereby quantum yield. For species highly susceptible to collisional quenching with oxygen, detected LIF signal is significantly attenuated by increase in oxygen (or air) partial pressure. In engine diagnostics applications, temperature and pressure inside the combustion chamber vary in a constant and coupled way, and hence variations in the measured LIF signals arise from more than the to-be-observed inhomogeneous distribution of fluorescing species [504][505][506][507][508][509][510]. Additionally, excitation wavelength determines photon energy and thus the initial vibronic states populated by absorption, which in turn define the transition probability, relative importance, and thermodynamic dependence of each relaxation pathway. To reduce systematic variability, a definite and consistent laser illumination is of practical preference.

In order to investigate fuel distribution in a clear and controlled way, preferably a single species in the system fluoresces. The common practice is to uniformly seed a well-characterized fluorescing species, termed tracer, to the non-fluorescing fuel within the feasible spectral range. Polyatomic organic molecules are typically used as tracers, due to their chemical similarity with hydrocarbon fuels and high density of vibronic states leading to broad-band absorption spectra accessible to standard laser wavelengths. The adoption of a specific tracer relies on physical compatibility with the fuel, mainly the volatility (or boiling point) that are then determined by the molecular weight and configuration. A variety of organic species are chosen as LIF tracers for fuels. Single-ring aromatics such as toluene and 1,2,4-trimethylbenzene (TMB) have been selected to match the heavy components in gasoline [511][512]. For gaseous fuels (natural gas and hydrogen), lightweight chromophore-containing

aliphatic ketones, diketones and amines such as acetone [318][322][349][382][459][477][478][482][484], biacetyl [479], triethylamine (TEA) [360][455][480][513] and trimethylamine (TMA) [481][483][514] have been routinely used. On the basis of the selected tracer and laser wavelength, characterization of the varying imaged LIF signal, as a consequence of each individual temperature-pressure combination, may differ from engine to engine, from operating point to operating point, and from crank angle to crank angle. The signal intensity is moreover quantitatively affected by constant features including laser energy, optical transparency, and electric signal conversion and amplification.

4.3.2 Experimental setup

A single-cylinder optical version of the full engine under study is built with the same combustion chamber and port design, except for substituting the metallic liner (along with the water jacket and external block) with a transparent fused-silica one for lateral optical accessibility. The cylindrical liner is thus constantly exposed to the exterior and uncooled, imposing constraints on the experimental procedure in that the engine can be fired continuously for a limited number of cycles especially at high loads. For this reason, combustion is enabled for about 200 cycles of which the last 50 are measured to ensure that the measurements correspond to steady-state operations. Due to differences in thermal conductivity and cooling environment, liner temperature, on the one hand, inevitably differs from that of the multi-cylinder engine, and, on the other hand, fluctuates more with in-cylinder fluid temperature (hence the investigated engine load). In addition, the glass liner and sealing thereof with the cylinder head can sustain a maximum pressure of 70 bar for which ignition has to be delayed to decrease peak firing pressure for high-load points. Despite that temperature boundary and combustion behavior may not be fully comparable with the full engine, the effect of injection at a given operating point is still meaningful.

A double-sided PLIF is implemented wherein, via an optical system of mirrors and lenses, a krypton fluoride (KrF) excimer laser beam with a wavelength of 248 nm is reshaped and evenly split into two planar light sheets that are coupled into the same vertical symmetry plane of the combustion chamber from two opposite sides through the liner. Such optical arrangement enhances coverage of illumination over the target plane, especially corners otherwise inaccessible from one side. The setup of the optical engine and some components is presented in Figure 4.3.

The optical engine is fueled with TMA-doped methane for tracer-LIF detection of the air-fuel mixing process. Owing to high fluorescence signal sensitivity, tracer seeding is normally restricted to a minute concentration (4000 ppm herein) within the non-perturbating level to avoid attenuation of the incident laser or fluorescence trapping [515]. TMA is deemed a suitable tracer for CNG-engine application [481][513]. Given that the standard boiling points of common gas-fuel tracer candidates, i.e. acetone, TEA and TMA, are about 56°C, 88-90°C and 3-7°C respectively, TMA

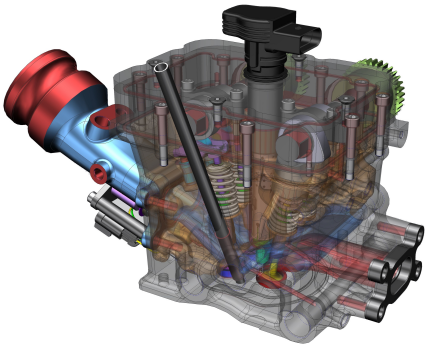

(a) cylinder head (same as multi-cylinder engine)

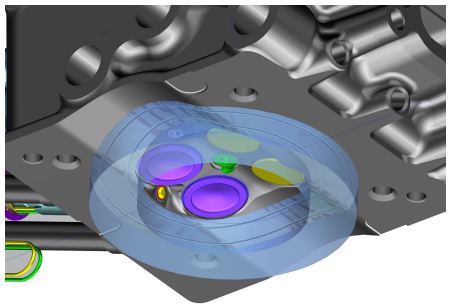

(b) fused-silica liner

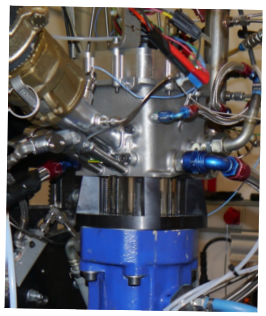

(c) single cylinder

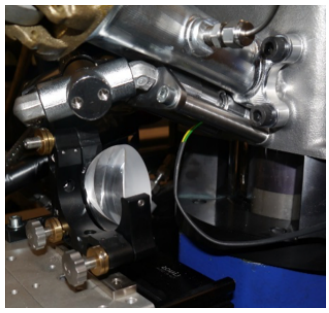

(d) final lens for laser sheet coupling (intake side)

Figure 4.3 PLIF experiment and optical engine setup (intake on the lefthand side)

is a gas at room temperature which obviates the need to seed with evaporator or hot stream and prevents tracer condensation (hence de-mixing) [479][480]. Moreover, the branched tertiary-amine structure of TMA molecules gives rise to high density of excited energy states and broad-band absorption spectrum compatible with KrF excimer 248-nm laser, the wavelength at which air and methane (as most saturated aliphatic hydrocarbons) have negligible absorption cross-section and thereby do not fluoresce. The subsequent red-shifted fluorescence at a wavelength of around 300 nm emitted from the tracer molecules residing in the laser-illuminated plane during laser pulse is imaged by a perpendicularly-placed intensified charge-coupled device (ICCD) camera with an intensifier quantum efficiency of 20% at 300 nm and an UV-compatible Micro Nikkor lens.

4.3.3 Image processing

LIF intensity is supposed to be directly associated with local fuel concentration and, being uniformly mixed together, the gaseous fuel concentration in the probed plane [488]. The acquired images are in a grayscale, representing the relative signal intensity that depends on signal intensification and analog-to-digital conversion of the camera sensor. TMA has well-characterized photophysical properties and, like TEA LIF signal, shows a linear correlation between the detected intensity scale and the mixture equivalence ratio at given pressure and temperature (i.e. at each engine crank angle) [360][481][513].

The thus-acquired raw images are however tracer-LIF response on which other noise and artificial distortions are superimposed. Additional processing is required to isolate the LIF intensity scale. At each imaged crank angle, a background image, i.e. no injection under otherwise the same engine conditions and laser illumination, is acquired in order to remove constant offset (e.g. background noise and scattered or leaked light). In addition, reference LIF images of homogeneous air-fuel mixture, realized by PI of the same TMA-doped fuel, are acquired at the same crank angles of interest. The raw LIF images are then corrected according to the expression

$$I_{CORR} = \frac{I_{RAW} - I_{BG}}{\left[\frac{I_{REF} - I_{BG}}{\frac{1}{w \cdot h}\sum\sum(I_{REF} - I_{BG})}\right]} \tag{71}$$

where w and h are the number of pixels in the image width and height respectively. The denominator is in fact the background-corrected reference image normalized by its mean, which gives a unit gain matrix to correct the LIF signal for nonuniform gains and nonlinear response of camera sensor, inhomogeneous laser illumination, and fluorescence reflection and refraction by the cylinder. Furthermore, considering intrinsic CCV of the highly unsteady turbulent jet, sensitivity of jet evolution to the CCV of in-cylinder backpressure due to compressibility effect, regular laser energy fluctuations and slight mixture inhomogeneity in the reference PI cases, 36 images are acquired for each of the three groups of images and the respective averages are substituted in Equation (71) to represent the ensemble-averaged engine cycle.

An example of the image processing procedure is presented in Figure 4.4. It is observed that fair variations in jet shape and mixture distribution exist between the two random instantaneous raw LIF images acquired in two cycles, and that the raw image averaged over 36 cycles reveals the coherent mean field. The dark lines, dim upper and lower regions, background light, and most of the reflections by the glass liner are corrected by the procedure. The remaining reflections of the illuminant jet are neither a constant nor a uniform feature, and hence cannot be corrected by either the background or the reference images. The thus-corrected image corresponds to a semi-quantitative representation in that the intensity grayscale correlates linearly with mixture equivalence ratio, with the brighter being richer in fuel and the darker

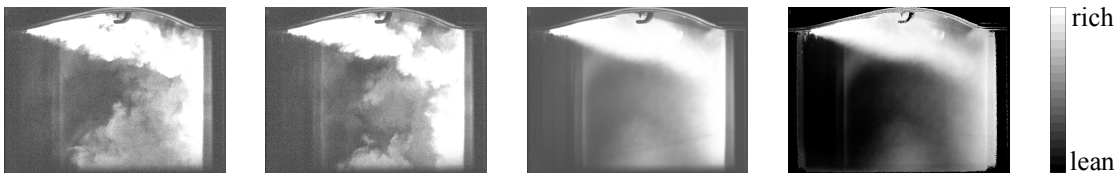

(a) raw image 1 **(b)** raw image 2 **(c)** averaged raw image **(d)** corrected image

Figure 4.4 PLIF image processing procedure (intake on the lefthand side)

leaner. The LIF-measured equivalence ratio field is subject to several uncertainties that alter the linear correlation. The instantaneous amount of electronically excited tracer molecules and the total LIF quantum yield are directly influenced by the shot-to-shot fluctuations in laser energy which, in the present work, are countered by an advanced laser energy monitor and further reduced by averaging over 36 measured cycles. The resultant fluctuation is estimated to be ~1%. Moreover, despite the fact that the crank-angle-resolved variations in in-cylinder pressure and temperature are taken into account by homogeneous reference LIF images, the nonuniform spatial distributions of pressure and temperature at each crank angle are a priori unknown and not corrected. The influences are, however, insignificant during the intake and compression strokes, except for the underexpanded fuel jet whose pronounced drop in pressure and temperature may be approximated by simplified theoretical means. Additional uncertainties of minor significance include nonuniform illumination and reflections, inhomogeneous reference mixture, and camera sensor noise. If a fully-quantitative interpretation is to be obtained, a set of homogeneous reference images with precisely defined equivalence ratios has to be repeated for each investigated crank angle in order to determine the linear correlation in absolute terms, which is not conducted in the present work. Nevertheless, for the same in-cylinder mixture composition, the semi-quantitative representation suffices to compare experimental and numerical results for the validation purpose.

4.4 Numerical modeling

A companion three-dimensional CFD analysis is undertaken in order to reveal further details about the gas injection and subsequent air-fuel mixing characteristics that are otherwise scarcely accessible to experimental methods.

For the purpose of investigating the target process in combination with the LIF visualization, the computational domain encompasses the same engine geometry as that in the experimental setup including the combustion chamber and ports extended up to the respective collecting manifolds. The finite-volume numerical model of the single-cylinder engine is developed in the commercial AVL FIRE (version 2014) environment, and, with the moving hexahedral grid, faithfully reproduces the valve and piston movement so as to enable the simulation of real four-stroke engine cycle. In particular, the previously developed moving injector model is embedded in the engine grid through an arbitrary connecting boundary, a mathematical treatment on the interface between two physically separate domains across which the cell-face fluxes are calculated by area-weighted averaging thus virtually allowing for domain continuation. The grid embedding feature is only implemented during the injection events, whereas the engine grid encompassing the whole internal volume, including that reserved for the injector model, is used otherwise. This strategy fulfils the grid resolution requirement for the gas injection and optimizes the overall computational costs. According to preliminary studies, little perturbation is introduced to the flow

across the arbitrary interface provided that cell sizes on the both sides are close. For this reason, and given the fact that the injector grid is much more refined than the engine grid, a gradual cell-size transition surrounding the arbitrary interface is built. Figure 4.5 presents an overview of the computational domain and three examples of the final engine grid used for the numerical investigation, in which inclusion and exclusion of the embedded injector model, depending on specific injection timing, are demonstrated.

The three-dimensional time-dependent turbulent flowfields are solved by the RANS approach together with the k-ζ-f formulation of the eddy-viscosity model for turbulence closure. Such numerical strategy is feasible for the complete engine-cycle simulation with moving grid and underexpanded gas injection, and requires a reasonable computational time. In addition, the k-ζ-f model with the hybrid near-wall treatment is suitable for applications with complex flow domain, by which the prerequisites for the wall-nearest grid position and grid uniformities can be relaxed while results in satisfactory agreement with experimental data are still obtainable. Moreover, due to the lack of cooling circuit and low thermal conductivity of fused silica (see Figure 4.3), all geometric boundaries are considered as adiabatic no-slip walls. Inflow-outflow boundary conditions with crank-angle-resolved pressure and temperature data are imposed on the intake, exhaust and injector inlet sections.

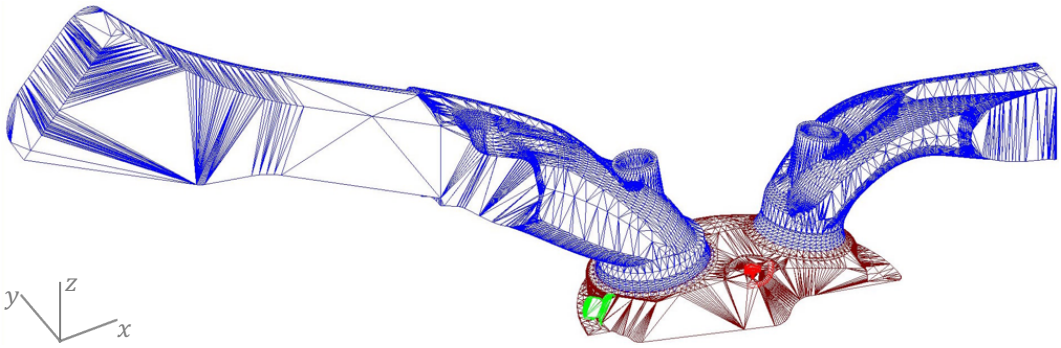

(a) overview of the computational domain

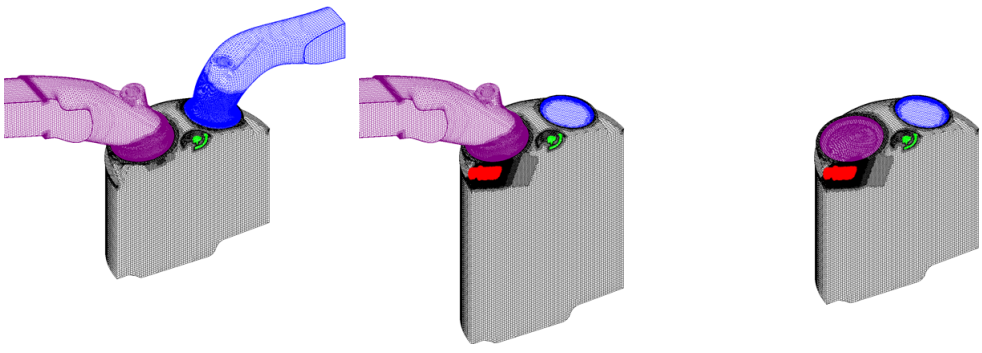

(b) valve overlap **(c)** intake stroke **(d)** compression stroke

Figure 4.5 Internal fluid volume geometry and examples of final computational grid at various stages of the engine cycle (a half of the engine model is shown, intake on the lefthand side)

4.5 Results and discussion

Experimental and numerical results pertaining to the CNG engine development in three aspects are presented and discussed in detail, including (1) implementation of the side-mounted direct gas injector wherein the considerations behind injector angle choice specific to gaseous fuels and the constraints on the injection operation are addressed; (2) a thorough analysis of the gas injection and mixing process for three representative operating points; (3) bench-test results of full-load performance optimization of the developed prototype CNG engine with reference to power curve of the target GDI engine.

For the sake of clarity, crank angles are all expressed by referring to the firing TDC as 0 or cyclically 720 degCA hereinafter.

4.5.1 Injector implementation

The positioning, orientation and flow characteristics of the direct gas injector are essential prerequisites for the DI engine design and mixture formation analysis. A special design concept is applied to the side-mounted outward-opening injector.

Apart from the advantages of relatively large space available for injector niche installation and mechanical strength of the combustion chamber, the side-mounted injector configuration is preferred due to the fact that the injected fuel is constantly in gas state and that the potential interaction between gas jet and intake-induced air flow can be exploited. As a matter of fact, the penetration length of underexpanded gas jet, unlike liquid spray featuring high momentum and mixing capability owing to mass, viscosity and evaporation effects, is largely limited by the lower speed of sound despite strong supersonic compressibility effects [451][516]. Consequently, in the case of central mounting, the low and rapidly decaying axial momentum may significantly hinder the gas jet penetration, and the peculiar advantageous mixing-enhancing mechanism through jet-piston impingement without wall-wetting issues is hard to accomplish, especially for injection events occurring during late intake or early compression stroke when the piston is too far away to exert any effective jet reflection. It has been observed that, in most cases, the optimum injection timing is around 180 degCA before firing TDC and thereby the mixture formation process is predominantly through free jet mixing [320][321][324].

Therefore, the side-mounted gas injector is implemented in such a way that the gas jet, on the one hand, can be transported across the combustion chamber by the intake-induced tumble flow to overcome limited fuel penetration, and, on the other hand, can energize the coherent tumble flow motion with the injection momentum. The tumble ratio increased by the injection and turbocharging has in turn proven to intensify turbulence level towards the end of compression stroke and thus improve the subsequent combustion process [517][518][519]. According to this concept, the tumble-oriented injector configuration is realized by setting a quite flat angle of the

injector axis. As the injector implementation can be reduced to a simplified modal case of gas injection into crossflow and it has been argued that increase in crossflow momentum facilitates air entrainment in the jet [520], the side-mounted injector is paired with a high-tumble intake port design. Moreover, as schematically shown in Figure 4.6, a geometrical estimation suggests that the jet cone would interfere with the injector niche and thus the actual jet is expected to be deflected towards the pent roof, further aligned with the intake-induced tumble flow. The underlying principle of jet deflection is the Coandă effect, the formation of a low-pressure zone between the high-velocity jet and adjacent approximately-parallel surface as a result of the entrainment of surrounding air. The prospective occurrence of the Coandă effect, the extent to which the jet cone is thus deflected and the resultant flowfield are to be investigated in detail by the LIF experiment and numerical simulations. It has to be stressed that such configuration is conceived with specific reference to gaseous fuels owing to their inherent gas state devoid of wall-wetting or evaporation issues. The side-mounted position also provides some valve cooling with underexpansion-associated low temperature flow, partially compensating for the lack of evaporation latent heat of natural gas.

Operating characteristics of the gas injector imposes constraints to be respected when designing injection events. Firstly, precise fuel metering is instrumental to the engine operation which is commonly facilitated by enforcing chocked flow in the injector nozzle and thus independence of fuel mass flow rate from the continuously varying backpressure. As in-cylinder pressure rises rapidly during the compression stroke, maintaining the rail-to-backpressure ratio above the critical value ($p_0/p_a \approx 1.845$ for CH_4) constitutes a limit to the latest possible EOI. Secondly, to ensure a secure closure of the injector poppet valve prior to the combustion onset, a safety margin of 2 ms between the EOI and ignition timing is necessary, which constitutes another EOI limit. Specifically, the maximum rail pressure of the developed CNG engine is set at 16 bar, and the EOI limits, at full loads for instance, are reported in Figure 4.7. The values of EOI limit for sonic flow condition correspond to the crank angles where the in-cylinder pressure approaches 8.5 bar. The exact values depend on the boost levels and intake valve actuation at respective operating point, and are estimated by a one-dimensional engine model with GT-Power. The SA is empirical

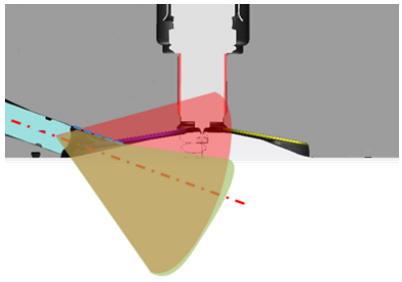

Figure 4.6 Estimated jet cone of the side-mounted injector
Red – unaffected jet cone, Green – jet cone intersected by the injector niche

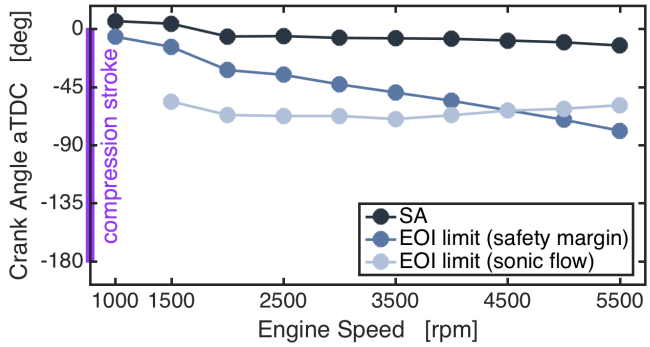

Figure 4.7 EOI limits for full-load operating points with rail pressure of 16 bar (the ordinate is expressed in degCA after firing TDC)

values derived from comparable CNG engines. It is observed that above 4500 rpm the limiting factor for the latest EOI is the injector safety margin, and the elevating backpressure during compression stroke becomes critical at lower engine speeds. In addition, should further postponing the EOI be pursued, increasing the fuel rail pressure in this case would bring about feeble effects since the gap between the two constraints is small, especially above 3000 rpm. Higher injection pressure shortens the total injection duration, but the ultimate benefits are dependent on the specific injector design and combustion system (e.g. stratified or homogenous mixture).

Another characteristic of the injector, depending on the engine operating point, is the intended variation in the injection pressure. When the requested fuel quantity is large, e.g. at rated power, the rail pressure should be at the maximum to limit the injection window within the allowable timing range and to maintain the flexibility of postponing SOI relative to IVC for volumetric efficiency gains, if necessary. On the contrary, when the requested fuel quantity dwindles, e.g. at engine idle or low loads, the injection duration should be prolonged by lowering the injection pressure to avoid the injector working majorly in the nonlinear transients and thus unstable fuel flow rate caused by irregular pressure drop or needle lift (see Figure 3.7). For this reason, being 16 bar the maximum, a variable rail-pressure control is employed wherein the injection pressure can be decreased down to 6 bar by an electronic two-stage pressure regulator mounted between the gas container and injector rail. The injection duration and corresponding injected fuel quantity with different injection pressures are experimentally characterized, as presented in Figure 4.8 wherein the linear operation range is reported since the nonlinear transients due to excessively short injection events are to be avoided. It is verified above all that the rail pressure of 16 bar is sufficient to deliver the requested fuel quantities for all full-load points with reasonable injection durations within the allowable timing limit. The viability of low injection pressure is attributable to the outward-opening poppet-valve design with large flow cross section and volume flow rate, which obviates the need of high injection pressure for non-gas-specific injectors to achieve adequate mass flow rate

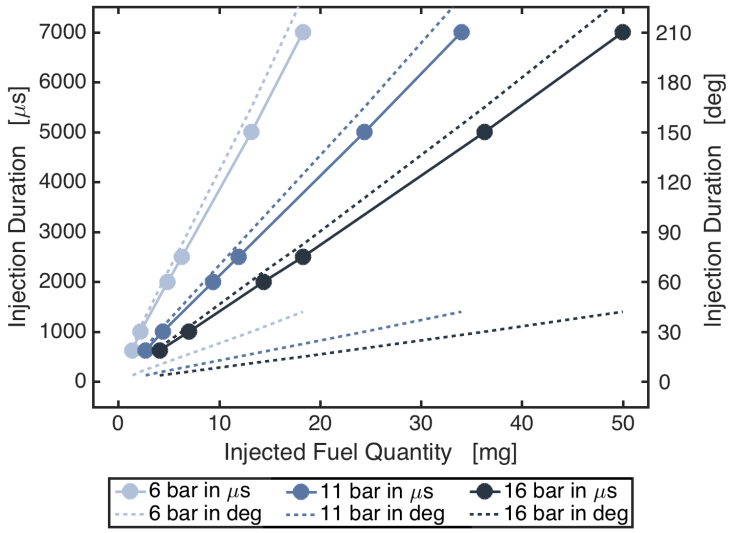

Figure 4.8 Rig-testing results of the injection duration and corresponding injected fuel quantity at three different injection pressures
Upper dotted line – 5500 rpm, Lower dotted line – 1000 rpm

[332][448][450]. The characterization of injected quantity is used to determine the injection duration for each individual engine operating point.

In summary, characterization of the direct gas injector provides insight into the two prerequisites that circumscribe the DI operation design, namely the EOI limit and injection duration-quantity correlation with variable rail pressure. The former is used to prescribe injection timing and the latter injection window. The two factors in combination establish the fundamentals of injection event design over the entire engine map.

4.5.2 Mixture formation: low-end full-load

The low-end-torque point, i.e. 1500 rpm full-load, is first considered. The very late injection timing, with SOI after IVC (see Figure 4.9), is of practical interest as it is anticipated that the target low-end torque has to be achieved by maximizing the volumetric efficiency and displacing fresh air by injected gaseous fuel during intake

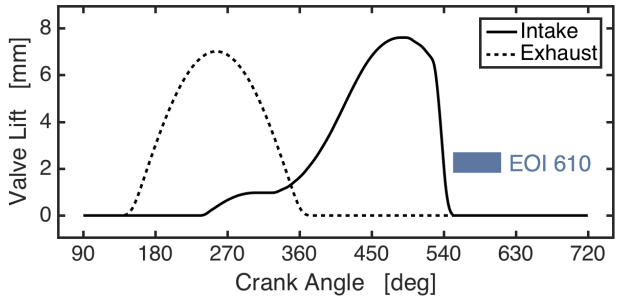

Figure 4.9 VVA profiles and injection timing: 1500 rpm full-load

phase therefore avoided. The low-end-torque point is regarded as the most critical operating point with respect to charge motion and hence air-fuel mixing capability, due to low piston velocity and large injected fuel quantity. The unfavorably limited mixing time resulting from the very late injection makes the mixture formation even more problematic. Accordingly, investigation into the 1500 rpm full-load operating point focuses on the effectiveness of the enhanced air-fuel mixing mechanism and mixture homogeneity.

The processed PLIF and numerical results are presented in Figure 4.10 wherein, and in other similar figures, the PLIF images show the mixing process in the laser-illuminated symmetry plane whereas the numerical results are represented in three mutually perpendicular planes – the same symmetry plane as well as the horizontal plane coincident with the cylinder head gasket (called gasket plane hereinafter) and a vertical plane on the intake side passing through the nearfield of the injector exit (called intake plane hereinafter).

It is observed in the PLIF image at 570 degCA that the Coandă effect emerges immediately after SOI, as the jet is deflected to the pent roof rather than proceeding along the injector axis in the expected conical shape. As shown in the PLIF image at 610 degCA, the jet, under the persistent Coandă effect, remains attracted towards the pent roof from the intake up to the exhaust side, where the jet is then redirected downwards to the piston along the liner. Viewed in the laser-illuminated symmetry plane, the entire course of the fuel-rich cloud established by the injection process is well aligned with the primary tumble motion (clockwise in this case) that is typical of pent-roofed SI engines. Due to the risk of laser ignition at high thermodynamic state of the mixture, the last PLIF image is acquired 50 degCA before TDC wherein a modest degree of inhomogeneity exists with the mixture on the intake side being slightly richer than the exhaust side. On the basis of the experimental visualization,

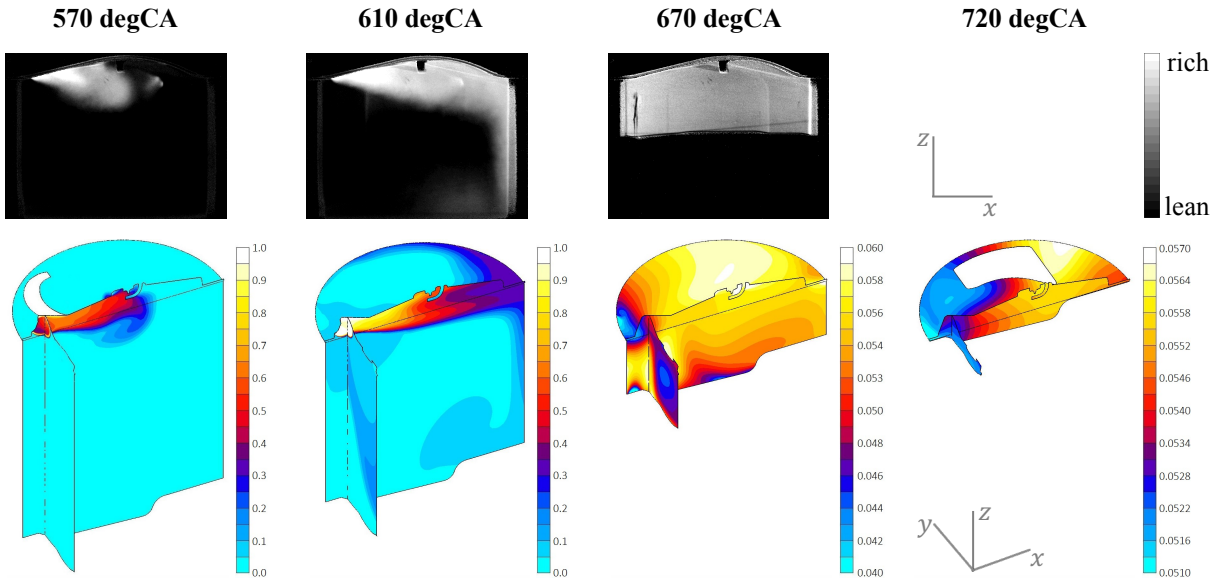

Figure 4.10 Processed PLIF images (grayscale) and numerical fuel mass fraction contours (color): 1500 rpm full-load

effectiveness of the side-mounted injector is confirmed as far as the Coandă effect and the enhanced jet penetration through tumble motion transport are concerned. In addition, the air-fuel mixing process is limited by the fact that the rich cloud follows and in the meanwhile confined within the clockwise tumble motion, and is attached to the bounding walls with inadequate mixing with air across the bulk combustion chamber. Nevertheless, the subsequent combustion measurement indicates that the IMEP reaches the target value and that the CoV in IMEP measures less than 1.2%, implying that the mixture, albeit inhomogeneous as shown in the last PLIF image, is of good enough quality for an efficient combustion.

Numerical results of fuel distribution at the same crank angles are juxtaposed with PLIF images for comparison. The numerical results in the symmetry plane, in regard to initial deflection of the jet and redirection of the rich cloud on the exhaust side in particular, are in good agreement with the PLIF images, substantiating the validity of the developed numerical model. It has to be pointed out that the injector niche, being recessed in and therefore blocked by the cylinder head roof, is invisible in the PLIF images. Moreover, without the practical constraint of laser ignition as in the experiment, the mixing process beyond the last PLIF-imaged crank angle is shown by the numerical simulation. Whilst the modest inhomogeneity with intake-side richer mixture at 670 degCA is predicted by the numerical model, the mixture quality is noticeably improved during the remaining 50 degCA till the ignition event around firing TDC, accounting for the subsequent experimentally-verified efficient combustion process.

Supplementary to the experimentation, the numerical model enables additional insight into the air-fuel mixing mechanism. Upon reaching the exhaust side in line with the tumble motion, the fuel-rich cloud is, on the one hand, redirected vertically downwards following the clockwise tumble flow pattern as confirmed by the PLIF visualization, and on the other hand, reflected tangentially sideways into swirl-like motion as shown in the gasket plane at 610 degCA. Moreover, the contours of fuel mass fraction indicate that the amount of injected fuel involved in the swirl motion is comparable with, or even larger than, that in the tumble motion. It is additionally observed that the transport speed of the swirl motion is higher, as the rich cloud at the same crank angle already circulates sideways back to the intake side. The reason is assumedly that the semicircular course followed by the tangential swirl motion is more flow-favorable than the rectangular course of the tumble motion. Considering furthermore the symmetric existence of two swirls on both sides, the ellipse-shaped swirl motion, traveling from the redirection point in the exhaust upper corner to the intake lower corner, is beneficial to the overall air-fuel mixing process. Therefore, the tumble motion of the rich cloud occurring in the vertical plane of the cylinder, is partly the mixture homogenization mechanism, which is in fact augmented by the pair of elliptic swirl flows and turns out to be very effective.

Additional fluid-dynamic information relevant to the injection event is derived from the numerical simulations and presented in Figure 4.11, wherein CoV in local

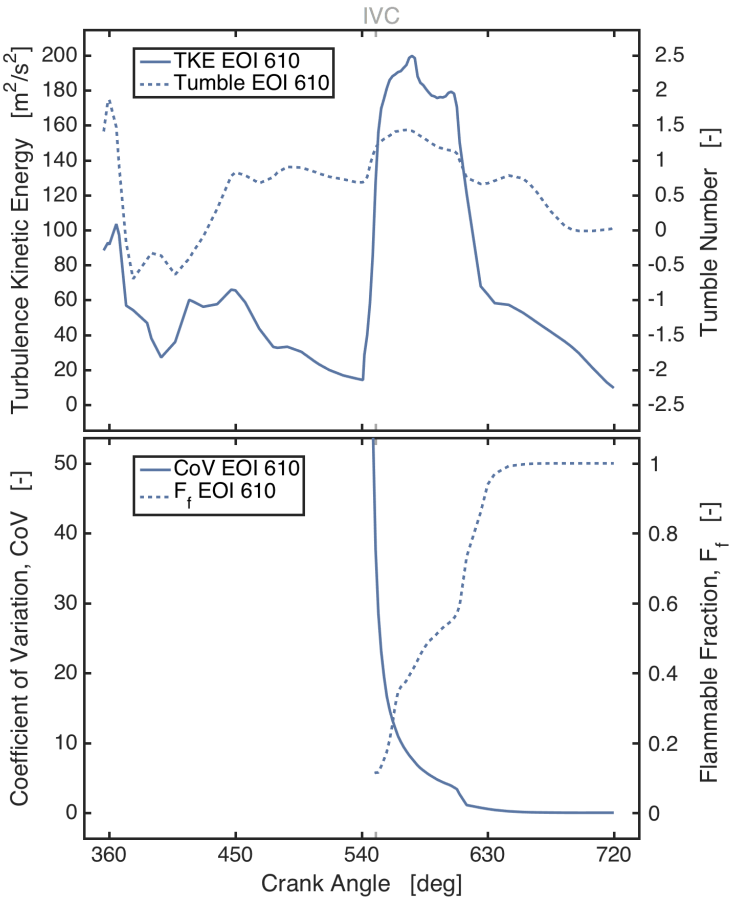

Figure 4.11 Time evolution of turbulence, tumble motion and mixing process inside the combustion chamber: 1500 rpm full-load

fuel mass fraction distribution across the combustion chamber and flammable fuel mass fraction quantify the air-fuel mixing process. Pronounced intensification of the tumble motion and turbulence during the injection is observed, as expected from the flat side-injector orientation and high-velocity underexpanded gas jet. Despite anticipated low-end piston speed and charge motion, the mixing rate shown as slope of the declining CoV curve is impressive. Specifically, the mixing rate is substantial during the injection event and considerably decreases after EOI, which constitutes the first evidence that the mixing process is dominated by the ongoing gas jet and thus-promoted flow patterns, i.e. the tumble and elliptic swirl motions. Moreover, the mixing rate already decreases shortly prior to EOI, suggesting the abatement of jet-promoted flow as the injector closing transient reduces the jet momentum.

The momentary increase in mixing rate (the steep decline in CoV) immediately after EOI is likely attributable to strong dilution of the jet trail previously supplied by the injection and attached to the pent roof due to the Coandă effect, with limited bulk mixing with ambient air. In fact, whereas CoV quantifies overall homogeneity of the mixture, flammable fraction distinguishes the mixture composition between being within the 0.7-1.7 range of relative air-to-fuel ratio and extremely rich or lean.

Specific to the time instant under discussion, the short-lived increase in mixing rate coincides with a remarkable increase in flammable fraction, implying that a drastic mixture recomposition occurs at the fuel-rich or lean end. The aforementioned jet trail dilution seems to be a plausible explanation since the appearance of rich trail due to discontinued injection is the only change that arises shortly before and after EOI. Furthermore, the flammable fraction curve suggests that, while the mixture is still slowly homogenizing, the entire in-cylinder charge is within the flammability range well ahead of firing TDC, accounting for the combustion stability.

4.5.3 Mixture formation: low-speed part-load

The 2000 rpm part-load (IMEP of 4 bar) point is secondly investigated for the sensitivity to mixture homogeneity. From engine operation point of view, the part-load operating points are commonly optimized for fuel consumption and therefore work with early IVC which inevitably compromises intake-induced charge motion, and consequently deteriorates mixing capability and turbulence level to the extent close to the combustion stability limit. To investigate the influences of injection on mixture quality and turbulence, three injection timings with distinct characteristics are designed, as presented in Figure 4.12 together with the significantly diminished intake valve actuation. In particular, starting from a very late injection close to the EOI limit and fully completed after IVC (EOI 610), the injection event is advanced to an intermediate timing partially before IVC (EOI 470), and further advanced to a very early timing when the injection occurs during intake phase (EOI 390) and is hence similar to a PI situation.

Figure 4.13 presents the results from PLIF imaging and numerical simulations. Since the numerically predicted distributions of fuel mass fraction in the symmetry plane, as in the 1500 rpm full-load case, are in good agreement with PLIF images, the side-by-side comparison is omitted and the numerical results are presented as a supplementary perspective to the experiments where suitable. The additional fluid-dynamic quantities representing turbulence level, tumble motion intensity and air-fuel mixing process are reported in Figure 4.14. As a result of the different injection timings relative to the intake phase, interaction between the jet and intake air flow

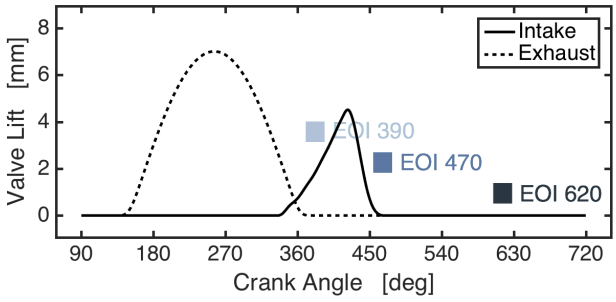

Figure 4.12 VVA profiles and injection timings: 2000 rpm part-load

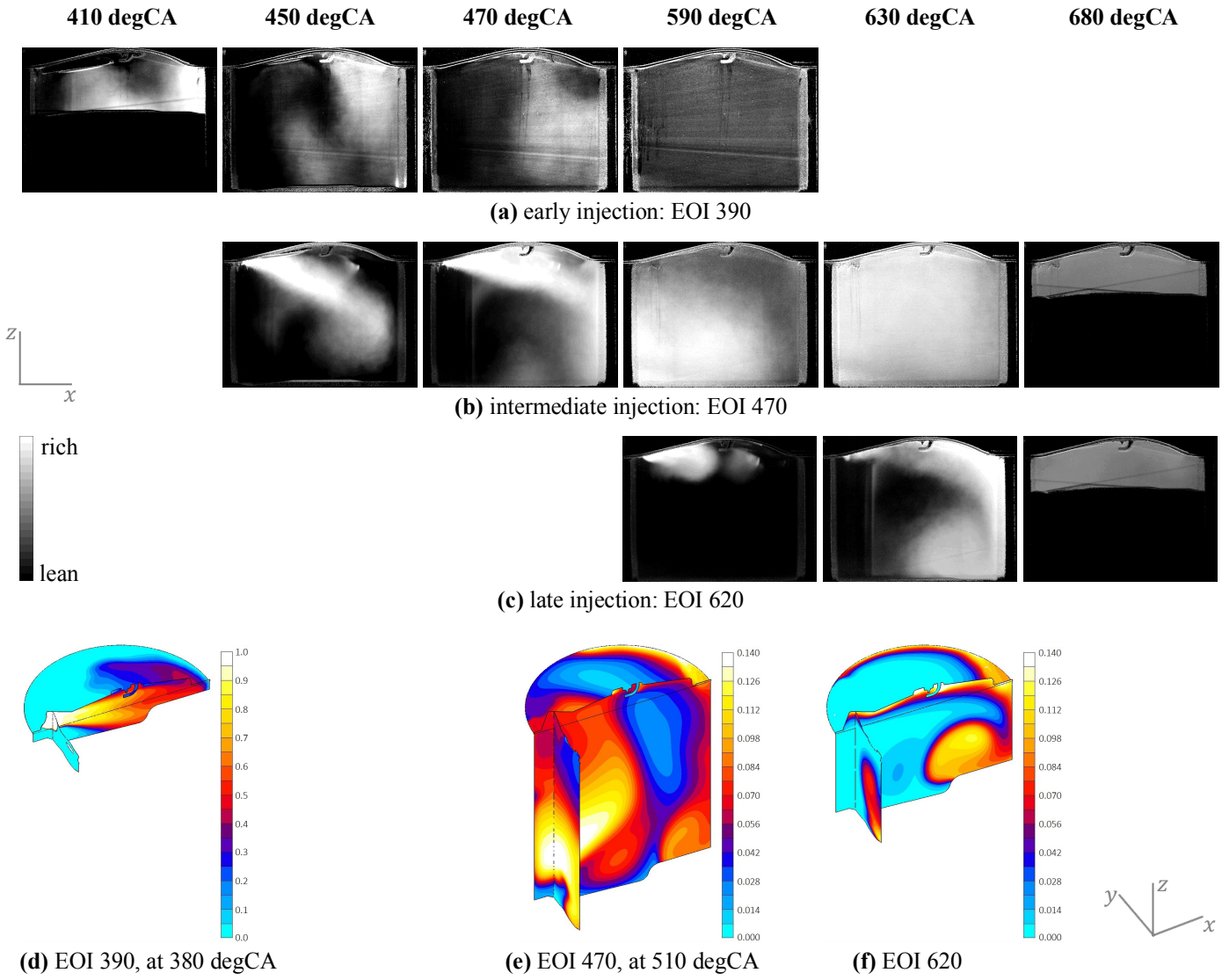

(a) early injection: EOI 390

(b) intermediate injection: EOI 470

(c) late injection: EOI 620

(d) EOI 390, at 380 degCA

(e) EOI 470, at 510 degCA

(f) EOI 620

Figure 4.13 Processed PLIF images (grayscale) and numerical fuel mass fraction contours (color): 2000 rpm part-load

differs, which leads to distinct jet development and mixing characteristics.

As for the early injection case EOI 390 (see Figure 4.13 (a)), no PLIF image is acquired during the injection process near the valve-overlap TDC, as the accessible space is insufficient for the laser sheet to induce reliable fluorescence response and high signal-to-noise ratio. The subsequent PLIF images indicate that the rich cloud moves in the anticlockwise direction, opposite to the typical primary tumble motion of the intake air. The reason is that the intake phase is heavily impeded by the low intake valve lift and very early IVC, and more importantly, that the shape of piston bowl favors anticlockwise flow rotation when moving downwards. Consequently, when the intake-induced in-cylinder coherent flow motion is weakened, the overall flowfield is dominated by the inverse tumble shaped by the piston movement. Such explanation is supported by the time evolution of tumble number (see Figure 4.14) in that, except for the ongoing injection windows, the tumble of all the three cases are majorly negative (denoting anticlockwise rotation). As a matter of fact, even in

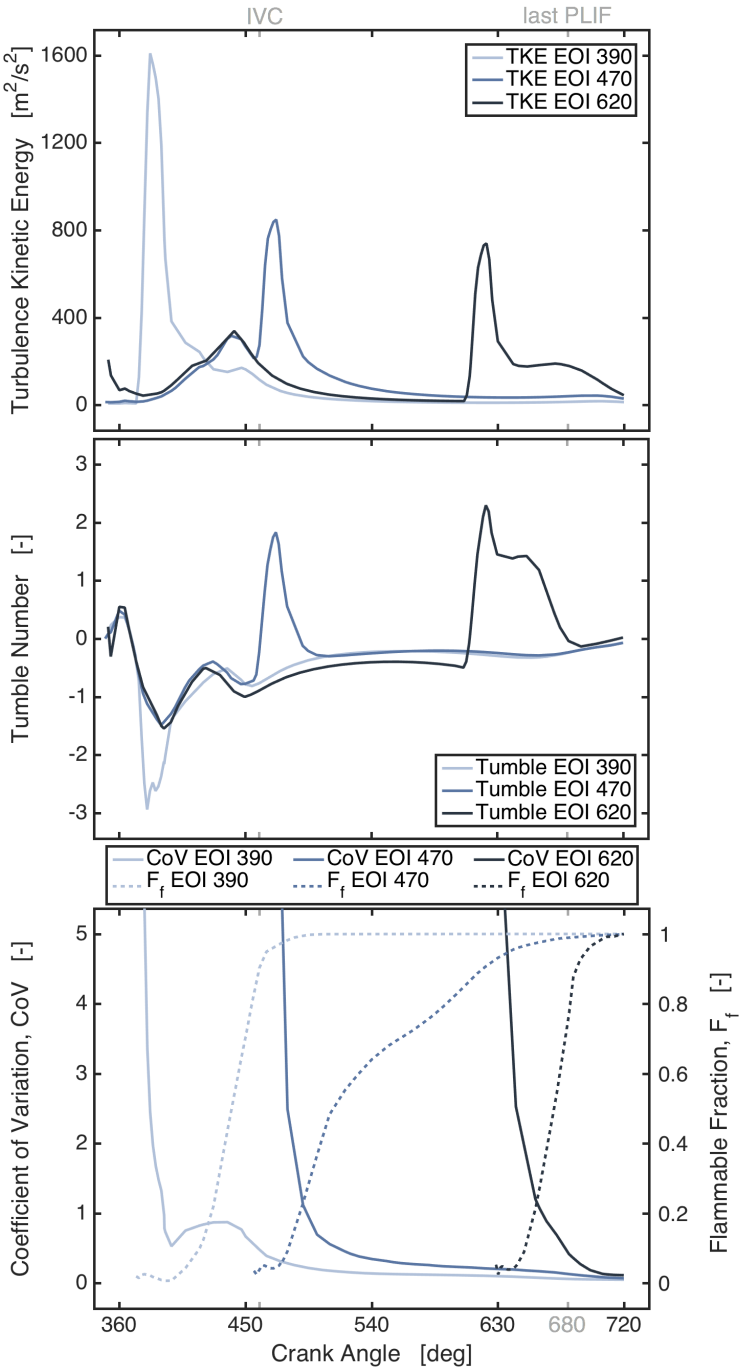

Figure 4.14 Time evolution of turbulence, tumble motion and mixing process inside the combustion chamber: 2000 rpm part-load

the 1500 rpm full-load case wherein the intake valve actuation is enlarged, the trend of inverse tumble formation due to piston downward movement still persists during the first half of intake stroke (see the negative tumble number between 360 and 450 degCA in Figure 4.11). The inverse tumble motion is most pronounced for the early injection timing (see Figure 4.14) for two reasons. On the one hand, the gas jet is constantly deflected by intake air flow that disrupts the Coandă effect. On the other, the piston bowl guides the impinging jet to the anticlockwise rotation in alignment

with the inverse tumble as illustrated by the numerical simulation (see Figure 4.13 (d)). The entire engine cycle therefore features the inverse tumble motion with the injection process further intensifying it. In regard to the mixing process, substantial mixing rate is found during the injection which resembles the behavior of the 1500 rpm full-load case. The underlying mechanism is however disparate. The mixing in this case is attributable to the jet impingement on piston without noticeable tumble-swirl transport of fuel. Furthermore, the flammable fraction rises slower, also with a delay compared to the decline of CoV, opposite to the simultaneous steep changes in F_f and CoV curves in the full-load case. In fact, even though the mixing process is greatly expedited by piston reflection, i.e. the fast CoV decline, the fuel is injected within a small portion of intake phase and the overall mixture composition thereby remains beyond the rich end of flammability range, i.e. negligible F_f increase. This also explains the small CoV fluctuation after the major decline, being the increase in fresh air during the remaining intake phase. The mixing process resulting from jet-piston interaction, rather than relying on the tumble-swirl transport mechanism, is nonetheless effective for the abundant mixing time of very early injection timing. The final mixture is highly homogeneous, completely within the flammability range more than 200 degCA ahead of the firing TDC.

The injection of the intermediate case EOI 470 starts when strong air flow has been initiated by the wide-open intake valves and suction force from the piston. The intake air inhibits immediate manifestation of the Coandă effect, and consequently the jet is allowed to develop along the geometric injector axis (see Figure 4.13 (b)). As IVC precedes EOI, during the post-IVC injection the Coandă effect comes back into force whereby the jet is deflected towards the pent roof and the tumble-swirl motion of rich cloud established. The PLIF image at 590 and 630 degCA feature a rich cloud appearing in the intake lower corner, which, according to the simulation (see Figure 4.13 (e)), is not related to the tumble motion but to the swirl transporting the fuel from the exhaust upper corner along its elliptic path.

The late injection case EOI 620 degCA is critical for both the much decreased mixing time and the weak charge motion by the time of SOI due to very early IVC. The PLIF images verify that the Coandă effect, when undisturbed by intake air flow, directs the gas jet towards pent roof immediately after SOI in line with the tumble motion. The numerical results (see Figure 4.13 (f)), showing the faithful prediction of fuel mass fraction distribution to the PLIF image at the same crank angle of 630 degCA, underlines formation of the elliptic swirl motion accompanying the tumble.

The enhanced mixing mechanism of the intermediate and late injection timings is consistent with the findings from the 1500 rpm full-load case. The two part-load cases differ specifically in the strength of the jet-promoted tumble and swirl motion. Since the gas jet in the intermediate timing initially counteracts the tumble motion, the tumbling flow is less energized by the jet momentum and the proportion of fuel thus-conveyed is lower than that in the late injection case. Indeed, it is observed in the numerical results that the amount of fuel involved in the tumble motion is much

less than that in the elliptic swirl for the intermediate injection timing, whereas such discrepancy is not as evident for the late timing (see Figure 4.13 (e) and (f)). Since it is concluded previously that the mixing mechanism depends on the combinative effect of jet-promoted tumble and swirl, the lower mixing rate of the intermediate case substantiates the less effective mixing due to the weaker tumble induced during the injection event. Furthermore, the significantly slower increase in the flammable fraction implies a lack of mixing site that is mostly ascribable to the lower amount of fuel transported by the tumble motion.

According to the time evolution of tumble number, the tumble motion is vastly intensified by the jet momentum, in the intermediate and late cases, to predominate over the negative one formed by piston-guided intake flow and to result in an overall positive tumble number during the, albeit short, injection period. Additionally and more importantly, the fact that the short-lived occurrence of jet-promoted positive tumble and accompanying swirl motions is responsible for the major CoV decline and hence mixture homogenization, constitutes the second evidence that the mixing process is dominated by the gas jet and thus-promoted flow patterns. Comparison of CoV and F_f curves between the early and late injection implies that the mixing mechanism of tumble-swirl transport is comparable with direct jet impingement on piston in terms of mixing capability.

Despite the unfavorable mixing process, the intermediate injection is still early enough to attain sufficiently homogeneous mixture. And owing to high mixing rate of the late injection with enhanced mechanism, even though the last PLIF image at 680 degCA shows richer intake side and in general less homogeneous mixture than the intermediate case, the mixture is in fact of good homogeneity short afterwards. With respect to the final mixture quality, all the three injection timings end up with almost identical mixture quality and flammable fraction (= 1), with the late injection having slightly higher CoV at the ignition event. In this regard, it is confirmed that the part-load VVA profile with low lift and early IVC, albeit significantly reducing coherent flow motion compared to full-load operation, is able to guarantee adequate mixture quality even with very late injection timings for optimization of volumetric efficiency, thanks to the mixing mechanism introduced by the side-mounted direct gas injector configuration.

The experimentally measured combustion rate and stability for the three part-load injection cases are presented in Table 4.2 wherein the combustion phasing is expressed relative to the firing TDC as 0 instead of 720 degCA for convenience. In particular, the target phase of 50% mass fraction burned (MFB50) is set to 8 degCA that results in the maximum efficiency in common. The derived IMEP is lower than the nominal value since the optical engine has a lower CR than the designed multi-cylinder prototype. The first combustion phase, represented by the period between SA and MFB5, is appreciably longer for more advanced injection timing. And the combustion duration, represented by the period from MFB5 to MFB90, exhibits the same trend. In addition, the combustion stability increases with postponed injection

Table 4.2
Experimentally measured combustion phasing and stability from the single-cylinder optical engine 2000 rpm part-load: IMEP = 4 bar (upper) and IMEP = 8 bar (lower)

Timing	IMEP [bar]	CoV IMEP	SA [degCA aTDC]	Combustion Phasing [degCA]			
				MFB5	MFB50	MFB90	Duration
Early	3.50	2.6%	-27	-8	8	22	30
Intermediate	3.71	2.4%	-18	-4	7	16	30
Late	3.71	1.9%	-14	-2	8	15	17
Early	5.89	1.5%	-24	-7	7	18	25
Intermediate	6.49	1.4%	-20	-6	7	17	23
Late	6.44	0.9%	-12	-2	7	14	16

timing. Based on the mixing analysis concluding that the final mixture homogeneity is identical for the three timings, the differences in flame kernel development and flame front propagation are supposed to be mainly determined by turbulence levels inside the combustion chamber. The combustion measurement is performed for an additional part-load operating point at the same engine speed of 2000 with a higher IMEP (= 8 bar), and shows the same trend with respect to injection timings.

The difference in turbulence level is in turn connected with the differently timed injection events since the other engine operation parameters are identical. As shown both by numerical study with methane DI and by experimental study with combined CNG PI and nitrogen DI [205][386], the gas jet enhances the in-cylinder turbulence in a twofold manner. First, small-scale vortices are directly introduced in the shear region around the high-velocity jet. Second, the gas jet transfers momentum to the large-scale tumble motion that decays and transforms into turbulent motion shortly before ignition. With reference to the turbulence kinetic energy (see Figure 4.14), the abrupt increase coincident with each SOI is attributable to the jet-induced small-scale vortices. Such increase is the largest for the early injection case due to piston impingement, moderate for the intermediate case due to interaction between the jet and intake air crossflow, and the smallest for the late injection due to the absence of extra effects other than shear region of the high-velocity jet. However, the direct jet-induced turbulence diminishes rapidly upon EOI as the small-scale vortices are easily dissipated over time, hence retaining minor effect on combustion. The greater turbulence effect arises from the jet-intensified large-scale coherent charge motion that carries more kinetic energy for later turbulence production. In fact, turbulence level of the early case, despite the highest peak value during injection, drops below the level of the late injection case even before SOI of the latter. The reason is likely that the inverse tumble generated by the early injection is in contradiction with the intake-induced tumble and thus the resultant net charge motion persisting through the compression stroke up to firing TDC remains low.

Accordingly, later injection benefits more from the turbulence enhancement, as tumble flow intensified by the jet is less disrupted by intake air and less dissipated

before combustion onset, thus energizing more, well-timed turbulent motion. This observation is evidenced by the late injection case wherein, as shown in Figure 4.14, the increase in turbulence kinetic energy at about 680 degCA is preceded by a rapid decline in tumble number and corresponds to the turbulence production through jet-promoted tumble flow. The turbulence enhancing mechanism by means of coherent interaction with charge motion is a unique characteristic of gaseous fuel injection, since in conventional GDI engines the turbulence mainly originates from organized intake-induced airflow and not as much from charge motion promoted by the liquid spray as by the gas jet.

4.5.4 Mixture formation: high-speed full-load

Thirdly, the 5500 rpm full-load point is investigated for the reason of the ample intake window and high piston speed creating potent and long-lasting intake airflow that would interact with the gas jet in a different way. The injection windows are in addition inevitably long from the perspective of engine cycle due to large requested fuel quantity and, more importantly, high engine speed. The three selected injection timings are reported in Figure 4.15, which, as a result of long injection duration and high intake VVA with IVC extended up to mid-compression stroke near EOI limit, are all similarly confined within the intake phase even for the very late injection.

This operating point is numerically investigated, as the engine speed and peak pressure exceed the maximum allowable values of the glass liner of optical engine. Numerical results of the intermediate case (EOI 600) are presented in Figure 4.16, representing all the three timings due to their similitude. Since the entire injection process occurs during the enlarged intake phase, the gas jet is mostly deflected by the intake airflow and the Coandă effect restricted. The jet is therefore not redirected to the exhaust upper corner and the subsequent formation of the elliptic swirl motion observed in the 1500 rpm full-load case is suppressed. Nonetheless, the tumble flow in this case is particularly substantial and the fuel still effectively transported. When the intake valve lift reduces towards the EOI, the Coandă effect predominates over intake airflow to deflect the jet upwards to the pent roof, and the jet-promoted near-wall tumble and swirl motions are re-established. The result at 10 degCA after EOI

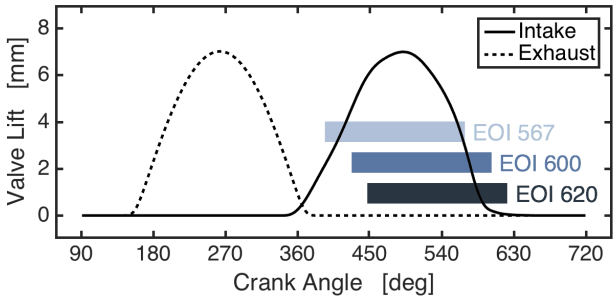

Figure 4.15 VVA profiles and injection timings: 5500 rpm full-load

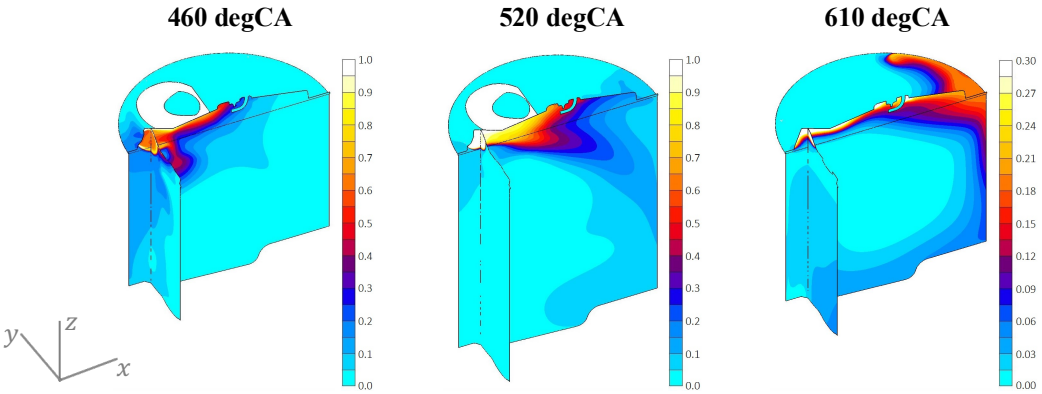

Figure 4.16 Numerical fuel mass fraction contours: 1500 rpm full-load, EOI = 600 degCA

(610 degCA) shows that the rich cloud conveyed by the tumble motion has already circulated back to the intake side whereas the swirl motion is relatively weak, which is exactly the opposite of the findings in the low-speed full-load case.

The relevant fluid-dynamic quantities are presented in Figure 4.17. Firstly, the inverse tumble with negative tumble number formed by the piston crown close to intake TDC is recognized also in this case. The strong intake-induced tumble, along with the gas jet in the same orientation, then dominates the entire flowfield with the tumbling motion that accounts for the effective transport of injected fuel. Moreover, the tumble remains at a quite high level as it is constantly sustained by the late IVC and long injection process. With respect to turbulence, a noticeable increase in the turbulence level shortly before firing TDC implies the dissipation of high-kinetic-energy large-scale flow and hence the existence of a substantial tumble motion. In addition, owing to the immense similarities between the three injection timings and the contribution of potent intake-induced airflow to the formation of predominant tumble motion, the turbulence levels at ignition near firing TDC are not expected to be distinctive enough to affect combustion to perceivably different extents.

As far as the final mixture quality at firing TDC is concerned, the three injection timings are equivalent in terms of both flammable mass fraction and homogeneity. However, the converging trend of the CoV and F_f curves, i.e. the later injection case having higher mixing rate, indicates that the mixture formation processes differ. In fact, later injection features an earlier appearance of the Coandă effect relative to its injection duration, and thus has longer time for the development of jet-promoted tumble and swirl motions. Specific to the current cases, differences in jet-promoted tumble motion are overshadowed by the reinforcing contribution of strong airflow. Nevertheless, the time evolutions of tumble number still remain different in that the later injection gives rise to higher tumble number starting from the respective SOI.

The CoV curves of the intermediate and late injection timings are quite similar to that of the 1500 rpm full-load point, since the high and low-speed cases run with very close EOI timings and, despite the differences in the relative strength of tumble and elliptic swirl, share the same mixing mechanism of jet-promoted flow motions.

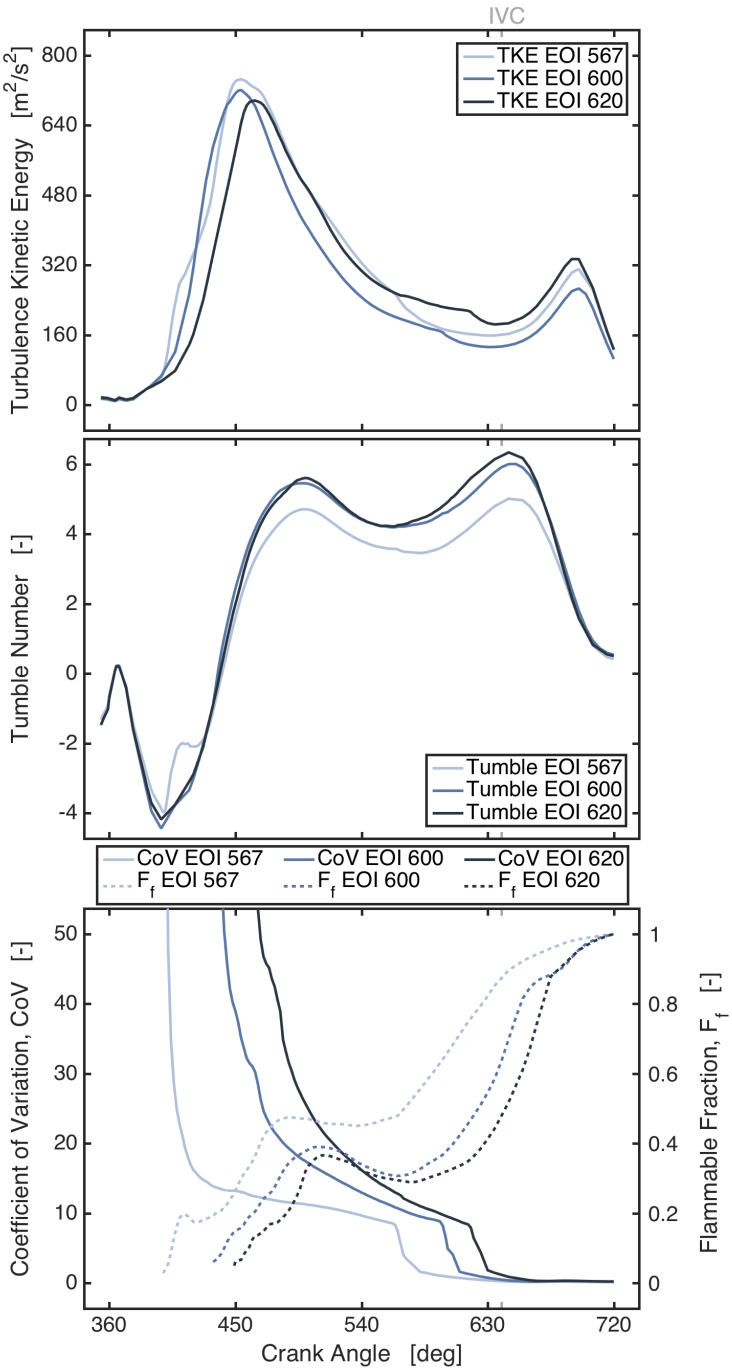

Figure 4.17 Time evolution of turbulence, tumble motion and mixing process inside the combustion chamber: 5500 rpm full-load

However, mixing rates of the 5500 rpm and 1500 rpm full-load cases, denoted by the time period between SOI and almost-zero CoV, bear significant difference when expressed in crank angles. Should the mixing process depend on charge motion, the mixing rate would be scaled with engine speed, i.e. the high and low-speed cases having the same mixing rate in crank angles. In fact, considering the implication of different engine speeds, mixing rates of the two later 5500 rpm full-load timings in absolute time appear to be nearly equal to the 1500 rpm full-load case. The fact that

the former is slightly higher is plausible as in the high-speed cases the jet-promoted tumble is combined with stronger intake-induced airflow due to larger VVA to form a quite substantial tumble motion, partially augmenting the mixing mechanism. The observation that the mixing rate is scaled with absolute time instead of engine speed constitutes the third evidence that the air-fuel mixing process is dominated by the gas jet during injection and thus-promoted flow patterns. Moreover, mixing due to trail dilution, the momentary increase in mixing rate immediately after EOI, is also present in all the three 5500 rpm full-load cases.

4.5.5 Engine power curve

Based on the outcome of the specific implementation of the direct gas injector and of the mixture formation analysis in the combustion chamber, a multi-cylinder prototype engine is built for optimization bench testing. The objective is to achieve the same rated torque and power of the boosted GDI version from which the CNG engine combustion chamber is derived, in order to eventually improve the overall appealing of natural gas engine and vehicle performance to end consumers with the environmental benefits. The power curve of an existing PISI CNG engine is referred to as the starting point. Accomplishment of the target power curve is divided into multiple optimization stages wherein contributions ascribable to various improving factors are identified. Figure 4.18 describes the roadmap of resultant power curve from each stage of improvement.

The first improvement stage, in comparison with the reference PI engine with a larger displacement, consists in a properly sized turbocharger in combination with the early IVC strategy, when necessary, to amplify the volumetric efficiency gains arising from switching to DI, which fulfils the performance target above 2500 rpm. Due to the elevated CR and advanced ignition specifically devised for natural gas,

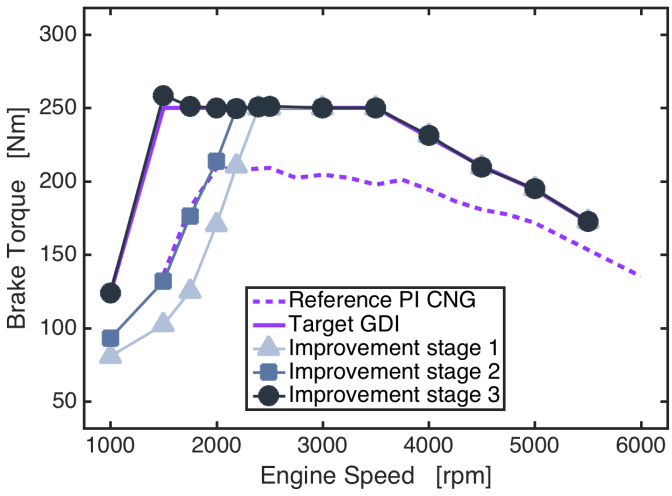

Figure 4.18 Power curve optimization of the prototype engine

however, the exhaust temperature decreases as a result of improved engine internal efficiency and advanced combustion, which in turn reduces the enthalpy delivered to the downstream turbine and limits the performance thereof at low engine speeds. The downsized low-speed power curve thereby lacks sufficient charge boosting and lies below the reference PI engine.

Attainment of the highest possible low-end torque is of crucial importance for warranting prompt acceleration maneuver. Moreover, higher gear ratios are thereby allowed to be implemented, further benefiting fuel economy. Incorporating cooling effect of the underexpanded jet during intake phase in an attempt to raise volumetric efficiency proves counterproductive, since the injected gaseous fuel occupying the volume otherwise available for fresh air outweighs the benefit of charge cooling. It is instead found advantageous to postpone the injection event after IVC to free up the space for air. According to the mixture formation analysis at 1500 rpm full-load, the mixing mechanism resulting from the injector and combustion chamber design ensures adequate mixture homogeneity with very late injection timing. In addition, the CoV and F_f curves in Figure 4.11 imply the margin for even later injection as long as the EOI limit is respected. Therefore, by fixing the EOI to the numerically investigated or a slightly postponed value, the second improvement stage arranges the injection window completely (at low speed) or mostly (at medium speed) after IVC in order to boost the low-end torque. Such enabling factor for improvement in volumetric efficiency is however inaccessible to high-speed operating points as the injection duration is too long. The loss of volumetric efficiency due to unavoidable overlap between fuel injection and intake phase is compensated by adopting higher boost levels than for the GDI engine, since the enthalpy delivered to turbine proves sufficient in this case and the fuel is more knock-resistant.

The remaining low-end performance gap between GDI and CNG DI is bridged by implementing an innovative VVA system with a special feature, activated at low engine speed, which realizes an intake valve boost-lift prior to the normal IVO (see Figure 4.9). Essentially, the intake valves are partially open during the late exhaust discharge phase for an enhanced scavenging that considerably increases volumetric efficiencies. Retaining the full benefit of scavenging and minimizing HC emissions entail very late injection timings, and the applicability thereof is assured by the air-fuel mixing mechanism. Upon the implementation of the third improvement stage, the target GDI power curve is achieved by the developed DI CNG engine.

Chapter 5

Conclusions

> All men dream: but not equally. Those who dream by night in the dusty recesses of their minds wake up in the day to find that it was vanity: but the dreamers of the day are dangerous men, for they may act their dreams with open eyes, to make it possible.
>
> — Thomas Edward Lawrence
>
> "Seven Pillars of Wisdom: A Triumph"

The present work deals with experimental and numerical analysis of natural gas fueled SI engines with particular focus on the gas fuel injection and air-fuel mixing processes. In general, control of mixture quality plays a critical role in setting course for the proximate combustion and emission formation characteristics. Specifically, as a result of its constant gas state and low density, the operation of gas injector and gas-phase mixing bear peculiar differences from conventional liquid-fueled engines and therefore warrant detailed insight. Both PI and DI systems have been studied.

First and foremost, an overall ideology has been proposed in the first chapter which is believed to be the underlying motivation for the present as well as many other works in the same field. Further developed upon that ideology, the three major challenges facing the transport sector, namely GHG-related anthropogenic climate change, air quality deterioration, and energy security and sustainability, have been clarified in fair detail, to which natural gas, as an alternative transport fuel, has been pinpointed as a promising solution. General implications of natural gas as transport fuel as well as of specific characteristics of viable combustion systems for natural gas-fueled vehicles have been examined. Finally, additional aspects different from engine technicalities, including social and economic pictures as well as a potential gas future vision (natural gas with or to hydrogen), have been depicted. The general arguments in the first chapter are intended to build an overarching and systematic framework of natural gas fueling for engine applications, and to point out the related potentials and limitations.

As underlined by the subtitle of the present dissertation, research activities and hence the conclusions thereof have focused on three aspects, i.e. the methodologies, the applications as examples, and findings from those applications.

PISI natural gas engine

The gas fuel injection and air-fuel mixture formation processes in a PISI CNG engine have been numerically investigated. Numerical modeling of the injector and the entire engine volume has been developed as diagnostic tools, in order to identify underlying physical mechanisms that have led to the observed experimental results of calibration on a prototype engine. The downsized high-performance dedicated CNG engine to which the numerical methodology has been applied is intended as a clean urban mobility solution, featuring a high CR, intercooled turbocharging and intake VVA.

- An injector model with the source cell approach has been developed and further generalized with respect to location of source cells and local mesh refinement. This modeling method has the conveniences of prescribing directly fuel mass flow rate rather than inlet pressure boundary, and of omitting inner injector flow passage by introducing proper source terms to the governing equations for a cluster of finite-volume cells near the injector nozzle.

- The injector model has been methodologically validated by referring to relevant grid dependence studies on circular nozzle jet. The predicted position of Mach disk is in good agreement with available data from literature. And the model is able to capture shock structures typical of highly to very highly underexpanded jets that are of practical interest for gas fuel injection applications, and therefore considered suitable for numerical investigation of air-fuel mixing process.
- It has been found that for highly underexpanded jets resulting from the pressure ratio range usually found in engine fuel injections, differences in describing the minor shock structures downstream of the predominant first shock cell and the Mach disk have virtually negligible influences on fuel jet structure or resultant mixing process in the combustion chamber. Whether such differences are due to source cell location or downstream grid refinement is irrelevant, provided that a reasonable spatial resolution not disrupting the minor shock waves is used. For the specific purpose of the present work, a resolution consisting of the cell size at the nozzle critical section up to the Mach disk and double the cell size further downstream covering the entire supersonic core has been identified as a good compromise between numerical accuracy and computational costs.
- There appears to be a threshold for injection timing, earlier than which injected fuel is drawn back to the intake manifold before IVO, and the consequent inter-cylinder fuel crossing is responsible for the combustion abnormalities observed experimentally with very early EOI timings.
- The two-stage mixing process has been revealed to be a fundamental mixture formation mechanism peculiar to PI gas engines. The first-stage induction of residual fuel from previous cycle and second-stage induction of injected fuel in the current cycle, and the proportion between the two stages, profoundly affect mixing rate and, from the numerical aspect, necessitate special initialization of the residual fuel in the intake ports.
- Restricted by local sonic speed at nozzle exit and low density, the fuel jet has relatively low momentum. Consequently, the injected fuel travels at a limited speed and arrives from the injection site to intake valves after a noticeable delay. Fuel traveling in the intake ports is determined by the relative timing between injection and intake valve actuation. Prior to IVO, the distance traveled by fuel is proportional to time as the ongoing injection is the sole propelling source. If the injection happens during intake phase, the piston movement acts as the main driving force, and fuel penetration scales with crank angle, with slightly longer distance traveled at lower engine speed due to the propelling effect, albeit minor, of injection. In the case of very early injection such that the fuel arrives at intake port branch before IVO, fuel penetration stalls and is later resumed by the start of intake phase, irrespective of how much early the EOI timings are. The fuel stagnation is also a peculiar feature of PI gas engines, negating fuel penetration benefit of further advanced injection timings and rendering the engine prone to

fuel crossing.

- The correlation between mixing rate and EOI timing is notably complicated by the two-stage mixing mechanism and fuel traveling in addition to the premixing level achieved in the intake ports. The effects of EOI timing can be categorized into a cascade of three components. Above all, variation in EOI timing leads to two counterbalancing effects, the first being better premixing attained by earlier injections, and the second being more evenly distributed fuel mass between the two mixing stages with more postponed injections. Furthermore, the respective inducted quantities of residual and freshly injected fuel are determined by the relative timing between fuel arrival and intake phase. And finally, the delay of fuel arrival depends on the relative phasing between injection and intake valve lift profile. The influence of injection timing on mixing process is therefore less straightforward and less intuitive.
- EOI timing has been found to affect the intake mass flow rate as a result of local variation of charge density, since the amount of fuel involved in two induction stages and delay of injected fuel arrival, i.e. the start of second stage, vary with injection timings. In particular, the differences are most pronounced during the high intake valve lift period, and more so for the exhaust-side half section of the intake valve flow passage than for the intake-side half. Furthermore, on the basis of fuel mass fraction and hence density of the local charge being inducted, volumetric efficiency is directly influenced.
- Turbulence created by the injection event is locally comparable. The turbulence transported downstream to intake valves, however, has been found to decrease with advanced EOI timing, due to the fuel traveling and stagnation phenomena. The turbulence level inside the combustion chamber, on the other hand, appears to be insignificantly affected by turbulence upstream of intake valves, but rather dependent on the high-velocity intake flows. In particular, when intake flows abate near IVC and tumble motion decelerates towards intake BDC, in-cylinder turbulence declines rapidly and no differences due to EOI timings are noticed. Therefore, it has been concluded that the direct effect of injection on in-cylinder turbulence is virtually negligible.
- A clear correlation between the coherent mean-flow tumble motion and mixture inhomogeneity has been revealed. The mechanism seems to be associated with the spatial distribution of fuel mass fraction, and hence of mass, relative to the instant center of rotation, given the disparate density of CH_4 and air. Turbulence enhancement close to firing TDC, through kinetic energy transfer from mean-flow motion to turbulent eddies, is then intrinsically influenced by EOI timings. And the differences are considered nonnegligible. Therefore, injection affects in-cylinder turbulence in an indirect but significant way, by influencing mixing process and in turn the tumble motion intensity.
- Based on experimental calibration and numerical investigation, the combustion

quality depends on both mixture homogeneity and proper spatial distribution of fuel. For the investigated low-speed part-load operating point, the EOI timing that leads to desirable spatial distribution of fuel prevails over both the timing with better homogeneity but improper fuel distribution, and another timing with higher turbulence level but less homogeneous mixture. Accordingly, mixture inhomogeneity, fuel distribution, turbulence etc. are of noticeable relevance to PI engines and hence worth analyzing.

Mixture formation process in a PISI CNG engine has been characterized by the development and application of a source-cell injector model and a full engine model with moving mesh. Experimental calibration results obtained from a corresponding prototype engine have been referred to and served as baseline for further detailed diagnostics and investigations. The methods and various underlying mechanisms found thereby may be equally applicable to PISI engines running on other gaseous fuels as well as to other combustion systems involving gas PI (e.g. dual-fuel engines and bi-fuel concomitant injection engines).

Direct gas injector

The jet structure and development of a highly underexpanded jet issuing from an outward-opening poppet valve injector have been detailed through experimental and numerical investigation. The injector is intended for direct natural gas injection application in engines. The design of a fast jet collapse has been verified, which is particularly purposed for combining the advantages of high volume flow rate of an outward-opening injector and an acceptable longitudinal jet penetration.

- Experimentally, the schlieren optics with a Z-type monochrome configuration and a high-speed camera has been implemented to visualize an entire injection process. The images thus recorded by the schlieren imaging system have been processed to remove irregularities in the optical system and yield the schlieren contrast fields that preserve the information on density distribution according to the optical working principle.
- Numerically, the injection process has been modeled by means of the RANS approach with the k-ζ-f turbulence formulation and a specific computational domain that genuinely mimics the experimental conditions of helium injection into quiescent open environment of standard air. In particular, a moving injector grid that replicates the real geometry and needle movement with great accuracy has been manually built. And the simulations cover both injector transients and steady-state operations. Density fields obtained with the numerical model have been interpolated, partially differentiated and integrated to derive intermediate quantities that are directly comparable with the experimental schlieren contrasts in accord with the governing equation of schlieren imaging in order to study jet morphological characteristics.

- Three distinctive jet development stages have been identified by the combined transilluminated and tomographic results from the experimental and numerical investigations. The first stage consists in the formation of a toroidal vortex ring as the jet issuing from the annular flow passage coils inwards to create a hollow cone with no injected gas present in the central region beneath the poppet valve face. In the second stage, the toroidal vortex ring enlarges and converges on the jet centerline, due to increasing air entrainment and decreasing pressure in the center, which establishes an ellipsoidal structure in turn filled up by a main flow recirculation zone and enveloped by the underexpanded potential core. The jet continues to advance along the injector axis in the shape of a head vortex ring sustained by injected gas passing the recirculation zone, exteriorly resembling a circular jet. Those two stages are momentary of the initial transient operation after SOI. The third jet development stage covers the principal part of injection process starting before the end of transient and features coherent unsteadiness of large-scale mean-flow vortex shedding phenomenon that are insignificant at the previous stages due to miniscule flow scale. Nearly the entire jet from head vortex upwind to most of the recirculation zone is subjected to highly unsteady flowfield by the von Kármán vortices combined with the usual instability types for flows with high velocity and large gradients. Axisymmetry of the overall jet is thereby lost, except for the upstream portion of the recirculation zone that is dominated by the compressibility-governed underexpanded potential core. In addition, the jet stem, albeit featuring the von Kármán vortex pattern, maintains a constant conical shape throughout the injection process. And the hollow cone jet has a targeting profile equivalent to a circular jet.
- In the jet nearfield region appears a series of cell-like shock structures generated by the oblique intercepting and reflected shock waves which conform to typical flowfield of highly underexpanded jet. Nevertheless, the shock structures are altered by the peculiar geometry of the annular flow passage. The flow passage contains a divergent part that accelerates the gas to supersonic state prior to the exit. The first shock cell therefore occurs inside and is bounded by the miniscule opening. The potential core is distributed continuously around the hollow cone and bent by the low-pressure recirculation zone, which essentially differs from the nearfield structures of a free underexpanded circular jet.
- The overall jet is similar to bluff body wakes in that the poppet valve constitutes a semicircular obstacle. Formation of the hollow cone and recirculation zone is analogous to flow separation and reattachment in the presence of a blunt edge, and coherent mean-flow unsteadiness to the periodic shedding and rolling-up of von Kármán vortices. The jet in the present work is however complicated by the three-dimensional flow domain and boundaries and by the underexpanded potential core that encircles the bluff body and a portion of near-wake region.
- From the perspective of numerical modeling, resolving the flow passage with 20 cells is supposed to suffice to provide satisfactory results and minimize grid

dependence. Excessively coarser grids (e.g. with 10 cells) introduce significant numerical dissipation, which underestimate the supersonic flow velocity (hence related static pressure drop) and fail to resolve detailed flowfields. The direct influence resides in the predicted timing of toroidal vortex ring collapse during the initial transient. In addition, advantages of the moving injector grid over a static grid is demonstrated with respect to dynamic jet development and proper imposition of transient boundary conditions. Deviation of the jet structure from axisymmetry and the resultant issue of symmetry assumption of computational domains are also revealed.

The transient and steady-state structures and behaviors of a gas jet issuing from an outward-opening poppet valve injector have been characterized by experimental and numerical means. It has been verified that the underlying flow characteristics of a hollow cone jet are fundamentally different from a circular jet and hence worth dedicated study. And the injector model developed in the present work is validated and methodologically pertinent to the investigation of pulsed intermittent gas jet for engine fuel injection applications.

DISI natural gas engine

For the purpose of developing a high-performance mono-fuel downsized DISI natural gas engine equipped with advanced VVA system and a side-mounted direct gas injector, the coherent flow motion, gas injection and mixing process, which are dependent on the injector implementation and VVA profiles, have been investigated both experimentally and numerically. All these aspects combined together allow a thorough and insightful understanding of the underlying flowfield characteristics of mixture quality and turbulence that in turn set course for the proximate process of inflammation, combustion and emission formation.

- Taking account of the challenging task of mixture preparation for homogeneous stoichiometric-charge combustion with CNG DI, the concept of side-mounted tumble-oriented injector configuration has been designed in order to overcome the typical penetration issue of gas jet. The design of a flat injection angle with injector niche interfering with the jet cone to exploit the Coandă effect, has been verified to be an effective mixing mechanism enhancement, especially for the problematic, very late injection timings.
- The EOI limits have been established considering the constraints of sonic flow condition and safe closure of the injector poppet valve. And due to the request of variable fuel rail pressure for engine operation, flow characterization of the injector has been tested with respect to injected quantity and injection duration. The EOI limits and quantity-duration characteristics are useful for determining the injection window, and constitute the fundamentals of injection event design for all engine operating points.

- The gas injection, the interaction thereof with geometrical bounding walls and intake-induced airflow, and the resultant mixing process have been analyzed in detail by experiments and numerical simulations. Three representative engine operating points have been examined whereby it is evidenced that the mixing process is dominated by the gas jet and thus-promoted flow patterns. In general, the principal mixing mechanism is fuel transport through the jet-promoted flow motions, namely the tumble and elliptic swirl. In particular, the Coandă effect forces the high-velocity gas jet to attach to the pent roof up to the exhaust upper corner where the jet is redirected downwards, tracing the tumble, and sideways, generating two symmetric swirls. The air-fuel mixing rate is determined by the strength of the two motions. The jet-promoted tumble depends on factors that determine the intake-induced tumble typical of SI combustion chamber, e.g. the VVA profile, piston crown shape and engine speed. And the jet-promoted swirl largely relies on the Coandă effect that is in turn influenced by deflection of the gas jet by intake airflow and hence by the relative phasing of injection window and intake VVA profile. It has been concluded, from study of the present engine, that factors influence the mixture formation process through exerting influences on the jet-promoted motions.
- Early injection timing close to valve-overlap TDC is however an exception in that the jet impingement on piston is the major mixing mechanism. And in fact, the jet-promoted motions resulting from the flat side-mounted injector turn out to have comparable mixing capability with direct jet-piston interaction.
- Since the mixing mechanism is injection-driven, the mixing rate is scaled with absolute time rather than crank angle. And accordingly, the mixture formation process is more critical for higher-speed operating point as the number of crank angles corresponding to unit time increases proportionally.
- Apart from mixture quality, turbulence level profoundly affects the combustion process. The gas injection has been found to contribute to combustion-relevant turbulence majorly by intensifying the large-scale coherent charge motion, and marginally by creating small-scale vortices around the jet shear zones, as far as the side-mounted injector configuration in the present work is concerned. Very late injection timing may preserve enough jet-induced turbulence and introduce direct turbulence effects on combustion by means of high injection pressure or sophisticated injection strategy with proper hardware support. The numerical model developed herein can be readily utilized to investigate potential future work as such, especially considering the implications of the mixing mechanism that is able to produce homogeneous mixture with late injection.
- The rated torque and power performance have been compared with a target GDI engine whereby the low-end torque is found to be a critical drawback. The gap is bridged thanks to the combinative effects of fuel knock resistance, advanced VVA control and good mixing capability. The prototype engine is hence ready

for extensive performance and emission analysis on dynamic test rig.

The methodology of planar tracer-LIF visualization, combustion measurement and numerical modeling of moving injector and engine domains has been developed and implemented to verify the combustion system design and to analyze the air-fuel mixing mechanisms. The gas-specific outward-opening poppet valve injector with high volume flow rate and the side-mounted tumble-oriented configuration thereof have proven to be an effective design for DISI natural gas engine application, which is capable of achieving mixture homogeneity across the engine map with reasonable requirement on injection pressure. And in particular the high mixing capability of the developed engine concept can be an important enabling factor for gas engine in general.

The present work deals with experimental and numerical techniques specific to the investigation into gas fuel injection and air-fuel mixture formation process, with the purpose of establishing appropriate methodologies for such engine development, both predictive and diagnostic. The methodologies have been applied herein to two natural gas combustion systems, i.e. PISI and DISI, and to two types of gas injector, i.e. inward-opening single hole and outward-opening poppet valve, whereby flow and operation characteristics of the investigated CNG engines have been disclosed and discussed. Apart from natural gas, the addressed methodologies, experimental or numerical, can be extended to additional combustion concept wherein alternative gaseous fuels are involved (e.g. biogas, hydrogen, HCNG, bi-fuel or dual-fuel with stoichiometric homogeneous, stratified lean, HCCI or RCCI combustion [521]).

Based on the present analyses of the two most widespread combustion systems, natural gas has been reconfirmed to be a promising and convenient alternative fuel to be incorporated into the transport sector. From the environmental perspective, a well-controlled natural gas engine enables immediate GHG emission, air pollution and energy diversity benefits. From the technical perspective, natural gas features a considerably simpler combustion chemistry system [522] than other hydrocarbon fuels, and may bring forth unprecedented improvement opportunities with distinct fuel properties. Pursuing alternative-fuel engine technology on environmental and technical basis alone is nevertheless likely to fail. Research in general is supported by the industry if a prospective commercially viable product is to result to reimburse the investment, regardless of the long-term interest of society. Therefore, economic or regulatory incentives may be necessitated to ensure the common good and avoid the tragedy of commons.

The present work attempts to constitute one piece of the puzzle, the puzzle that the entire transport industry and all end consumers have been striving to reconcile – the dilemma between the rising demand for the freedom of human mobility and the imperative to curb the associated negative environmental impacts.

References

[1] Exxon Mobil. The outlook for energy: A view to 2040. 2017, p. 18.

[2] United Nations. UNFCCC: United Nations Framework Convention on Climate Change. FCCC/INFORMAL/84 GE.05-62220 (E) 200705, 1992.

[3] Intergovernmental Panel on Climate Change. Climate change 2013: The physical science basis. Contribution of working group I to the Fifth Assessment Report of the Intergovernmental Panel on Climate Change. Cambridge University Press, 2013. ISBN 9781107661820

[4] Intergovernmental Panel on Climate Change. Climate change 2014: Impacts, adaptation, and vulnerability. Part A: Global and sectoral aspects. Contribution of working group II to the Fifth Assessment Report of the Intergovernmental Panel on Climate Change. Cambridge University Press, 2014. ISBN 9781107641655

[5] Intergovernmental Panel on Climate Change. Climate change 2014: Mitigation of climate change. Contribution of working group III to the Fifth Assessment Report of the Intergovernmental Panel on Climate Change. Cambridge University Press, 2014. ISBN 9781107654815

[6] United Nations. Kyoto Protocol to the United Nations Framework Convention on Climate Change. 1998.

[7] Conference of Parties to the Kyoto Protocol (CMP). Doha Amendment to the Kyoto Protocol. 2012.

[8] United Nations. Paris Agreement. 2015.

[9] International Energy Agency. Global energy & CO_2 status repot 2017. OECD/IEA, 2018, p. 3.

[10] International Energy Agency. CO_2 emissions from fuel combustion, 2012 edition. Paris: OECD Publishing, 2012.

[11] Heywood JB. Internal combustion engine fundamentals. McGraw-Hill Education, 1988, p. 567-646. ISBN 0071004998

[12] Van Basshuysen R and Schäfer F. Internal combustion engine handbook: Basics, components, systems and perspectives. SAE International, 2004, p. 574-8. ISBN 0768011396

[13] World Health Organization. Air quality guidelines for particulate matter, ozone, nitrogen dioxide and sulfur dioxide – Global update 2005 – Summary of risk assessment. WHO, 2006.

[14] Colvile RN, Hutchinson EJ, Mindell JS and Warren RF. The transport

sector as a source of air pollution. *Atmos Environ* 35(9):1537-65, 2001.

[15] International Agency for Research on Cancer. Press release No.221: Outdoor air pollution a leading environmental cause of cancer deaths. 2013.

[16] World Health Organization. World health statistics 2017: Monitoring health for the SDGs Sustainable Development Goals. WHO, 2017, p. 33. ISBN 9789241565486

[17] World Health Organization. Ambient air pollution: A global assessment of exposure and burden of disease. WHO, 2016, p. 40. ISBN 9789241511353

[18] World Health Organization. Global health risks: Mortality and burden of disease attributable to selected major risks. WHO, 2009, p. 9-12. ISBN 9789241563871

[19] International Agency for Research on Cancer. Outdoor air pollution, IARC working group on the evaluation of carcinogenic risks to humans 2013. IARC, 2015, p. 43-50. ISBN 9789283201755

[20] Organization of the Petroleum Exporting Countries. 2017 OPEC world oil outlook. OPEC, 2017, p. 117-30. ISBN 9783950393644

[21] United Nations, Department of Economic and Social Affairs, Population Division. World population prospects: The 2017 revision, volume I: Comprehensive tables (ST/ESA/SER.A/399). UN, 2017.

[22] International Transport Forum. ITF transport outlook 2015. OECD/ITF, 2015, p. 50-65. ISBN 9789282107782

[23] International Energy Agency. Technology roadmap – Fuel economy of road vehicles. OECD/IEA, 2012, p. 16.

[24] U.S. Energy Information Administration. International energy outlook 2017 (DOE/EIA-0484). EIA, 2017, p. 120.

[25] Heywood JB. Automotive engines and fuels: A review of future options. *Prog Energy Combust Sci* 7(3):155-84, 1981.

[26] SAE International. Alternative automotive fuels (J1297_201710). 2017.

[27] Bae C and Kim J. Alternative fuels for internal combustion engines. *Proc Combust Inst* 36:3389-413, 2017.

[28] Bergthorson JM and Thomson MJ. A review of the combustion and emissions properties of advanced transportation biofuels and their impact on existing and future engines. *Renew Sust Energy Rev* 42:1393-417, 2015.

[29] Geng P, Cao E, Tan Q and Wei L. Effects of alternative fuels on the combustion characteristics and emission products from diesel engines: A review. *Renew Sust Energy Rev* 71:523-34, 2017.

[30] Ugurlu A and Oztuna S. A comparative analysis study of alternative energy

sources for automobiles. *Int J Hydrog Energy* 40(34):11178-88, 2015.

[31] U.S. Energy Information Administration. International Energy Outlook 2016 (DOE/EIA-0484). EIA, 2016, p. 5.

[32] Kalam MA and Masjuki HH. An experimental investigation of high performance natural gas engine with direct injection. *Energy* 36(5):3563-71, 2011.

[33] Huang J and Crookes RJ. Assessment of simulated biogas as a fuel for the spark-ignition engine. *Fuel* 77(15):1793-801, 1998.

[34] Kakaee AH, Paykani A and Ghajar M. The influence of fuel composition on the combustion and emission characteristics of natural gas fueled engines. *Renew Sust Energy Rev* 38:64-78, 2014.

[35] Korakianitis T, Namasivayam AM and Crookes RJ. Natural-gas fueled spark-ignition (SI) and compression-ignition (CI) engine performance and emissions. *Prog Energy Combust Sci* 37:89-112, 2011.

[36] Khan MI, Yasmin T and Shakoor A. Technical overview of compressed natural gas (CNG) as a transportation fuel. *Renew Sust Energy Rev* 51:785-97, 2015.

[37] Cho HM and He BQ. Spark ignition natural gas engines – A review. *Energy Convers Manag* 48:608-18, 2007.

[38] McTaggart-Cowan GP, Reynolds CCO and Bushe WK. Natural gas fueling for heavy-duty on-road use: Current trends and future direction. *Int J Eviron Stud* 63(4):421-40, 2006.

[39] Thiruvengadam A, Besch M, Padmanaban V, Pradhan S and Demirgok B. Natural gas vehicles in heavy-duty transportation – A review. *Energy Policy* 122:253-9, 2018.

[40] Khan MI. Identifying and addressing barriers for the sustainable development of natural gas as automotive fuel. *Int J Hydrog Energy* 42(40):25453-73, 2017.

[41] Liu Y, Yeom J and Chung S. A study of spray development and combustion propagation processes of spark-ignited direct injection (SIDI) compressed natural gas (CNG). *Math Comput Model* 57(1-2):228-44, 2013.

[42] Alagumalai A. Internal combustion engines: Progress and prospects. *Renew Sust Energy Rev* 38:561-71, 2014.

[43] Aslam MU, Masjuki HH, Kalam MA, Abdesselam H, Mahlia TMI and Amalina MA. An experimental investigation of CNG as an alternative fuel for a retrofitted gasoline vehicle. *Fuel* 85(5-6):717-24, 2006.

[44] Mello P, Pelliza G, Cataluña R and Da Silva R. Evaluation of the maximum horsepower of vehicles converted for use with natural gas fuel. *Fuel* 85(14-

15):2180-96, 2006.

[45] Reynolds CCO, Evans RL, Andreassi L, Cordiner S and Mulone V. The effect of varying the injected charge stoichiometry in a partially stratified charge natural gas engine. SAE Technical Paper 2005-01-0247, 2005.

[46] Kado NY, Okamoto RA, Kuzmicky PA, Kobayashi R, Ayala A, Gebel ME et al. Emission of toxic pollutants from compressed natural gas and low sulfur diesel-fueled heavy-duty transit buses tested over multiple driving cycles. *Environ Sci Technol* 39(19):7638-49, 2005.

[47] McTaggart-Cowan GP, Jones HL, Rogak SN, Bushe WK, Hill PG and Munshi SR. The effect of high-pressure injection on a compression-ignition, direct injection of natural gas engine. *J Eng Gas Turbines Power* 129(2):579-88, 2006.

[48] Hesterberg TW, Lapin CA and Bunn WB. A comparison of emissions from vehicles fueled with diesel or compressed natural gas. *Environ Sci Technol* 42(16):6437-45, 2008.

[49] Ullman TL, Smith LR, Anthony JW, Slodowske WJ, Trestrail B, Cook AL et al. Comparison of exhaust emissions, including toxic air contaminants, from school buses in compressed natural gas, low emitting diesel, and conventional diesel engine configurations. SAE Technical Paper 2003-01-1381, 2003.

[50] Rabl A. Environmental benefits of natural gas for buses. *Transp Res D: Transp Environ* 7(6):391-405, 2002.

[51] Zeldovich YB. Regime classification of an exothermic reaction with nonuniform initial conditions. *Combust Flame* 39(2):211-4, 1980.

[52] Simmie JM. Detailed chemical kinetic models for the combustion of hydrocarbon fuels. *Prog Energy Combust Sci* 29(6):599-634, 2003.

[53] Zádor J, Taatjes CA and Fernandes RX. Kinetics of elementary reactions in low-temperature autoignition chemistry. *Prog Energy Combust Sci* 37(4):371-421, 2011.

[54] Spadaccini LJ and Colket III MB. Ignition delay characteristics of methane fuels. *Prog Energy Combust Sci* 20(5):431-60, 1994.

[55] Hu E, Li X, Meng X, Chen Y, Cheng Y, Xie Y et al. Laminar flame speeds and ignition delay times of methane-air mixtures at elevated temperatures and pressures. *Fuel* 158:1-10, 2015.

[56] El Merhubi H, Kéromnès A, Catalano G, Lefort B and Le Moyne L. A high pressure experimental and numerical study of methane ignition. *Fuel* 177:164-72, 2016.

[57] Goswami M, Derks SCR, Coumans K, Slikker WJ, de Andrade Oliveira

MH, Bastiaans RJM et al. The effect of elevated pressures on the laminar burning velocity of methane + air mixtures. *Combust Flame* 160(9):1627-35, 2013.

[58] Ranzi E, Frassoldati A, Grana R, Cuoci A, Faravelli T, Kelley AP et al. Hierarchical and comparative kinetic modeling of laminar flame speeds of hydrocarbon and oxygenated fuels. *Prog Energy Combust Sci* 38(4):468-501, 2012.

[59] Bauer CG and Forest TW. Effect of hydrogen addition on the performance of methane-fueled vehicles. Part I: Effect on S.I. engine performance. *Int J Hydrog Energy* 26(1):55-70, 2001.

[60] Manivannan A, Porai PT, Chandrasekaran S and Ramprabhu R. Lean burn natural gas spark ignition engine – An overview. SAE Technical Paper 2003-01-0638, 2003.

[61] Varde KS and Asar GMM. Burn rates in natural gas fueled single cylinder spark ignition engine. SAE Technical Paper 2001-28-0023, 2001.

[62] Das A and Watson HC. Development of a natural gas spark ignition engine for optimum performance. *Proc Inst Mech Eng D: J Automob Eng* 211(5):361-78, 1997.

[63] Jahirul MI, Masjuki HH, Saidur R, Kalam MA, Jayed MH and Wazed MA. Comparative engine performance and emission analysis of CNG and gasoline in a retrofitted car engine. *Appl Therm Eng* 30(4):2219-26, 2010.

[64] Kato K, Igarashi K, Masuda M, Otsubo K, Yasuda A, Takeda K et al. Development of engine for natural gas vehicle. SAE Technical Paper 1999-01-0574, 1999.

[65] Tilagone R and Venturi S. Development of natural gas demonstrator based on an urban vehicle with a down-sized turbocharged engine. *Oil Gas Sci Technol – Rev IFP* 59(6):581-91, 2004.

[66] Poulton ML. Alternative fuels for road vehicles. WIT Press/Computational Mechanics, 1994. ISBN 9781853123016

[67] Attar AA and Karim GA. Knock rating of gaseous fuels. *J Eng Gas Turbines Power* 125(2):500-4, 2003.

[68] Wayne WS, Clark NN and Atkinson CM. A parametric study of knock control strategies for a bi-fuel engine. SAE Technical Paper 980895, 1998.

[69] Baratta M, Misul DA, Xu J, Fuerhapter A, Heindl R, Cesare P et al. Development of a high performance natural gas engine with direct gas injection and variable valve actuation. *SAE Int J Engines* 10(5):2535-51, 2017.

[70] Evans RL and Blaszczyk J. A comparative study of the performance and

exhaust emissions of a spark ignition engine fuelled by natural gas and gasoline. *Proc Inst Mech Eng D: J Automob Eng* 211(1):39-47, 1997.

[71] Darade PM and Dalu RS. Investigation of performance and emissions of CNG fuelled VCR engine. *Int J Emerg Technol Adv Eng* 3(1):77-83, 2013.

[72] Jones AL and Evans RL. Comparison of burning rates in a natural-gas-fueled spark ignition engine. *J Eng Gas Turbines Power* 107(4):908-13, 1985.

[73] Kalam MA, Kazi SN and Jayed MH. Power boosting of a modified natural gas engine. *Int J Phys Sci* 6(28):6548-57, 2011.

[74] Beck NJ, Barkhimer RL, Johnson WP, Wong HC and Gebert K. Evolution of heavy duty natural gas engines – Stoichiometric, carbureted and spark ignited to lean burn, fuel injected and micro-pilot. SAE Technical Paper 972665, 1997.

[75] Gupta M, Bell SR and Tillman ST. An investigation of lean combustion in a natural gas-fueled spark-ignited engine. *J Energy Resour Technol* 118(2):145-51, 1996.

[76] Ishii M, Ishizawa S, Inada E, Idoguchi R and Sekiba T. Experimental studies on a natural gas vehicle. SAE Technical Paper 942005, 1994.

[77] Kubesh JT, Podnar DJ, Guglielmo KH and McCaw D. Development of an electronically-controlled natural gas-fueled John Deere PowerTech 8.1L engine. SAE Technical Paper 951940, 1995.

[78] Tilagone R, Monnier G, Chaouche A, Baguelin Y and De Chauveron S. Development of a high efficiency, low emission SI-CNG bus engine. SAE Technical Paper 961080, 1996.

[79] Maxwell TT and Jones JC. Alternative fuels: Emissions, economics, and performance. SAE International, 1994. ISBN 9781560915232

[80] Beretta GP, Rashidi M and Keck JC. Turbulent flame propagation and combustion in spark ignition engines. *Combust Flame* 52:217-45, 1983.

[81] Thurnheer T, Soltic P and Eggenschwiler PD. S.I. engine fuelled with gasoline, methane and methane/hydrogen blends: Heat release and loss analysis. *Int J Hydrog Energy* 34(5):2494-503, 2009.

[82] Zhao F, Lai MC and Harrington DL. Automotive spark-ignited direct-injection gasoline engines. *Prog Energy Combust Sci* 25(5):437-562, 1999.

[83] Kesgin U. Effect of turbocharging system on the performance of a natural gas engine. *Energy Convers Manag* 46(1):11-32, 2005.

[84] Bach C, Lämmle C, Bill R, Soltic P, Dyntar D, Janner P et al. Clean engine vehicle a natural gas driven Euro-4/SULEV with 30% reduced CO_2-emissions. SAE Technical Paper 2004-01-0645, 2004.

[85] Ristovski Z, Morawska L, Ayako GA, Johnson G, Gilbert D and Greenaway C. Emissions from a vehicle fitted to operate on either petrol or compressed natural gas. *Sci Total Environ* 323(1-3):179-94, 2004.

[86] Dondero L and Goldmberg J. Environmental implications of converting light gas vehicles: The Brazilian experience. *Energy Policy* 33(13):1703-8, 2005.

[87] Jayaratne ER, Ristovski ZD, Meyer N and Morawska L. Particle and gaseous emissions from compressed natural gas and ultralow Sulphur diesel-fuelled buses at four steady engine loads. *Sci Total Environ* 407(8):2845-52, 2009.

[88] Chandler K, Norton P and Clark N. Interim results from alternative fuel truck evaluation project. SAE Technical Paper 1999-01-1505, 1999.

[89] Kamel M, Lyford-Pike E, Frailey M, Bolin M, Clark N, Nine R et al. An emission and performance comparison of the natural gas Cummins Westport Inc. C-Gas Plus versus diesel in heavy-duty trucks. SAE Technical Paper 2002-01-2737, 2002.

[90] Einewall P, Tunestål P and Johansson B. Lean burn natural gas operation vs. stoichiometric operation with EGR and a three way catalyst. SAE Technical Paper 2005-01-0250, 2005.

[91] Chiu JP, Wegrzyn J and Murphy KE. Low emissions Class 8 heavy-duty on-highway natural gas and gasoline engine. SAE Technical Paper 2004-01-2982, 2004.

[92] Lanni T, Frank BP, Tang S, Rosenblatt D and Lowell D. Performance and emissions evaluation of compressed natural gas and clean diesel busses at New York City's Metropolitan Transit Authority. SAE Technical Paper 2003-01-0300, 2003.

[93] Johnson TV. Diesel emission control technology 2003 in review. SAE Technical Paper 2004-01-0070, 2004.

[94] Ma F and Wang Y. Study on the extension of lean operation limit through hydrogen enrichment in a natural gas spark-ignition engine. *Int J Hydrog Energy* 33(4):1416-24, 2008.

[95] Ayala A, Gebel ME, Okamoto RA, Rieger PL, Kado NY, Cotter C et al. Oxidation catalyst effect on CNG transit bus emissions. SAE Technical Paper 2003-01-1900, 2003.

[96] Varde KS, Patro N and Drouillard K. Lean burn natural gas fueled S.I. engine and exhaust emissions. SAE Technical Paper 952499, 1995.

[97] Petrov AW, Ferri D, Tarik M, Kröcher O and van Bokhoven JA. Deactivation aspects of methane oxidation catalysts based on palladium and

ZSM-5. *Top Catal* 60(1-2):123-30, 2017.

[98] Hutter R, De Libero L, Elbert P and Onder CH. Catalytic methane oxidation in the exhaust gas aftertreatment of a lean-burn natural gas engine. *Chem Eng J* 349:156-67, 2018.

[99] McCormick RL, Graboski MS, Alleman T, Herring AM and Nelson P. In-use emissions from natural gas fueled heavy-duty vehicles. SAE Technical Paper 1999-01-1507, 1999.

[100] Hassaneen AE, Varde KS, Bawady AH and Morgan AA. A study of the flame development and rapid burn durations in a lean-burn fuel injected natural gas S.I. engine. SAE Technical Paper 981384, 1998.

[101] Kato T, Saeki K, Nishide H and Yamada T. Development of CNG fueled engine with lean burn for small size commercial van. *JSAE Rev* 22(3):365-8, 2001.

[102] Adb-Alla GH. Using exhaust gas recirculation in internal combustion engines: A review. *Energy Convers Manag* 43(8):1027-42, 2002.

[103] Dimopoulos P, Rechsteiner C, Soltic P, Lämmle C and Boulouchos K. Increase of passenger car engine efficiency with low engine-out emissions using hydrogen-natural gas mixtures: A thermodynamic analysis. *Int J Hydrog Energy* 32(14):3073-83, 2007.

[104] Franklin ML, Kittelson DB, Leuer RH and Pipho MJ. A PC-based fuel and ignition control system used to map the 3-D surfaces of torque and emissions versus air-fuel ratio and ignition timing. SAE Technical Paper 940546, 1994.

[105] Chen SK and Beck NJ. Gas engine combustion principles and applications. SAE Technical Paper 2001-01-2489, 2001.

[106] Lancaster DR, Krieger RB, Sorenson SC and Hull WL. Effects of turbulence on spark-ignition engine combustion. SAE Technical Paper 760160, 1976.

[107] Ting DSK, Checkel MD, Haley R and Smy PR. Early flame acceleration measurements in a turbulent spark-ignited mixture. SAE Technical Paper 940687, 1994.

[108] Andrews GE, Bradley D and Lwakabamba SB. Turbulence and turbulent flame propagation – A critical appraisal. *Combust Flame* 24:285-304, 1975.

[109] Peters N. Laminar flamelet concepts in turbulent combustion. *Symp Int Combust* 21(1):1231-50, 1988.

[110] Peters N. The turbulent burning velocity for large-scale and small-scale turbulence. *J Fluid Mech* 384:107-32, 1999.

[111] Peters N. Turbulent Combustion. Cambridge University Press, 2000. ISBN

0521660823

[112] Kubesh JT, Podnar DJ and Colucci CP. Lean limit and performance improvements for a heavy-duty natural gas engine. SAE Technical Paper 961939, 1996.

[113] Evans RL and Blaszczyk J. Fast-burn combustion chamber design for natural gas engines. *J Eng Gas Turbines Power* 120(1):232-6, 1998.

[114] Reynolds CCOB and Evans RL. Improving emissions and performance characteristics of lean burn natural gas engines through partial stratification. *Int J Engine Res* 5(1):105-14, 2004.

[115] Lloyd AC and Cackette TA. Diesel engines: Environmental impact and control. *J Air Waste Manag Assoc* 51(6):809-47, 2001.

[116] Cheung KL, Ntziachristos L, Tzamkiozis T, Schauer JJ, Samaras Z, Moore KF et al. Emissions of particulate trace elements, metals and organic species from gasoline, diesel, and biodiesel passenger vehicles and their relation to oxidative potential. *Aerosol Sci Technol* 44(7):500-13, 2010.

[117] Huang J, Hill PG, Bushe WK and Munshi SR. Shock-tube study of methane ignition under engine-relevant conditions: Experiments and modeling. *Combust Flame* 136(1-2):25-42, 2004.

[118] Kabori S, Kamimoto T and Aradi AA. A study of ignition delay of diesel fuel sprays. *Int J Engine Res* 1(1):29-39, 2000.

[119] Karim GA. Combustion in gas fueled compression ignition engines of the dual fuel type. *J Eng Gas Turbines Power* 125(3):827-36, 2003.

[120] Abdelaal MM and Hegab AH. Combustion and emission characteristics of a natural gas-fueled diesel engine with EGR. *Energy Convers Manag* 64:301-12, 2012.

[121] Kokjohn SL, Hanson RM, Splitter AD and Reitz RD. Fuel reactivity controlled compression ignition (RCCI): A pathway to controlled high-efficiency clean combustion. *Int J Engine Res* 12(3):209-26, 2011.

[122] Harrington J, Munshi S, Nedelcu C, Ouellette P, Thompson J and Whitfield S. Direct injection of natural gas in a heavy-duty diesel engine. SAE Technical Paper 2002-01-1630, 2002.

[123] Papagiannakis RG and Hountalas DT. Combustion and exhaust emission characteristics of a dual fuel compression ignition engine operated with pilot Diesel fuel and natural gas. *Energy Convers Manag* 45(18-19):2971-87, 2004.

[124] Liu J, Zhang X, Wang T, Zhang J and Wang H. Experimental and numerical study of the pollution formation in a diesel/CNG dual fuel engine. *Fuel* 159:418-29, 2015.

[125] Yousefi A, Birouk M, Lawler B and Gharehghani A. Performance and emissions of a dual-fuel pilot diesel ignition engine operating on various premixed fuels. *Energy Convers Manag* 106:322-36, 2015.

[126] Carlucci AP, de Risi A, Laforgia D and Naccarato F. Experimental investigation and combustion analysis of a direct injection dual-fuel diesel-natural gas engine. *Energy* 33(2):256-63, 2008.

[127] Yang B, Xi C, Wei X, Zeng K and Lai MC. Parametric investigation of natural gas port injection and diesel pilot injection on the combustion and emissions of a turbocharged common rail dual-fuel engine at low load. *Appl Energy* 143:130-7, 2015.

[128] Papagiannakis RG and Hountalas DT. Experimental investigation concerning the effect of natural gas percentage on performance and emissions of a DI dual fuel diesel engine. *Appl Therm Eng* 23(3):353-65, 2003.

[129] Kakaee AH, Rahnama P and Paykani A. Influence of fuel composition on combustion and emissions characteristics of natural gas/diesel RCCI engine. *J Nat Gas Sci Eng* 25:58-65, 2015.

[130] Shenghua L, Ziyan W and Jiang R. Development of compressed natural gas/diesel dual-fuel turbocharged compression ignition engine. *Proc Inst Mech Eng D: J Automob Eng* 217(9):839-45, 2003.

[131] Singh S, Krishnan SR, Srinivasan KK, Midkiff KC and Bell SR. Effect of pilot injection timing, pilot quantity and intake charge conditions on performance and emissions for an advanced low-pilot-ignited natural gas engine. *Int J Engine Res* 5(4):329-48, 2004.

[132] Kusaka J, Okamoto T, Daisho Y, Kihara R and Saito T. Combustion and exhaust gas emission characteristics of a diesel engine dual-fueled with natural gas. *JSAE Rev* 21(4):489-96, 2000.

[133] Selim MYE. Effect of exhaust gas recirculation on some combustion characteristics of dual fuel engine. *Energy Convers Manag* 44(5):707-21, 2003.

[134] Pirouzpanah V, Khoshbakhti Saray R, Sohrabi A and Niaei A. Comparison of thermal and radical effects of EGR gases on combustion process in dual fuel engines at part loads. *Energy Convers Manag* 48(7):1909-18, 2007.

[135] Selim MYE. Sensitivity of dual fuel engine combustion and knocking limits to gaseous fuel composition. *Energy Convers Manag* 45(3):411-25, 2004.

[136] Park T, Atkinson RJ, Clark NN, Traver ML and Atkinson CM. Operation of a compression ignition engine with a HEUI injection system on natural gas with diesel pilot injection. SAE Technical Paper 1999-01-3522, 1999.

[137] Selim MYE. Effect of engine parameters and gaseous fuel type on the cyclic variability of dual fuel engines. *Fuel* 84(7-8):961-71, 2005.

[138] Benajes J, Molina S, García A and Monsalve-Serrano J. Effects of low reactivity fuel characteristics and blending ratio on low load RCCI (reactivity controlled compression ignition) performance and emissions in a heavy-duty diesel engine. *Energy* 90(2):1261-71, 2015.

[139] Zuo C and Yang M. Operating characteristics and description of a dual fuel engine for diesel-natural gas heavy-duty operation. SAE Technical Paper 1999-01-3523, 1999.

[140] Mbarawa M, Milton BE and Casey RT. Experiments and modelling of natural gas combustion ignited by a pilot diesel fuel spray. *Int J Therm Sci* 40(10):927-36, 2001.

[141] Nazemi M and Shahbakhti M. Modeling and analysis of fuel injection parameters for combustion and performance of an RCCI engine. *Appl Energy* 165:135-50, 2016.

[142] Litzke WL and Wegrzyn JE. Natural gas as a future fuel for heavy-duty vehicles. SAE Technical Paper 2001-01-2067, 2001.

[143] Yoon S, Collins J, Thiruvengadam A, Gautam M, Herner J and Ayala A. Criteria pollutant and greenhouse gas emissions from CNG transit buses equipped with three-way catalysts compared to lean-burn engines and oxidation catalyst technologies. *J Air Waste Manag Assoc* 63(8):926-33, 2013.

[144] Hajbabaei M, Karavalakis G, Johnson KC, Lee L and Durbin TD. Impact of natural gas fuel composition on criteria toxic, and particle emissions from transit buses equipped with lean burn and stoichiometric engines. *Energy* 62:425-34, 2013.

[145] Saanum I, Bysveen M, Tunestål P and Johansson B. Lean burn versus stoichiometric operation with EGR and 3-way catalyst of an engine fueled with natural gas and hydrogen enriched natural gas. SAE Technical Paper 2007-01-0015, 2007.

[146] Ibrahim A and Bari S. Optimization of a natural gas SI engine employing EGR strategy using a two-zone combustion model. *Fuel* 87(10-11):1824-34, 2008.

[147] Ibrahim A and Bari S. A comparison between EGR and lean-burn strategies employed in a natural gas SI engine using a two-zone combustion model. *Energy Convers Manag* 50(12):3129-39, 2009.

[148] Kalghatgi GT. Developments in internal combustion engines and implications for combustion science and future transport fuels. *Proc Combust Inst* 35(1):101-15, 2015.

[149] European Commission Joint Research Center. Well-to-wheels analysis of future automotive fuels and powertrains in the European context. Well-to-wheels report version 4a. Luxembourg: Publications Office of the European Union, 2014. ISBN 9789279338878

[150] Al-Sarkhi A, Jaber JO and Probert SD. Efficiency of a Miller engine. *Appl Energy* 83(4):343-51, 2006.

[151] Wan Y and Du A. Reducing part load pumping loss and improving thermal efficiency through high compression ratio over-expanded cycle. SAE Technical Paper 2013-01-1744, 2013.

[152] Wang C, Daniel R and Xu H. Research of the Atkinson cycle in the spark ignition engine. SAE Technical Paper 2012-01-0390, 2012.

[153] Su J, Xu M, Li T, Gao Y and Wang J. Combined effects of cooled EGR and a higher geometric compression ratio on thermal efficiency improvement of a downsized boosted spark-ignition direct-injection engine. *Energy Convers Manag* 78:65-73, 2014.

[154] Cai H, Burnham A, Chen R and Wang M. Wells to wheels: Environmental implications of natural gas as a transportation fuel. *Energy Policy* 109:565-78, 2017.

[155] Tong F, Jaramillo P and Azevedo IML. Comparison of life cycle greenhouse gases from natural gas pathways for medium and heavy-duty vehicles. *Environ Sci Technol* 49(12):7123-33, 2015.

[156] Clark NN, McKain DL, Johnson DR, Wayne WS, Li H, Akkerman V et al. Pump-to-wheels methane emissions from the heavy-duty transportation sector. *Environ Sci Technol* 51(2):968-76, 2017.

[157] Alvarez RA, Pacala SW, Winebrake JJ, Chameides WL and Hamburg SP. Greater focus needed on methane leakage from natural gas infrastructure. *Proc Natl Acad Sci USA* 109(17):6435-40, 2012.

[158] British Petroleum. BP statistical review of world energy 2017. BP p.l.c., 2017, p. 12, 26.

[159] International Energy Agency. World energy outlook 2017. OECD/IEA, 2017. ISBN 9789264282308

[160] Economides MJ and Wood DA. The state of natural gas. *J Nat Gas Sci Eng* 1(1-2):1-13, 2009.

[161] Porpatham E, Ramesh A and Nagalingam B. Investigation on the effect of concentration of methane in biogas when used as a fuel for a spark ignition engine. *Fuel* 87(8-9):1651-9, 2008.

[162] Bade Shrestha SO and Narayanan G. Landfill gas with hydrogen addition – A fuel for SI engines. *Fuel* 87(17-18):3616-26, 2008.

[163] Alamia A, Magnusson I, Johnsson F and Thunman H. Well-to-wheel analysis of bio-methane via gasification, in heavy duty engines within the transport sector of European Union. *Appl Energy* 170:445-54, 2016.

[164] Stempien JP, Ni M, Sun Q and Chan SH. Production of sustainable methane from renewable energy and captured carbon dioxide with the use of Solid Oxide Electrolyzer: A thermodynamic assessment. *Energy* 82:714-21, 2015.

[165] Chong ZR, Yang SHB, Babu P, Linga P and Li X. Review of natural gas hydrates as an energy resource: Prospects and challenges. *Appl Energy* 162:1633-52, 2016.

[166] Wood DA. A review and outlook for the global LNG trade. *J Nat Gas Sci Eng* 9:16-27, 2012.

[167] U.S. Department of Energy. Clean Cities alternative fuel price report. January 2014, p. 3.

[168] U.S. Department of Energy. Clean Cities alternative fuel price report. October 2017, p. 4.

[169] Janssen A, Lienin SF, Gassmann F and Wokaun A. Model aided policy development for the market penetration of natural gas vehicles in Switzerland. *Transp Res Part A Policy Pract* 40(4):316-33, 2006.

[170] Büyükkaya E, Engin T and Cerit M. Effects of thermal barrier coating on gas emissions and performance of a LHR engine with different injection timings and valve adjustments. *Energy Convers Manag* 47(9-10):1298-310, 2006.

[171] Kamo R, Assanis DN and Bryzik W. Thin thermal barrier coatings for engines. SAE Technical Paper 890143, 1989.

[172] Yao Z and Qian Z. Thermal analysis of Nano ceramic coated piston used in natural gas engine. *J Alloys Compd* 768:441-50, 2018.

[173] Yeh S. An empirical analysis on the adoption of alternative fuel vehicles: The case of natural gas vehicles. *Energy Policy* 35(11):5865-75, 2007.

[174] Huang Z, Zhang Y, Zeng K, Liu B, Wang Q and Jiang D. Measurements of laminar burning velocities for natural gas-hydrogen-air mixtures. *Combust Flame* 146(1-2):302-11, 2006.

[175] Huang Z, Zhang Y, Wang Q, Wang J, Jiang D and Miao H. Study on flame propagation characteristics of natural gas-hydrogen-air mixtures. *Energy Fuels* 20(6):2385-90, 2006.

[176] Donohoe N, Heufer A, Metcalfe WK, Curran HJ, Davis ML, Mathieu O et al. Ignition delay times, laminar flame speeds, and mechanism validation for natural gas/hydrogen blends at elevated pressures. *Combust Flame*

161(6):1432-43, 2014.

[177] Kahraman N, Çeper B, Akansu SO and Aydin K. Investigation of combustion characteristics and emissions in a spark-ignition engine fuelled with natural gas-hydrogen blends. *Int J Hydrog Energy* 34(2):1026-34, 2009.

[178] Hu E, Huang Z, Liu B, Zheng J and Gu X. Experimental study on combustion characteristics of a spark-ignition engine fueled with natural gas-hydrogen blends combining with EGR. *Int J Hydrog Energy* 34(2):1035-44, 2009.

[179] de Ferrières S, El Bakali A, Lefort B, Montero M and Pauwels JF. Experimental and numerical investigation of low-pressure laminar premixed synthetic natural gas/O_2/N_2 and natural gas/H_2/O_2/N_2 flames. *Combust Flame* 154(3):601-23, 2008.

[180] de Ferrières S, El Bakali A, Gasnot L, Montero M and Pauwels JF. Kinetic effect of hydrogen addition on natural gas premixed flames. *Fuel* 106:88-97, 2013.

[181] Nilsson EJK, van Sprang A, Larfeldt J and Konnov AA. The comparative and combined effects of hydrogen addition on the laminar burning velocities of methane and its blends with ethane and propane. *Fuel* 189:369-76, 2017.

[182] Dagaut P and Nicolle A. Experimental and detailed kinetic modeling study of hydrogen-enriched natural gas blend oxidation over extended temperature and equivalence ratio ranges. *Proc Combust Inst* 30(2):2631-8, 2005.

[183] Tang CL, Huang ZH and Law CK. Determination, correlation, and mechanistic interpretation of effects of hydrogen addition on laminar flame speeds of hydrocarbon-air mixtures. *Proc Combust Inst* 33(1):921-8, 2011.

[184] Dimopoulos P, Bach C, Soltic P and Boulouchos K. Hydrogen-natural gas blends fuelling passenger car engines: Combustion, emissions and well-to-wheels assessment. *Int J Hydrog Energy* 33(23):7224-36, 2008.

[185] Göckeler K, Krüger O and Paschereit CO. Laminar burning velocities and emissions of hydrogen-methane-air-steam mixtures. *J Eng Gas Turbines Power* 137(3), 031503, 2014.

[186] Lantz A, Collin R, Aldén M, Lindholm A, Larfeldt J and Lörstad D. Investigation of hydrogen enriched natural gas flames in a SGT-700/800 burner using OH PLIF and chemiluminescence imaging. *J Eng Gas Turbines Power* 137(3), 031505, 2014.

[187] Hoekstra RL, van Blarigan P and Mulligan N. NO_X emissions and efficiency of hydrogen, natural gas, and hydrogen/natural gas blended fuels.

SAE Technical Paper 961103, 1996.

[188] Ma F, Wang Y, Liu H, Li Y, Wang J and Zhao S. Experimental study on thermal efficiency and emission characteristics of a lean burn hydrogen enriched natural gas engine. *Int J Hydrog Energy* 32(18):5067-75, 2007.

[189] Akansu SO, Dulger Z, Kahraman N and Veziroğlu TN. Internal combustion engines fueled by natural gas-hydrogen mixtures. *Int J Hydrog Energy* 29(14):1527-39, 2004.

[190] Mehra RK, Duan H, Juknelevičius R, Ma F and Li J. Progress in hydrogen enriched compressed natural gas (HCNG) internal combustion engines – A comprehensive review. *Renew Sust Energy Rev* 80:1458-98, 2017.

[191] Ma F, Ding S, Wang Y, Wang Y, Wang J and Zhao S. Study on combustion behaviors and cycle-by-cycle variations in a turbocharged lean burn natural gas S.I. engine with hydrogen enrichment. *Int J Hydrog Energy* 33(23):7245-55, 2008.

[192] Alrazen HA and Ahmad KA. HCNG fueled spark-ignition (SI) engine with its effects on performance and emissions. *Renew Sust Energy Rev* 82(1):324-42, 2018.

[193] Larsen JF and Wallace JS. Comparison of emissions and efficiency of a turbocharged lean-burn natural gas and hythane-fueled engine. *J Eng Gas Turbines Power* 119(1):218-26, 1997.

[194] Munshi SR, Nedelcu C, Harris J, Edwards T, Williams J, Lynch F et al. Hydrogen blended natural gas operation of a heavy duty turbocharged lean burn spark ignition engine. SAE Technical Paper 2004-01-2956, 2004.

[195] Klell M, Eichlseder H and Sartory M. Mixtures of hydrogen and methane in the internal combustion engine – Synergies, potential and regulations. *Int J Hydrog Energy* 37(15):11531-40, 2012.

[196] Verhelst S and Wallner T. Hydrogen-fueled internal combustion engines. *Prog Energy Combust Sci* 35(6):490-527, 2009.

[197] Yilanci A, Dincer I and Ozturk HK. A review on solar-hydrogen/fuel cell hybrid energy systems for stationary applications. *Prog Energy Combust Sci* 35(3):231-44, 2009.

[198] Lee HS, Vermaas WFJ and Rittmann BE. Biological hydrogen production: Prospects and challenges. *Trends Biotechnol* 28(5):262-71, 2010.

[199] Nikolaidis P and Poullikkas A. A comparative overview of hydrogen production processes. *Renew Sust Energy Rev* 67:597-611, 2017.

[200] Browne D, O'Mahony M and Caulfield B. How should barriers to alternative fuels and vehicles be classified and potential policies to promote innovative technologies be evaluated? *J Clean Prod* 35:140-51, 2012.

[201] Flynn PC. Commercializing an alternative vehicle fuel: Lessons learned from natural gas for vehicles. *Energy Policy* 30(7):613-9, 2002.

[202] United Nations. Resolution adopted by the General Assembly on 25 September 2015. Transforming out world: The 2030 Agenda for Sustainable Development (A/RES/70/1). 2015.

[203] Song J, Choi M and Park S. Comparisons of the volumetric efficiency and combustion characteristics between CNG-DI and CNG-PFI engines. *Appl Therm Eng* 121:595-603, 2017.

[204] Erfan I, Chitsaz I, Ziabasharhagh M, Hajialimohammadi A and Fleck B. Injection characteristics of gaseous jet injected by a single-hole nozzle direct injector. *Fuel* 160:24-34, 2015.

[205] Moon S. Potential of direct-injection for the improvement of homogeneous-charge combustion in spark-ignition natural gas engines. *Appl Therm Eng* 136:41-8, 2018.

[206] Pourkhesalian AM, Shamekhi AH and Salimi F. Alternative fuel and gasoline in an SI engine: A comparative study of performance and emissions characteristics. *Fuel* 89(5):1056-63, 2010.

[207] Zhang CH, Xie YL, Wang FS, Ma ZY, Qi DH and Qiu ZW. Emission comparison of light-duty in-use flexible-fuel vehicles fuelled with gasoline and compressed natural gas based on the ECE 15 driving cycle. *Proc Inst Mech Eng D: J Automob Eng* 225(1):90-8, 2011.

[208] Yao Z, Cao X, Shen X, Zhang Y, Wang X and He K. On-road emission characteristics of CNG-fueled bi-fuel taxis. *Atmos Environ* 84:198-204, 2014.

[209] Collantes G and Melaina MW. The co-evolution of alternative fuel infrastructure and vehicles: A study of the experience of Argentina with compressed natural gas. *Energy Policy* 39(2):664-75, 2011.

[210] Donateo T, Tornese F and Laforgia D. Computer-aided conversion of an engine from diesel to methane. *Appl Energy* 108:8-23, 2013.

[211] Liu J and Dumitrescu CE. Flame development analysis in a diesel optical engine converted to spark ignition natural gas operation. *Appl Energy* 230:1205-17, 2018.

[212] Chandra R, Vijay VK, Subbarao PMV and Khura TK. Performance evaluation of a constant speed IC engine on CNG, methane enriched biogas and biogas. *Appl Energy* 88(11):3969-77, 2011.

[213] Kobayashi K, Sako T, Sakaguchi Y, Morimoto S, Kanematsu S, Suzuki K et al. Development of HCCI natural gas engines. *J Nat Gas Sci Eng* 3(5):651-6, 2011.

[214] Oh C and Cha G. Impact of fuel, injection type and after-treatment system on particulate emissions of light-duty vehicles using different fuels on FTP-75 and HWFET test cycles. *Int J Automot Technol* 16(6):895-901, 2015.

[215] Li W, Liu Z, Wang Z and Xu Y. Experimental investigation of thermal and diluent effects of EGR components on combustion and NO_X emissions of a turbocharged natural gas SI engine. *Energy Convers Manag* 88:1041-50, 2014.

[216] Wohlgemuth S, Roesler S and Wachtmeister G. Piston design optimization for a two-cylinder lean-burn natural gas engine – 3D-CFD-simulation and test bed measurements. SAE Technical Paper 2014-01-1326, 2014.

[217] Yu X, Liu Z, Wang Z and Dou H. Optimize combustion of compressed natural gas engine by improving in-cylinder flows. *Int J Automot Technol* 14(4):539-49, 2013.

[218] Sen AK, Litak G, Yao BF and Li GX. Analysis of pressure fluctuations in a natural gas engine under lean burn conditions. *Appl Therm Eng* 30(6-7):776-9, 2010.

[219] Yang LP, Song EZ, Ding SL, Brown RJ, Marwan N and Ma XZ. Analysis of the dynamic characteristics of combustion instabilities in a pre-mixed lean-burn natural gas engine. *Appl Energy* 183:746-59, 2016.

[220] Ji S, Lan X, Cheng Y, Zhao X, Li X and Wang F. Cyclic variation of large-bore multi point injection engine fuelled by natural gas with different types of injection systems. *Appl Therm Eng* 102:1241-9, 2016.

[221] Rogers T, Petersen P, Koopmans L, Lappas P and Boretti A. Structural characteristics of hydrogen and compressed natural gas fuel jets. *Int J Hydrog Energy* 40(3):1584-97, 2015.

[222] Dong Q, Li Y, Song E, Yao C, Fan L and Sun J. The characteristic analysis of high-pressure gas jets for natural gas engine based on shock wave structure. *Energy Convers Manag* 149:26-38, 2017.

[223] Yan B, Wang H, Zheng Z, Qin Y and Yao M. The effects of LIVC Miller cycle on the combustion characteristics and thermal efficiency in a stoichiometric operation natural gas engine with EGR. *Appl Therm Eng* 122:439-50, 2017.

[224] Fan BW, Pan JF, Pan ZH, Tang AK, Zhu YJ and Xue H. Effects of pocket shape and ignition slot locations on the combustion processes of a rotary engine fueled with natural gas. *Appl Therm Eng* 89:11-27, 2015.

[225] Fan B, Pan J, Yang W, Liu Y, Bani S and Chen W. Numerical investigation of the effect of injection strategy on mixture formation and combustion process in a port injection natural gas rotary engine. *Energy Convers Manag* 133:511-23, 2017.

[226] Adlercreutz L, Cronhjort A, Andersen J and Ogink R. Optimizing the natural gas engine for CO_2 reduction. SAE Technical Paper 2016-01-0875, 2016.

[227] Thiruvengadam A, Besch MC, Thiruvengadam P, Pradhan S, Carder D, Kappanna H et al. Emission rates of regulated pollutants from current technology heavy-duty diesel and natural gas goods movement vehicles. *Environ Sci Technol* 49(8):5236-44, 2015.

[228] Quiros DC, Thiruvengadam A, Pradhan S, Besch M, Thiruvengadam P, Demirgok B et al. Real-world emissions from modern heavy-duty diesel, natural gas, and hybrid diesel trucks operating along major California freight corridors. *Emiss Control Sci Technol* 2(3):156-72, 2016.

[229] Misra C, Ruehl C, Collins J, Chernich D and Herner J. In-use NO_X emissions from diesel and liquefied natural gas refuse trucks equipped with SCR and TWC, respectively. *Environ Sci Technol* 51(12):6981-9, 2017.

[230] Zhang S, Wu Y, Liu H, Huang R, Yang L, Li Z et al. Real-world fuel consumption and CO_2 emissions of urban public buses in Beijing. *Appl Energy* 113:1645-55, 2014.

[231] López JM, Gómez Á, Aparicio F and Sánchez FJ. Comparison of GHG emissions from diesel, biodiesel and natural gas refuse trucks of the City of Madrid. *Appl Energy* 86(5):610-5, 2009.

[232] Hallstrom K, Voss KE and Shah S. The formation of N_2O on the SCR catalyst in a heavy duty US 2010 emission control system. SAE Technical Paper 2013-01-2463, 2013.

[233] Thiruvengadam A, Besch M, Carder D, Oshinuga A, Pasek R, Hogo H et al. Unregulated greenhouse gas and ammonia emissions from current technology heavy-duty vehicles. *J Air Waste Manag Assoc* 66(11):1045-60, 2016.

[234] Rose L, Hussain M, Ahmed S, Malek K, Costanzo R and Kjeang E. A comparative life cycle assessment of diesel and compressed natural gas powered refuse collection vehicles in a Canadian city. *Energy Policy* 52:453-61, 2013.

[235] Navarro E, Leo TJ and Corral R. CO_2 emissions from a spark ignition engine operating on natural gas-hydrogen blends (HCNG). *Appl Energy* 101:112-20, 2013.

[236] Moreno F, Arroyo J, Muñoz M and Monné C. Combustion analysis of a spark ignition engine fueled with gaseous blends containing hydrogen. *Int J Hydrog Energy* 37(18):13564-73, 2012.

[237] Flekiewicz B, Flekiewicz M and Kubica G. Identification of optimal CNG-hydrogen enrichment ratio in the small SI engines. SAE Technical Paper

2012-32-0015, 2012.

[238] Diéguez PM, Urroz JC, Marcelino-Sádaba S, Pérez-Ezcurdia A, Benito-Amurrio M, Sáinz D et al. Experimental study of the performance and emission characteristics of an adapted commercial four-cylinder spark ignition engine running on hydrogen-methane mixtures. *Appl Energy* 113:1068-76, 2014.

[239] Sagar SMV and Agarwal AK. Experimental validation of accuracy of dynamic hydrogen-compressed natural gas mixing system using a single cylinder spark ignition engine. *Int J Hydrog Energy* 41(32):14272-82, 2016.

[240] Verma G, Prasad RK, Agarwal RA, Jain S and Agarwal AK. Experimental investigations of combustion, performance and emission characteristics of a hydrogen enriched natural gas fuelled prototype spark ignition engine. *Fuel* 178:209-17, 2016.

[241] Arroyo J, Moreno F, Muñoz M, Monné C and Bernal N. Combustion behavior of a spark ignition engine fueled with synthetic gases derived from biogas. *Fuel* 117(A):50-8, 2014.

[242] Yang B and Zeng K. Effects of natural gas injection timing and split pilot fuel injection strategy on the combustion performance and emissions in a dual-fuel engine fueled with diesel and natural gas. *Energy Convers Manag* 168:162-9, 2018.

[243] Ansari E, Shahbakhti M and Naber J. Optimization of performance and operational cost for a dual mode diesel-natural gas RCCI and diesel combustion engine. *Appl Energy* 231:549-61, 2018.

[244] Yousefi A and Birouk M. Investigation of natural gas energy fraction and injection timing on the performance and emissions of a dual-fuel engine with pre-combustion chamber under low engine load. *Appl Energy* 189:492-505, 2017.

[245] Mustafi NN, Raine RR and Verhelst S. Combustion and emissions characteristics of a dual fuel engine operated on alternative gaseous fuels. *Fuel* 109:669-78, 2013.

[246] Ryu K. Effects of pilot injection timing on the combustion and emissions characteristics in a diesel engine using biodiesel-CNG dual fuel. *Appl Energy* 111:721-30, 2013.

[247] Imran S, Emberson DR, Diez A, Wen DS, Crookes RJ and Korakianitis T. Natural gas fueled compression ignition engine performance and emissions maps with diesel and RME pilot fuels. *Appl Energy* 124:354-65, 2014.

[248] Saravanan N and Nagarajan G. Performance and emission studies on port injection of hydrogen with varied flow rate with Diesel as an ignition source. *Appl Energy* 87(7):2218-29, 2010.

[249] Wang Y, Zhao Y, Xiao F and Li D. Combustion and emission characteristics of a diesel engine with DME as port premixing fuel under different injection timing. *Energy Convers Manag* 77:52-60, 2014.

[250] Fathi M, Saray RK and Checkel MD. The influence of exhaust gas recirculation (EGR) on combustion and emissions of n-heptane/natural gas fueled homogeneous charge compression ignition (HCCI) engines. *Appl Energy* 88(12):4719-24, 2011.

[251] Delpech V, Obiols J, Soleri D, Mispreuve L, Magere E and Kermarrec S. Towards an innovative combination of natural gas and liquid fuel injection in spark ignition engines. *SAE Int J Fuels Lubr* 3(2):196-209, 2010.

[252] Movahed MM, Tabrizi HB and Mirsalim M. Experimental investigation of the concomitant injection of gasoline and CNG in a turbocharged spark ignition engine. *Energy Convers Manag* 80:126-36, 2014.

[253] Tabar AR, Hamidi AA and Ghadamian H. Experimental investigation of CNG and gasoline fuels combination on a 1.7L bi-fuel turbocharged engine. *Int J Energy Environ Eng* 8(1):37-45, 2017.

[254] Obiols J, Soleri D, Dioc N and Moreau M. Potential of concomitant injection of CNG and gasoline on a 1.6L gasoline direct injection turbocharged engine. SAE Technical Paper 2011-01-1995, 2011.

[255] Yang Z, Rao S, Wang Y, Harsulkar J, Ansari E, Narasimhamurthy NM et al. Investigation of combustion knock distribution in a boosted methane-gasoline blended fueled SI engine. SAE Technical Paper 2018-01-0215, 2018.

[256] Singh E, Morganti K and Dibble R. Dual-fuel operation of gasoline and natural gas in a turbocharged engine. *Fuel* 237:694-706, 2019.

[257] Pipitone E and Beccari S. Performances and emissions improvement of an S.I. engine fuelled by LGP/Gasoline mixtures. SAE Technical Paper 2010-01-0615, 2010.

[258] Ji C, Wang S and Zhang B. Performance of a hybrid hydrogen-gasoline engine under various operating conditions. *Appl Energy* 97:584-9, 2012.

[259] Wang S and Ji C. Cyclic variation in a hydrogen-enriched spark-ignition gasoline engine under various operating conditions. *Int J Hydrog Energy* 37(1):1112-9, 2012.

[260] Liang C, Ji C and Liu X. Combustion and emissions performance of a DME-enriched spark-ignited methanol engine at idle condition. *Appl Energy* 88(11):3704-11, 2011.

[261] de Saint-Venant AJC and Wantzel PL. Mémoire et expériences sur l'écoulement de l'air. *J Ecole Polytech* (Paris) 16:85-122, 1839.

[262] Mach E and Salcher P. Photographische Fixierung der durch Projectile in der Luft eingeleiteten Vorgänge. *Ann Phys* (Berlin) 268(10):277-91, 1887.

[263] Prandtl L. Über die stationären Wellen in einem Gasstrahl. *Phys Z* 5(19):599-601, 1904.

[264] Courant R and Friedrichs KO. Supersonic flow and shock waves. New York: Springer-Verlag, 1976. ISBN 9780387902326

[265] Donaldson CD and Snedeker RS. A study of free jet impingement. Part 1. Mean properties of free and impinging jets. *J Fluid Mech* 45(2):281-319, 1971.

[266] Adamson Jr TC and Nicholls JA. On the structure of jets from highly underexpanded nozzles into still air. *J Aerosp Sci* 26(1):16-24, 1959.

[267] Crist S, Sherman PM and Glass DR. Study of the highly underexpanded sonic jet. *AIAA J* 4(1):68-71, 1966.

[268] Chuech SG, Lai MC and Faeth GM. Structure of turbulent sonic underexpanded free jets. *AIAA J* 27(5):549-59, 1989.

[269] Cumber PS, Fairweather M, Falle SAEG and Giddings JR. Predictions of the structure of turbulent, highly underexpanded jets. *J Fluids Eng* 117(4):599-604, 1995.

[270] Inman JAW, Danehy PM, Nowak RJ and Alderfer DW. Fluorescence imaging study of impinging underexpanded jets. 46th Aerospace Sciences Meeting and Exhibit, AIAA 2008-619, 2008.

[271] Franquet E, Perrier V, Gibout S and Bruel P. Free underexpanded jets in a quiescent medium: A review. *Prog Aerosp Sci* 77:25-53, 2015.

[272] Love ES, Grigsby CE, Lee LP and Woodling MJ. Experimental and theoretical studies of axisymmetric free jets. NASA Technical Report R-6, 1959.

[273] Aleshin AP, Denisov IN, Rogachev NM and Sivirkin VF. Effect of the cone angle and the degree of contraction of a sonic nozzle on the geometrical structure of the first roll of an underexpanded jet. *J Eng Phys* 28(2):207-10, 1975.

[274] Ewan BCR and Moodie K. Structure and velocity measurements in underexpanded jets. *Combust Sci Technol* 45(5-6):275-88, 1986.

[275] Hsu AG, Srinivasan R, Bowersox RDW and North SW. Molecular tagging using vibrationally excited nitric oxide in an underexpanded jet flowfield. *AIAA J* 47(11):2597-604, 2009.

[276] Wilcox DE, Weir Jr A, Nicholls JA and Dunlap R. Location of Mach discs and diamonds in supersonic air jets. *J Aeronaut Sci* 24(2):145-60, 1957.

[277] Ashkenas H and Sherman FS. The structure and utilization of supersonic free jets in low density wind tunnels. In: de Leeuw JH, editor. Proceedings of the 4th International Symposium on Rarefied Gas Dynamics 2(7). New York: Academic Press, 1965, p. 84-105.

[278] Driftmyer RT. A correlation of freejet data. *AIAA J* 10(8):1093-5, 1972.

[279] Addy AL. Effects of axisymmetric sonic nozzle geometry on Mach disk characteristics. *AIAA J* 19(1):121-2, 1981.

[280] Powell A. The sound-producing oscillations of round underexpanded jets impinging on normal plates. *J Acoust Soc Am* 83(2):515-33, 1988.

[281] Lewis Jr CH and Carlson DJ. Normal shock location in underexpanded gas and gas-particle jets. *AIAA J* 2(4):776-7, 1964.

[282] D'Attore L and Harshbarger FC. Parameters affecting the normal shock location in underexpanded gas jets. *AIAA J* 3(3):530-1, 1965.

[283] Avduevskii VS, Ivanov AV, Karpman IM, Traskovskii VD and Yudelovich MY. Flow in supersonic viscous underexpanded jet. *Fluid Dyn* 5(3):409-14, 1970.

[284] Billig FS, Orth RC and Lasky M. A unified analysis of gaseous jet penetration. *AIAA J* 9(6):1048-58, 1971.

[285] Young WS. Derivation of the free-jet Mach-disk location using the entropy-balance principle. *Phys Fluids* 18(11):1421-5, 1975.

[286] Narayanan AK and Damodaran KA. Mach disk of dual coaxial axisymmetric jets. *AIAA J* 31(7):1343-5, 1993.

[287] Abbett M. Mach disk in underexpanded exhaust plumes. *AIAA J* 9(3):512-4, 1971.

[288] Novopashin SA and Perepelkin AL. Axial symmetry loss of a supersonic preturbulent jet. *Phys Lett A* 135(4-5):290-3, 1989.

[289] Oertel H, Seiler F and Srulijes J. New explanation of noise production by supersonic jets with gas dredging. In: Dillmann A, Heller G, Klaas M, Kreplin HP and Nitsche W, editors. New results in numerical and experimental fluid mechanics VII. Springer, 2010, p. 389-97.

[290] Oertel H, Seiler F and Srulijes J. Vortex induced Mach waves in supersonic jets. In: Kontis K, editor. 28th International Symposium on Shock Waves 2. Springer, 2012, p. 657-63.

[291] Zapryagaev VI and Solotchin AV. Spectral characteristics of unstable flow in the mixing layer of supersonic underexpanded jet over its initial region. *Thermophys Aeromech* 16(2):209-18, 2009.

[292] Meshkov EE. Instability of the interface of two gases accelerated by a shock

wave. *Fluid Dyn* 4(5):101-4, 1969.

[293] Inman JAW, Danehy PM, Nowak RJ and Alderfer DW. Identification of instability modes of transition in underexpanded jets. 38th Fluid Dynamics Conference and Exhibit, AIAA 2008-4389, 2008.

[294] Zaman KBMQ. Asymptotic spreading rate of initially compressible jets – Experiment and analysis. *Phys Fluids* 10(10):2652-60, 1998.

[295] Palmer JL and Hanson RK. Application of method of characteristics to underexpanded, freejet flows with vibrational nonequilibrium. *AIAA J* 36(2):193-200, 1998.

[296] Prudhomme SM and Haj-Hariri H. Investigation of supersonic underexpanded jets using adaptive unstructured finite elements. *Finite Elem Anal Des* 17(1):21-40, 1994.

[297] Cheng TS and Lee KS. Numerical simulations of underexpanded supersonic jet and free shear layer using WENO schemes. *Int J Heat Fluid Flow* 26(5):755-70, 2005.

[298] Otobe Y, Kashimura H, Matsuo S, Setoguchi T and Kim HD. Influence of nozzle geometry on the near-field structure of a highly underexpanded sonic jet. *J Fluids Structures* 24(2):281-93, 2008.

[299] Oertel H. Prandtl essentials of fluid mechanics. 3rd ed. New York: Springer, 2010. ISBN 9781441915634

[300] Tannehill JC, Anderson DA and Pletcher RH. Computational fluid mechanics and heat transfer. 2nd ed. Washington DC: Taylor & Francis, 1997. ISBN 156032046X

[301] Wilcox DC. Turbulence modeling for CFD. La Cañada: DCW Industries, 1994. ISBN 0963605100

[302] Ferziger JH and Perić M. Computational methods for fluid dynamics. 3rd ed. Heidelberg: Springer, 2002. ISBN 3540420746

[303] Hirsch C. Numerical computation of internal and external flows, vol 1: The fundamentals of computational fluid dynamics. 2nd ed. Elsevier Science, 2007. ISBN 9780750665940

[304] Schmidt L, King J, Stokes J, Mullineux J, Ramasamy CR, Amiruddin AN et al. Validation of a CFD model of a hollow-cone spray with gasoline fuel blends. SAE Technical Paper 2011-01-3079, 2011.

[305] Yang X, Long X and Yao X. Numerical investigation on the mixing process in a steam ejector with different nozzle structures. *Int J Therm Sci* 56:95-106, 2012.

[306] Yan B, Wang H, Zheng Z, Qin Y and Yao M. The effect of combustion chamber geometry on in-cylinder flow and combustion process in a

stoichiometric operation natural gas engine with EGR. *Appl Therm Eng* 129:199-211.

[307] Baratta M, Misul D, Spessa E, Viglione L, Carpegna G and Perna F. Experimental and numerical approaches for the quantification of tumble intensity in high-performance SI engines. *Energy Convers Manag* 138:435-51, 2017.

[308] Yan B, Tong L, Wang H, Zheng Z, Qin Y and Yao M. Experimental and numerical investigation of the effects of combustion chamber reentrant level on combustion characteristics and thermal efficiency of stoichiometric operation natural gas engine with EGR. *Appl Therm Eng* 123:1473-83, 2017.

[309] Yakhot V, Orszag SA, Thangam S, Gatski TB and Speziale CG. Development of turbulence models for shear flows by a double expansion technique. *Phys Fluids A: Fluid Dyn* 4(7):1510-20, 1992.

[310] Han Z and Reitz D. Turbulence modeling of internal combustion engines using RNG k-ε models. *Combust Sci Technol* 106(4-6):267-95, 1995.

[311] El Tahry SH. k-ε equation for compressible reciprocating engine flows. *J Energy* 7(4):345-53, 1983.

[312] Shu J, Fu J, Liu J, Ma Y, Wang S, Deng B et al. Effects of injector spray angle on combustion and emissions characteristics of a natural gas (NG)-diesel dual fuel engine based on CFD coupled with reduced chemical kinetic model. *Appl Energy* 233-234:182-95, 2019.

[313] Poorghasemi K, Saray RK, Ansari E, Irdmousa BK, Shahbakhti M and Naber JD. Effect of diesel injection strategies on natural gas/diesel RCCI combustion characteristics in a light duty diesel engine. *Appl Energy* 199:430-46, 2017.

[314] Wang F, Reitz RD, Pera C, Wang Z and Wang J. Application of generalized RNG turbulence model to flow in motored single-cylinder PFI engine. *Eng Appl Comp Fluid* 7(4):486-95, 2013.

[315] Chan EC, Davy MH, de Simone G and Mulone V. Numerical and experimental characterization of a natural gas engine with partially stratified charge spark ignition. *J Eng Gas Turbines Power* 133(2), 022801, 2010.

[316] Swantek AB, Duke DJ, Kastengren AL, Sovis N, Powell CF, Bartolucci L et al. An experimental investigation of gas fuel injection with X-ray radiography. *Exp Therm Fluid Sci* 87:15-29, 2017.

[317] Bartolucci L, Scarcelli R, Wallner T, Swantek A, Powell CF, Kastengren A et al. CFD and X-ray analysis of gaseous direct injection from an outward opening injector. SAE Technical Paper 2016-01-0850, 2016.

[318] Choi M, Lee S and Park S. Numerical and experimental study of gaseous fuel injection for CNG direct injection. *Fuel* 140:693-700, 2015.

[319] Chitsaz I, Saidi MH, Mozafari AA and Hajialimohammadi A. Experimental and numerical investigation on the jet characteristics of spark ignition direct injection gaseous injector. *Appl Energy* 105:8-16, 2013.

[320] Keskinen K, Kaario O, Nuutinen M, Vuorinen V, Künsch Z, Liavåg O et al. Mixture formation in a direct injection gas engine: Numerical study on nozzle type, injection pressure and injection timing effects. *Energy* 94:542-56, 2016.

[321] Douailler B, Ravet F, Delpech V, Soleri D, Reveille B and Kumar R. Direct injection of CNG on high compression ratio spark ignition engine: Numerical and experimental investigation. SAE Technical Paper 2011-01-0923, 2011.

[322] Scarcelli R, Wallner T, Matthias N, Salazar V and Kaiser S. Numerical and optical evolution of gaseous jets in direct injection hydrogen engines. SAE Technical Paper 2011-01-0675, 2011.

[323] Papageorgakis G and Assanis DN. Optimizing gaseous fuel-air mixing in direct injection engines using an RNG based k-ε model. SAE Technical Paper 980135, 1998.

[324] Baratta M and Rapetto N. Fluid-dynamic and numerical aspects in the simulation of direct CNG injection in spark-ignition engines. *Comput Fluids* 103:215-33, 2014.

[325] Deshmukh A, Vishwanathan G, Bode M, Pitsch H, Khosravi M and van Bebber D. Characterization of hollow cone gas jets in the context of direct gas injection in internal combustion engines. *SAE Int J Fuels Lubr* 11(4):353-77, 2018.

[326] Bonelli F, Viggiano A and Magi V. A numerical analysis of hydrogen underexpanded jets under real gas assumption. *J Fluids Eng* 135(12), 121101, 2013.

[327] Lemmon EW, McLinden MO and Friend DG. Thermophysical properties of fluid systems. In: Linstrom PJ and Mallard WG, editors. NIST chemistry webbook, NIST standard reference database 69. Washington DC: National Institute of Standards and Technology (U.S.), 1998.

[328] Launder BE and Spalding DB. The numerical computation of turbulent flows. *Comput Methods Appl Mech Eng* 3(2):269-89, 1974.

[329] Issa RI. Solution of the implicitly discretised fluid flow equations by operator-splitting. *J Comput Phys* 62(1):40-65, 1986.

[330] Issa RI, Ahmadi-Befrui B, Beshay KR and Gosman AD. Solution of the

implicitly discretised reacting flow equations by operator-splitting. *J Comput Phys* 93(2):388-410, 1991.

[331] Li Y, Kirkpatrick A, Mitchell C and Willson B. Characteristic and computational fluid dynamics modeling of high-pressure gas jet injection. *J Eng Gas Turbines Power* 126(1):192-7, 2004.

[332] Yadollahi B and Boroomand M. The effect of combustion chamber geometry on injection and mixture preparation in a CNG direct injection SI engine. *Fuel* 107:52-62, 2013.

[333] Maté B, Graur IA, Elizarova T, Chirokov I, Tejeda G, Fernández JM et al. Experimental and numerical investigation of an axisymmetric supersonic jet. *J Fluid Mech* 426:177-97, 2001.

[334] Velikorodny A and Kudriakov S. Numerical study of the near-field of highly underexpanded turbulent gas jets. *Int J Hydrog Energy* 37(22):17390-9, 2012.

[335] Volchkov VV and Ivanov AV. Thickness and internal structure of a normal shock formed by discharge of a highly underexpanded jet into a low-density space. *Fluid Dyn* 4(3):113-5, 1969.

[336] Di Rosa MD, Change AY and Hanson RK. Continuous wave dye-laser technique for simultaneous, spatially resolved measurements of temperature, pressure, and velocity of NO in an underexpanded free jet. *Appl Opt* 32(21):4074-87, 1993.

[337] Yee HC. A class of high-resolution explicit and implicit shock-capturing methods. NASA Technical Memorandum 101088, 1989.

[338] Baratta M, d'Ambrosio S and Misul D. Performance and emissions of a turbocharged spark ignition engine fuelled with CNG and CNG/hydrogen blends. SAE Technical Paper 2013-01-0866, 2013.

[339] Baratta M, d'Ambrosio S, Misul D and Spessa E. Effects of H_2 addition to compressed natural gas blends on cycle-to-cycle and cylinder-to-cylinder combustion variation in a spark-ignition engine. *J Eng Gas Turbines Power* 136(5), 051502, 2014.

[340] Veser A, Kuznetsov M, Fast G, Friedrich A, Kotchourko N, Stern G et al. The structure and flame propagation regimes in turbulent hydrogen jets. *Int J Hydrog Energy* 36(3):2351-9, 2011.

[341] Mitchell DM, Honnery DR and Soria J. Near-field structure of underexpanded elliptic jets. *Exp Fluids* 54:1578-90, 2013.

[342] Valentich G, Upadhyay P and Kumar R. Mixing characteristics of a moderate aspect ratio screeching supersonic rectangular jet. *Exp Fluids* 57:71-84, 2016.

[343] Saddington AJ, Lawson NJ and Knowles K. An experimental and numerical investigation of under-expanded turbulent jets. *Aeronaut J* 108(1081):145-52, 2004.

[344] Yüceil KB, Ötügen MV and Arik E. Interferometric Rayleigh scattering and PIV measurements in the near field of underexpanded sonic jets. 41st Aerospace Sciences Meeting and Exhibit, AIAA 2003-917, 2003.

[345] Boguszko M and Elliott GS. On the use of filtered Rayleigh scattering for measurements in compressible flows and thermal fields. *Exp Fluids* 38(1):33-49, 2005.

[346] Baert R, Klaassen A and Doosje E. Direct injection of high pressure gas: Scaling properties of pulsed turbulent jets. *SAE Int J Engines* 3(2):383-95, 2010.

[347] Rao SMV and Jagadeesh G. Novel supersonic nozzles for mixing enhancement in supersonic ejectors. *Appl Therm Eng* 71(1):62-71, 2014.

[348] Hatanaka K, Hirota M, Saito T, Nakamura Y, Suzuki Y and Koyaguchi T. Flow visualization of supersonic free jet utilizing acetone LIF. In: Kontis K, editor. 28th International Symposium on Shock Waves 2. Springer, 2012, p. 179-84.

[349] Yu J, Vuorinen V, Kaario O, Sarjovaara T and Larmi M. Visualization and analysis of the characteristics of transitional underexpanded jets. *Int J Heat Fluid Flow* 44:140-54, 2013.

[350] Goldstein RJ and Kuehn TH. Optical systems for flow measurement: Shadowgraph, schlieren, and interferometric techniques. In: Goldstein RJ, editor. Fluid mechanics measurements. 2nd ed. London: Taylor & Francis, 1996, p. 451-508. ISBN 9781560323068

[351] Schöpf W, Patterson JC and Brooker AMH. Evaluation of the shadowgraph method for the convective flow in a side-heated cavity. *Exp Fluids* 21(5):331-40, 1996.

[352] White TR and Milton BE. Shock wave calibration of under-expanded natural gas fuel jets. *Shock Waves* 18(5):353-64, 2008.

[353] Menon N and Skews BW. Shock wave configurations and flow structures in non-axisymmetric underexpanded sonic jets. *Shock Waves* 20(3):175-90, 2010.

[354] Hatanaka K and Saito T. Influence of nozzle geometry on underexpanded axisymmetric free jet characteristics. *Shock Waves* 22(5):427-34, 2012.

[355] Behrouzi P and McGuirk JJ. Underexpanded jet development from a rectangular nozzle with aft-deck. *AIAA J* 53(5):1287-98, 2015.

[356] Hajialimohammadi A, Honnery D, Abdullah A and Mirsalim MA. Time

resolved characteristics of gaseous jet injected by a group-hole nozzle. *Fuel* 113:497-505, 2013.

[357] Gerold J, Vogl P and Pfitzner M. New correlation of subsonic, supersonic and cryo gas jets validated by highly accurate schlieren measurements. *Exp Fluids* 54:1542-56, 2013.

[358] Johansen LCR, de Benito Sienes E and Dahlander P. Analysis of transient compressible gas jets using high speed schlieren imaging. SAE Technical Paper 2013-01-0871, 2013.

[359] Hajialimohammadi A, Edgington-Mitchell D, Honnery D, Montazerin N, Abdullah A and Mirsalim MA. Ultra high speed investigation of gaseous jet injected by a single-hole injector and proposing of an analytical method for pressure loss prediction during transient injection. *Fuel* 184:100-9, 2016.

[360] Friedrich W, Grzeszik R, Lauschke P, Zelenov V and Wensing M. The impact of a combustion chamber optimization on the mixture formation and combustion in a CNG-DI engine in stratified operation. SAE Technical Paper 2017-01-0779, 2017.

[361] Sankesh D, Petersen P and Lappas P. Flow characteristics of natural-gas from an outward-opening nozzle for direct injection engines. *Fuel* 218:188-202, 2018.

[362] Toepler A. Beobachtungen nach einer neuen optischen Methode: ein Beitrag zur experimental-Physik. Bonn: Cohen, 1864.

[363] Hecht E. Optics. 5th ed. Pearson Education, 2017, p. 96-158. ISBN 9781292096933

[364] Schardin H. Schlieren methods and their applications. NASA Technical Translation F-12,731, 1970. Ergebnisse der exakten Naturwissenschaften, vol 20. Berlin: Springer-Verlag, 1942, p. 303-439.

[365] Settles GS. Schlieren and shadowgraph techniques: Visualizing phenomena in transparent media. Springer-Verlag, 2001, p. 25-38. ISBN 9783540661559

[366] Mitchell DM, Honnery DR and Soria J. The visualization of the acoustic feedback loop in impinging underexpanded supersonic jet flows using ultra-high frame rate schlieren. *J Vis* 15(4):333-41, 2012.

[367] Canny J. A computational approach to edge detection. *IEEE Trans Pattern Anal Mach Intell* PAMI-8(6):679-98, 1986.

[368] Williams TC and Shaddix CR. Simultaneous correction of flat field and nonlinearity response of intensified charge-coupled devices. *Rev Sci Instrum* 78(12):1-6, 2007.

[369] Ouellette P and Hill PG. Turbulent transient gas injections. *J Fluids Eng* 122(4):743-52, 2000.

[370] Hagemann G, Immich H, Nguyen TV and Dumnov GE. Advanced rocket nozzles. *J Propul Power* 14(5):620-34, 1998.

[371] Verma SB. Performance characteristics of an annular conical aerospike nozzle with freestream effect. *J Propul Power* 25(3):783-91, 2009.

[372] Martin D, Cardenas M, Pischke P and Kneer R. Experimental investigation of near nozzle spray structure and velocity for a GDI hollowcone spray. *Atomization Sprays* 20(12):1065-76, 2010.

[373] Sukumaran S and Kong SC. Numerical study on mixture formation characteristics in a direct-injection hydrogen engine. *Int J Hydrog Energy* 35(15):7991-8007, 2010.

[374] Chiodi M, Berner HJ and Bargende M. Investigation on different injection strategies in a direct-injected turbocharged CNG-engine. SAE Technical Paper 2006-01-3000, 2006.

[375] Seboldt D, Lejsek D, Wentsch M, Chiodi M and Bargende M. Numerical and experimental studies on mixture formation with an outward-opening nozzle in a SI engine with CNG-DI. SAE Technical Paper 2016-01-0801, 2016.

[376] Whitesides R, Hessel RP, Flowers DL and Aceves SM. Application of gaseous sphere injection method for modeling under-expanded H_2 injection. *Combust Theor Model* 15(3):373-84, 2011.

[377] Choi M, Song J and Park S. Modeling of the fuel injection and combustion process in a CNG direct injection engine. *Fuel* 179:168-78, 2016.

[378] Kim GH, Kirkpatrick A and Mitchell C. Computational modeling of natural gas injection in a large bore engine. *J Eng Gas Turbines Power* 126(3):656-64, 2004.

[379] Baratta M, Catania AE, Spessa E, Herrmann L and Roessler K. Multi-dimensional modeling of direct natural-gas injection and mixture formation in a stratified-charge SI engine with centrally mounted injector. *SAE Int J Engines* 1(1):607-26, 2009.

[380] Seboldt D, Lejsek D and Bargende M. Experimental study on the impact of the jet shape of an outward-opening nozzle on mixture formation with CNG-DI. In: Bargende M, Reuss HC and Wiedemann J, editors. 16 Internationales Stuttgarter Symposium. Wiesbaden: Springer, 2016, p. 1295-313.

[381] Ouellette P and Hill PG. Visualization of natural gas injection for a compression ignition engine. SAE Technical Paper 921555, 1992.

[382] Kuensch ZA, Schlatter S, Keskinen K, Hulkkonen T, Larmi M and Boulouchos K. Experimental investigation on the gas jet behavior for a hollow cone piezoelectric injector. SAE Technical Paper 2014-01-2749, 2014.

[383] Ruggles AJ and Ekoto IW. Ignitability and mixing of underexpanded hydrogen jets. *Int J Hydrog Energy* 37(22):17549-60, 2012.

[384] Müller F, Schmitt M, Wright YM and Boulouchos K. Determination of supersonic inlet boundaries for gaseous engines based on detailed RANS and LES simulations. *SAE Int J Engines* 6(3):1532-43, 2013.

[385] Vuorinen V, Wehrfritz A, Duwig C and Boersma BJ. Large-eddy simulation on the effect of injection pressure and density on fuel jet mixing in gas engines. *Fuel* 130:241-50, 2014.

[386] Schmitt M, Hu R, Wright YM, Soltic P and Boulouchos K. Multiple cycle LES simulations of a direct injection natural gas engine. *Flow Turbulence Combust* 95(4):645-68, 2015.

[387] Li X, Wu K, Yao W and Fan X. A comparative study of highly underexpanded nitrogen and hydrogen jets using large eddy simulation. *Int J Hydrog Energy* 41(9):5151-61, 2016.

[388] Hamzehloo A and Aleiferis PG. Gas dynamics and flow characteristics of highly turbulent under-expanded hydrogen and methane jets under various nozzle pressure ratios and ambient pressures. *Int J Hydrog Energy* 41(15):6544-66, 2016.

[389] Li X, Zhou R, Yao W and Fan X. Flow characteristic of highly underexpanded jets from various nozzle geometries. *Appl Therm Eng* 125:240-53, 2017.

[390] Bartolucci L, Cordiner S, Mulone V and Rocco V. Natural gas partially stratified lean combustion: Analysis of the enhancing mechanisms into a constant volume combustion chamber. *Fuel* 211:737-53, 2018.

[391] Durbin PA. Near-wall turbulence closure modeling without "damping functions". *Theoret Comput Fluid Dynamics* 3(1):1-13, 1991.

[392] Durbin PA. Separated flow computations with the k-ε-v^2 model. *AIAA J* 33(4):659-64, 1995.

[393] Hanjalić K, Popovac M and Hadžiabdić M. A robust near-wall elliptic-relaxation eddy-viscosity turbulence model for CFD. *Int J Heat Fluid Flow* 25(6):1047-51, 2004.

[394] Popovac M and Hanjalić K. Compound wall treatment for RANS computation of complex turbulent flows and heat transfer. *Flow Turbulence Combust* 78(2):177-202, 2007.

[395] Kader BA. Temperature and concentration profiles in fully turbulent boundary layers. *Int J Heat Mass Transfer* 24(9):1541-4, 1981.

[396] Lam CKG and Bremhorst K. A modified form of the k-ε model for predicting wall turbulence. *J Fluids Eng* 103(3):456-60, 1981.

[397] Roe PL. Characteristic-based schemes for the Euler equations. *Annu Rev Fluid Mech* 18(1):337-65, 1986.

[398] Patankar SV and Spalding DB. A calculation procedure for heat, mass and momentum transfer in three-dimensional parabolic flows. *Int J Heat Mass Transfer* 15(10):1787-806, 1972.

[399] Karki KC and Patankar SV. Pressure based calculation procedure for viscous flows at all speeds in arbitrary configurations. *AIAA J* 27(9):1167-74, 1989.

[400] Demirdžić I, Lilek Ž and Perić M. A collocated finite volume method for predicting flows at all speeds. *Int J Numer Meth Fluids* 16(12):1029-50, 1993.

[401] Kee RJ, Rupley FM and Miller JA. The Chemkin thermodynamic data base. Sandia National Laboratories Report, SAND87-8215B, 1990.

[402] Gordon S and McBride BJ. Computer program for calculation of complex chemical equilibrium compositions, rocket performance, incident and reflected shocks, and Chapman-Jouguet detonations. NASA Technical report, NASA-SP-273, 1976.

[403] Chapman S and Cowling TG. The mathematical theory of non-uniform gases: An account of the kinetic theory of viscosity, thermal conduction and diffusion in gases. 3rd ed. Cambridge: Cambridge University Press, 1970. ISBN 052140844X

[404] Monchick L and Mason EA. Transport properties of polar gases. *J Chem Phys* 35(5):1676-97, 1961.

[405] Warnatz J. Influence of transport models and boundary conditions on flame structure. In: Peters N and Warnatz J, editors. Numerical methods in laminar flame propagation. Wiesbaden: Springer, 1982, p. 87-111.

[406] Parker JG. Rotational and vibrational relaxation in diatomic gases. *Phys Fluids* 2(4):449-62, 1959.

[407] Brau CA and Jonkman RM. Classical theory of rotational relaxation in diatomic gases. *J Chem Phys* 52(2):477-84, 1970.

[408] McBride BJ, Gordon S and Reno MA. Coefficients for calculating thermodynamic and transport properties of individual species. NASA Technical Memorandum 4513, 1993.

[409] Kee RJ, Dixon-Lewis G, Warnatz J, Coltrin ME, Miller JA and Moffat HK.

A Fortran computer code package for the evaluation of gas-phase, multicomponent transport properties. Sandia National Laboratories Report, SAND86-8246B, 1998.

[410] Barin I. Thermochemical data of pure substances. 3rd ed. Weinheim: VCH, 1995. ISBN 3527287450

[411] Poling BE, Prausnitz JM and O'Connell JP. Properties of gases and liquids. 5th ed. McGraw-Hill Education, 2001. ISBN 0070116822

[412] Fuller EN, Schettler PD and Giddings JC. New method for prediction of binary gas-phase diffusion coefficients. *Ind Eng Chem* 58(5):18-27, 1966.

[413] Crank J. The mathematics of diffusion. 2nd ed. Oxford: Clarendon Press, 1975, p. 1-11. ISBN 0198533446

[414] Duncan JB and Toor HL. An experimental study of three component gas diffusion. *AIChE J* 8(1):38-41, 1962.

[415] Krishna R and Wesselingh JA. The Maxwell-Stefan approach to mass transfer. *Chem Eng Sci* 52(6):861-911, 1997.

[416] Maxwell JC. On the dynamical theory of gases. *Philos Trans R Soc Lond* 157:49-88, 1867.

[417] J Stefan. Über das Gleichgewicht und die Bewegung, insbesondere die Diffusion von Gasgemengen. *Sitzungsber Kaiserl Akad Wiss Wien* 63:63-124, 1871.

[418] Taylor R and Krishna R. Multicomponent mass transfer. John Wiley & Sons Inc, 1993. ISBN 0471574171

[419] Richard H and Raffel M. Principle and applications of the background oriented schlieren (BOS) method. *Meas Sci Technol* 12(9):1576-85, 2001.

[420] Meier GEA. Computerized background-oriented schlieren. *Exp Fluids* 33(1):181-7, 2002.

[421] Venkatakrishnan L and Meier GEA. Density measurements using the Background Oriented Schlieren technique. *Exp Fluids* 37(2):237-47, 2004.

[422] Venkatakrishnan L and Suriyanarayanan P. Density field of supersonic separated flow past an afterbody nozzle using tomographic reconstruction of BOS data. *Exp Fluids* 47(3):463-73, 2009.

[423] Leopold F, Ota M, Klatt D and Maeno K. Reconstruction of the unsteady supersonic flow around a spike using the colored background oriented schlieren technique. *J Flow Control Meas Vis* 1(2):69-76, 2013.

[424] Sourgen F, Leopold F and Klatt D. Reconstruction of the density field using the Colored Background Oriented Schlieren Technique (CBOS). *Opt Laser Eng* 50(1):29-38, 2012.

[425] Cabaleiro JM, Aider JL, Artana G and Wesfreid JE. Single camera time-resolved 3D tomographic reconstruction of a pulsed gas jet. *J Vis* 16(4):263-74, 2013.

[426] Nicolas F, Todoroff V, Plyer A, Le Besnerais G, Donjat D, Micheli F et al. A direct approach for instantaneous 3D density field reconstruction from background-oriented schlieren (BOS) measurements. *Exp Fluids* 57:13, 2016.

[427] Delaunay B. Sur la sphère vide. *Bulletin de l'Académie des Sciences de l'URSS, Classe des sciences mathématiques et naturelles* 6:793-800, 1934.

[428] Nielson GM. Tools for triangulations and tetrahedrizations. In: Nielson GM, Hagen H and Müller H, editors. Scientific visualization: Overviews, methodologies, and techniques. Washington: IEEE Computer Society, 1997, p. 429-525.

[429] de Berg M, Cheong O, van Kreveld M and Overmars M. Computational geometry: Algorithms and applications. 3rd ed. Heidelberg: Springer-Verlag, 2008, p. 191-218. ISBN 9783540779735

[430] Amidror I. Scattered data interpolation methods for electronic imaging systems: A survey. *J Electron Imaging* 11(2):157-76, 2002.

[431] Celik I, Yavuz I and Smirnov A. Large eddy simulations of in-cylinder turbulence for internal combustion engines: A review. *Int J Engine Res* 2(2):119-48, 2001.

[432] Hamzehloo A and Aleiferis PG. Large eddy simulation of highly turbulent under-expanded hydrogen and methane jets for gaseous-fuelled internal combustion engines. *Int J Hydrog Energy* 39(36):21275-96, 2014.

[433] Rao SMV, Asano S and Saito T. Comparative studies on supersonic free jets from nozzles of complex geometry. *Appl Therm Eng* 99:599-612, 2016.

[434] Dauptain A, Cuenot B and Gicquel LYM. Large eddy simulation of stable supersonic jet impinging on flat plate. *AIAA J* 48(10):2325-38, 2010.

[435] Rana ZA, Thornber B and Drikakis D. Transvers jet injection into a supersonic turbulent cross-flow. *Phys Fluids* 23(4), 046103, 2011.

[436] Tam CKW. Supersonic jet noise. *Annu Rev Fluid Mech* 27:17-43, 1995.

[437] Williamson CHK. Vortex dynamics in the cylinder wake. *Annu Rev Fluid Mech* 28:477-539, 1996.

[438] Choi H, Jeon WP and Kim J. Control of flow over a bluff body. *Annu Rev Fluid Mech* 40:113-39, 2008.

[439] Williamson CHK and Govardhan R. Vortex-induced vibrations. *Annu Rev Fluid Mech* 36:413-55, 2004.

[440] Hamed AM, Vega J, Liu B and Chamorro LP. Flow around a semicircular cylinder with passive flow control mechanisms. *Exp Fluids* 58:22, 2017.

[441] Prasad A and Williamson CHK. The instability of the shear layer separating from a bluff body. *J Fluid Mech* 333:375-402, 1997.

[442] Alkidas AC and El Tahry SH. Contributors to the fuel economy advantage of DISI engines over PFI engines. SAE Technical Paper 2003-01-3101, 2003.

[443] Bai Y, Wang Z and Wang J. Part-load characteristics of direct injection spark ignition engine using exhaust gas trap. *Appl Energy* 87(8):2640-6, 2010.

[444] Hu C and Hou S. Investigations on combustion process of low-pressure CNG compound direct injection park-ignited engines. SAE Technical Paper 2010-32-0052, 2010.

[445] Fawzi Mohd Ali M, Kodoguchi Y, Oka Y and Kaida T. Improvement of combustion of CNG engine using CNG direct injection and gas-jet ignition method. SAE Technical Paper 2011-01-1994, 2011.

[446] Boretti A, Lappas P, Zhang B and Mazlan SK. CNG fueling strategies for commercial vehicles engines – a literature review. SAE Technical Paper 2013-01-2812, 2013.

[447] Thipse SS, Sonawane SB, D'Souza AF, Rairikar SD, Kavathekar KK and Marathe NV. Injection strategies, optimization and simulation techniques on DI CNG technology. SAE Technique Paper 2015-26-0046, 2015.

[448] Huang Z, Wang J, Liu B, Zeng K, Yu J and Jiang D. Combustion characteristics of a direct-injection engine fueled with natural gas-hydrogen blends under different ignition timings. *Fuel* 86(3):381-7, 2007.

[449] Sevik J, Pamminger M, Wallner T, Scarcelli R, Reese R, Iqbal A et al. Performance, efficiency and emissions assessment of natural gas direct injection compared to gasoline and natural gas port-fuel injection in an automotive engine. *SAE Int J Engines* 9(2):1130-42, 2016.

[450] Zeng K, Huang Z, Liu B, Liu L, Jiang D, Ren Y et al. Combustion characteristics of a direct-injection natural gas engine under various fuel injection timings. *Appl Therm Eng* 26(8-9):806-13, 2006.

[451] Abraham J, Magi V, MacInnes J and Bracco FV. Gas versus spay injection: Which mixes faster? SAE Technical Paper 940895, 1994.

[452] Kubesh JT. Development of a throttleless natural gas engine. SAE Technical Paper 2001-01-2522, 2001.

[453] A-Aziz A and Firmansyah. The effect of fuel rail pressure on the performance of a CNG-direct injection engine. SAE Technical Paper 2009-

01-1498, 2009.

[454] Mohammed SE, Baharom MB, A-Aziz AR and Firmansyah. The effects of fuel-injection timing at medium injection pressure on the engine characteristics and emissions of a CNG-DI engine fueled by a small amount of hydrogen in CNG. *Int J Hydrog Energy* 36(18):11997-2006, 2011.

[455] Friedrich W, Grzeszik R and Wensing M. Mixture formation in a CNG-DI engine in stratified operation. SAE Technical Paper 2015-24-2474, 2015.

[456] Zoldak P and Naber J. Spark ignited direct injection natural gas combustion in a heavy duty single cylinder test engine – Start of injection and spark timing effects. SAE Technical Paper 2015-01-2813, 2015.

[457] Sankesh D and Lappas P. Natural-gas direct-injection for spark-ignition engines – A review of late-injection studies. SAE Technical Paper 2017-26-0067, 2017.

[458] Melaika M and Dahlander P. Experimental investigation of methane direct injection with stratified charge combustion in optical SI single cylinder engine. SAE Technical Paper 2016-01-0797, 2016.

[459] Salazar VM and Kaiser SA. Influence of the in-cylinder flow field (tumble) on the fuel distribution in a DI hydrogen engine using a single-hole injector. SAE Technical Paper 2010-01-0579, 2010.

[460] Wei L and Geng P. A review on natural gas/diesel dual fuel combustion, emissions and performance. *Fuel Process Technol* 142:264-78, 2016.

[461] Hodgins KB, Hill PG, Ouellette P and Hung P. Directly injected natural gas fueling of diesel engines. SAE Technical Paper 961671, 1996.

[462] Faghani E, Patychuk B, McTaggart-Cowan G and Rogak S. Soot emission reduction from post injection strategies in a high pressure direct-injection natural gas engine. SAE Technical Paper 2013-24-0114, 2013.

[463] Mabson CWJ, Faghani E, Kheirkhah P, Kirchen P, Rogak SN and McTaggart-Cowan G. Combustion and emissions of paired-nozzle jets in a pilot-ignited direct-injection natural gas engine. SAE Technical Paper 2016-01-0807, 2016.

[464] Mikulski M and Bekdemir C. Understanding the role of low reactivity fuel stratification in a dual fuel RCCI engine – A simulation study. *Appl Energy* 191:689-708, 2017.

[465] Qiang Z, Li M and Shao S. Combustion process and emissions of a heavy-duty engine fueled with directly injected natural gas and pilot diesel. *Appl Energy* 157:217-28, 2015.

[466] Graves B, Olfert J, Patychuk B, Dastanpour R and Rogak S. Characterization of particulate matter morphology and volatility from a

compression-ignition natural-gas direct-injection engine. *Aerosol Sci Technol* 49(8):589-98, 2015.

[467] Tree DR and Svensson KI. Soot processes in compression ignition engines. *Prog Energy Combust Sci* 33(3):272-309, 2007.

[468] Gogolev IM and Wallace JS. Study of assisted compression ignition in a direct injected natural gas engine. *J Eng Gas Turbines Power* 139(12), 122802, 2017.

[469] Gogolev IM and Wallace JS. Performance and emissions of a compression-ignition direct-injected natural gas engine with shielded glow plug ignition assist. *Energy Convers Manag* 164:70-82, 2018.

[470] Di Iorio S, Sementa P and Vaglieco BM. Experimental investigation of a methane-gasoline dual-fuel combustion in a small displacement optical engine. SAE Technical Paper 2013-24-0046, 2013.

[471] Pamminger M, Sevik J, Scarcelli R, Wallner T, Wooldridge S, Boyer B et al. Evaluation of knock behavior for natural gas-gasoline blends in a light duty spark ignited engine. *SAE Int J Engines* 9(4):2153-65, 2016.

[472] Ghazal OH. A comparative evaluation of the performance of different fuel induction techniques for blends hydrogen-methane SI engine. *Int J Hydrog Energy* 38(16):6848-56, 2013.

[473] Verhelst S. Recent progress in the use of hydrogen as a fuel for internal combustion engines. *Int J Hydrog Energy* 39(2):1071-85, 2014.

[474] Dimitriou P and Tsujimura T. A review of hydrogen as a compression ignition engine fuel. *Int J Hydrog Energy* 42(38):24470-86, 2017.

[475] Zheng JJ, Wang JH, Wang B and Huang ZH. Effect of the compression ratio on the performance and combustion of a natural-gas direct-injection engine. *Proc Inst Mech Eng D: J Automob Eng* 223(1):85-98, 2009.

[476] Kinsey JL. Laser-induced fluorescence. *Ann Rev Phys Chem* 28(1):349-72, 1977.

[477] Yu J, Vuorinen V, Hillamo H, Sarjovaara T, Kaario O and Larmi M. An experimental study on high pressure pulsed jets for DI gas engine using planar laser-induced fluorescence. SAE Technical Paper 2012-01-1655, 2012.

[478] Mohamad TI, Harrison M, Jermy M and How HG. The structure of the high-pressure gas jet from a spark plug fuel injector for direct fuel injection. *J Vis* 13(2):121-31, 2010.

[479] Bruneaux G, Causse M and Omrane A. Air entrainment in diesel-like gas jet by simultaneous flow velocity and fuel concentration measurements, comparison of free and wall impinging jet configurations. *SAE Int J engines*

5(2):76-93, 2012.

[480] Blotevogel T, Egermann J, Goldlücke J, Leipertz A, Hartmann M, Schenk M et al. Developing planar laser-induced fluorescence for the investigation of the mixture formation process in hydrogen engines. SAE Technical Paper 2004-01-1408, 2004.

[481] Engel SR, Koch P, Braeuer A and Leipertz A. Simultaneous laser-induced fluorescence and Raman imaging inside a hydrogen engine. *Appl Opt* 48(35):6643-50, 2009.

[482] Salazar VM and Kaiser SA. An optical study of mixture preparation in a hydrogen-fueled engine with direct injection using different nozzle designs. *SAE Int J Engines* 2(2):119-31, 2010.

[483] Mederer T, Wensing M and Leipertz A. Laser-induced fluorescence to visualize gas mixture formation in an optically accessible hydrogen engine. In: The proceedings of the International Symposium on Diagnostics and Modeling of Combustion in Internal Combustion Engines. Japan Society of Mechanical Engineers, 2012, p. 374-9.

[484] Rubas PJ, Paul MA, Martin GC, Coverdill RE, Lucht RP, Peters JE et al. Methane jet penetration in a direct-injection natural gas engine. SAE Technical Paper 980143, 1998.

[485] Eckbreth AC. Laser diagnostics for combustion temperature and species. Abacus Press, 1988. ISBN 0856263443

[486] Zhao H and Ladommatos N. Optical diagnostics for in-cylinder mixture formation measurements in IC engines. *Prog Energy Combust Sci* 24(4):297-336, 1998.

[487] Melton LA and Lipp CW. Criteria for quantitative PLIF experiments using high-power lasers. *Exp Fluids* 35(4):310-6, 2003.

[488] Schulz C and Sick V. Tracer-LIF diagnostics: Quantitative measurement of fuel concentration, temperature and fuel/air ratio in practical combustion systems. *Prog Energy Combust Sci* 31(1):75-121, 2005.

[489] Stokes GG. On the change of refrangibility of light. *Philos Trans R Soc Lond* 142:463-562, 1852.

[490] Atkins P and de Paula J. Elements of physical chemistry. 5th ed. Oxford University Press, 2009, p. 472-96. ISBN 9781429218139

[491] Atkins P and Friedman R. Molecular quantum mechanics. 4th ed. Oxford University Press, 2005, p. 386-99. ISBN 0199274983

[492] Suppan P. Chemistry and light. Cambridge: Royal Society of Chemistry, 1994, p. 49-64. ISBN 0851868142

[493] Förster T. Zwischenmolekulare Energiewanderung und Fluoreszenz. *Ann*

Phys 437(1-2):55-75, 1948.

[494] Dexter DL. A theory of sensitized luminescence in solids. *J Chem Phys* 21(5):836-50, 1953.

[495] Barrett J. Atomic structure and periodicity. Cambridge: Royal Society of Chemistry, 2002, p. 153. ISBN 0854046577

[496] Kikuchi K, Sato C, Watabe M, Ikeda H, Takahashi Y and Miyashi T. New aspects of fluorescence quenching by molecular oxygen. *J Am Chem Soc* 115(12):5180-4, 1993.

[497] Astholz DC, Brouwer L and Troe J. High temperature ultraviolet absorption spectra of polyatomic molecules in shock waves. *Berichte der Bunsengesellschaft für physikalische Chemie* 85(7):559-64, 1981.

[498] Burton CS and Noyes AN Jr. Electronic energy relaxation in toluene vapor. *J Chem Phys* 49(4):1705-14, 1968.

[499] Koban W, Koch JD, Hanson RK and Schulz C. Absorption and fluorescence of toluene vapor at elevated temperatures. *Phys Chem Chem Phys* 6(11):2940-5, 2004.

[500] Koban W and Schulz C. Toluene laser-induced fluorescence (LIF) under engine-related pressures, temperatures and oxygen mole fractions. SAE Technical Paper 2005-01-2091, 2005.

[501] Guibert P, Modica V and Morin C. Influence of pressure, temperature and gas phase composition on biacetyl laser-induced fluorescence. *Exp Fluids* 40(2):245-56, 2006.

[502] Thurber MC, Grisch F, Kirby BJ, Votsmeier M and Hanson RK. Measurements and modeling of acetone laser-induced fluorescence with implications for temperature-imaging diagnostics. *Appl Opt* 37(21):4963-78, 1998.

[503] Thurber MC and Hanson RK. Pressure and composition dependences of acetone laser-induced fluorescence with excitation at 248, 266, and 308 nm. *Appl Phys B* 69(3):229-40, 1999.

[504] Baritaud TA and Heinze TA. Gasoline distribution measurements with PLIF in a SI engine. SAE Technical Paper 922355, 1992.

[505] Reboux J, Puechberty D and Dionnet F. A new approach of planar laser induced fluorescence applied to fuel/air ratio measurement in the compression stroke of an optical S.I. engine. SAE Technical Paper 941988, 1994.

[506] Reboux J, Puechberty D and Dionnet F. Study of mixture inhomogeneity and combustion development in a S.I. engine using a new approach of laser induced fluorescence (FARLIF). SAE Technical Paper 961205, 1996.

[507] Sacadura JC, Robin L, Dionnet F, Gervais D, Gastaldi P and Ahmed A. Experimental investigation of an optical direct injection S.I. engine using fuel-air ratio laser induced fluorescence. SAE Technical Paper 2000-01-1794, 2000.

[508] Frieden D, Sick V, Gronki J and Schulz C. Quantitative oxygen imaging in an engine. *Appl Phys B* 75(1):137-41, 2002.

[509] Koban W, Koch JD, Hanson RK and Schulz C. Toluene LIF at elevated temperatures: Implications for fuel-air ratio measurements. *Appl Phys B* 80(2):147-50, 2005.

[510] Koban W, Koch JD, Sick V, Wermuth N, Hanson RK and Schulz C. Predicting LIF signal strength for toluene and 3-pentanone under engine-related temperature and pressure conditions. *Proc Combust Inst* 30(1):1545-53, 2005.

[511] Williams B, Ewart P, Wang X, Stone R, Ma H, Walmsley H et al. Quantitative planar laser-induced fluorescence imaging of multi-component fuel/air mixing in a firing gasoline-direct-injection engine: Effects of residual exhaust gas on quantitative PLIF. *Combust Flame* 157(10):1866-78, 2010.

[512] Ma X, He X, Wang J and Shuai S. Co-evaporative multi-component fuel design for in-cylinder PLIF measurement and application in gasoline direct injection research. *Appl Energy* 88(8):2617-27, 2011.

[513] Mederer T, Wensing M and Leipertz A. Investigation of the interaction of charge motion and residual gas concentration in an optically accessible SI engine. SAE Technical Paper 2013-01-0558, 2013.

[514] Lind S, Aßmann S, Zigan L and Will S. Fluorescence characteristics of the fuel tracers triethylamine and trimethylamine for the investigation of fuel distribution in internal combustion engines. *Appl Opt* 55(7):1551-8, 2016.

[515] Gordon RL, Heeger C and Dreizler A. High-speed mixture fraction imaging. *Appl Phys B* 96(4):745-8, 2009.

[516] Lee KH, Lee CH and Lee CS. An experimental study on the spray behavior and fuel distribution of GDI injectors using the entropy analysis and PIV method. *Fuel* 83(7-8):971-80, 2004.

[517] Takahashi D, Nakata K, Yoshihara Y and Omura T. Combustion development to realize high thermal efficiency engines. *SAE Int J Engines* 9(3):1486-93, 2016.

[518] Yang J, Dong X, Wu Q and Xu M. Effects of enhanced tumble ratios on the in-cylinder performance of a gasoline direct injection optical engine. *Appl Energy* 236:137-46, 2019.

[519] Baratta M, Misul D, Viglione L and Xu J. Combustion chamber design for a high-performance natural gas engine: CFD modeling and experimental investigation. *Energy Convers Manag* 192:221-31, 2019.

[520] Desantes JM, Arrègle J, López J and García JM. Turbulent gas jets and diesel-like sprays in a crossflow: A study on axis deflection and air entrainment. *Fuel* 85(14-15):2120-32, 2006.

[521] Dryer FL. Chemical kinetic and combustion characteristics of transportation fuels. *Proc Combust Inst* 35(1):117-44, 2015.

[522] Huang J and Bushe WK. Experimental and kinetic study of autoignition in methane/ethane/air and methane/propane/air mixtures under engine-relevant conditions. *Combust Flame* 144(1-2):74-88, 2006.

Acknowledgment

Many consider accomplishing a PhD a lengthy and arduous journey. The path to being accorded the degree has admittedly been Odyssean with all the star gazing and mental adventures. And besides the necessary gain in technical expertise, such experience is as, if not more, invaluable. More precisely, this path is but one part of a far greater ultimate Odyssey – the life. And life itself, the existence spanning from an unconscious entrance of the conditio humana to a mere oblivion sans everything, or the process of decrease in internal entropy in an organized manner at the expense of energy, is all about experience.

At the end of such an eventful journey, I would like to acknowledge all the help provided to me, as a communing companion, an encouraging milestone, a guiding lighthouse, a soothing harbor, a carrying breeze, or a serendipitous treasure on an uncharted island.

In particular, I would like to express my gratitude to my academic tutors, Prof. Mirko Baratta and Prof. Ezio Spessa for their meticulous mentorship and continuing inspiration are ever-appreciated. I would like to thank Cesare Peletto from Centro Ricerche Fiat, Italy for supplying the studied engines, Jürgen Schneider from AVL Austria for the AVL FIRE code support, Alois Fürhapter, René Heindl and Heribert Fuchs from AVL Austria for the help with PLIF experiments, and Jean Preuhs and Patrick Salemi from Delphi Luxembourg for the information on injector details and schlieren experiments. I am in addition grateful to my parents and grandparents for their heartening, at many times from-a-distance, support.